SHRINK FIT EFFECTS ON ROTORDYNAMIC STABILITY: EXPERIMENTAL AND THEORETICAL STUDY

A Dissertation

by

SYED MUHAMMAD MOHSIN JAFRI

Submitted to the Office of Graduate Studies of
Texas A&M University
in partial fulfillment of the requirements for the degree of

DOCTOR OF PHILOSOPHY

May 2007

Major Subject: Mechanical Engineering

SHRINK FIT EFFECTS ON ROTORDYNAMIC STABILITY: EXPERIMENTAL AND THEORETICAL STUDY

A Dissertation

by

SYED MUHAMMAD MOHSIN JAFRI

Submitted to the Office of Graduate Studies of
Texas A&M University
in partial fulfillment of the requirements for the degree of

DOCTOR OF PHILOSOPHY

Approved by:

Chair of Committee,	John M. Vance
Committee Members,	Alan B. Palazzolo
	Luciana R. Barroso
	Guy Battle
Head of Department,	Dennis L. O'Neal

May 2007

Major Subject: Mechanical Engineering

ABSTRACT

Shrink Fit Effects on Rotordynamic Stability: Experimental and Theoretical Study. (May 2007)

Syed Muhammad Mohsin Jafri, B.E., NED University of Engineering & Technology, Karachi;

M.S., Texas A&M University

Chair of Advisory Committee: Dr. John M. Vance

This dissertation presents an experimental and theoretical study of sub-synchronous rotordynamic instability in rotors caused by interference and shrink fit interfaces. The experimental studies show the presence of strong unstable sub-synchronous vibrations in two different rotor setups with interference and shrink fit interfaces that were operated above their first critical speeds. The unstable vibrations occur at the first natural frequency of the rotor-bearing system. The instability caused complete wreckage of the test rig in one of the setups showing that these vibrations are potentially dangerous to the safe operation of rotating machines. The two different rotor setups that are studied are a single-disk rotor mounted on a uniform diameter shaft and a two-disk rotor with an aluminum sleeve shrink fitted to it at the outer surface of the two disks. In the single-disk rotor, an adjustable interference arrangement between the disk and the shaft is obtained through a tapered sleeve arrangement, which acts as the interference fit joint. The unstable sub-synchronous vibrations originate from slippage in the shrink fit and the interference fit interfaces that develop friction forces, which act as destabilizing cross-coupled moments when the rotor is operated above its first critical speed. The unique contribution offered through this work is the experimental validation of a physically correct model of internal friction which models the destabilizing

mechanism as a system of cross-coupled internal moments at the shrink fit interface. The dissertation describes stability simulations of various test rotor setups using the correct internal moments model. A commercial finite-element based software called XLTRC^{TM} is used to perform rotordynamic simulations for stability studies. The method of stability study is the computation of eigenvalues of the rotor-bearing system. A negative real part of the eigenvalue indicates instability. The simulations include the test rotors that were experimentally observed as stable and unstable with shrink and interference fit interfaces in their assemblies. The dissertation also describes the simulations of various imagined rotor configurations with shrink fit interfaces, and seeks to explain how configurations differ on rotordynamic stability depending upon several rotor-bearing parameters such as geometry and elastic properties, as well as upon the amount of internal friction parameters, which differ from configuration to configuration.

DEDICATION

To Almighty Allah for His help and blessings

To Abbu, Ammee, Deeju and all of my Family

"Study thou, in the name of thy Lord who created;-
Created man from Clots of Blood:-
Study thou! For thy Lord is the most Beneficent
Who hath taught the use of the Pen;-
Hath taught Man that which he knoweth not…"

——————— *Al-Koran- Chapter XCVI*
The Clot

ACKNOWLEDGEMENTS

My first and foremost acknowledgement in completing this intellectually challenging project that culminated in my Doctorate dissertation goes to Dr. John M. Vance. I am grateful to him for providing me with an opportunity to work on the project, along the way providing me unconditional technical and moral support. I have benefited immensely from his vast and extremely useful knowledge while completing my dissertation. I will forever remember him as being one of the greatest influences of the development of my technical knowledge and insight into the highest level of engineering.

My sincere appreciation is for my committee members, Dr. Palazzolo, Dr. Battle and Dr. Barroso, for agreeing to serve on my committee. I took classes under Dr. Palazzolo and Dr. Battle and benefited immensely from them, not only learning new material from the classes, but actually applying the knowledge and skills gained from there for the completion of my dissertation.

My sincere appreciation for the Turbomachinery Research Consortium (TRC) for their financial support of the Internal Friction Project. Without their support, it would not have been possible to conduct any experiments and therefore, the research would never have materialized.

Last, but not least, my acknowledgements go to my colleagues and co-workers at the Turbomachinery Laboratory, especially Eddie Denk, for helping me tremendously along the way in my research. Without Eddie's help and guidance at the machine shop and the test cell, no substantial progress would have been possible in these experiments. I do not have enough words to thank Eddie for his selfless help.

I am thankful to all of you.

NOMENCLATURE

X, Y, Z	Inertial frame coordinate axes
x, y, z	Rotating frame coordinate axes
t	Time [T]
ω	Rotational speed of a rotor [1/T]
Ω	Precessional or whirling speed of a rotor [1/T]
θ	Angular micro-slip at a shrink fit interface about the X-axis [-]
ϕ	Angular micro-slip at a shrink fit interface about the Y-axis [-]
θ_f	Forward whirl component of micro-slip about the X-axis [-]
θ_b	Forward whirl component of micro-slip about the X-axis [-]
α	Angular micro-slip at a shrink fit interface about the x-axis [-]
β	Angular micro-slip at a shrink fit interface about the y-axis [-]
$\dot{(\ )}$	Differentiation with respect to time [( ) / T]
$K_{\theta\theta}$	Direct moment stiffness at a shrink fit interface about the X-axis [FL]
$K_{\phi\phi}$	Direct moment stiffness at a shrink fit interface about the Y-axis [FL]
$K_{\theta\phi}$	Cross-coupled moment stiffness about the X-axis [FL]
$K_{\phi\theta}$	Cross-coupled moment stiffness about the Y-axis [FL]
$C_{\theta\theta}$	Direct moment damping at a shrink fit interface about the X-axis [FL]
$C_{\phi\phi}$	Direct moment damping at a shrink fit interface about the Y-axis [FL]
M_θ	Moment at a shrink fit interface about the X-axis [FL]
M_ϕ	Moment at a shrink fit interface about the Y-axis [FL]
M_α	Moment at a shrink fit interface about the x-axis [FL]
M_β	Moment at a shrink fit interface about the y-axis [FL]
i	Imaginary number operator ($\sqrt{-1}$) [-]
$e^{i\Omega t}$	Complex exponential-harmonic function [-]

sgn	The signum function (± 1) [-]
E_{diss}	Energy dissipated [LF]
E	Modulus of elasticity of a solid [F/L^2]
r	Radial coordinate [L]
σ	Applied stress on a solid [F/L^2]
ν	Poisson's ratio value of a solid [-]
N	Normal reaction or force from contact [F]
σ_r	Radial stress at an interface [F/L^2]
σ_t	Tangential stress at an interface [F/L^2]
δ_0	Radial interference or shrink fit at zero rotational speed [L]
$\delta(\omega)$	Radial interference or shrink fit as a function of rotational speed [L]
ψ	Circumferential location of a point at an interface [-]
R	Interface radius [L]
L	Axial contact length of an interface [L]
$V_{sliding}$	Relative sliding velocity at an interface [L/T]
$\underline{e_r}$	Unit vector in radial direction as measured in x,y,z frame [-]
$\underline{e_\psi}$	Unit vector in circumferential direction as measured in x,y,z frame [-]
μ_S	Coefficient of static friction [-]
μ_K	Coefficient of dynamic friction [-]

TABLE OF CONTENTS

Page

CHAPTER Page

LIST OF FIGURES

FIGURE Page

FIGURE Page

LIST OF TABLES

CHAPTER I

INTRODUCTION: THE IMPORTANCE OF THE RESEARCH

BACKGROUND OF PROBLEM

In the early 1920's it was observed that, with some rotors running well above their first critical speed, there occurred a series of rotor wrecks and damages which at first were not understandable and were attributed to improper balancing of the rotors. The General Electric Company (GE) encountered a series of serious damages to their blast furnace compressors running well above their first critical speeds. Dr. B.L. Newkirk from the GE Research Laboratories was appointed to research and investigate these damages and come up with some practical solutions to these problems. Newkirk discovered oil whip from fluid-film bearings as one of the causes of these rotors wrecks. However, there were other rotors operating without the fluid-film bearings and they had similar wreckages. At this time (1924), Dr. A.L. Kimball from the GE came up with an explanation of the latter type of rotor behaviors and proposed *internal friction* as a cause of rotor damages. He maintained that during rotational motion of the rotors, the rotor shafts bend and produce longitudinal friction forces inside the rotor material itself. This friction produces a disturbing torque on the rotor shaft, causing the shaft to move in the forward whirl direction, when the rotational speed is above the first critical speed. When the rotational speed is below the first critical speed of the rotor, the internal forces tend to dampen the system and reduce the vibrations. However, above the first critical speed, these forces provide a positive energy input to the system and thus increase the vibrations level, leading to the rotor damage.

This recognition of damping acting as energy addition to the system as in contrast to the strictly accepted view of damping as an energy dissipation was a remarkable intellectual achievement. It continues to be an intellectually challenging

---

This dissertation follows the style and format of Journal of Applied Mechanics.

problem to understand as to how a damping which is produced within a rotating system itself can lead to destabilization of the rotor motion, and in most cases, can cause serious rotor wreckages. Kimball showed in his paper, by deriving the equations of motion that the internal friction force tends to put the shaft motion in an ever-increasing spiral path. In the language of vibrations theory, this is called rotordynamic instability.

Thus, the phenomena came to be known as rotordynamic instability due to internal friction. He also modeled the internal friction force due to shrink fits in the rotor systems and mentioned that the effects of internal friction due to shrink fits are far more pronounced and predominant than those due to internal friction in the rotating shaft itself. Newkirk confirmed Kimball's observations through experiments and proposed shrink fits as the main reason for this rotordynamic instability.

Today, internal friction is seen to be a potential source of rotordynamic problems in advanced, high pressure Oxygen-Hydrogen propulsion equipment **[1].** Turbopumps such as the Space Shuttle Main Engine (SSME) High Pressure Oxidizer Turbopump (HPOTP) are of built-up design with many joints, fits, and areas for friction-induced excitation if slippage takes place. These rotors operate at supercritical speeds with light external damping. The power densities of these turbomachines are high. Therefore, the forces on the rotors are very large, which tends to encourage joint slippage and friction force generation. This has resulted in highly expensive and troublesome shut downs of machine operations at various leading turbomachinery users such as National Aeronautics Space Administration (NASA) and General Electric (GE) **[1, 2]**, to name only but a few. Therefore, the importance of research underlies in the motivation to safeguard the expensive rotating machines against permanent and costly damages and to understand the mechanics of destabilizing forces and moments produced due to slippage in shrink fit and interference fit interface joints, so as to propose better designs to the industry that will ensure stable operations throughout the operating speed range of turbomachines.

LITERATURE REVIEW

The design philosophy applied to rotating machinery initially began with the construction of very stiff rotors that would ensure operation below the first critical speed. It was only after Jeffcott's **[3]** analysis in 1919, when he showed that the rotors could be operated safely beyond their first critical speeds with proper rotor balancing that the trend in rotordynamics design changed. As the rigid rotor model was replaced by more flexible models, several failures were encountered when operating at speeds above the first critical speed. Most of the failures were of unknown origin at that time. Newkirk **[2]** of the General Electric Research Laboratory investigated the failures of compressor units in 1924, and found that these units encountered violent whirling at speeds above their first critical speeds, with the whirling rate equal to the first natural frequency. If the rotor speed were increased above its initial whirl speed, the whirl amplitude would increase, leading to the rotor failure. The speed at which the rotor begins to whirl is the threshold speed of instability. Kimball **[4]**, working with Newkirk, suggested the internal friction as a cause of shaft whirling. He showed that below the first critical speed, the internal friction would damp out the whirl motion, while above the first critical speed, it would sustain the whirl.

After a series of experiments on internal friction, Newkirk and Kimball arrived at a number of conclusions, the most important being: (1) the onset speed of whirling and the whirl amplitude is unaffected by the rotor balance, (2) whirling always occurs above the first critical, (3) whirling is encountered only in the built-up rotors, and (4) increasing the foundation flexibility or increasing the damping to the foundation increases the whirl threshold speed.

Gunter **[5]** explained some of the experimental results of Newkirk. He developed a linear rotordynamic model which includes the effects of bearings and foundation support flexibility and damping, besides the flexibility and internal damping of the rotor. He modeled the internal friction as a cross-coupled force. Through this model, he showed that external damping stabilizes the rotor bearing system, by increasing its threshold speed of instability. However, there is a limit to the external damping; a so-

called optimum damping that stabilizes the rotor. He also showed that the foundation flexibility, even without external damping, stabilizes the rotor. This means that no additional external damping is required to stabilize an unstable rotor; support flexibility alone may prevent a rotor to become unstable. However, in the case of fluid-film bearings, in which there is an appreciable amount of the cross-coupling forces due to thin, pressurized oil films which support the rotor loads, there is a strong tendency for the oil whirl and whip, in which case it is necessary to have an external damping source to stabilize the rotor running above its first critical speed.

Walton, Martin, and Lund **[1, 6]** conducted experimental and theoretical research on internal friction using a test rotor facility with axial spline and interference (shrink) fit joints. They proposed the internal friction model as a system of internal moments rather than the forces. Transient and steady-state simulations of their internal friction model showed close agreement with the experiments on their test rotor. Their experiments showed that both the axial spline joint and the shrink fit joints cause sub-synchronous instabilities and in some cases, super-synchronous instabilities at the rotor's first natural frequency. Their experiments also showed that the dry-film lubrication in the axial joints causes the instability component. Balancing of the rotor does not decrease the sub-synchronous instability due to the shrink fits to the same extent as the synchronous component is decreased. They modeled the rotor using finite elements and employed a Coulomb friction model to analyze both the axial spline joints and the shrink fit joints.

Kimball **[7, 8]** described experimental measurements of internal friction in different rotor materials, both with and without shrink fits. He postulated that internal hysteresis in a material during spin will cause the shaft to deflect sideways in the direction of forward whirl. He measured the magnitude of internal friction force by the sideways deflection of a loaded overhung shaft during spin. From the measurements, he concluded that the sideways deflection is independent of the spin velocity (or the rate of strain of the shaft fibers) and that shrink fits cause larger deflection of the shaft as compared to the case of no shrink fit on the shaft. These experiments showed that shrink

fits, rather than the material internal hysteresis, are a much more important mechanism of the forward whirl instability.

Lund **[9]** analyzed various models of internal friction due to axial splines and shrink fit joints in a rotor. His analysis showed that cross-coupled moments developed due to internal friction at the interface of the joints are a cause for rotor instability. Specifically, his analysis showed that the linear viscous damping model predicts instability above the first critical speed of the rotor, subject to the condition that the external backward whirl stabilizing effect due to bearing support asymmetry should not exceed the forward whirl destabilizing effect, whereas the solid friction model predicts some instability ranges above the first critical speed. He also showed that a micro-slip model for the axial splines predicts rotor instability above certain whirl amplitudes when the rotor speed exceeds the first critical speed.

Artilles **[10]** analyzed the effects of internal friction on rotor stability due to axial spline couplings. In the analysis, the internal friction is modeled as a system of cross-coupled moments which are developed at the spline interface due to relative sliding between the spline teeth. The simulations of the non-linear differential equations of motion for a rotor model which include the cross-coupled moments highlight the effects of various system parameters such as unbalance, side loads and initial conditions on the stability of the rotor. The simulations showed that the amplitude of the unstable sub-synchronous component is not dependent on the amount of imbalance included in the model. In most cases of the simulations, limit cycle amplitudes are predicted for the sub-synchronous component.

Black **[11]** analyzed different internal friction models for investigating the stability of a flexible rotor supported on damped, flexible bearings with no cross-coupling. The internal friction models were viscous friction, Coulomb friction and hysteretic friction. He showed that the viscous friction model predicts a threshold speed of instability for the rotor-bearing system which is greater than the rotor first critical speed, with the value of the threshold speed of instability dependent on external and internal damping parameters of the system. The analysis of the viscous friction model

predicted the rotor instability once the threshold speed is reached. For the Coulomb friction model, Black's analysis predicted that the rotor-bearing system becomes unstable as soon as the first critical speed of the rotor is traversed, if a certain parameter of the rotor, called relaxation strength (an indicative of friction inside the shaft material) is greater than twice the external damping ratio. This model predicts instability above the first critical speed for all subsequent higher speeds, subject to the condition that the relaxation strength is higher than the external damping ratio for instability to occur. That is, if the relaxation strength is not greater than twice the external damping ratio, the operations above the first critical speed will be stable, according to the Coulomb friction model. The hysteretic friction model predicts a range of speeds (above the first critical speed) in which the rotor-bearing system becomes unstable, but above that range, the operation is stable. The hysteretic friction and Coulomb friction are more realistic models as compared to the viscous friction model, due to: (1) prediction for a range of limited unstable operation, (2) instability of the rotor upon traversing its first critical speed. Both of these predictions have been verified experimentally. Black also analyzed the effects of bearing stiffness asymmetry on the rotor stability and concluded that the stiffness asymmetry promotes the system stability while the damping asymmetry demotes the stability to some extent.

Ehrich **[12]** presented a model of internal friction which showed that the internal friction stresses act in a direction perpendicular to the shaft deflection plane and that their magnitude is proportional to the rate of change of strain of the shaft fibers. His analysis showed that the ratio of the threshold speed of instability to the first critical speed depends upon the amount of internal and external damping of the rotor. His analysis also predicts instability above multiple critical speeds and shows that it is not necessarily the first mode of the rotor-bearing system which is always excited in an unstable whirl caused by the internal friction, but that it can be any mode, including any higher than the first mode, that can be excited.

Yamamoto and Ishida **[13]** formulated internal friction as a system of internal moments, which do not produce any instability below the first critical speed, but produce

a sub-synchronous forward whirl instability component above the first critical speed. Their formulation showed that the internal moments based on Coulomb's friction model are non-linear functions of the rotor's instantaneous position. Their formulation is of the same form as Walton, Martin and Lund's **[1]** formulation.

Vance and Ying **[14]** conducted an experimental study on a two-disk steel rotor with an aluminum sleeve having two shrink fit interfaces with the disks. Their experiments consisted of transient (run-up and coast-down) and steady state (fixed speed) tests of the rotor which supported Black's analysis **[10]**. Some tests showed that as soon as the rotor's first critical speed was traversed, the forward whirl instability appeared, suggesting the Coulomb friction model. The experiments also showed that the instability appeared in some speed ranges, both during the run-up and the coast-down and not over all the speeds above the first critical speed. The later observation is predicted by the hysteretic friction model. They also utilized a heat gun in the steady-state tests to heat the aluminum sleeve above the first critical speed and observed violent instability of the rotor, due to loosening of the shrink fit and generation of the internal friction effects at the shrink fit interface due to possible sliding/slipping between the disks and the sleeve which was caused by thermal expansion of the aluminum sleeve at the interface.

Mir **[15]** conducted rap tests on a single-disk rotor with an adjustable interference fit mechanism. His experimental results showed both Coulomb and hysteretic damping caused by interference fit in the rotor. He showed that the presence of either Coulomb or the hysteretic damping is dependent upon the amplitude of excitation of the rotor. From the rap test experiments, he showed that logarithmic decrement of the time traces of rotor vibrations decreased by increasing the tightness of the fit. From the analysis of logarithmic decrements, he concluded that the hysteretic damping coefficients will vary with the running speed. He acquired the data for forward whirl instability caused by interference fit in the running tests as the initial interference was reduced.

Srinivasan **[16]** conducted free-free tests on the same single-disk rotor as described in Chapter II of this dissertation. From the experiments, he obtained the time

traces of rotor vibrations with the interference fit values varied over a certain range. By analyzing the time traces, he obtained logarithmic decays and equivalent damping coefficients for internal friction in the rotor (because there was almost negligible external damping during those free-free tests). He converted the damping coefficients into equivalent cross-coupled coefficients to model the internal friction acting in mutually orthogonal directions. With these inputs in the XLTRC^{TM} software, he predicted the single-disk rotor's threshold speed of instability, although his experimental observations concerning the threshold speed of instability were not always repeatable. Anand's experimental work also showed that with a bonding tape wrapped around the shaft, internal damping in the rotor material was enhanced as shown by logarithmic decrements obtained from the free-free tests of the rotor.

Murphy **[17]** analyzed the effects of cross-coupled stiffness and damping coefficients as well as direct stiffness coefficients on the stability of a simple rigid rotor model, which is supported in horizontal and vertical directions by linear bearings. His analysis showed that the direct stiffness asymmetry stabilizes the rotor, whereas the cross-coupled stiffness coefficients cause instability when they are equal and opposite in sign and exceed certain range of values. With equal direct stiffness coefficients with cross-coupled stiffness coefficients of equal magnitude and opposite signs, the analysis predicts rotordynamic instability.

Robertson **[18]** described the elastic hysteresis and the clamping fit effects and how they are destabilizing to the rotors running above their first critical speeds. He described the inadequacy of the linear viscous damping model and showed that the internal damping can be described more accurately with the hysteretic damping model. He also showed that just as Kimball's and Newkirk's explanation for the elastic hysteresis (which depends upon the normal strain rates) results in a destabilizing force in the direction of the forward whirl for a rotor running above the first critical speed, similarly, a clamping fit effect such as that due to shrink fit and flexible couplings, creates friction forces that oppose relative motion between the rotating parts. These forces induce instability in the forward whirl for the rotors running above their first

critical speeds, but act as an external, stabilizing damping below the first critical speeds. He also described and discussed some potential designs in the rotating machineries that should be avoided to prevent rotordynamic instability caused by the internal friction.

Smalley and Pantermuehl et al. **[19]** presented an analysis of some centrifugal compressor designs assembled with shrink fit joints. The analysis investigated the stiffening effect caused by the shrink fits on the centrifugal compressors. ANSYS software was used to investigate the compressor designs. Through the analysis, they showed that the shrink fits stiffened the compressors and raised their first critical speeds slightly. In some cases, the increase in the first critical speeds was as high as 6 percent. They further showed that the increase in stiffness is proportional to the interference fit's length to the shaft diameter ratio. The larger this ratio is the larger is the stiffness induced in the model. The numerical simulations from the models validate the field data.

Nelson and McVaugh **[20]** applied finite element analysis technique to rotor-bearing systems. The rotor model can be a uniform or a non-uniform shaft, with any specified number of inertias. They considered all six degrees of freedom for the model. They demonstrated the finite element methodology and the solutions by demonstrating a numerical example of a rotor. They incorporated internal friction in the analysis by using two models: the linear viscous and the hysteretic. Zorzi and Nelson **[21]** in their analysis included external and internal (hysteretic) damping in the equations of motion. Hashish and Sankar **[22]** investigated a damped rotor system using a finite element model with the viscous damping and the hysteretic damping as models for internal friction.

Ginsberg **[23]** and Meriam and Kraige **[24]** provide simple mechanical models of various types of friction such as viscous friction, the Coulomb friction and the hysteretic friction. The mechanical models used to illustrate different friction models show important features of the models such as non-linearity in the Coulomb and the hysteretic friction models, as well as the difference between the models such as the dependence of friction forces on the rate of strain change in the viscous friction model and dependence of sign of rate of strain change in the hysteretic friction model.

DISSERTATION OBJECTIVES

The main objectives of this research work are as follows:

1. To develop a practical capability to predict threshold speeds of whirl instability for built-up rotors with shrink fit interfaced joints. A related goal is to develop a way to determine the correct numerical values of the internal friction coefficients or how cross-coupled coefficients (for any particular rotor assembly) should be used in computer codes for stability predictions (typically logarithmic decrement).
2. To understand how shrink fits in a given rotor assembly affect dynamic stability of a rotor-bearing system.

The major tasks that support the main objectives (1) and (2) above are as follows:

(a) To conduct experiments with different rotors and shrink fit setups to observe instability and establish some values of the shrink fits that induce forward whirl instability.
(b) To develop various computer models with different geometries and configurations for a single-disk and a two-disk rotor to understand and develop a pattern for instability in various system parameters, such as the geometry and the material properties, which could be related to stability of the single-disk and the two-disk rotordynamic systems.
(c) To explain the experimental results on the stability of particular configurations of the single-disk and the two-disk rotors at the Turbomachinery Laboratory.

RESEARCH METHODOLOGY

The research is divided into experimental and theoretical studies. The methodology for the research in each of the two areas is described as follows:

1. For experimental study, vibration measurement results from a single-disk and a two-disk rotor serve as a foundation on which some fundamental hypotheses and assumptions about the effect of shrink fits on rotordynamic stability are based. The experimental results on both the single-disk rotor and the two-disk rotors show sub-synchronous instability due to the internal friction at the first eigenvalue of the rotor-bearing system.
2. For theoretical study, modeling and simulation of the internal friction due to shrink fits in a rotor-bearing assembly using XLTRC^{TM} Rotordynamics Analysis Software are carried out extensively to analyze the stability of various configurations, both experimental as well as imagined.

CHAPTER II

EXPERIMENTAL TEST FACILITY

DRIVE MOTORS

The major parts of the test rig consist of a drive train and data acquisition instrumentation. The drive system is a 30 hp variable speed motor that is connected to a jackshaft via a toothed belt that has a speed ratio of 1 to 4.8 (Fig.1). The jackshaft is mounted on two five-pad tilt pad bearings. The jackshaft is connected to the rotor by a flexible coupling. The rotor is supported on two ball bearings of model number SKF 1215 K. The two bearings are double row self-aligning ball bearings. There are twenty balls in each row and the ball diameter is 0.5 inch (12.5 mm) (Fig.2). The bearings are lubricated by a pressurized lubrication oil system. The two bearings are mounted on split-type SAF 515 pillow block housings.

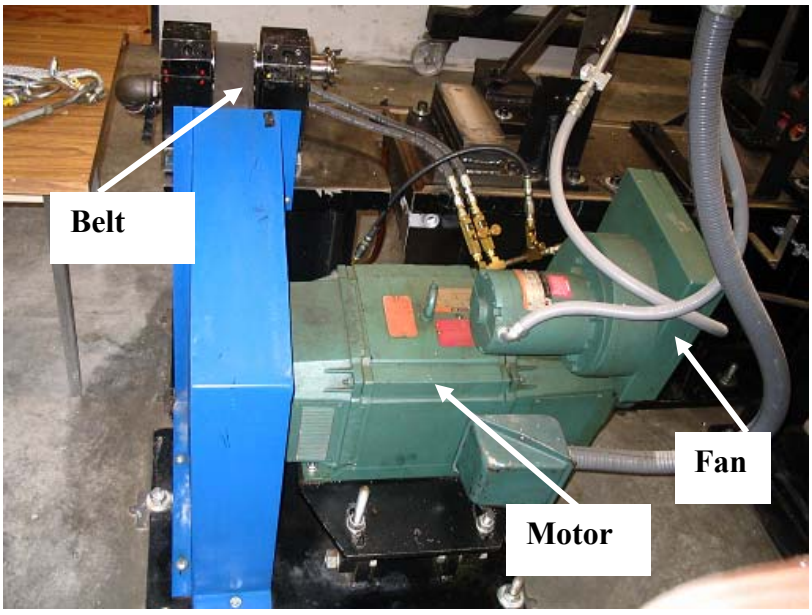

Fig. 1 Drive motor arrangement with belt and bearings supporting the drive shaft

Fig. 2 Double-row self aligning ball bearing used with the bearing housing for rotor support

INSTRUMENTATION

The instrumentation consists of two 8 mm Metrix non-contact eddy current proximity probes (Fig. 3) mounted on a probe pedestal which is bolted close to the mid-span of the shaft. A keyphasor (which is also an 8 mm non-contact eddy current probe) is mounted 15^{o} from the vertical axis. The keyphasor measures the phase and the angular speed of the shaft. The proximity probes are powered by 24 V Bently-Nevada proximitors (Fig. 4). They are connected to a Bently-Nevada ADRE 208 data acquisition system for acquiring and analyzing the running test data.

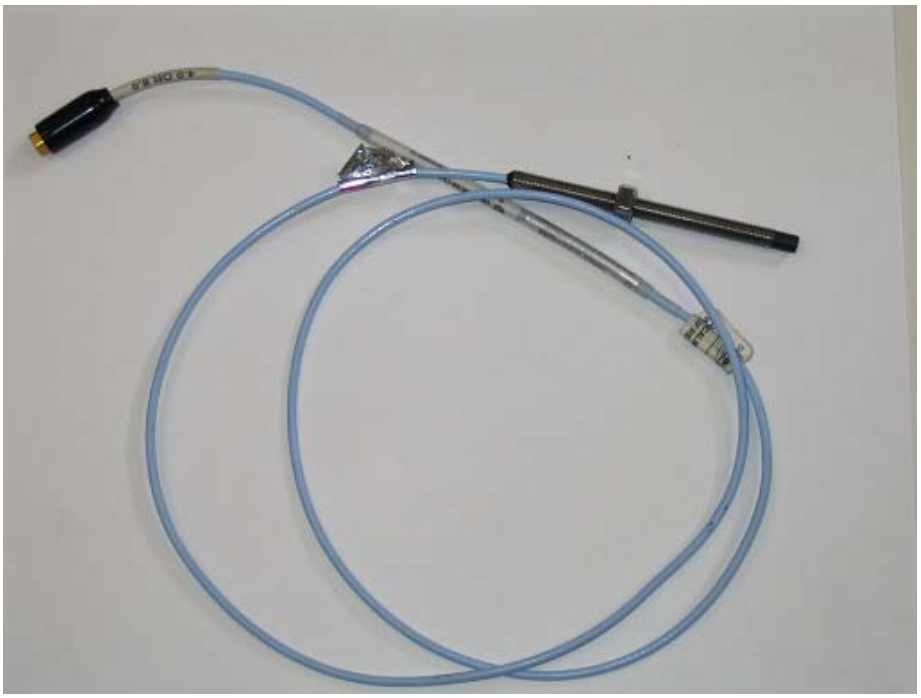

Fig. 3 A Metrix proximity probe

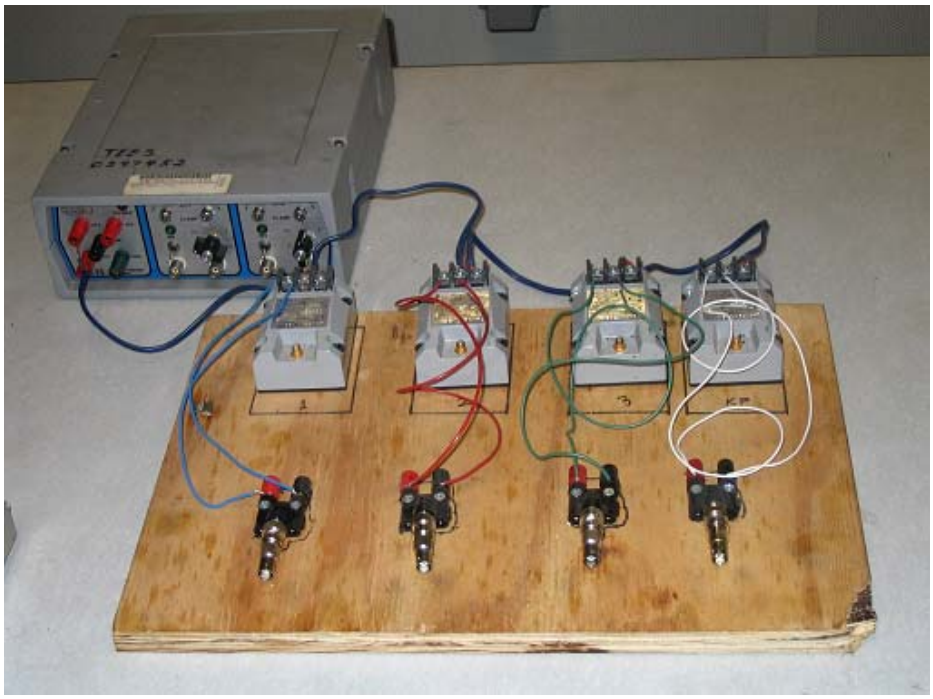

Fig. 4 Proximitors and power supply for powering the proximity probes

TEST ROTORS

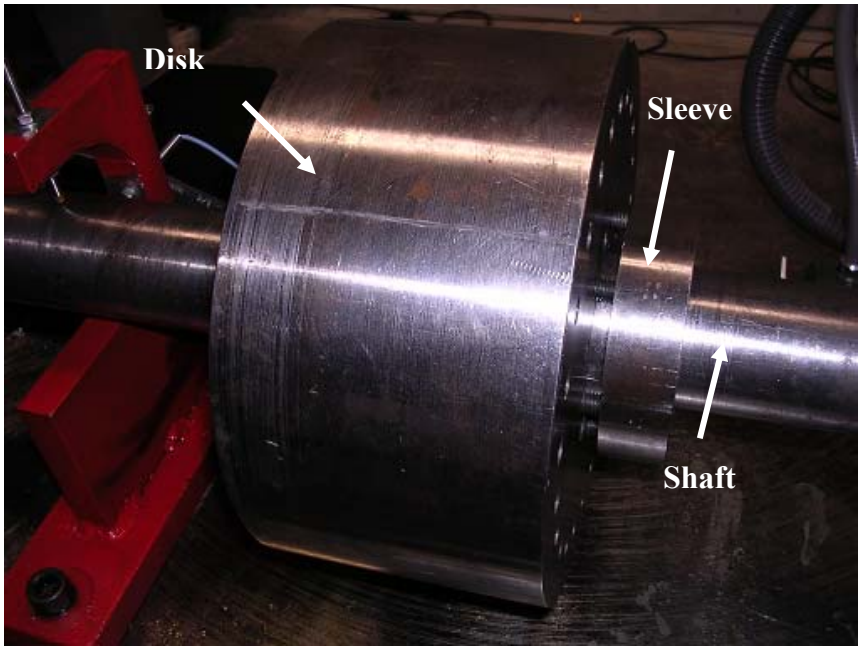

Fig. 5 Close-up view of a single-disk rotor bearing system tested at the Turbomachinery Laboratory

Fig. 5 shows a close-up view of a single-disk rotor tested at the Turbomachinery Laboratory. The interference fit exists at the interface between the shaft and the disk through a specially designed tapered sleeve. Fig. 6 shows a full view of the single-disk rotor installed on the ball bearings:

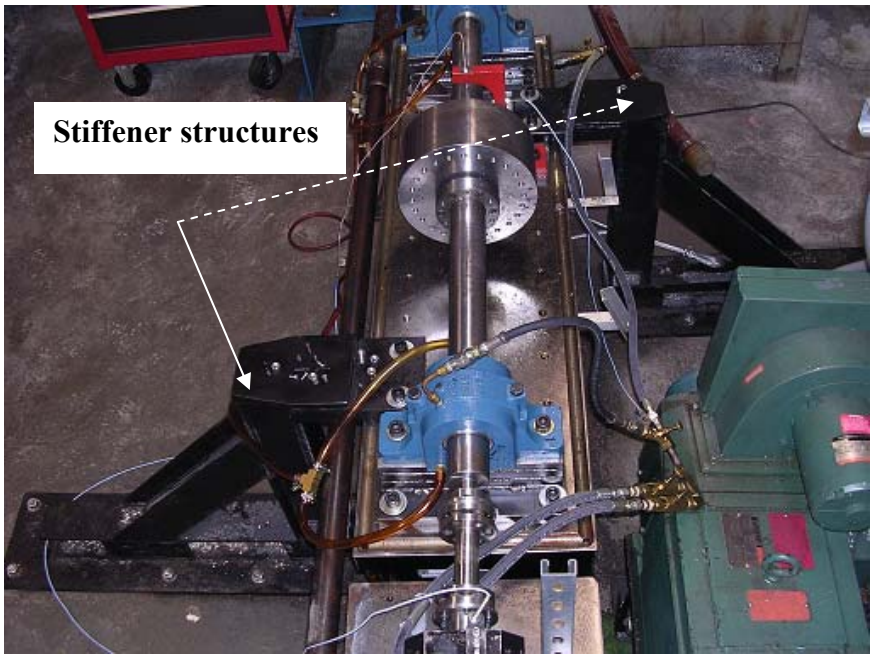

Fig. 6 Single-disk rotor installed on the ball bearings at the Turbomachinery Laboratory

Fig. 7 shows the two-disk rotor tested at the Turbomachinery Laboratory. This rotor has shrink fit contacts at the interface between the two steel disks and an aluminum sleeve at the two ends of the sleeve. The interference axial length of the sleeve and the wheel near the coupling end is 1 inches, whereas at the other end of the sleeve, the contact length is 2 inches (Fig. 8). The axial width of both wheels is 2 inches.

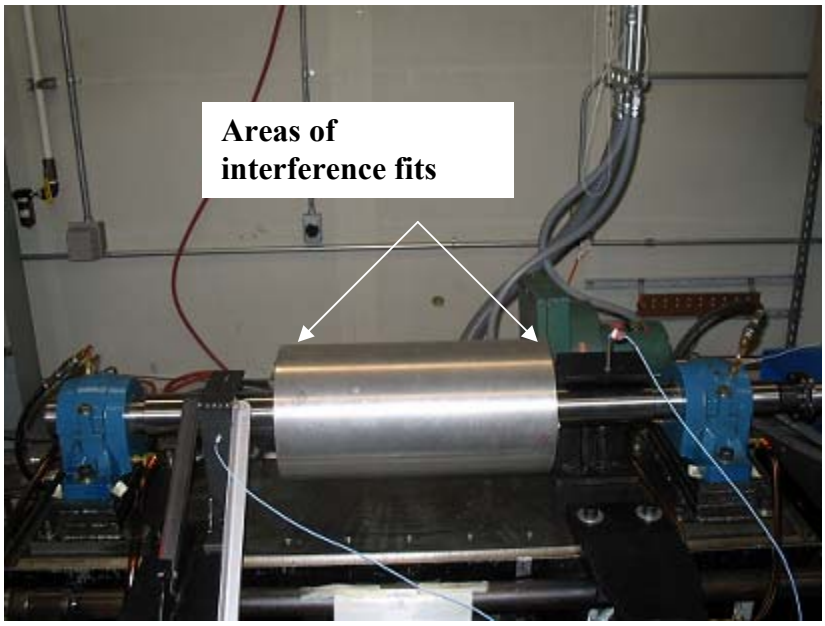

Fig. 7 Two-disk rotor installed on the ball bearings at the Turbomachinery Laboratory

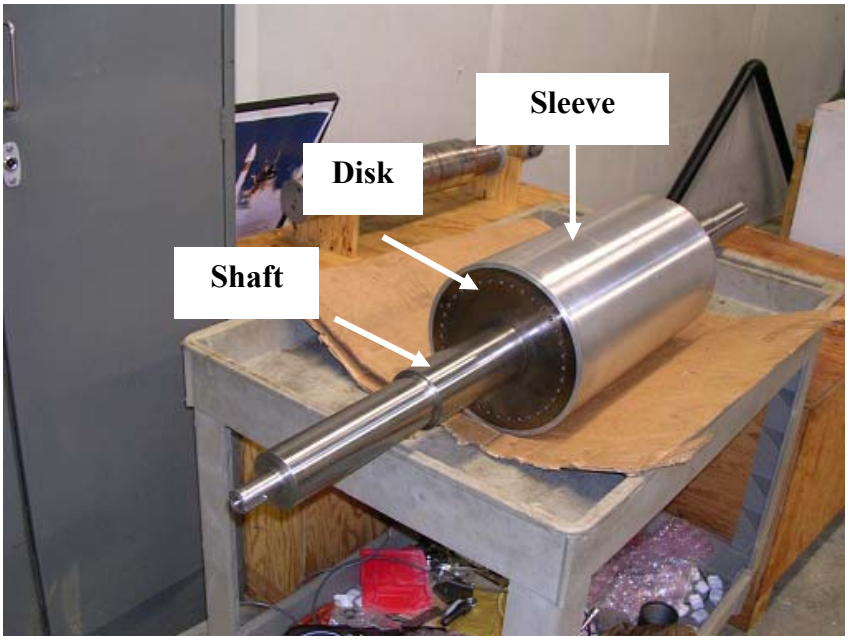

Fig. 8 Another view of the two-disk rotor, showing the steel rotor disk, which is shrink fitted with the aluminum sleeve at the ends.

STIFFENER STRUCTURES

The stiffener structures are mounted on the foundation to increase the stiffness of the foundation housing in the horizontal direction, thus reducing the asymmetry of the bearing support. These structures are shown in Fig.6. Lower foundation stiffness asymmetry reduces the stability of the system **[2]**. As experimental results for the running tests on the single-disk and the two-disk rotor show, installing these structures brought the onset speed of instability within the operating range of the rotor and made the instability caused by internal friction a repeatable experiment.

Each stiffener structure is made of three steel I-beams welded together at the base by a large plate that serves as the base. At the top, there is a thick steel plate (3/4 inches) that connects the stiffener with the foundation housing, using capscrews. The stiffeners are connected to the ground with the help of six foundation bolts passing through the base plate to the ground.

With stiffeners mounted on the foundation, impact and shaker tests were performed on the rig to determine the values of the modal mass, stiffness and damping of the foundation housing in both the horizontal and the vertical direction. This estimate is important, because these numerical values are required by XLTRC software to perform the simulations of the system. Secondly, but equally important, these modal parameters, especially stiffness, will provide an idea about the asymmetry of the foundation. With the help of running tests and observing the onset speeds of instability, it can then be seen how stiffness asymmetry will affect the onset speed of instability. The determination of the modal parameters of the foundation is discussed in Appendix D.

EXPERIMENTAL RESULTS

The experimental research with the single-disk and the two-disk rotor with the shrink fit interfaces shows evidence of sub-synchronous instability of the rotor-bearing system due to internal friction caused by the shrink fit joints. The two rotor setups are shown in Fig.9 and Fig.10:

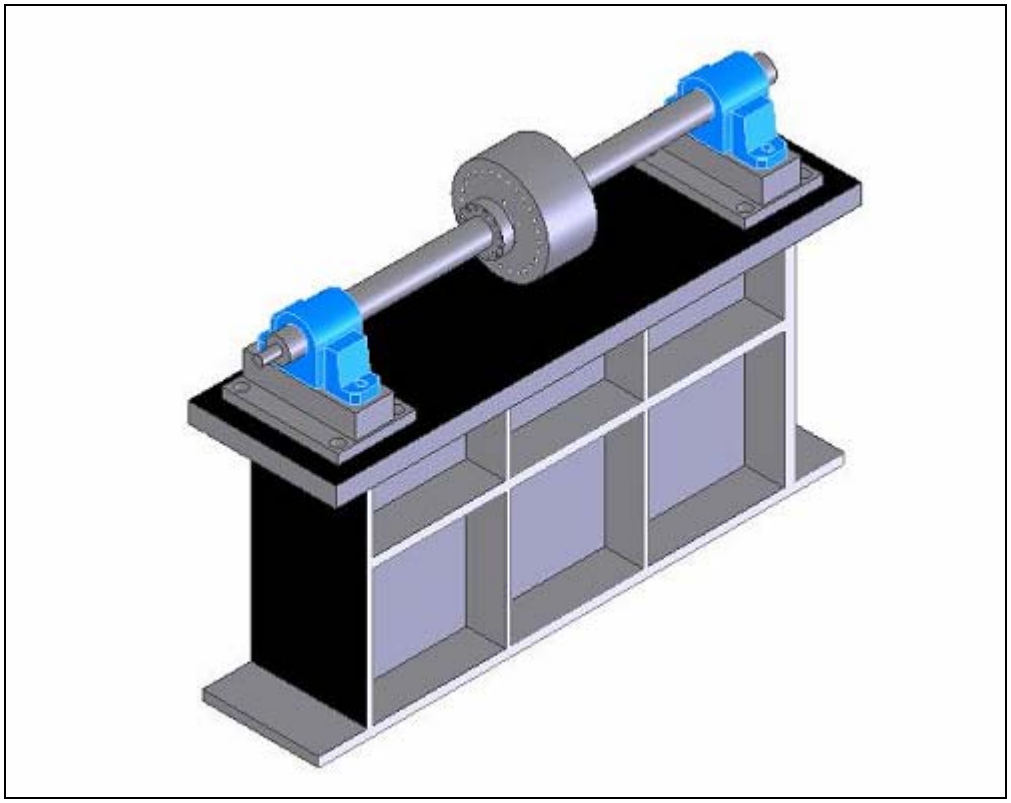

Fig. 9 Single-disk rotor on foundation

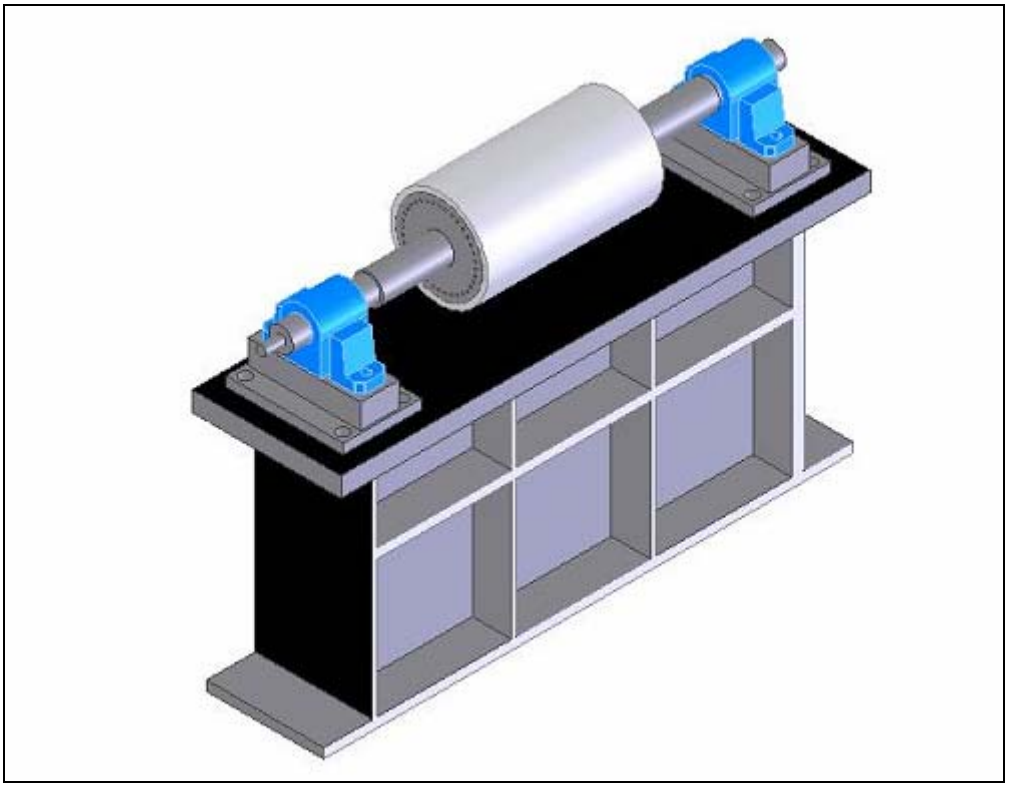

Fig. 10 Two-disk rotor on foundation

In the single-disk rotor, the shrink fit is created by a tapered sleeve which fits in the inside diameter of the wheel and acts as an interface between the wheel and the shaft. The shrink fit between the wheel and the sleeve is varied by changing the axial position of the sleeve. The sub-synchronous instability at the first eigenvalue of the rotor-bearing system (3000 cpm) occurred at a threshold speed of 6000 rpm, when the shrink fit at 6000 rpm was 1 mils radial. When the shrink fit at the zero speed was increased, the instability was suppressed up to a speed of 11,000 rpm, when suddenly the sub-synchronous instability re-appeared. From a shrink fit computation code (see Appendix A), it was found that the shrink fit at 11000 rpm was also 1 mils radial. The experiments with both the looser fit and the tighter fit were found to be completely repeatable.

Therefore, for the single-disk rotor, it was found that the 1 mils radial shrink fit is a "critical" value, in that it causes the sub-synchronous instability to occur consistently.

For the two-disk rotor, the rotor threshold speed of instability was 9600 rpm. A forward whirl sub-synchronous instability occurred at the first eigenvalue of the rotor-bearing system (5000 cpm). In this rotor-bearing system, it was found that making one end of the sleeve having a tighter fit on one of the wheels, while making the other end of the sleeve a relatively loose fit on the other wheel destabilized the rotor-bearing system. Heating of the looser end at a fixed speed of 9600 rpm was required for about 10 minutes. The heating was carried out using two heat guns on the loose end. The forward whirl sub-synchronous instability occurred suddenly after heating for about 8 minutes and then the instability started to increase in magnitude. Even as the rotor was coasted-down, the sub-synchronous component persisted up to about 8000 rpm, when the whole test rig wrecked, with the rotor completely damaged.

Both the single-disk and the two-disk rotors are 52.5 inches long. The shaft material for the two-disk rotor is AISI 4340 steel, with an aluminum sleeve shrink fitted at the two wheels. For the single-disk rotor, the material is AISI 4340, with a single-disk having an outside diameter equal to 10 inches and an inside diameter of 2.5 inches interference fitted with a uniform shaft through a tapered sleeve. For the two-disk rotor, several configurations were tested by changing the geometry of the sleeve. In all but one of the configurations, the rotor was found to be totally stable. The experimental results are described on the following pages.

The single-disk rotor results

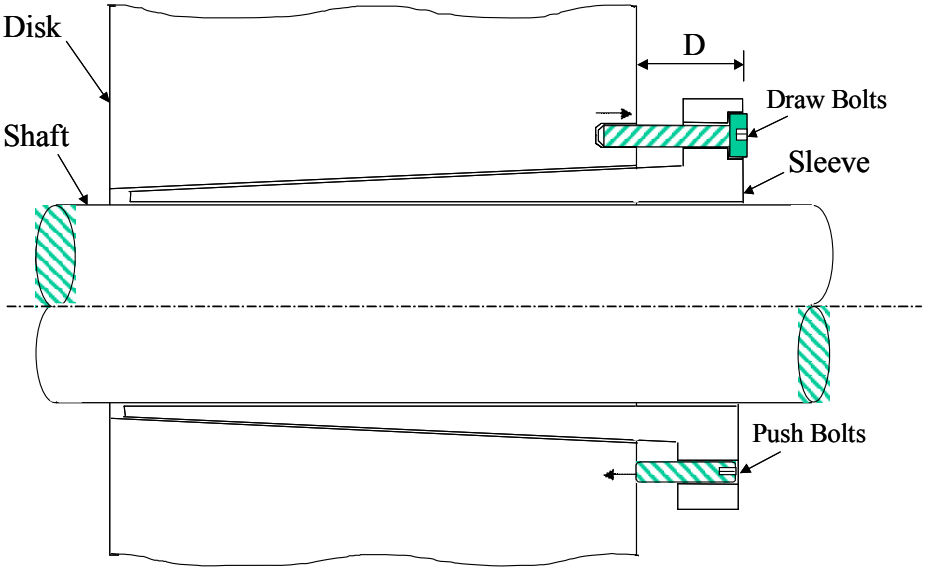

Fig. 11 Shrink fit in the single-disk rotor due to tapered sleeve **[16]**

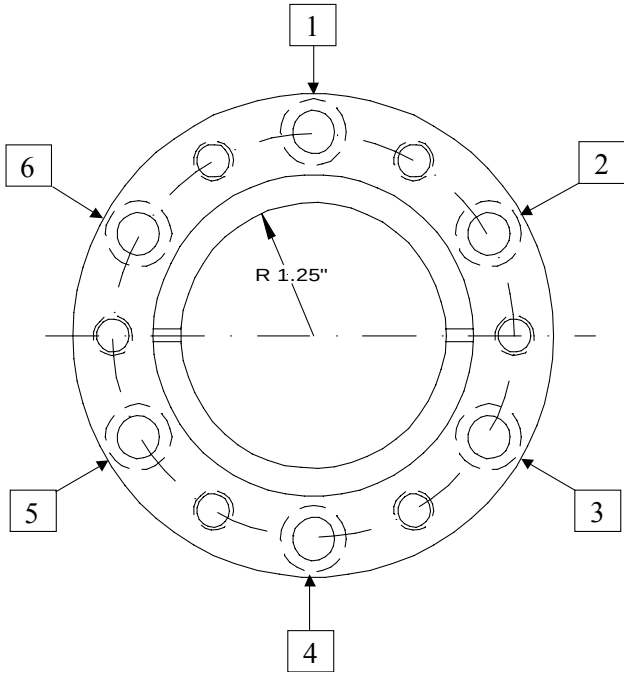

Fig. 12 Positions of draw bolts and push bolts on tapered sleeve **[16]**

In this experimental setup, a tapered steel sleeve fits inside the tapered bore of the steel disk by elastic deformation of the sleeve, as shown in Fig.12, thereby creating an interference fit between the disk and the shaft. There are six draw bolts and an equal number of push bolts, that can be mounted on the holes bored at the periphery of the tapered sleeve. These bolts are used to pull the disk up on the taper, thereby varying the distance between the sleeve's outer edge and the disk, and providing a way to vary the interference fit between the disk and the shaft. The sleeve-disk schematic is shown in Fig.11. The end view of the wheel with the sleeve and the shaft, along with the push and the draw bolts, is shown in Fig.12.

FORMULA FOR CALCULATING THE RADIAL INTERFERENCE FIT

Based on the geometry of the sleeve-disk interface as shown in figure 8, the following equation can be used to obtain the radial interference fit that is developed between the disk and the sleeve:

$$\delta_R = \frac{T}{2}(S - D) \tag{1}$$

In equation (1), 'T' is the taper ratio of sleeve, which is 1:24. 'S' is a calibration factor, which denotes the distance between the outer edge of the sleeve and the outer edge of the disk at zero interference fit, whereas 'D' is the distance between the outer edges of sleeve and the disk that can be varied by using push and draw bolts.

From experiments on the sleeve, it is found that:

S = 1.596 in. (40.538 mm)

Hence, equation (1) can be recast as follows:

$$\delta_R = 0.02083(1.596 - D) \tag{2}$$

1. Run up tests: Speed limited to around 8500 rpm

Ying **[14]** showed that incipience of the forward whirl sub-synchronous instability due to internal friction depends on tightness of the fit (not too tight). Some previous tests also showed that the internal friction instability is neither predominant at either too loose a fit nor at too tight a fit, but rather at some intermediate range of the fits. The earlier experimental results on the single-disk rotor showed that the rotor-bearing system was showing some sub-synchronous component at a fixed frequency beginning at the running speed of around 5500 rpm, but the amplitudes were very small. Thus, to differentiate those sub-synchronous components from any possible benign sub-synchronous components, it was decided to conduct running tests with different interference fits. Initially, in order to assess the instability of the system, the rotor was run up to a speed of about 6500 rpm and then coasted down. It was observed during those initial running tests that there was some sub-synchronous component of the vibration with the frequency equal to the first eigenvalue of the rotor in the vertical direction. Moreover, its amplitude was growing with every increment in the rotating speed. The running speed was increased to about 8500 rpm in subsequent experiments and the data was collected. Three such tests are described below:

(a) Test 1

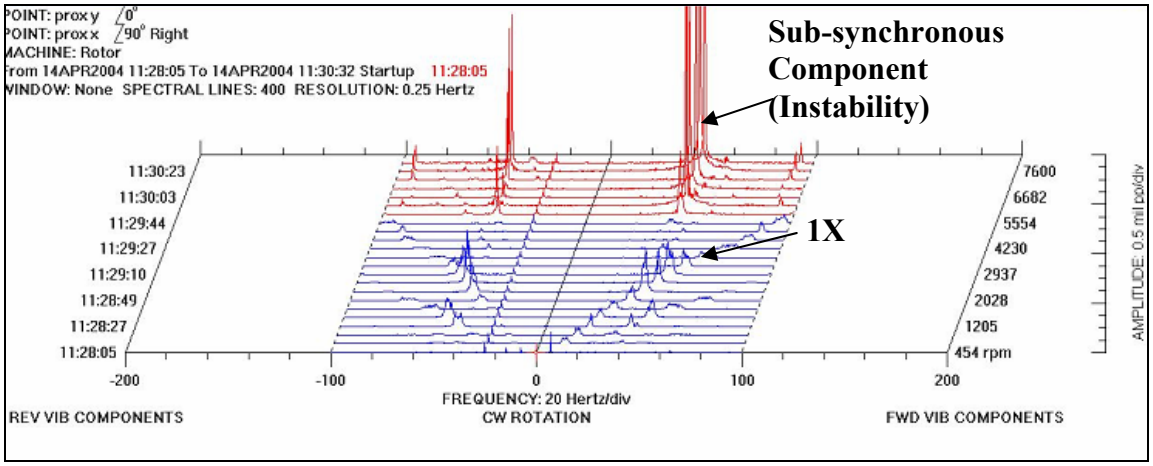

Fig. 13 Waterfall plot of test 1 showing significant instability starting from 5800 rpm

Figs. 13 and 14 are the snapshots of the data acquired from the ADRE data acquisition software. The waterfall plots in Fig.11 show a large sub-synchronous component at a frequency near the first critical speed of the rotor, which is around 2900 rpm. As shown in Fig.13, the sub-synchronous amplitudes grow with the rotating speed of the rotor. These are shown as red-colored lines in Figs. 13 and 14. The Bode plots in Fig. 14 show that the instability is roughly growing with the speed of the machine with large amplitudes (around 30 mils, peak-to-peak) at around 8000 rpm. Also, in the rotating speed range of 6000 to 8000 rpm, it can be noticed that the 1X component is very small, but the direct vibration component is large, showing that the instability is the predominant component of the rotor vibration.

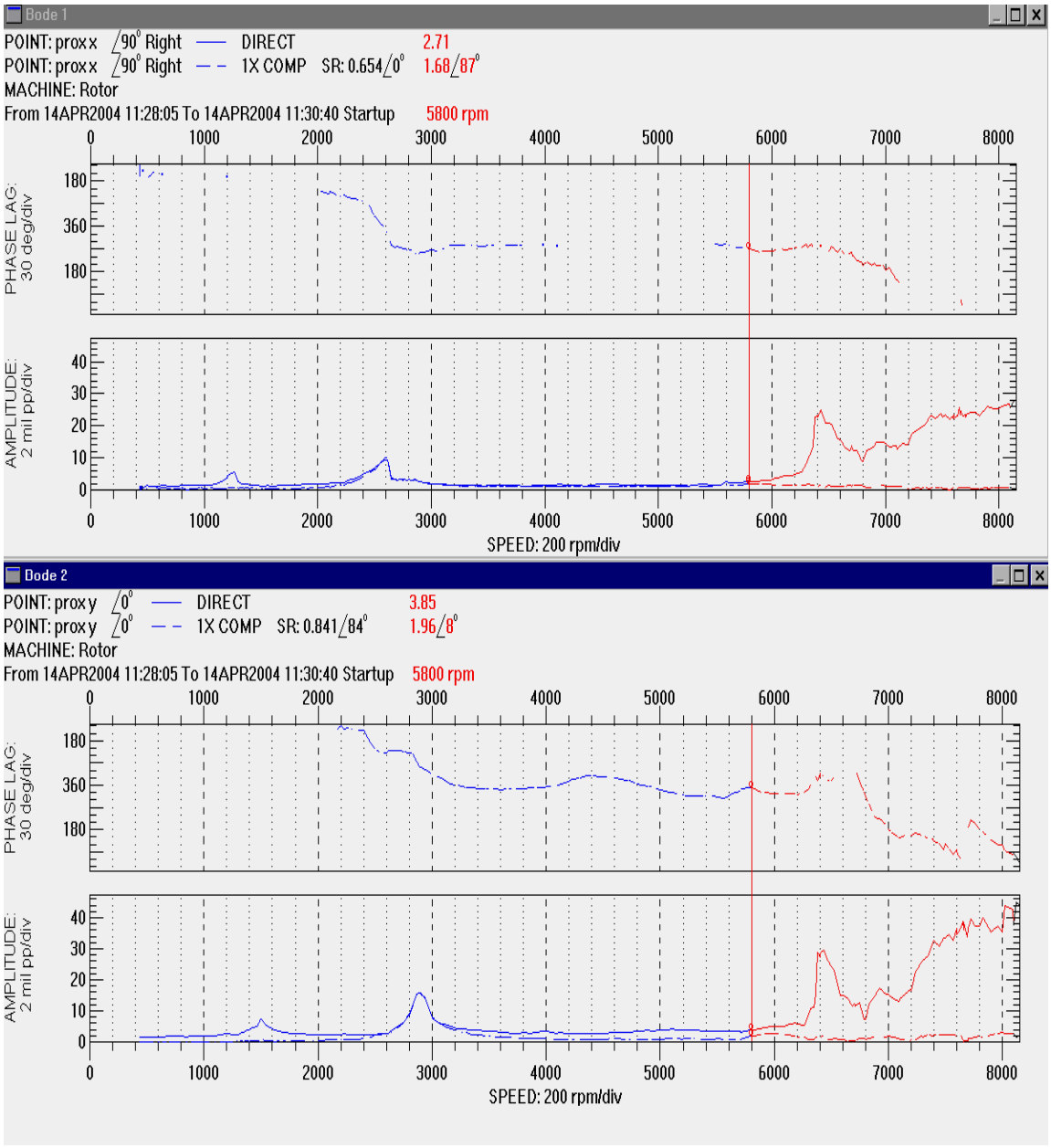

Fig. 14 Bode plot of test 1 showing growing amplitudes of vibrations above 5800 rpm

(b) Test 2

With the same shrink fit condition, the next experiment was conducted to assess the repeatability of the instability. The waterfall and the Bode plots for this test are shown in Figs. 15 and 16:

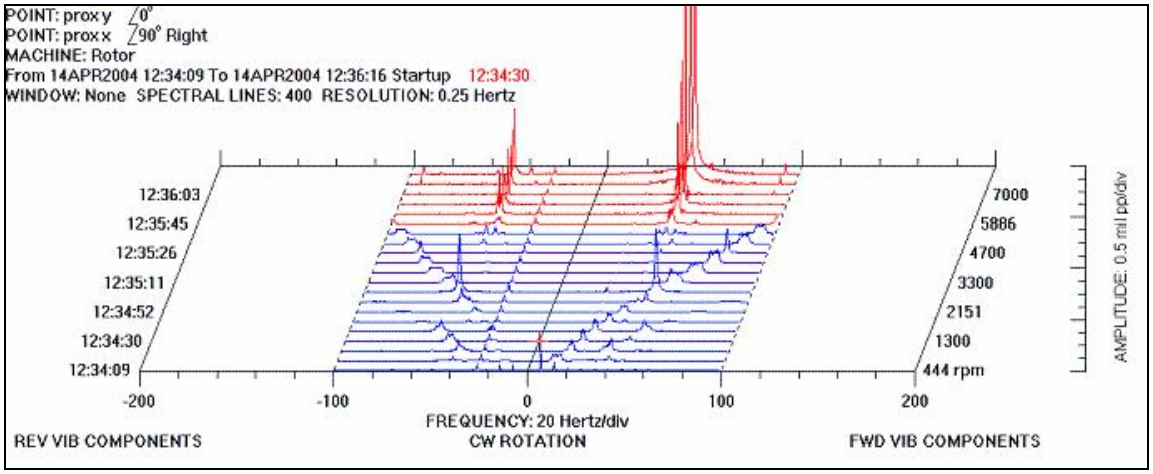

Fig. 15 Waterfall plot of test 2

Again, a significant instability is observed at the same speed and at the same frequency as in the first case (test 1). Therefore, the tests are repeatable and consistent.

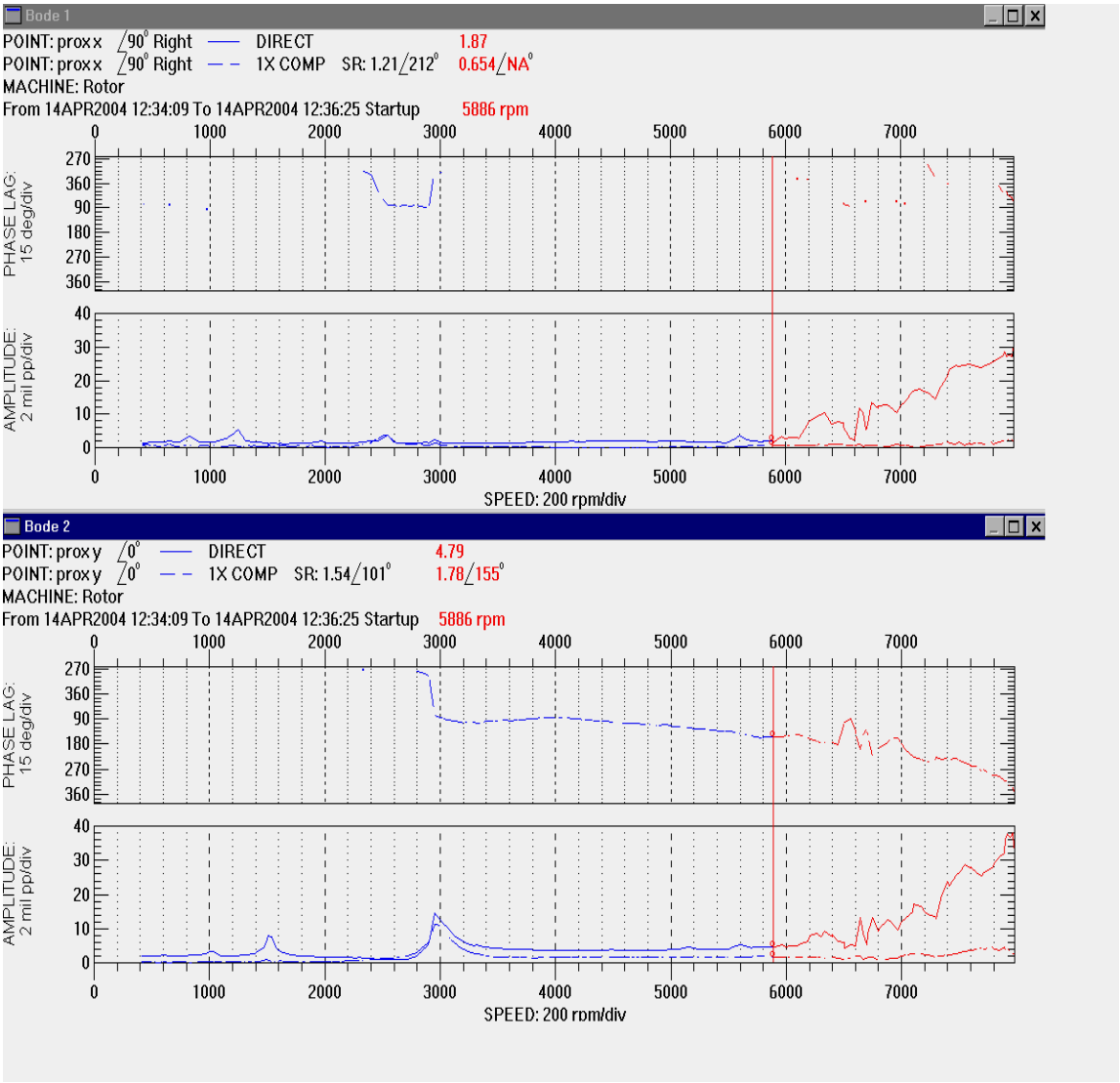

Fig. 16 Bode plot of test 2

The initial shrink fit values for both the tests were identical and the shrink fit at the threshold speed that caused the instability to occur was around 1 Mil (radial). This value of the shrink fit at the threshold speed was estimated using a code for the shrink fit variation with the rotational speed at the sleeve and the disk interface.

(c) Test 3

Some tests were conducted using a tighter initial shrink fit and it was observed that the instability was suppressed at the previous threshold speed of 6000 rpm. Instead, the threshold speed for tighter fits became 11000 rpm, with higher instability amplitude as shown in Fig.17 below:

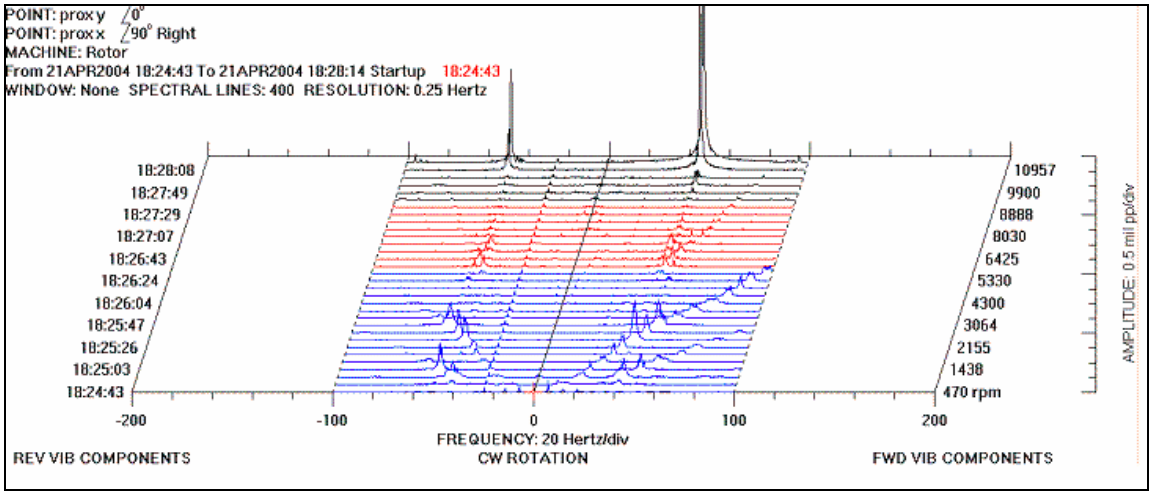

Fig. 17 Waterfall plot showing the threshold speed at 11,000 rpm

The two-disk rotor results

Several configurations for the two-disk rotor were tested. These are briefly outlined below:

(1) An aluminum sleeve 9.5 inch outside diameter, with the diametral shrink fit at both ends equal to 11 mils

(2) An aluminum sleeve 9.25 inch outside diameter, with the diametral shrink fit at both ends equal to 7 mils

(3) An aluminum sleeve 10 inch outside diameter, with the diametral shrink fit at one end being 11 mils diametral, whereas at the other end it was equal to 5 mils diametral. The end with the 5 mils diametral interference had only 1 inch axial contact with the corresponding steel wheel (it did not have complete 2 inch axial contact; the sleeve was undercut at the loose end intentionally).

From the experiments, it was found that the first two configurations were perfectly stable under all the operating conditions, and although there was some sub-synchronous component at the first natural frequency of the rotor for the rotor spin speeds above the first critical speed, the amplitudes of those sub-synchronous vibrations were too small to be conclusive. The configuration (3) above was found to be unstable, with two tests showing the repeatable results for the threshold speed of instability and a large sub-synchronous forward whirl instability above the first critical speed. However, in the second test, the amplitude of instability grew large suddenly and wrecked the entire test rig. The first critical speed of the rotor was around 5500 rpm.

The experimental results for the tests where the rotor-bearing system became unstable are described as follows:

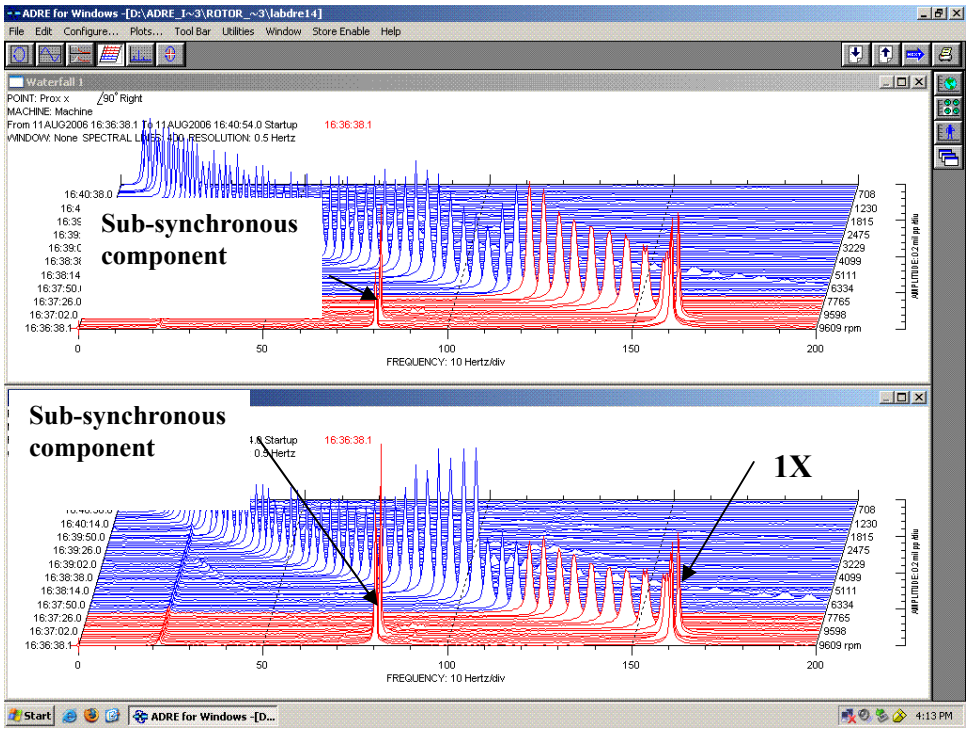

Fig. 18 Waterfall plot showing threshold speed of instability at 9600 rpm

Fig.18 shows the waterfall plot with the instability threshold at 9600 rpm. Fig.18 shows that the instability grew larger than the synchronous component (the 1X component is due to imbalance). The plot is a coast-down plot. The instability disappeared at 9100 rpm. The instability appeared as the loose shrink fit end was heated for about 8 minutes using the heat guns while the rotor speed was held constant at 9600 rpm.

This test was repeatable under identical conditions. However, in the second test, the rotor wrecked, as the rotor was coasted-down. The results for this experiment could be acquired using only the LVTRC data acquisition software, as the ADRE data acquisition software has some limitations on its file size. The snapshot taken from the LVTRC screen is shown in Fig.19:

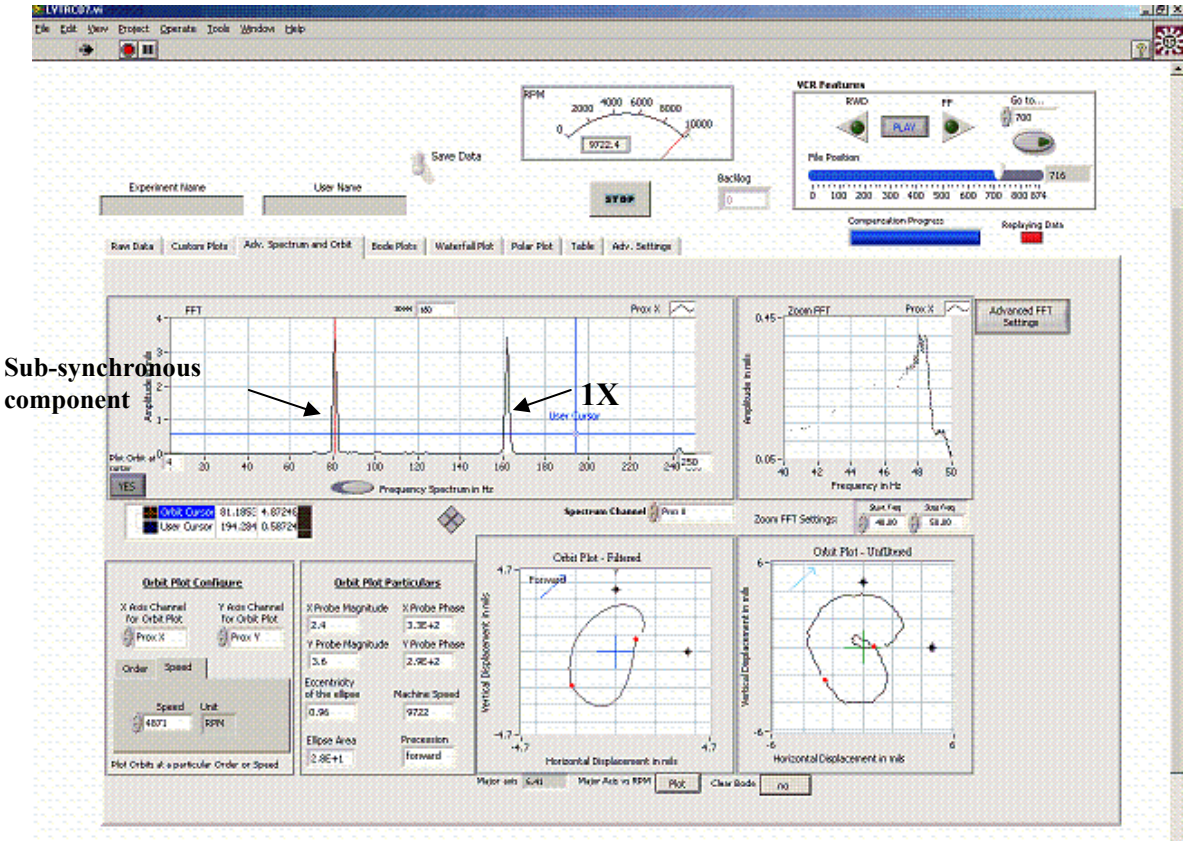

Fig. 19 Spectrum plot from LVTRC showing the sub-synchronous instability component

Fig.20 shows the picture of the wrecked two-disk rotor. The shaft is completely bent. The experimental results on the two-disk rotor show that the rotordynamic instability due to internal friction caused by slipping at the shrink fit interfaces can be potentially catastrophic.

Fig. 20 Wrecked two-disk rotor

CHAPTER III

INTERNAL FRICTION MOMENTS MODEL

This chapter describes a conceptual model of internal friction developed at the shrink fit interfaces in rotating machines. This chapter will show that the internal friction at the shrink fit interface due to relative sliding between the rotating and whirling mechanical components such as a shaft and a disk, or a disk and a sleeve gives rise to a system of moments (couples) that are internal to the mechanical system. These moments are internal because they occur in opposite pairs due to relative sliding between the rotating (and whirling) mechanical elements as described above. In addition, the internal moments are generated as a result of the motion of the rotor itself and not otherwise, just like an imbalance in the rotor exerts dynamic forces on the rotor system when the rotor executes the rotational motion and does not act on the rotor when the rotor is not rotating. In other words, the internal friction moments are not applied externally to the rotating system; instead they are the result of the rotor motion itself which can give rise to instability or self-excited motion of the rotor-bearing system above the first critical speed, and can lead to catastrophic failures of the rotor-bearing system, as shown experimentally in Chapter II.

Before describing the internal friction moments model, a widely known and used model of internal friction is described to provide some background of the analysis of internal friction. This model was initially postulated by Kimball **[4]**.It was explained and expanded in greater analytical detail by Gunter **[5]**. Although useful and easy to implement in most rotordynamic computer codes to assess stability of the rotor-bearing systems with hysteretic and shrink fit friction, the model has a flaw of being physically inconsistent with the principles of mechanics. On the other hand, the internal moments model, though not widely used or known, has the virtue of being realistic and consistent with the principles of mechanics.

GUNTER'S FOLLOWER FORCE MODEL

Gunter **[5]** analyzed an extended Jeffcott rotor model. The word "extended" means that in the mathematical analysis, the internal friction force acts at the geometric centre of the disk. Besides internal friction, the rotor foundation and bearings are assumed to have flexibility and damping properties, in addition to the shaft flexibility. The extended Jeffcott rotor model is shown in Fig.21:

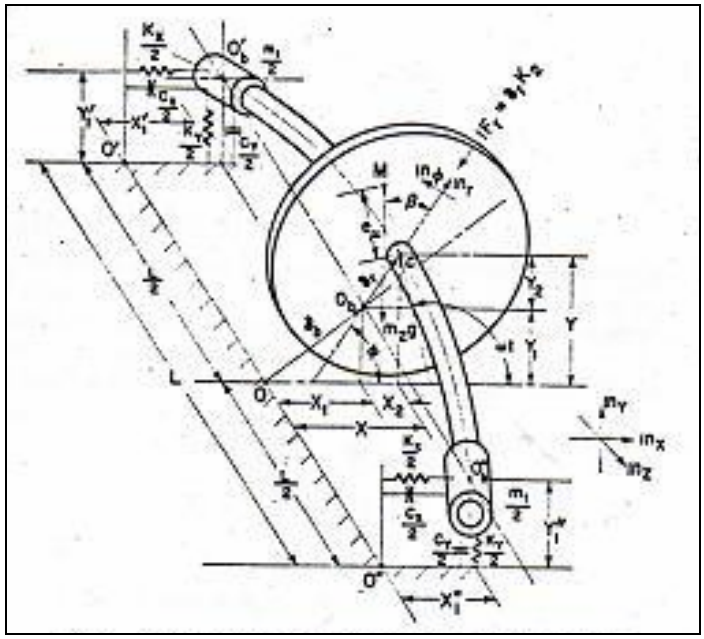

Fig. 21 Extended Jeffcott rotor model **[4]**

As discussed in Appendix A of reference **[5]**, Gunter modeled the internal friction due to shrink fits and other types of friction producing joints, besides the rotor material hysteresis, as a system of longitudinal stresses similar to the elastic stresses of the shaft, but instead dependent on the rate of change of strain of the shaft fibers. The friction forces in case of material hysteresis arise from the dynamic stretching of

material elements, whereas in the case of shrink fits, the longitudinal stresses are developed at the interfaces due to relative sliding between the shrink fit components. The total longitudinal stresses are assumed as the conventional elastic term which comes from the beam theory plus a strain rate term. This in effect models the internal hysteresis of the material as viscous damping. Gunter postulated that the shrink fit internal friction can be modeled in the same way as the material internal hysteresis, with the magnitude of shrink fit stresses many times larger than those produced by the material internal hysteresis. The equivalent moments can be depicted on a cross-section of the rotating and whirling shaft in Fig. 22 as follows:

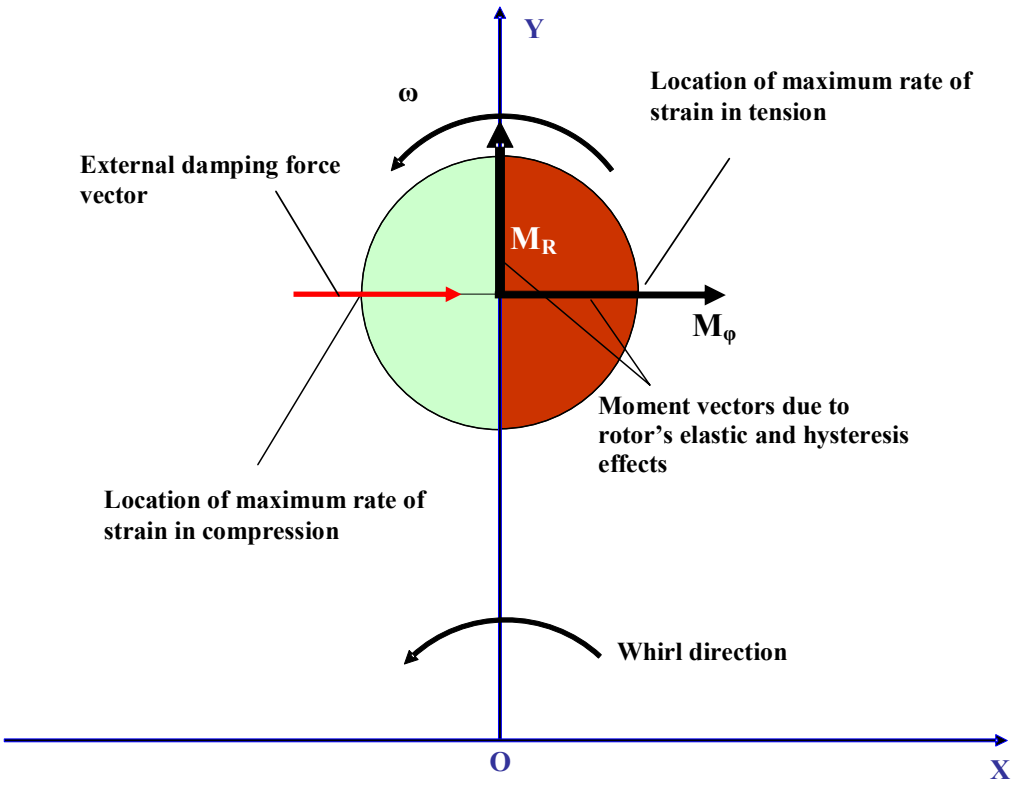

Fig. 22 Cross-section of the extended Jeffcott rotor showing the moment and force vectors

Fig. 22 shows the moment vectors and the external damping force vector acting on the rotor. The moment vector M_R is the result of shaft hysteresis (which will tend to bend the shaft in the direction of the forward whirl or backward whirl, depending upon whether the rotational speed is larger or smaller than the whirling speed, respectively) whereas the moment vector M_φ is the reaction to rotor elastic deformation. The direction of the moment vector M_R in Fig.22 is valid for the case when the rotational speed is larger than the whirling speed (sub-synchronous whirling). The direction of the moment vector M_R will be reversed if the rotational speed is smaller than the whirling speed.

Gunter postulated that the moment vector M_R is equivalent to a follower force which acts tangential to the whirl orbit and acts as a de-stabilizing or "energy adding" force when the rotor rotates above the first critical speed, and that the follower force acts as a stabilizing or damping force when the rotor rotates below its first critical speed. According to Gunter, the rotor cross-section with an equivalent tangential follower force looks as shown in Fig.23:

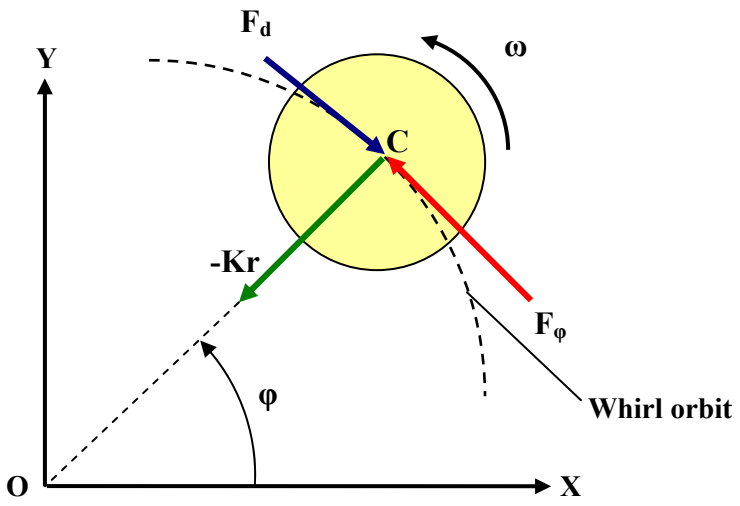

Fig. 23 Free-body diagram of a rotor with internal friction, according to Gunter **[4]**

As shown in Fig.23, the internal friction follower force F_φ acts in opposition to the external damping force F_d above the first critical speed of the rotor and tends to drive the rotor unstable, if the external damping is smaller than the internal friction force. Below the first critical speed, the follower force reverses its direction and acts as a damping force. This explains the experimental observations made by Newkirk **[2]** and Kimball **[3]**. However, this model is physically incorrect as explained below:

According to Newton's Third Law of Motion, for every action there is an equal and opposite collinear reaction. If a follower force acts on the rotor's geometric centre as shown in Fig.23, then according to Newton's Third Law, an equal and opposite collinear force must act on a physical attachment or component of the rotor. However, in a Jeffcott rotor, there is no physical connection from ground to the rotor i.e, to the disk. To assume that a follower force acts on the rotor due to internal friction or material hysteresis is the equivalent of assuming the force to be a bearing force reacting to the ground. In other words, the follower force model can be considered as if there is a bearing connected through the rotor's geometric centre to the ground, which is clearly incorrect, since in an actual physical situation, there is no bearing through the rotor's geometric centre to the ground. The only physical connections to the rotor are the support bearings at the two ends of the rotor. Therefore, the follower force can not physically exist.

However, Gunter's model is widely used in industry and research to model the internal friction. An example can be given of how the internal friction is modeled in industry by connecting a bearing to the ground through a rotor's geometric centre at the shrink fit interface, as shown in Fig.24:

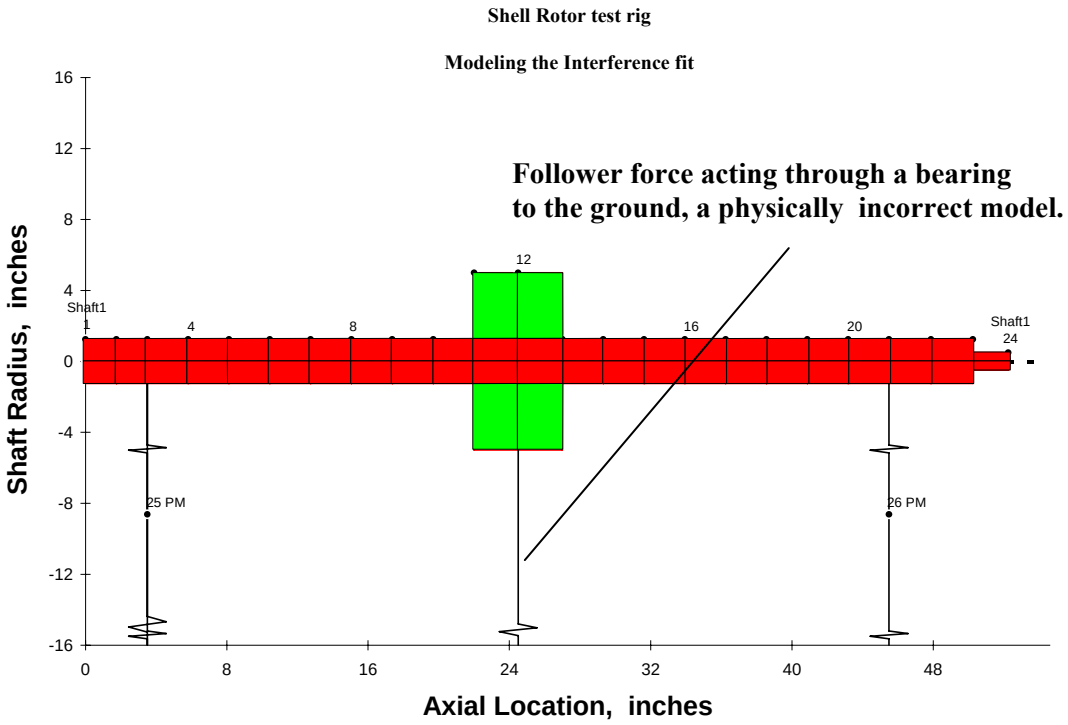

Fig. 24 Modeling of internal friction using Gunter's model

As shown in Fig.24, modeling a rotor system with internal friction using Gunter's follower force model requires applying a cross-coupled follower force to the centre of the disk. To apply this model in XLTRC^{TM} requires applying a user-defined cross-coupled force at the centre of the disk. This force is applied as a bearing connecting the rotor disk to the ground. Fig.24 clearly shows the physically incorrect concept of a "bearing to the ground" to model internal friction.

Therefore, instead of a follower force, it is an internal bending moment, labeled M_R in Fig.22, which acts on the rotor with hysteresis or shrink fit friction. This moment will tend to bend the rotor in the direction of forward whirl (perpendicular to the direction of shaft deflection vector) when the rotor operates above the first critical speed.

Below the first critical speed, the internal moment will tend to bend the shaft in the direction of backward whirl. The internal moments model as described in the next section addresses the inadequacy of the follower force model.

INTERNAL MOMENTS MODEL

A model to describe the action of internal friction due to the effects of shrink fits and how it can produce a de-stabilizing "internal moment" is explained by considering an example of a two-disk rotor as shown below:

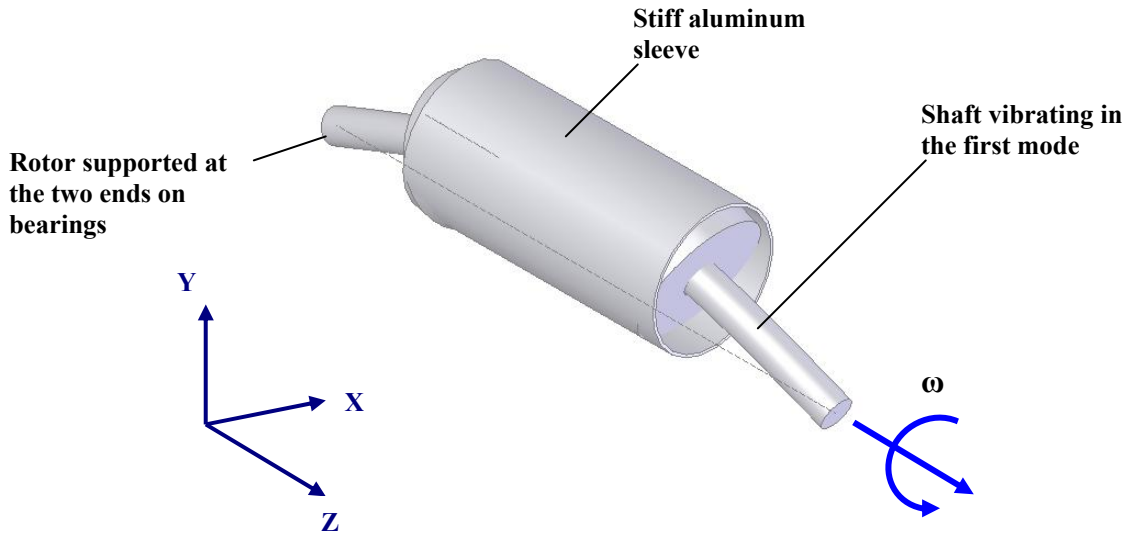

Fig. 25 A two-disk rotor whirling in first mode, along with a stiff aluminum sleeve (vibration of the shaft shown exaggerated to clarify explanation)

Fig.25 shows a two-disk rotor's solid model with a stiff aluminum sleeve press-fitted onto the steel disks. The discussion presented is qualitative in nature and quantitative models are described in Chapter IV. In Fig.25, the rotor is shown to whirl or vibrate in its first mode (during which the rotor's centerline assumes a nearly half-sinusoidal shape) and the exaggerated gap between the faces of the sleeve and the steel

disks shows that the disk is slipping at the interface, although total contact is not lost. Due to relative slipping between the disk and the sleeve, friction forces are generated at the side positions of the steel disks (plus and minus X locations). The friction forces occur in equal and opposite pairs (according to Newton's Third Law of Motion, which implies that the disks exert equal and opposite forces on the sleeve at the same locations). The friction forces act in the sense that since one side of the disk is slipping out, the friction force on it is opposite, whereas for the other side, the friction force will act so that the combined effect is a couple. An opposite couple acts on the other steel disk. This can be drawn as follows:

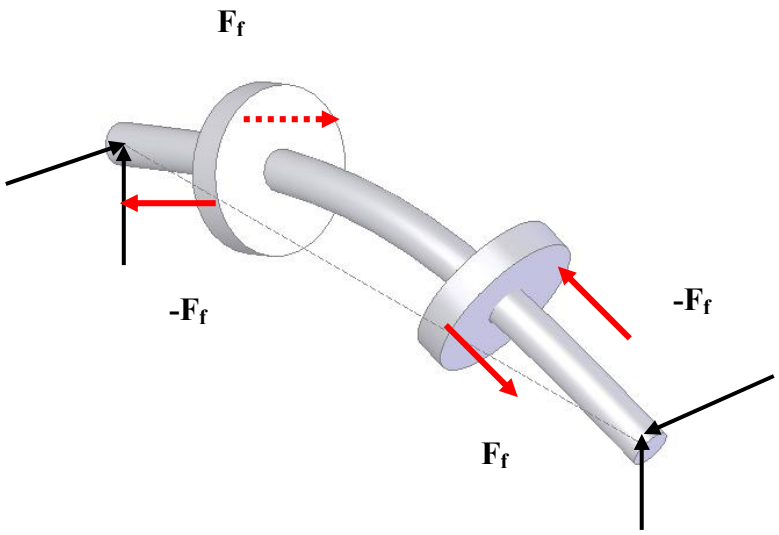

Fig. 26 Free-body diagram of the shaft carrying steel wheels

Fig.26 shows that although the *net* forces due to friction effects cancel out each other, there is still a *bending* effect due to these forces, since the forces form a system of couples.

1. Spin speed larger than whirl speed

Although the couples acting on the two disks are equal in magnitude and opposite in direction, they tend to bend the shaft in the direction of forward whirl. This bending of the shaft can maintain the forward whirl and instability of the rotor bearing system due to internal friction can occur. As the rotor traverses one whirl cycle, the largest friction forces act at the points of maximum slipping velocity on the disk against the direction of relative slip. As the disk completes a 90 degree rotation (spin relative to the whirl vector), the top portion tends to come inside the sleeve (because now it is moving toward the compression side of the shaft). While tending to come inside the sleeve, it experiences a friction force that opposes this motion. Similar and vice versa is the case for a bottom point on the disk. It will experience a friction force as it comes around towards the top. These forces will create a system of couples that tend to bend the shaft in the direction of forward whirl. Therefore, it can be seen that the instability due to internal friction can be represented suitably by means of internal acting moments that tend to bend the rotor shaft in the direction of forward whirl. These internal moments can be depicted in the free-body diagram of the two-disk shaft as shown in Fig.27:

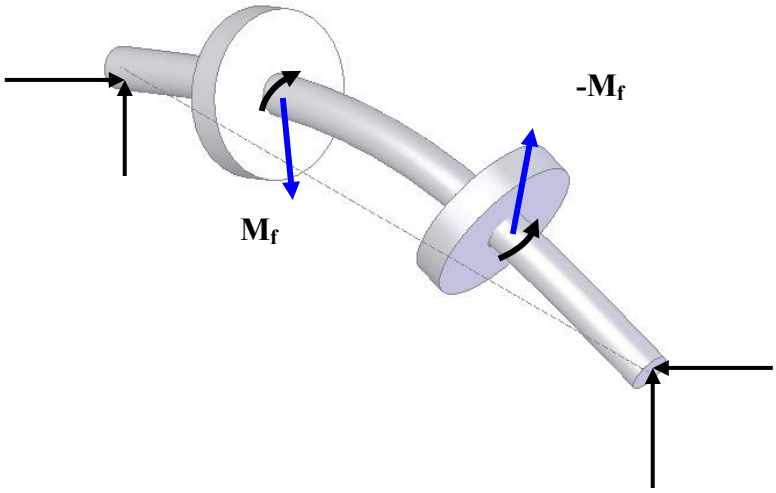

Fig. 27 Free-body diagram of the shaft showing equivalent internal friction moment vectors

2. Spin speed smaller than whirl speed

In this case, friction forces that act on the steel disks act in opposite way to the one described above. The reason is this that since the whirl speed is now larger than spin speed, the tension and compression portions (concave and convex sides) of the shaft are superseding the spin-rotated points on the disks, namely top and bottom points. As the shaft spins to one-half of the rotation, the top portion will be towards (or approaching) tension side of the shaft again. This means that it will tend to stick out of the sleeve and experience a friction force due to loose shrink fit in the direction, as shown in Fig.28. Similar and vice versa will be the case for a point on the bottom of the disk. Thus a system of equal and opposite forces will form on the surface of the disk as shown in Fig.28. This system of forces will create equal and opposite couples on the two disks, which will be as shown below:

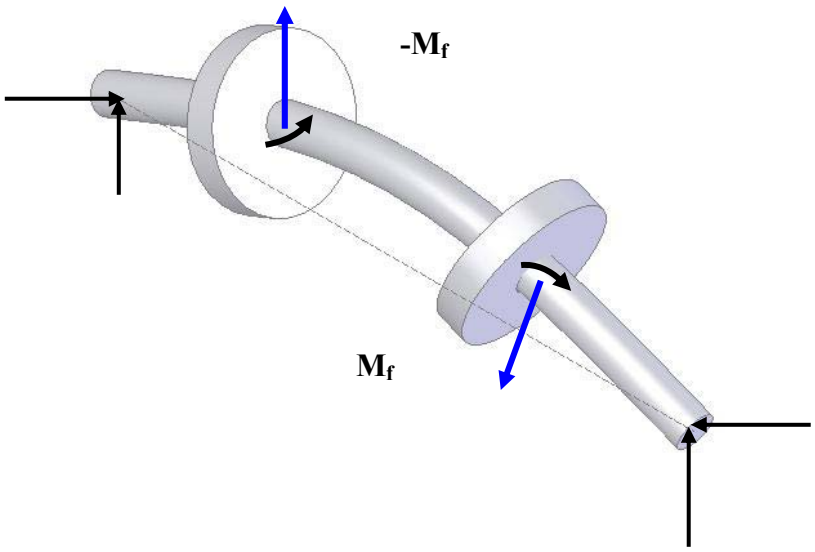

Fig. 28 Free-body diagram of the shaft showing equivalent internal friction moment vectors

Fig.28 shows that the internal friction moments are acting in a way that will tend to bend the shaft in the direction of backward whirl. Thus, for a spin speed smaller than the whirl speed, the internal friction moments will damp out the whirling and have a stabilizing effect.

CHAPTER IV

EQUATIONS OF CROSS-COUPLED MOMENTS FOR THREE INTERFACE FRICTION MODELS

The mathematical analysis for deriving the expressions for cross-coupled forces or moments for various internal friction models was carried out by some researchers, such as Gunter **[4]**, Walton **[5, 6]**, Lund **[8]** and Black **[10]**. In these references, the interface friction models which were primarily considered were viscous friction, Coulomb friction and hysteretic friction models and their effects on rotordynamic stability were analyzed. In addition, Lund analyzed a micro-slip model, which is mainly applicable for an analysis of slip in axial spline joints. Both Black and Gunter formulated the de-stabilizing mechanism as a follower force, which is a physically incorrect model but still provides some useful insight into the nature of rotordynamic stability due to internal friction. However, with the availability of high-speed computers and comprehensive rotordynamic analysis softwares such as XLTRC^{TM}, it is now possible to analyze a physically correct model of the problem by including the internal cross-coupled moments at the interface, rather than equivalent external follower forces, a procedure that has been followed widely in recent times. Even though the internal cross-coupled moments model can be implemented using the XLTRC^{TM} software, the software has a limitation of accepting only linear models for the forces and the moments.

The analysis for equations of cross-coupled moments for various interface friction models (except for the Coulomb friction model) which is developed in this chapter is drawn mainly from Lund's and Walton's work, with figures to help illustrate the derivation of cross-coupled moment equations. In addition, this chapter will explain each of these models in some detail and highlight the significance of models from point of view of how realistic their predictions are and how practical it is to implement them using the XLTRC^{TM} software. It will be shown that of the three models, only one model, namely the viscous friction, is the most practical in terms of its ease of implementation in the XLTRC^{TM} software, because it is a linear model. However, a drawback of using the viscous friction model is that although it will predict the threshold speeds of instability and give an overall knowledge of the stability of the rotor-bearing system, the predictions are not completely accurate, in that they predict an unlimited range of instability above the threshold speed of instability, which is in contradiction with the experimental research on internal friction **[14]**. On the other hand, even though Coulomb friction and the hysteretic friction models have the virtue of being realistic, as described in the Literature Review using the references **[10]** and **[5,6,14]**, it is impractical to implement them in the XLTRC^{TM} software due to their non-linear character.

BASIC ROTORDYNAMIC MODEL FOR ANALYSIS

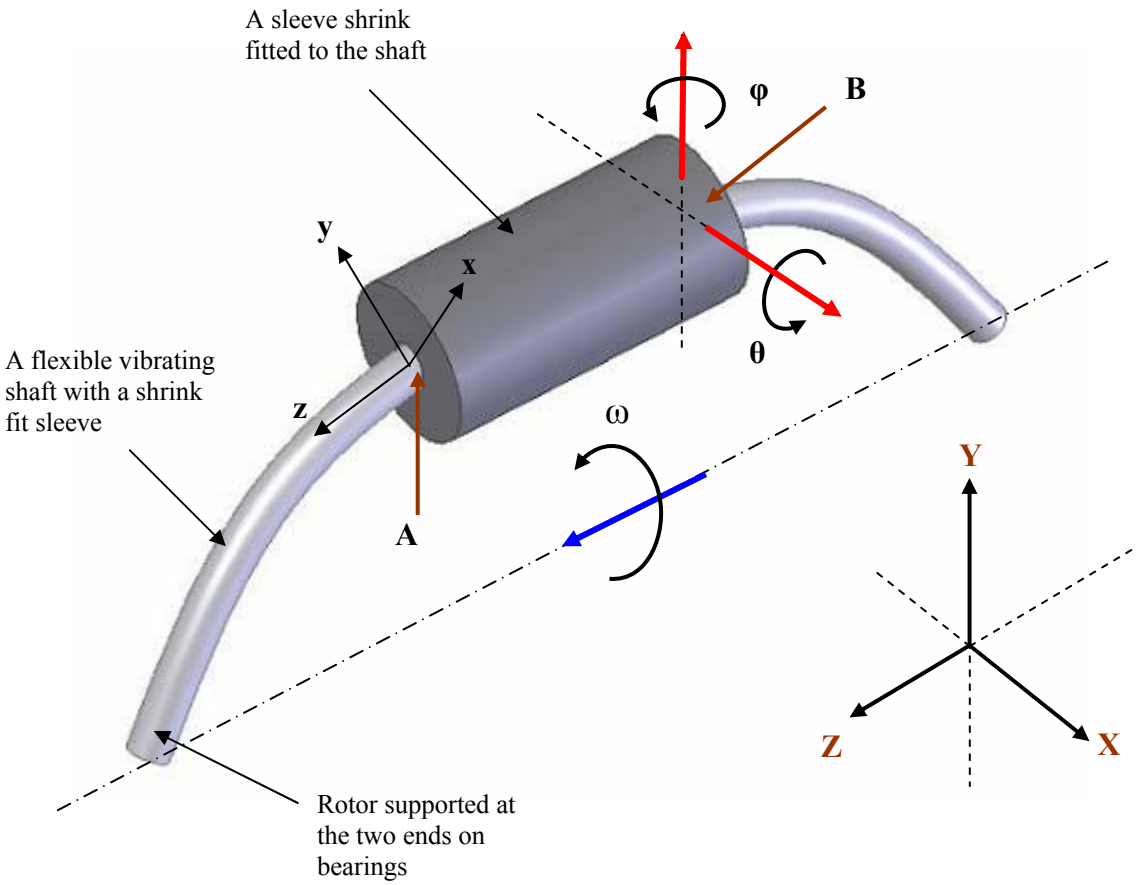

Fig. 29 Sketch of a flexible vibrating shaft with a shrink fitted sleeve. The geometry and kinematics are shown.

To derive the equations for cross-coupled moments that are developed due to internal friction at the shrink fit interfaces, consider a rotor model as shown in Fig.29. The model shown is useful in developing the equations of cross-coupled moments for the viscous friction, the Coulomb friction and the hysteretic friction models.

In Fig.29, ‘OXYZ’ is an inertial or a fixed frame of reference, whereas ‘oxyz’ is a rotating frame of reference which is attached to the rotor and which is rotating at a speed ‘ω’ with respect to the fixed frame of reference.

The basic kinematics of a joint such as a shrink fitted joint in a rotor is characterized by a discontinuity in slope of the rotor at the juncture of the joint. In Fig.29, the discontinuity in slope is shown where the shaft interfaces with the sleeve, such as at interfaces A and B. This is illustrated more clearly in the side view of the rotor as shown in Fig.30 below:

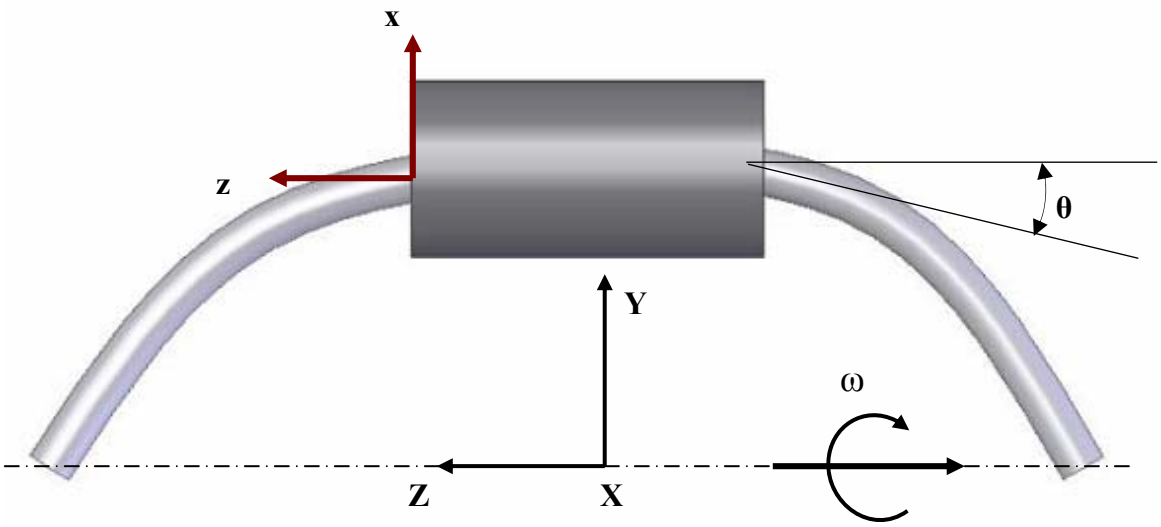

Fig. 30 Side view of the rotor model from Fig.29, showing the discontinuity of slope at the shrink fit interface between the shaft and the sleeve.

The change in slope at the shrink fit interface occurs because the shrink fitted sleeve may have different material and geometric properties as compared to the shaft due to which it may be stiffer in bending as compared to the shaft on which it is mounted

through the shrink fit. Therefore, at the shrink fit interface, the sleeve will not allow the shaft to bend as much as it would if there were no sleeve mounted on it. This will result in a difference in slope between the "interface free" and the "inside the interface" segments of the shaft. In Fig.29 and Fig.30, this difference in slopes is shown as angular displacements 'θ' and 'φ' about the X and the Y axes, respectively.

It follows that if there was a micro-slip between the shaft and the sleeve at the interface, it can be quantified using the angular displacements coordinates 'θ' and 'φ'. Since the micro-slip motion is described using the angular coordinates about the fixed OXYZ coordinate system, it follows that associated with this micro-slip angular motion at the interface will be corresponding friction bending moments, or couples, which will be developed due to the micro-slip angular motion of the shaft at the shrink fit interface. The couple is developed due to friction forces acting on the periphery of the shaft, which occur in equal and opposite pairs. That is, the diametrically opposite directions on the periphery of the disk and the shaft have friction force pairs equal in magnitude and opposite in direction due to slipping motion of the shaft that will be equivalent to a couple acting on the shaft, tending to bend it either in the direction of forward whirl (at supercritical speeds) or backward whirl (at sub critical speeds).

The generation of moments at the interface due to this angular micro-slip can be shown schematically as if there were a torsional spring and a damper at the interface between the shaft and the sleeve. The presence of torsional elements gives rise to the development of cross-coupled moments at the interface due to the micro-slip. This is shown in Fig. 31 on the next page:

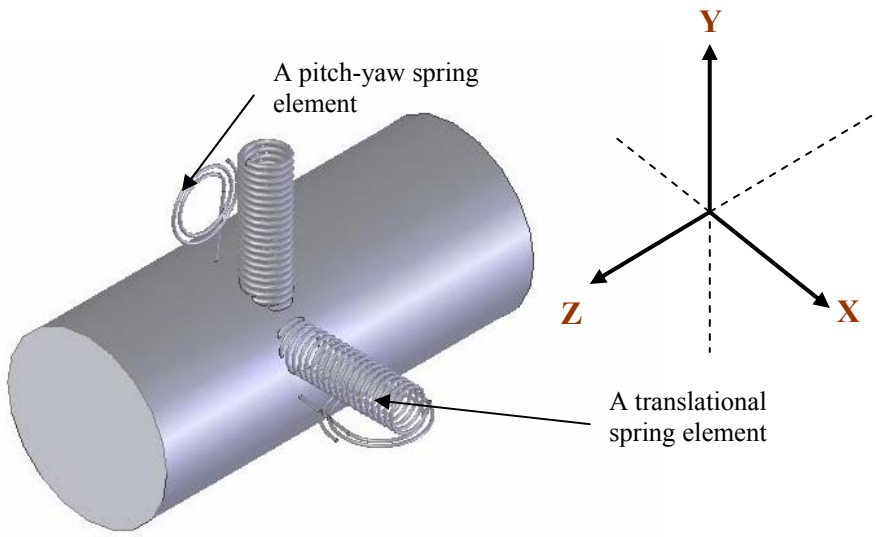

Fig. 31 A model of the shrink fit interface friction showing the spring elements. The torsional springs account for the cross-coupled moments.

In Fig.31, only torsional springs (but not the dampers) are shown for clarity, although the presence of dampers is implied. In addition, the translational springs in orthogonal directions are shown at the interface. The presence of translational springs implies the existence of a reasonably tight fit (with correspondingly high values of stiffness coefficients) that will not allow any substantial relative translational motion at the interface. Fig.31 is the model on which the XLTRC simulations for a rotor-bearing stability are based in this dissertation work.

In order to develop the equations for cross-coupled moments, consider the transformation for slopes ‘θ’ and ‘φ’ from fixed to the rotating frame of reference. Measured from the rotating frame of reference, if the differences in slopes at the interface are ‘α’ and ‘β’ about the x and the y axes respectively, the transformation can be derived using Fig.32 as shown below:

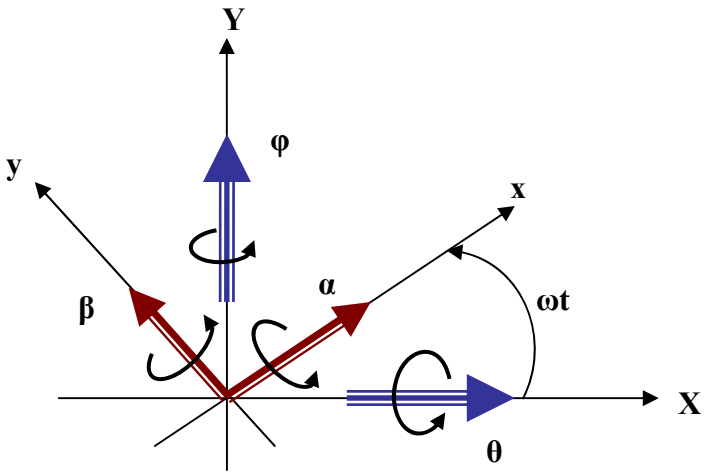

Fig. 32 Coordinate transformation between the fixed and the rotating frames of reference

$$\theta = \alpha \cos(\omega t) - \beta \sin(\omega t) \tag{3}$$

$$\phi = \alpha \sin(\omega t) + \beta \cos(\omega t) \tag{4}$$

In equations (3) and (4), 'ω' is the angular speed of rotation and 't' is time.

From equations (3) and (4), the following equations can be written:

$$\dot{\theta} + \omega\phi = \dot{\alpha} \cos(\omega t) - \dot{\beta} \sin(\omega t) \tag{5}$$

$$\dot{\phi} - \omega\theta = \dot{\alpha} \sin(\omega t) + \dot{\beta} \cos(\omega t) \tag{6}$$

The same transformation applies to the bending moment components (which arise due to micro-slip motion) measured in the fixed and the rotating frames of reference. The transformation from the fixed to the rotating frame can be expressed as follows:

$$M_\theta = M_\alpha \cos(\omega t) - M_\beta \sin(\omega t) \quad (7)$$

$$M_\phi = M_\alpha \sin(\omega t) + M_\beta \cos(\omega t) \quad (8)$$

KINEMATICS OF ROTOR MOTION

The motion is assumed to be harmonic with angular frequency 'Ω' (precession speed) such that:

$$\theta(t) = \theta_C \cos(\Omega t) - \theta_S \sin(\Omega t) = Re\{(\theta_C + i\theta_S)e^{i\Omega t}\} \quad (9)$$

In equation (9), the precession motion of rotor 'θ(t)' (angular motion about the X-axis) is defined in terms of the precession frequency 'Ω'. The physical interpretation of 'Ω' is the whirling frequency of the rotor, as would be measured through a signal analyzer when sub-synchronous vibrations are excited in the rotor. In equation (9), complex variables are used as an alternate and a convenient method to express the motion variables in a compact form. The symbol 'i' is for the complex variable operator:

$$i = \sqrt{-1}$$

In accordance with the usual convention θ(t) can be expressed in a compact form as follows:

$$\theta = \theta_C + i\theta_S \quad (10)$$

In writing equation (10), it is assumed that the real operator 'Re' and complex exponential function '$e^{i\Omega t}$' are implicit and they will be assumed to always apply, even though not shown in the expression, whenever a kinematic variable is expressed in its complex form.

The angular motion due to the micro-slip friction moments of the rotor, θ(t), can be expressed in a more general form as follows:

$$\theta = \theta_f + \theta_b \tag{11}$$

In equation (11), 'θ_f' and 'θ_b' are complex numbers. The subscripts denote "forward" and "backward" components, respectively. Equation (11) expresses the concept that the motion may be thought of as made up of two circular whirl motions, once with the forward whirl, 'θ_f', and another one with the backward whirl, 'θ_b'.

Without loss of generality, the micro-slip angular motion, φ(t), of the rotor about the Y-axis can be expressed as follow:

$$\phi = -i\theta_f + i\theta_b \tag{12}$$

The same convention applies to φ(t) in equation (12) as is applied to θ(t) in equation (11) (that the real operator 'Re' and the complex exponential function '$e^{i\Omega t}$' are assumed implicit and are not shown exclusively in writing equation (12)).

From equations (11) and (12), the forward and backward components, θ_f and θ_b can be expressed as follows:

$$\theta_f = \frac{1}{2}(\theta + i\phi) \tag{13}$$

$$\theta_b = \frac{1}{2}(\theta - i\phi) \tag{14}$$

Using the coordinate transformations (equations (3) and (4)) in conjunction with equations (11) and (12), the following equations result:

$$\alpha = \theta_f e^{i(\Omega-\omega)t} + \theta_b e^{i(\Omega+\omega)t} \tag{15}$$

$$\beta = -i\theta_f e^{i(\Omega-\omega)t} + i\theta_b e^{i(\Omega+\omega)t} \tag{16}$$

Equations (15) and (16) show that the motion which in the fixed frame has only the single frequency Ω, but with an elliptical orbit, splits up into two circular orbits, each with its own frequency, in the rotating frame.

1. Viscous friction model

Consider the moment stiffness of the shrink fit joint to be 'K' and damping at the interface to be 'C'. If the internal friction is modeled as viscous friction, the bending moment components (due to micro-slip) as measured in the rotating frame of reference 'oxyz' can be expressed as:

$$M_\alpha = K\alpha + C\dot{\alpha} \tag{17}$$

$$M_\beta = K\beta + C\dot{\beta} \tag{18}$$

By using the coordinate transformations from equations (3),(4),(5),(6),(7) and (8), the components of bending moments due to micro-slip in the fixed reference frame 'OXYZ' can be expressed as follows:

$$M_\theta = K\theta + C(\dot{\theta} + \omega\phi) \tag{19}$$

$$M_\phi = K\phi + C(\dot{\phi} - \omega\theta) \tag{20}$$

From equations (19) and (20), the bending moment components equations show the presence of cross-coupling stiffness terms ‘Cω’, which being of opposite sign, act destabilizing **[8]**. This can be shown by computing the energy dissipated in one cycle:

$$E_{diss} = \int_{0}^{2\pi/\omega} (M_{\theta}\dot{\theta} + M_{\phi}\dot{\phi})dt = 2\pi C[(\Omega - \omega)|\theta_f|^2 + (\Omega + \omega)|\theta_b|^2] \quad (21)$$

In deriving equation (21), the angular velocities of the micro-slip rotor motion about the X and the Y axes are calculated using equations (3), (4), (15) and (16).

Equation (21) shows that when the rotational speed ‘ω’ exceeds the natural frequency ‘Ω’, the first term becomes negative. Therefore, if the whirl mode is a circular orbit with forward whirl ($\theta_b = 0$), the rotor becomes unstable when $\omega = \Omega$. If the backward whirl component is not equal to zero, then the instability will occur depending upon the speed, when the first term exceeds the second term in equation (21).

2. Coulomb friction model

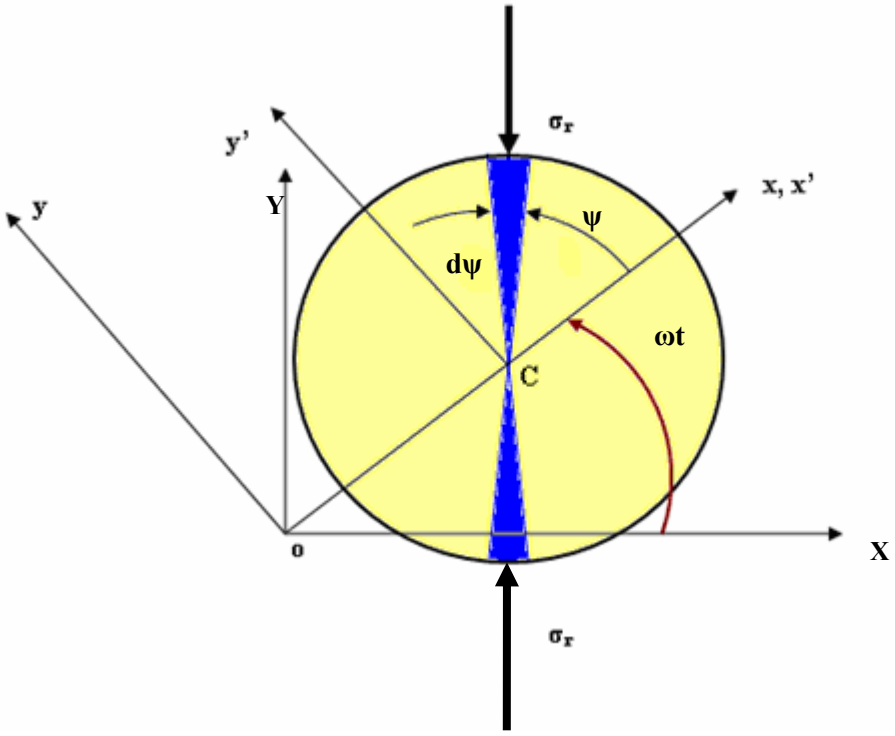

Fig. 33 End view of the disk showing the radial stresses acting on its surface

To formulate the internal friction moments using the Coulomb friction model for a rotor disk which is spinning, whirling and nutating (tilting), consider the plane of the disk and the rotating oxyz frame attached to the disk as shown in Fig.33. Consider another rotating frame which has its origin at the geometric center 'C' of the disk. The variable 'ψ' locates the position of a point on the disk, whereas 'σ_r' denotes the radial stress acting at a location 'ψ' of the disk due to the shrink fit and spin of the shaft.

Differential radial force acting on the disk in its first quadrant (as seen from o'x'y'z' frame) can be expressed as follows:

$$dF_r = \sigma_r dA \tag{22}$$

The differential area element over which the radial stress acts can be expressed as follows:

$$dA = (Rd\psi)L = RLd\psi \tag{23}$$

In equation (23), 'L' is the axial span of the disk and 'R' is its radius. Using equation (23), equation (22) can be expressed as:

$$dF_r = RL\sigma_r d\psi \tag{24}$$

A corresponding differential friction force acting over the same differential element of area is developed, based on Coulomb model, such that:

$$dF_z = \mu RL\sigma_r d\psi \, sgn(V_{Sliding}) \tag{25}$$

In equation (25), 'μ' is either the static friction coefficient, if $V_{Sliding} = 0$, or it is the kinetic coefficient of friction, if $V_{Sliding} \neq 0$. The differential friction force as expressed in equation (25) acts in the axial direction, because according to Coulomb friction law, the friction force acts perpendicular to the normal force, which is in the radial direction (due to the normal radial stress at the interface).

Based on above equations, the differential moment due to normal stress and the corresponding frictional shear stress on the surface above axis 'ox' can be expressed as:

$$d\vec{M} = \vec{R} \times d\vec{F}_z \tag{26}$$

In equation (26), the vector 'R' is moment arm of the differential force dF_z, and its magnitude is equal to the interface radius of the disk. The direction of vector 'R' is radial, with this direction being from geometric center 'C' to the periphery of the disk. Thus, 'R' can be expressed as:

$$\vec{R} = R\,\underline{e}_r \tag{27}$$

Carrying out the cross product in equation (27), the differential moment vector is expressed as:

$$d\vec{M} = -RdF_z\,\underline{e}_\psi\; sgn(V_{Sliding}) = -\mu R^2 L\sigma_r\,\underline{e}_\psi\; d\psi\; sgn(V_{Sliding}) \tag{28}$$

In equation (28), the unit vector in 'ψ' direction is a result of cross product of the radial unit vector and the 'k' vector, which is perpendicular to the plane of the disk. From simple geometry, a well-known transformation between the unit vectors in the disk (that is, $\mathbf{e_r}$ and $\mathbf{e_\psi}$) and the unit vectors in the rotating oxyz frame, is given by:

$$\underline{e}_r = \underline{i}\cos\psi + \underline{j}\sin\psi \tag{29}$$

$$\underline{e}_\psi = -\underline{i}\sin\psi + \underline{j}\cos\psi \tag{30}$$

Using equations (29) and (30), the differential moment vector can be integrated from 0 to 2π to give the value of the resultant moment vector due to the differential frictional force contributions.

To compute the integral of equation (28) in the interval 0 to 2π, it is necessary to establish an expression for the sliding velocity '$V_{Sliding}$', because the numerical sign of the differential moment in equation (20) depends upon the sign of the relative sliding velocity, which will vary from positive to negative along the circumference of the disk (the relative sliding velocity will switch signs from +1 to -1 in the interval 0 to 2π).

Relative sliding velocity

To derive an expression for the relative sliding velocity, consider Figs.1 and 5. In terms of position vectors and angular velocity vectors, the relative sliding velocity of a point P on the circumference of the disk (or the shaft) can be expressed as follows:

$$\vec{V}_P = \underline{\omega} \times \underline{r}_P \tag{31}$$

Equation (31) expresses the velocity of the point 'P' as measured from point 'C' due to angular velocity of the shaft relative to the sleeve due to slip at the interface.

The expression for the angular velocity to be used in equation (31) can be expressed as (using rotating frame coordinates):

$$\underline{\omega} = \dot{\alpha}\,\underline{i} + \dot{\beta}\,\underline{j} \tag{32}$$

The position vector '$\mathbf{r_P}$' using the rotating frame 'oxyz' can be expressed as follows:

$$\underline{r}_P = R\cos\psi\,\underline{i} + R\sin\psi\,\underline{j} \tag{33}$$

Carrying out the cross-product in equation (31) using equations (32) and (33), the expression for relative sliding velocity of a point 'P' on the shaft is:

$$\vec{V}_P = (R\dot{\alpha}\cos\psi - R\dot{\beta}\sin\psi)\underline{k} \tag{34}$$

Equation (34) shows that the relative sliding velocity of a point 'P' on the disk will vary sinusoidally as a function of the circumferential location on the disk as the shaft whirls and as the disk on the shaft undergoes slipping at the shrink fit interface.

The relative sliding velocity in equation (34) is in the axial direction (in the direction of the unit vector 'k').

From equation (34), the magnitude of relative sliding velocity can be expressed as follows:

$$V_{Sliding} = R\dot{\alpha}\cos\psi - R\dot{\beta}\sin\psi = R\sqrt{\dot{\alpha}^2 + \dot{\beta}^2}\ \sin(\psi - \gamma) \tag{35}$$

In equation (35), the argument 'γ' is defined as follows:

$$\cos\gamma = \frac{\dot{\alpha}}{\sqrt{\dot{\alpha}^2 + \dot{\beta}^2}} \tag{36}$$

$$\sin\gamma = \frac{\dot{\beta}}{\sqrt{\dot{\alpha}^2 + \dot{\beta}^2}} \tag{37}$$

From equation (35), the sliding velocity changes sign as the sinusoidal function changes sign. Using equation (35), the following conditions for sign function of the sliding velocity are defined:

$$sgn(V_{Sliding}) = +1\ ,\ \gamma < \psi < \pi + \gamma \tag{38}$$

$$sgn(V_{Sliding}) = -1\ ,\ \pi + \gamma < \psi < 2\pi + \gamma \tag{39}$$

Integrating equation (28) in the interval ψ = 0 to 2π by using equations (38) and (39):

$$\vec{M} = \int_0^{2\pi} d\vec{M} = \int_{\gamma}^{\pi+\gamma} d\vec{M} + \int_{\pi+\gamma}^{2\pi+\gamma} d\vec{M} = -4\mu R^2 L\sigma_r(\underline{i}\cos\gamma + \underline{j}\sin\gamma) \tag{40}$$

Equation (40) shows that the resultant moment due to frictional stresses and sliding velocity at the interface is a non-zero vector, with components along both the x and the y axes of the rotating frame of reference. Equation (40) shows the presence of a couple that is developed due to frictional forces acting at the interface. The frictional forces along the circumference reverse signs due to reversal of sign of the sliding

velocity (equation (35)) and thus form equal and opposite pairs of forces, which form a resultant couple as expressed by equation (40).

From equation (40) and equations (7) and (8), the frictional moment has components along both the X and the Y axes of the fixed frame of reference.

From equation (40), the components of frictional moments along the x and the y axes can be defined as follows:

$$M_{\alpha} = -4\mu R^2 L\sigma_r \frac{\dot{\alpha}}{\sqrt{\dot{\alpha}^2 + \dot{\beta}^2}} \tag{42}$$

$$M_{\beta} = -4\mu R^2 L\sigma_r \frac{\dot{\beta}}{\sqrt{\dot{\alpha}^2 + \dot{\beta}^2}} \tag{43}$$

Using equations (5),(6), (7) and (8) and applying them to equations (42) and (43) to obtain the components of the bending moments in the X and the Y directions, the following equations are obtained:

$$M_{\theta} = -4\mu R^2 L\sigma_r \frac{(\dot{\theta} + \omega\phi)}{\sqrt{\dot{\alpha}^2 + \dot{\beta}^2}} \tag{44}$$

$$M_{\phi} = -4\mu R^2 L\sigma_r \frac{(\dot{\phi} - \omega\theta)}{\sqrt{\dot{\alpha}^2 + \dot{\beta}^2}} \tag{45}$$

Equations (44) and (45) can be expressed completely in terms of the fixed frame coordinates as follows (using equations (3) and (4)):

$$M_\theta = -4\mu R^2 L\sigma_r \frac{(\dot{\theta}+\omega\phi)}{\sqrt{(\dot{\theta}+\omega\phi)^2+(\dot{\phi}-\omega\theta)^2}} \tag{46}$$

$$M_\phi = -4\mu R^2 L\sigma_r \frac{(\dot{\phi}-\omega\theta)}{\sqrt{(\dot{\theta}+\omega\phi)^2+(\dot{\phi}-\omega\theta)^2}} \tag{47}$$

Equations (46) and (47) show that the moment components due to Coulomb friction at the shrink fit interface are cross-coupled moments, due to the presence of speed dependent terms in the numerators, which are of opposite signs in the two equations. The internal moments in Coulomb friction model are non-linear functions of the rotating speed and amplitudes as well as angular velocities of the micro-slip. This is in contrast with the viscous friction model (equations (19) and (20)) where the cross-coupled moments are linear functions of the rotational speed as well as the amplitude and angular velocity of the micro-slip.

Therefore, the formulation shows that due to reversal of the friction force direction over the periphery of the disk, the resultant moment is not zero. The resultant moment depends upon several geometric and dynamic parameters of the rotor, such as the radius, axial span, friction coefficient, the normal radial stress (which in turn is a function of geometric and elastic properties of the disk, as well as the value of shrink fit at zero speed and the spin speed) and sign of the sliding velocity.

3. Hysteretic friction model

The hysteretic friction or the solid friction model assumes the interface internal friction moments to be of the following mathematical form:

$$M_\alpha = K\alpha + C\, sgn(\dot{\alpha})|\alpha| \tag{48}$$

$$M_\beta = K\beta + C\, sgn(\dot{\beta})|\beta| \tag{49}$$

In equations (48) and (49), ‘K’ is the moment stiffness coefficient whereas ‘C’ is also a moment stiffness coefficient, but it differs from ‘K’ in the sense that it contributes alternately positively and negatively to the moments in each direction, depending upon the frequency of micro-slip motion.

Using equations (7),(8), (15) and (16), the corresponding components of bending moments developed at the interface about the X and the Y axes can be expressed as follows:

$$M_\theta = [K + i\frac{1}{2}C(sgn(\Omega+\omega)+sgn(\Omega-\omega))]\theta + \frac{1}{2}C(sgn(\Omega+\omega)-sgn(\Omega-\omega))\phi \quad (50)$$

$$M_\phi = [K + i\frac{1}{2}C(sgn(\Omega+\omega)+sgn(\Omega-\omega))]\phi - \frac{1}{2}C(sgn(\Omega+\omega)-sgn(\Omega-\omega))\theta \quad (51)$$

From equations (50) and (51), there are cross-coupling terms in the expressions for moment components. These cross-coupled terms produce destabilizing motion of the rotor. As calculated for the case of viscous friction model in equation (13), the energy dissipated per cycle can also be calculated for the case of hysteretic friction model. It is expressed by the following equation:

$$E_{diss} = 2\pi C[sgn(\Omega-\omega)|\theta_f|^2 + sgn(\Omega+\omega)|\theta_b|^2] \quad (52)$$

Equation (52) shows that the energy dissipated per cycle depends upon the sign of the term that involves the frequency difference between whirling frequency and the rotational speed. When rotational speed exceeds the whirling frequency, the energy is “added” to the system, instead of being dissipated, provided the backward whirl component is smaller in magnitude as compared to the forward whirl component. However, the amount of energy added to the rotor or dissipated from the rotor due to slippage at the interface is independent of magnitude of whirling frequency. The independence of energy dissipation or addition from the magnitude of whirling

frequency is in better agreement with experiments, as compared to the viscous friction model prediction, in which case energy dissipation or addition is dependent upon the magnitude of whirling frequency, in addition to the numerical sign of frequency difference term Ω-ω.

PHYSICAL INTERPRETATION OF FRICTION MODELS

The various friction models discussed in previous pages can be interpreted physically based on the concept of energy dissipation per cycle for each of the models. The qualitative and quantitative description of each of the three models is as follows:

1. Viscous friction model

Viscous friction model is one of the most commonly used models in vibrations and rotordynamic analysis. The viscous friction model is especially useful because of its linear mathematical form. The governing differential equations for most mechanical systems with viscous damping terms have exact analytical solutions.

When the viscous friction model is applied to study the phenomenon of internal friction in solids, the governing physical model of the solid is called as Kelvin-Voigt model. In schematic form, such a model for a solid with internal friction is shown in Fig.34:

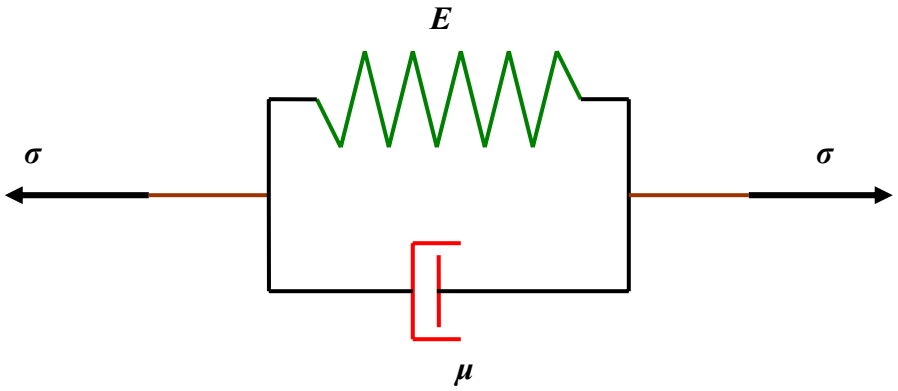

Fig. 34 Kelvin-Voigt model of internal friction in solids

This model is also commonly termed as viscoelastic model. From Fig.34, the model takes into account both elastic (energy absorbing and recovering) as well as friction (energy dissipation) behavior of a solid subjected to stresses. The constitutive equation of Kelvin model can be written as follows:

$$\sigma = E\varepsilon + \mu \dot{\varepsilon} \tag{53}$$

In equation (53), the applied stress on the body is σ, whereas ε is the strain induced in the body. The second term on the right hand side of equation (53) is the energy dissipation term due to strain rate. The elastic modulus is denoted by E.

To derive an expression for energy dissipated per cycle, consider the solid subjected to harmonically varying strain:

$$\varepsilon(t) = \varepsilon_0 \sin(\omega t) \tag{54}$$

Differentiating equation (52) with respect to time t, the equation for strain rate is:

$$\dot{\varepsilon} = \omega\varepsilon_0 \cos(\omega t) = \pm\varepsilon_0\omega[1-\sin^2(\omega t)]^{1/2} = \pm(\varepsilon_0{}^2 - \varepsilon^2)^{1/2} \qquad (55)$$

Substituting equation (55) in equation (53) leads to the following equation:

$$\sigma = E\varepsilon \pm \mu\omega(\varepsilon_0{}^2 - \varepsilon^2)^{1/2} \qquad (56)$$

The graph of equation (56) is an ellipse, with stress σ on vertical axis and the strain ε on horizontal axis. The area of the ellipse is energy dissipated per cycle. The graph of equation (56), which is called as hysteresis loop, is shown on the next page:

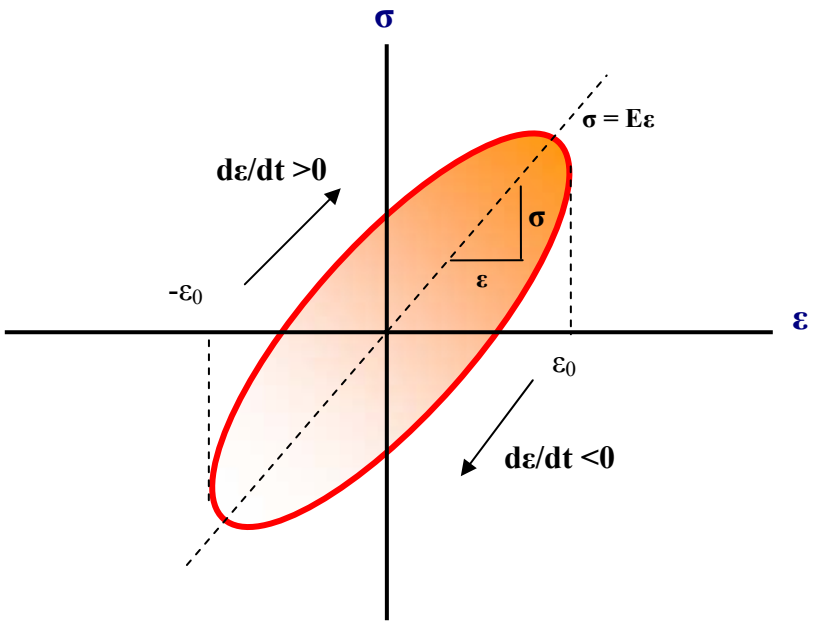

Fig. 35 Hysteresis loop due to viscous friction

Fig.35 shows the hysteresis loop formed by plotting equation (56). The major axis of the ellipse is the line: σ = Eε. The upper part of the ellipse corresponds to $\dot{\varepsilon} > 0$, because $\sigma > E\varepsilon$ in that case. The lower part corresponds to $\dot{\varepsilon} < 0$.

The energy dissipated per unit area per cycle can be obtained by calculating the area of the hysteresis loop. The energy dissipated per area per cycle is:

$$E_{diss} = \int_0^{2\pi/\omega} \mu \dot{\varepsilon}^2 \, dt = \pi\omega\mu\varepsilon_0^2 \tag{57}$$

From equation (57), the energy dissipated is proportional to the frequency of oscillation ω. This dependence on frequency comes about as a result of the term $\mu\dot{\varepsilon}$, which is proportional to ω.

The same concept of viscous friction can be extended to conceptualize interface friction moments in terms of a direct stiffness coefficient K and a direct damping coefficient C. The energy dissipated or added to the rotor system in the case of viscous friction model is proportional to the frequency difference, as shown in equation (13). Therefore, the viscous friction model assumes that the shrink fit interface friction moments are comprised of a direct spring effect, whereby the spring tends to restore the relative slip motion of the shaft, whereas simultaneously, there is an energy dissipation effect, the energy of micro-slip motion is dissipated or added, depending upon the difference of whirling frequency and the rotational speed. This can be depicted as shown in Fig.36:

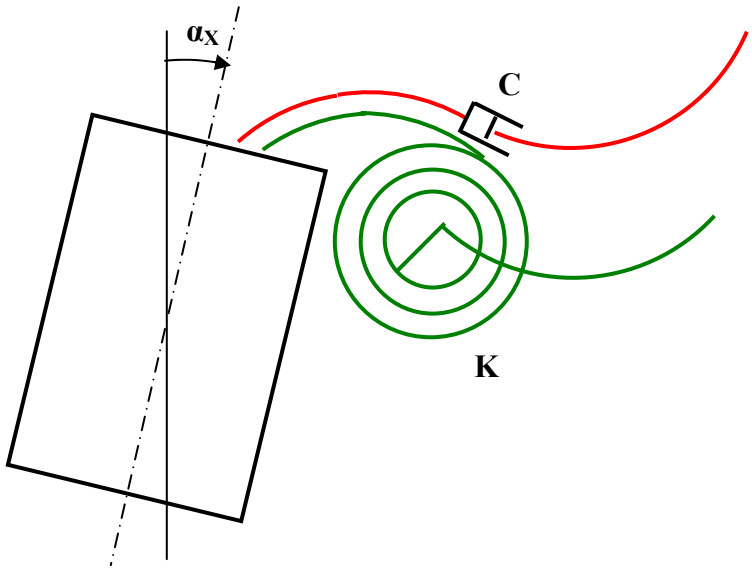

Fig. 36 Schematic description of a shrink fit interface using a torsional spring and a damper

2. Hysteretic friction model

Hysteretic friction model is less widely utilized in modeling damping and friction in mechanical systems, as compared to the viscous friction model. This is because it is a non-linear model. Nevertheless, the model is important, because the rotordynamic predictions of hysteretic friction model for slippage in the shrink fits joints are validated by experiments **[14]**. To explain a physical model for hysteretic friction, the following development is adopted from **[23]**.

In schematic form, a hysteretic friction model can be represented as the following mechanical model:

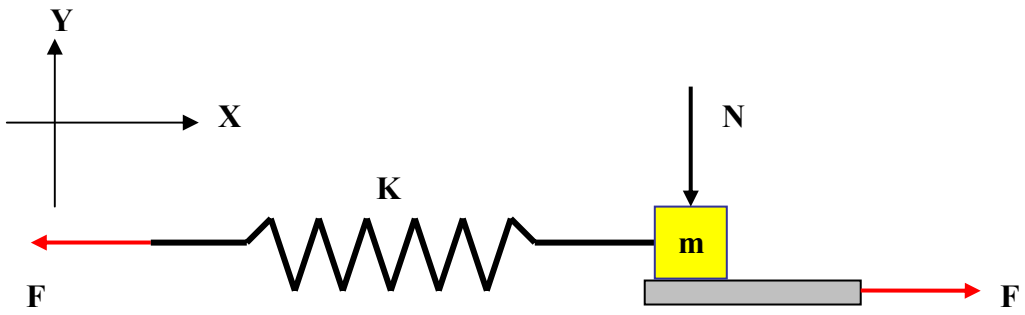

Fig. 37 A mechanical model for illustration of the hysteretic friction

As shown in Fig.37, consider a spring-mass system which is subjected to horizontal forces F. In addition, the mass is loaded by a vertical force N. The mass rests on a surface that has friction, which opposes the displacement of mass relative to the surface, when the horizontal forces are applied. The friction can be Coulomb friction or any other model which models the resistance of mass to sliding relative to the surface.

Initially, when the forces F are applied to the system, the spring of stiffness K will stretch or compress (if forces are in opposite direction to that shown in Fig.37), and the mass will not move, owing to the resistance offered by the surface on which it rests. The deflection in the spring is F/K only. As the force is gradually increased, a limiting value of the force (F_{max}) will reach at which the mass eventually starts to slide on the surface. In this case, the deflection of the spring will be equal to the deflection of the mass plus the static deflection F/K, with the same amount of limiting amount of applied force F_{max}. This is the case of increase or decrease of deformation of the spring without accompanying increase in the magnitude of limiting amount of force. In addition, the spring deformation (stretch or compression) depends on the sign of the relative velocity of the mass and the surface, and not on the magnitude of relative velocity. Therefore, the model in Fig.37 is a non-linear model.

As in the case of viscous friction model, a hysteresis loop can be drawn for such a model. Replacing the forces by stresses and the spring deformations by strains, the following figure illustrates the variation of applied stresses with accompanying strains in the system:

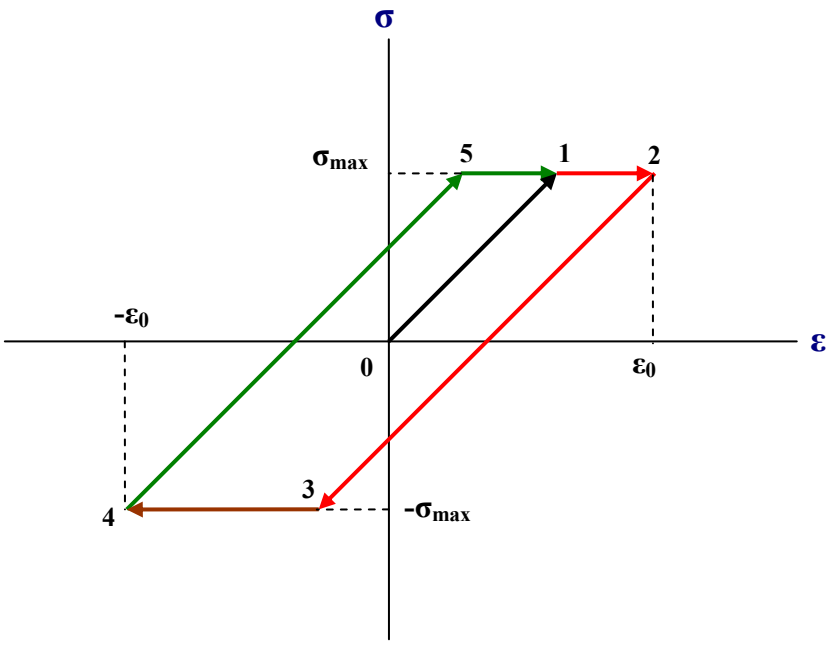

Fig. 38 Hysteresis loop for hysteretic friction model

Fig.38 shows the hysteresis loop for the mechanical model in Fig.37. From point '0' to '1', the only strain of the spring is due to the elastic strain, σ/E. As the limiting value of the stress σ_{max} is reached, the mass starts sliding on the surface and the strain in the spring increases as a result of the sliding, with no accompanying increase of stress. This is indicated in Fig.38 as part of the graph from point '1' to '2'. After a certain maximum strain ε_0 is reached, the spring force starts backward motion of the mass, which results in the decrease of strain, and is shown by line segment '2' to '3' in Fig.38.

Between points ‘2’ to ‘3’, the velocity of the mass is in the negative X direction. The path ‘2’ to ‘3’ is a straight line, because the spring strain is a linear function of stress. At point ‘3’, a maximum stress $-\sigma_{max}$ is reached. It can be seen that the hysteresis loop formed due to hysteretic friction is dependent upon the sign or sense of the velocity, but not on its magnitude.

As the mass is acted upon by the negative maximum stress $-\sigma_{max}$, it slides and the spring compresses at the same strain due to sliding motion. This is shown as points ‘3’ and ‘4’. When the spring undergoes a maximum compressive strain of $-\varepsilon_0$, the spring force tends to move the mass in the positive X direction. This is shown as segment ‘4’ to ‘5’. In this part of the loop, the velocity of the mass is in the positive X direction. Finally, the maximum stress σ_{max} is reached at point ‘5’ and from ‘5’ to ‘1’, the mass undergoes sliding and the cycle continues.

For hysteretic friction, it is concluded that the amount of energy dissipated is dependent on the magnitude of strain, but not on the magnitude of strain rate. It is, however, dependent upon the sense of strain rate (positive or negative).

3. Coulomb friction model

Coulomb friction model is one of the most widely known, but lesser widely used model (except for analysis of relatively simple dynamics problems) for analysis of friction between dry surfaces. It is known for its better agreement with experiments of relative motion between solid objects as compared to any other model, but it is less used due to its non-linear character. As shown in **[14]**, the experimental test rotor system with shrink fit interface joints exhibits a damping character that can be explained with Coulomb and hysteretic damping models, but less well by the viscous damping model.

To explain the physical model of Coulomb damping, the following development is extensively adopted from **[24]**.

Consider a solid block of weight W resting on a horizontal surface as shown in Fig.39 below:

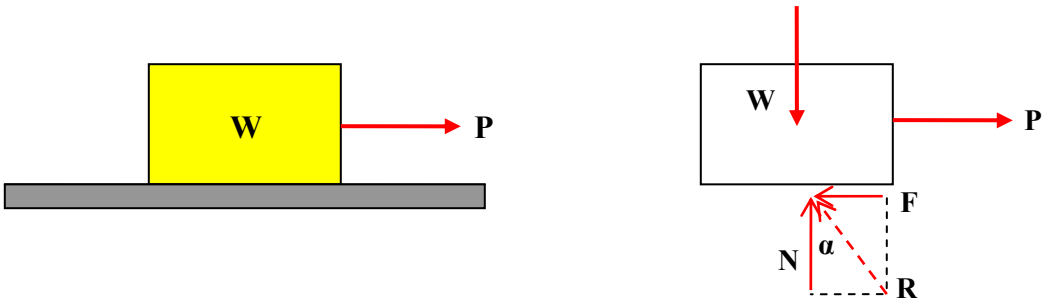

Fig. 39 Mechanical model to explain Coulomb friction

As shown in Fig.39, the block is subjected to a horizontal force P that tends to pull the block in the direction of application of force. In the model considered, the magnitude of P varies continuously from zero to a value sufficient to move the block and give it an appreciable velocity. The free-body diagram of the block for any value of P is also shown in Fig.39. In the free-body diagram, the tangential friction force exerted by the plane on the block is labeled F. This friction force will always be in a direction to oppose motion or the tendency toward motion of the block. There is also a normal force N which in this case is equal to W, and the total force R exerted by the supporting surface on the block is the resultant of N and F.

A magnified view of the irregularities of the mating surfaces will aid in visualizing the mechanical action of friction. The magnified view is shown in Fig.40 on the next page:

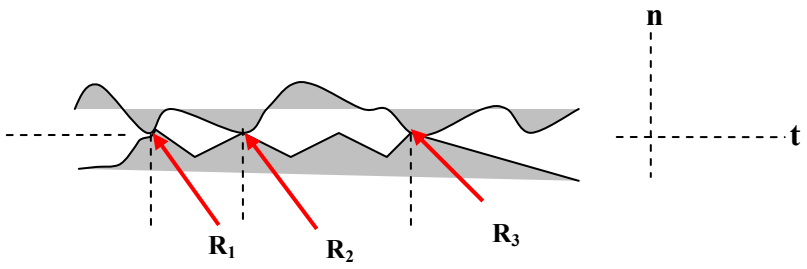

Fig. 40 A magnified view of the irregularities at the mating surfaces

Fig.40 shows that the support is necessarily intermittent and exists at the mating humps. The direction of each of the reactions on the block R_1, R_2, R_3 etc., will depend not only on the geometric profile of the irregularities but also on the extent of local deformations, as well as the welding that can take place on a minute scale at each contact point. The total normal force N is the sum of the n-components of the R's, and the total frictional force F is the sum of the t-components of the R's. When the surfaces are in relative motion, the contacts are more nearly along the tops of the humps, and the t-components of the R's will be smaller than when the surfaces are at rest relative to one another. This consideration helps to explain the known fact that the force P necessary to maintain motion is less than that required to start the block when the irregularities are more nearly in mesh.

In the model of Fig.39, assume that the friction force F is measured as a function of P. The resulting experimental relation is indicated in Fig.41 on the next page:

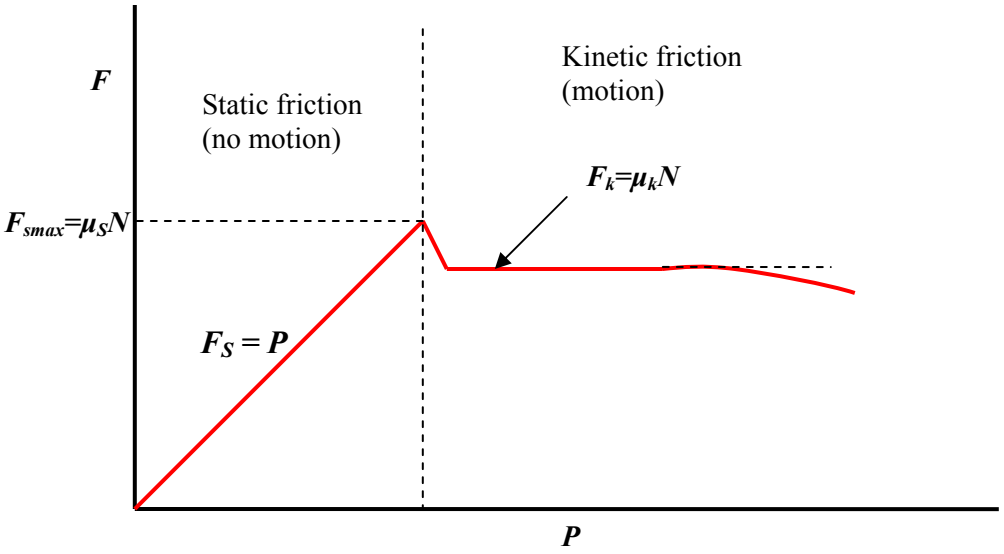

Fig. 41 Friction force F as a function of applied force P

From Fig.41, when P is zero, equilibrium requires that there be no friction force. As P is increased, the friction force must be equal and opposite to P as long as the block does not slip. During this period the block is in equilibrium, and all force acting on the block must satisfy the equilibrium conditions (zero net force and moment). Finally a value of P is reached which causes the block to slip and to move in the direction of the applied force. Simultaneously the friction force drops slightly and rather abruptly to a somewhat lower value. It remains essentially constant for a period but then drops off still more with higher velocities.

The region up to the point of slippage or impending motion is known as the range of static friction. This force may have any value from zero up to and including, in the limit, the maximum value. The magnitude of the maximum static friction force is determined from the Coulomb law of static friction as follows:

$$F_{S\,max} = \mu_S N \tag{58}$$

In equation (58), μ_S is a constant, called as the coefficient of static friction, which depends the materials of the mating surfaces and their geometry.

After slippage occurs a condition of kinetic friction is involved. Kinetic friction force is usually slightly lower than the maximum static friction force in magnitude. Moreover, the sense or direction of the kinetic friction force depends upon the direction of relative velocity of the mating surfaces. Coulomb's law of kinetic friction expresses the magnitude and sense of the kinetic friction force as follows:

$$F_K = \mu_K N \, sgn(V_{Rel}) \tag{59}$$

Equation (59) is a non-linear equation in the motion variable of the block because it involves the "signum" function, which is a non-linear function.

CHAPTER V

EXPLANATION OF KIMBALL'S EXPERIMENTS USING INTERNAL MOMENTS MODEL

BASIC THEORY OF ROTOR INTERNAL FRICTION

The fundamental theory to explain the rotor internal friction comes from the work of A.L. Kimball (1924). For this, consider the following figure:

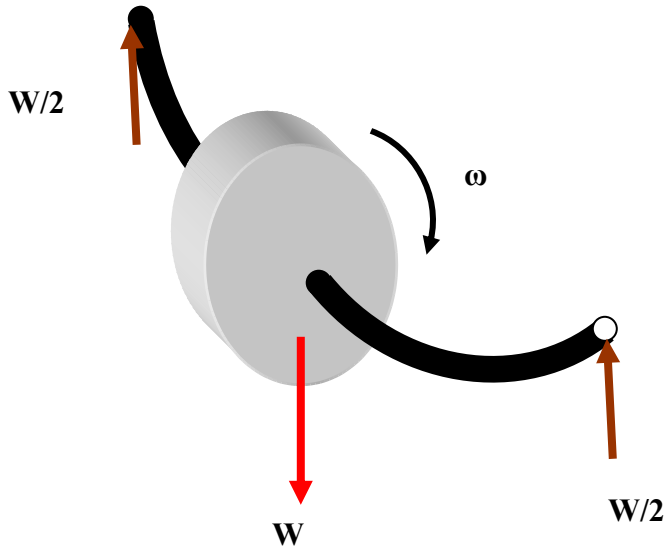

Fig. 42 A rotor disk supported on a flexible shaft rotating clockwise.

In Fig.42, the rotor disk is a heavy weight W and is supported on a flexible shaft with internal hysteresis. The reaction loads are acting on the two ends through the bearings. For simplicity, imbalance is neglected and the downwards deflection of the flexible shaft is due to gravity alone. If the shaft were purely elastic, the rotor will deflect vertically downwards. However, when the internal friction is present in the shaft fibers, the rotor does not deflect vertically downwards, and instead makes an inclination

angle φ with the vertical when the shaft spins, as shown in the end-view of the disk in Fig.43:

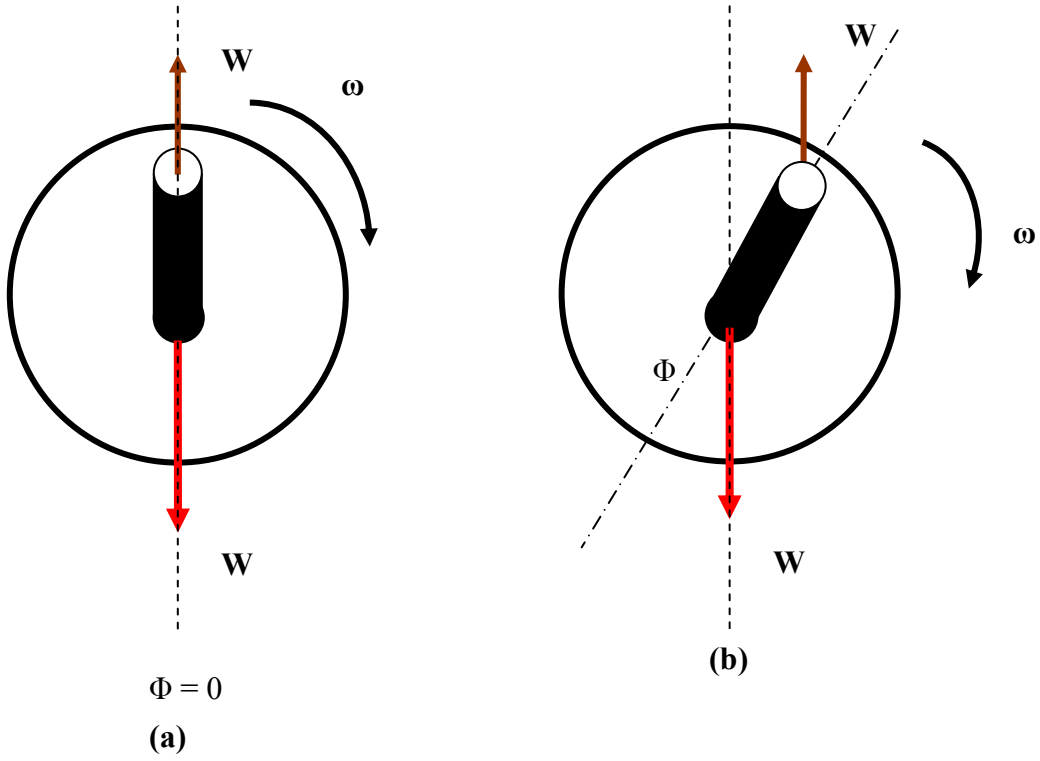

Fig. 43 Rotor disk side views (a) Purely elastic deflection (b) Deflection with internal friction

Fig.43 shows that the disk will be deflected sideways. The deflection will be in the direction of rotation. This can be explained as follows: When the rotor is being turned at a constant speed, there is applied torque acting on it, in addition to the reactions from the bearings. Due to bearings, the torque is dissipated, so that the rotor turns at a constant speed. If the rotor is turned at a speed with the supply torque cut-off, for example in a rotor coast-down, then still there will be a forward deflection of the shaft due to rate of change of strain in shaft fibers, which comes about as a result of shaft

rotation and the shaft fibers being in tension and compression due to initial sag of the shaft. As long is there is rotation of the shaft, the material internal hysteresis will be active. As there are frictional tensile and compressive forces acting on the shaft, they tend to bend the shaft in the direction of forward whirl, in the same way as an elastic reaction from the shaft tends to straighten the shaft. Therefore, it is seen that the friction can drive whirl instability of the system. Since the moment vector is parallel to the plane of deflection, it follows that it can be replaced by equal and opposite forces perpendicular to the plane of disk. As a result of these compressive and tensile frictional forces, the shaft deflects like in Fig. 43(b). This was the fundamental hypothesis of Kimball to explain forward whirl instability due to internal friction.

MODIFICATION TO KIMBALL'S HYPOTHESIS

As shown in Fig.43 (b), and as explained by Kimball, the internal friction forces due to material hysteresis are perpendicular to the plane of the disk. If this is so, then the consideration of the bending of the shaft due to these friction forces, which are equivalent to a couple moment in the plane of the disk (acting in the vertical direction upwards), should show bending of the shaft in a way which is not shown in Fig.43 (b), and it was actually not proposed, shown or discussed by Kimball in his papers. In Fig.43 (b), as the shaft deflects in the direction of forward whirl, at the same time, internal friction moments will cause it to bend in the following way:

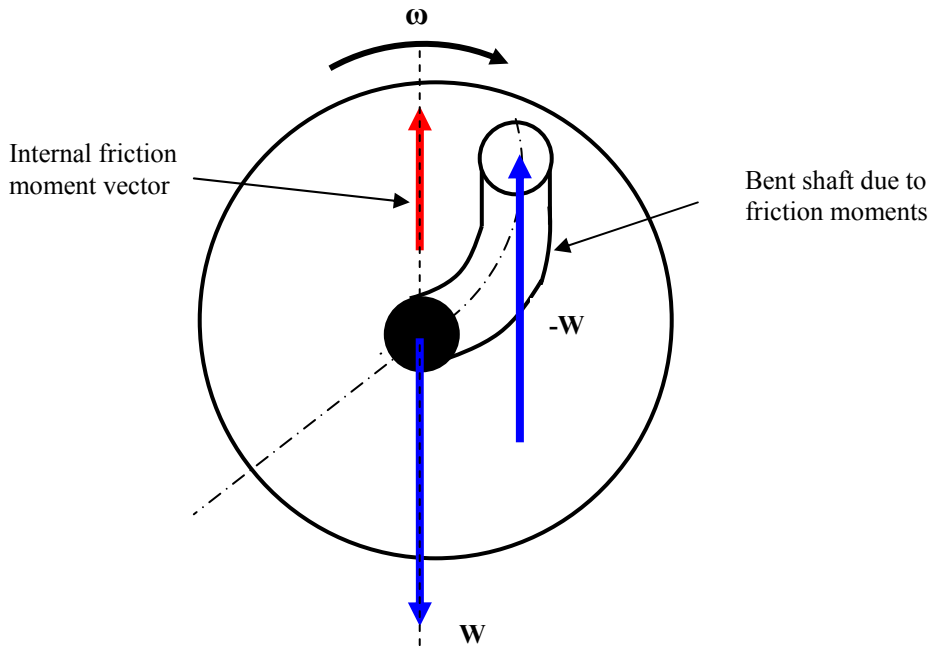

Fig. 44 Side view of the disk-shaft under the influence of internal hysteresis

A close-up view of the shaft with frictional tensile and compressive stresses, as seen from the top (top view) can be depicted as shown in Fig.45 on next page:

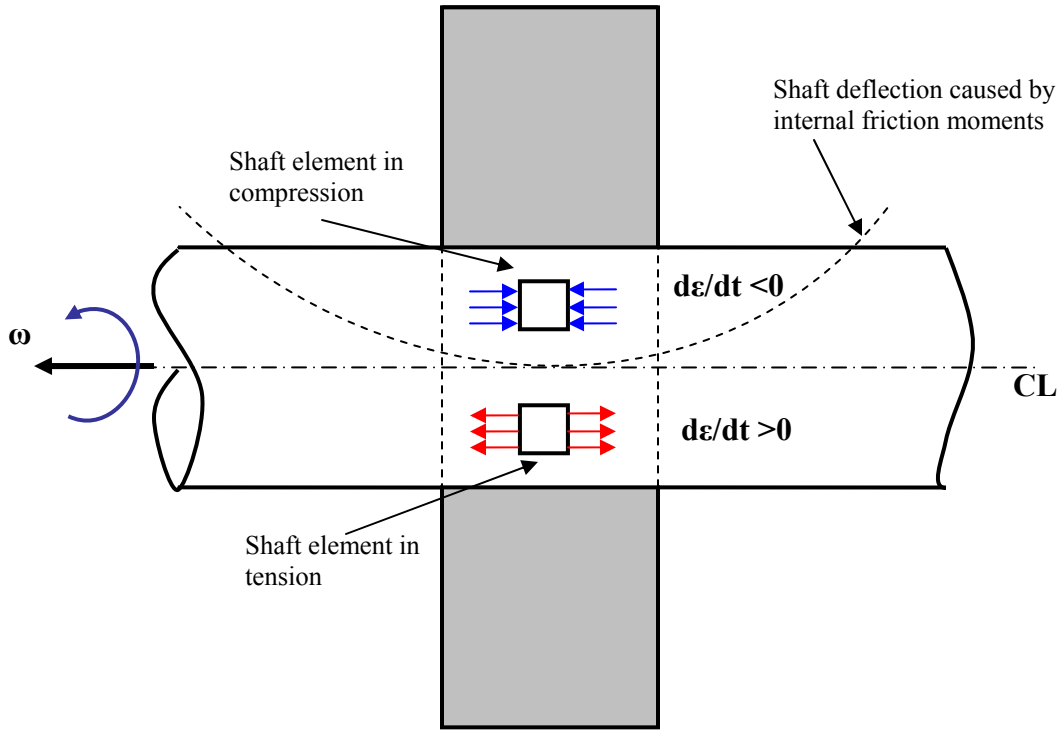

Fig. 45 Frictional tensile and compressive stresses acting on the shaft

Fig.45 shows the frictional tensile and compressive stresses acting on elements inside the shaft, due to material internal hysteresis. The case is for a supercritical speed. It can be seen that the compressive and the tensile stresses form equivalent bending moments (frictional moments) to be developed inside the shaft, that tend to bend the shaft in the direction of forward whirl. Therefore, in addition to the initial elastic sag, this bending of the shaft due to the internal hysteresis will be present to cause a deflection, which will look somewhat similar to that as illustrated in Fig.44.

Fig.46 shows the bent centerline of the shaft due to internal friction moments. It is possible that the measurements made by Kimball, in which he measured the sideways deflection of a thin, overhung shaft loaded vertically, were actually the measurements of

this “bent” deflection (as shown in Figs.44 and 45), rather than the postulated sideways deflection (as shown in Fig.43 (b)).

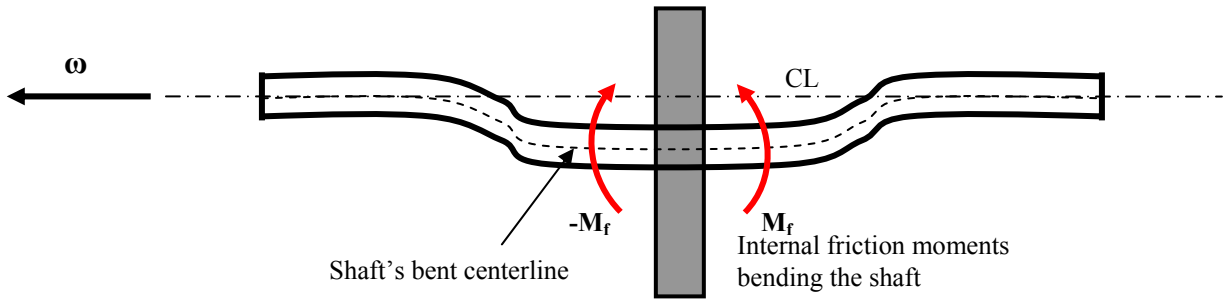

Fig. 46 Top-view of the rotor showing the bent centerline due to friction moments

In his experiments, Kimball also constructed a single-disk vertical rotor and observed violent whirling of the rotor (above its first critical speed) when the shaft was wrapped around with steel mesh wires. The rubbing of wire with the shaft produced the internal friction. However, he did not perform a similar experiment to assess the strength of internal rotor hysteresis on rotor stability (no shrinkage fit). Also, his measurements indicate that when the experimental rotors were shrink fitted with rings, the amount of sideways deflection was atleast 3 to 4 times stronger than with no shrinkage and that the shrinkages were the major source of internal friction instability as compared to the rotor internal hystersis.

From these facts, it can be argued that in shrink fit joints, there are internal friction forces produced that act perpendicular to the plane of the disk of the rotor. As a result, these forces form a de-stabilizing couple moment vector in the plane of the disk

that tends to bend the shaft in a way similar to that in Figs. 44, 45 and 46. This bending of the shaft produces the forward whirl sub-synchronous instability of the rotor. The material internal hysteresis effect of the experimental rotors, as investigated by Kimball, can therefore be said to lead to the same physical shape of the rotor as shown in Figs.44, 45 and 45.

Therefore, the internal friction moment model can explain Kimball's measurements results if it is assumed that his sideways deflection measurements were actually the measurements of the bent sideways deflection similar to Figs. 44 ,45 and 46, rather than that in Fig.43 (b). This can be particularly true, because Kimball's measurements were made while neither looking at the rotor's side-view directly, for example, from some optical instrument, nor the deflections measured could be said to be totally occurring for a shaft which is not bent from moments other than the elastic bending moments. Thus, the proposed modification to Kimball's hypothesis and measurements explanations would unify the mechanics of the shrink fits internal friction and the internal friction due to the material hysteresis.

CHAPTER VI

ROTORDYNAMIC MODELING USING XLTRC™

XLTRC™ is a Microsoft Excel based rotordynamic software. It presents the analysis results and inputs in Excel worksheets and is operated from Microsoft Excel. The code used to perform the rotordynamic analysis is finite element based (FEM). In this code, a rotor system for which the rotordynamic analysis is required is modeled as an assemblage of a finite number of elements (which explains the name of the method, the *finite element method*), with specified geometry and material elastic properties. The code assembles the system matrices and performs various rotordynamic analyses, such as free-free modes, damped eigenvalues, undamped critical speeds, unbalance response plots against rotating speeds (Bode plots), orbits at any given speed, and transient analysis. The XLTRC™ software allows users to specify the bearing connection from the rotor to the ground, or a bearing connection from one shaft to the other shaft with any stiffness and damping coefficients for the bearing that the user wants to apply for a particular problem at hand. The XLTRC™ suit also includes various built-in files for computation of rotordynamic coefficients of hydrodynamic bearings. In these files, the user specifies the geometrical and tribological properties of the bearings and the software computes the bearing rotordynamic coefficients. These bearings can then be "connected" to the rotor, such that the rotor is simulated as if it is mounted on some particular hydrodynamic bearing. In addition, there are ball bearing codes that compute the rotordynamic coefficients for any given configuration and then that file could be connected to the rotor model to model the rotor mounted on given ball bearings. Another application of user-defined bearing files is to connect different parts of a rotor to model internal friction. For modeling the internal friction due to shrink fit and interference fits, the internal friction parameters can be specified in the form of direct moment stiffness and damping coefficients at an interface of a rotor. The concept is illustrated in more detail in the following pages when the rotor modeling with shrink fit interface is described.

OVERVIEW OF MODELING USING XLTRC™

The construction of a rotordynamic model in XLTRC is explained in a step- by - step manner as follows:

(a) Rotor model

In XLTRC™, there is a worksheet called the "Model" worksheet. This is the input worksheet. It is a highly important worksheet, because all the modeling starts from here. In this worksheet, the user specifies the material and geometry of various elements that will constitute the rotor. Often times, it happens that the model is a complicated one such that it requires various rotating parts that are either separate material or such that some parts that are non-rotating. In instances like these, XLTRC™ provides the users with the option of specifying multiple shafts within the model.

There are three sections in the "Model" worksheet.

(i) Shafts

In this section, the user specifies the number of shafts that will be used in the model. The shafts are labeled as 1, 2….etc. In addition, the user specifies the Cartesian coordinates of the starting points of the various shafts. Also, the user has to specify whether the shaft is rotating or if it is a stationary shaft. To include material hysteresis, there is an option for specifying the coefficient of hysteresis. Finally, a column in this section is "Whirl to Spin Ratio". This means the user has to specify whether a particular shaft, for steady state motion, will be executing the synchronous whirl (in which case the ratio should be equal to 1) or asynchronous whirl (in which case the ratio is different from 1).

(ii) Material properties

In this section, the user specifies the elastic properties of the materials that will constitute the rotor model. The user can specify multiple materials. The material

properties that need to be inputted are the weight density, Young's elastic modulus, the shear modulus and the shear constant. The most common material that is used in industry to build turbomachinery is steel. There are various grades of steel that are used in industry, such as AISI 4140 or AISI 4340. However, their material properties are very similar. Thus, as is the most common case, if the material employed is steel for the rotor, then the material properties for steel are : weight density = 0.283 lb/in^3, elastic modulus = 30 x 10^6 psi, and shear modulus = 12 x 10^6 psi. The shear constant is generally taken to be zero for Bernoulli-Euler beam model, whereas it is taken to be -1 for Timoshenko beam model (in which case the effects of rotary inertia are also considered). Apart from steel, the user can specify any different material properties for any other metal or material to construct the appropriate models.

(iii) Shaft elements

This section of the worksheet is where the user specifies the geometry of the elements and associates them with the material properties. This is where building of the rotor model begins, based on information provided in (i) and (ii) above. In this section, the user specifies the shaft number, the element number, the sub-element number, the layer, the length of the element, the outside diameter of the left end of the element, the inside diameter of the left element, the outside diameter of the right end of the element, the inside diameter of the right end, the shear interaction factor (0 or 1), and the associated material with each element.

Associated with each shaft are the elements. Elements are the building blocks of a rotor shaft. For example, consider the modeling of a cylindrical rotor of uniform outside diameter, which is 24 inches in length. Finite element method requires that the domain of interest (in this case, the rotor shaft) be divided into a number of elements so that corresponding to each element, the calculations could be carried out and then the system matrices are assembled together to perform various rotordynamic calculations of interest. So suppose that the 24 inches shaft is divided into 12 equal length pieces. These twelve pieces are the elements. However, the elements need not be of the same length,

neither they need to be made of the same material. Also, the total number of elements used to model the rotor can be different from twelve. As a rule, the larger the number of elements, the more accurate the analysis is, but the penalty associated with higher number of elements is the larger calculation time. For simple enough rotor systems such as the cylindrical shaft of uniform outside diameter, it is unnecessary to divide it into a large number of elements, when a reasonably well analysis could be carried out with smaller number of elements.

Horizontal (axial) sub-division of an element is called as Sub-Element. Similarly, radial sub-division of an element is called a Layer. Accordingly, when sub-elements for an element are specified in "Model" worksheet, then the element number corresponding to each of them is the same, but in the sub-element column, they are specified as 1,2…etc. Similarly, when layers are specified for an element, then the element number corresponding to the two layers will be the same, but in the layer column, they will be labeled as 1,2…etc. For layers, the length should be the same, because they belong to the same element. But the outside and inside diameters for layers need not be same. However, for sub-elements, the lengths need not be same. Their individual lengths sum will determine the total length of that particular element.

In this way, the rotor geometry is constructed. This is the most basic and important step towards the rotordynamic analysis. Once the geometry is developed, it can be viewed as a front view (which means in a plane) using the "Geo Plot" tool in XLTRC^{TM}. This tool can be accessed through the XLTRC^{TM} toolbar or through the XLTRC drop-down menu. Viewing the "Geo Plot" worksheet shows user how the rotor model looks like. It may give a clue to the user to detect any discrepancy to note in the geometry that may not agree with how the model is supposed to look like. In other words, viewing the geometric plot is a good practice to check for possible geometric errors in the "Model" worksheet, besides checking the model geometry data entries.

CONSTRUCTION OF A SINGLE-DISK ROTOR MODEL

Construction of a single-disk rotor model will be explained in a detailed and step-by-step manner as follows:

(a) Rotor model

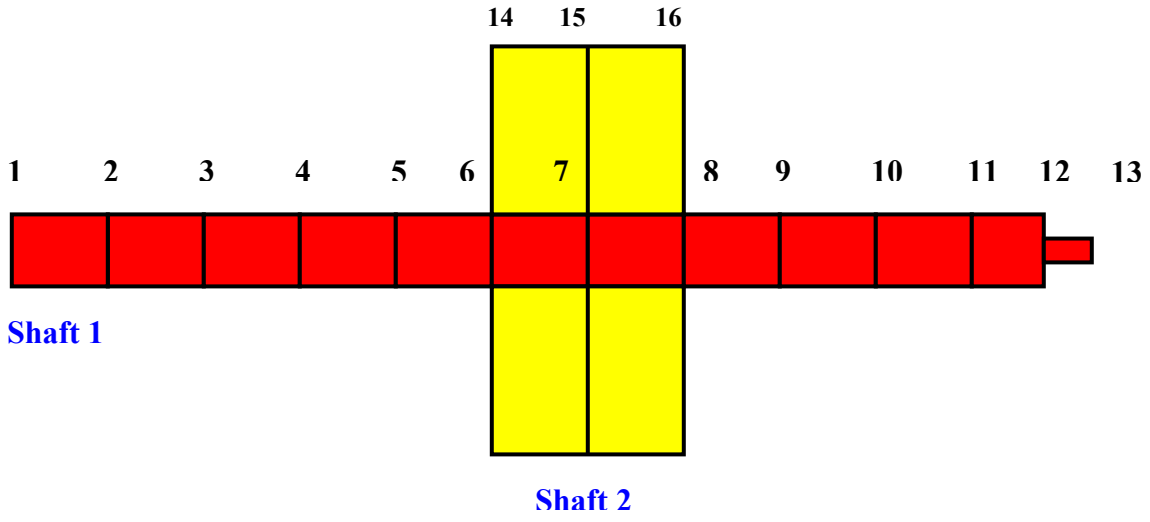

Fig. 47 Finite element model of a single-disk rotor using XLTRC™

Fig.47 shows the view of the single-disk model as viewed through Geo Plot tool using XLTRC™. It can be seen from Fig.47 that the rotor is modeled as a system of finite elements of the main rotor shaft (Shaft 1) and the disk (Shaft 2). The station numbers are numbered consecutively from 1 (at the far left position, for shaft 1) to 13 (far right position of Shaft 1) and 14 to 16 (the elements constituting the disk, which is considered as Shaft 2). In figure 1, each horizontal division of a shaft constitutes one element. Therefore, there are 12 elements of Shaft 1, while there are two elements of Shaft 2. Each element has a left-end station number and a right-end station number. In figure 1, for example, associated with Shaft 1, element 1 has left end station number as 1

and right-end station number as 2. Similarly, for Shaft 1, element 2 has left-end station number 2 and right-end station number 3, and so on. It should be emphasized here that since the interest is to model internal friction that occurs between the main rotor shaft and the disk at the interface, the main shaft and the disk are modeled as separate shafts in XLTRC^{TM}. If these were modeled as one shaft, then it would be necessary to specify the "Layer" option and the appropriate nomenclature for the layers in the "Model" worksheet. However, it would then not be possible to model the internal friction, because the latter model would mean physically a single shaft and will assume no interaction between the main rotor shaft and the disk. Therefore, to model internal friction, it is necessary to model this system as a system containing two shafts (Shafts 1 and 2) and then specifying some internal friction parameters at the interface of Shafts 1 and 2.

(b) Bearing support connection

Once the rotor model is constructed, it is then necessary to specify the bearings that support the rotor to initiate some useful rotordynamic analysis on it. Most often, it is necessary to begin the analysis by first finding out the free-free mode shapes and natural frequencies of the rotor. To accomplish this, the user can either: (1) specify the zero mass, stiffness and damping bearings that connect the two rotor ends to the ground and then running the damped eigenvalue worksheet, or (2) without having specified the zero bearings attached to the rotor, the user can directly use the "Free-Free Modes" command from XLTRC^{TM} pull-down menu and it will compute the free-free modes values for the user.

Once the free-free analysis is accomplished, however, it is necessary for further analysis that the user specifies a non-zero bearing connection from the rotor to the ground. For analysis on the single-disk rotor, the bearings that were used were the ball bearings. The rotordynamic coefficients files for the ball bearings of various configurations can be obtained through XLTRC^{TM} suit. Once the bearing specifications are described and the bearing coefficients are obtained, the title of that file is copied.

Then the rotor model file is opened and then that title head is “Paste Special” to the right most column, with heading “Connection” in “Brg” worksheet in the rotor model file. The result for this operation will look as follows:

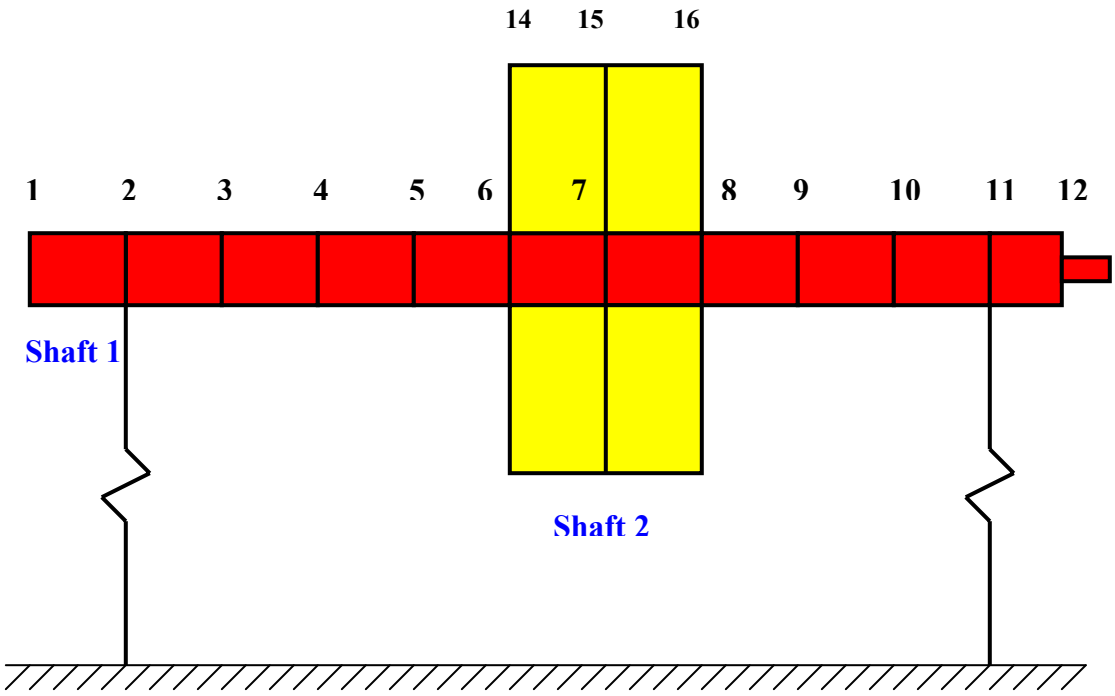

Fig. 48 Rotor model with bearing connections, connecting the rotor with the ground

In Fig.48, the bearing connections are from stations 2 and 11 to the ground. In XLTRC^{TM}, this will be specified in the “Brg” worksheet file as connecting station 2 to station 0 and station 11 to station 0. In XLTRC^{TM}, station “0” is always considered as ground with no exception. Now the model shown in figure 2 can be used to evaluate several rotordynamic results of interest such as response plots against speed due to

imbalance, the damped eigenvalues, the undamped critical speeds and the transient analysis. The model shown in Fig.41 will be suitable to model a rotor that has the bearings mounted on very stiff (or almost rigid) foundations, such that the foundation flexibility effect can be ignored. However, for foundations showing flexibility and motion in either or both horizontal and vertical direction need to be modeled as a separate shaft in the model and connected to the rotor model through the bearings coefficients, while to the grounds, they should be connected through their modal parameters.

(c) Foundation effect

As stated, the foundation effect can be incorporated by connecting the foundation mass to the bearings and the ground through the foundation modal parameters, such as stiffness, mass and damping through user-defined file in XLTRC^{TM}, which is called XLUseKCM. In the simulation of single-disk rotor, the foundation modal parameters were determined through experimental modal testing on the foundation using a calibrated modal hammer and an accelerometer. When the foundation modal parameters are established, they can then be inputted into a user-defined stiffness, mass and damping file. This file is then connected to the rotor through bearing connection, and it is also connected to the ground. When such operations are performed, then the Geo Plot tool in XLTRC^{TM} shows the modified model as shown in Fig. 49:

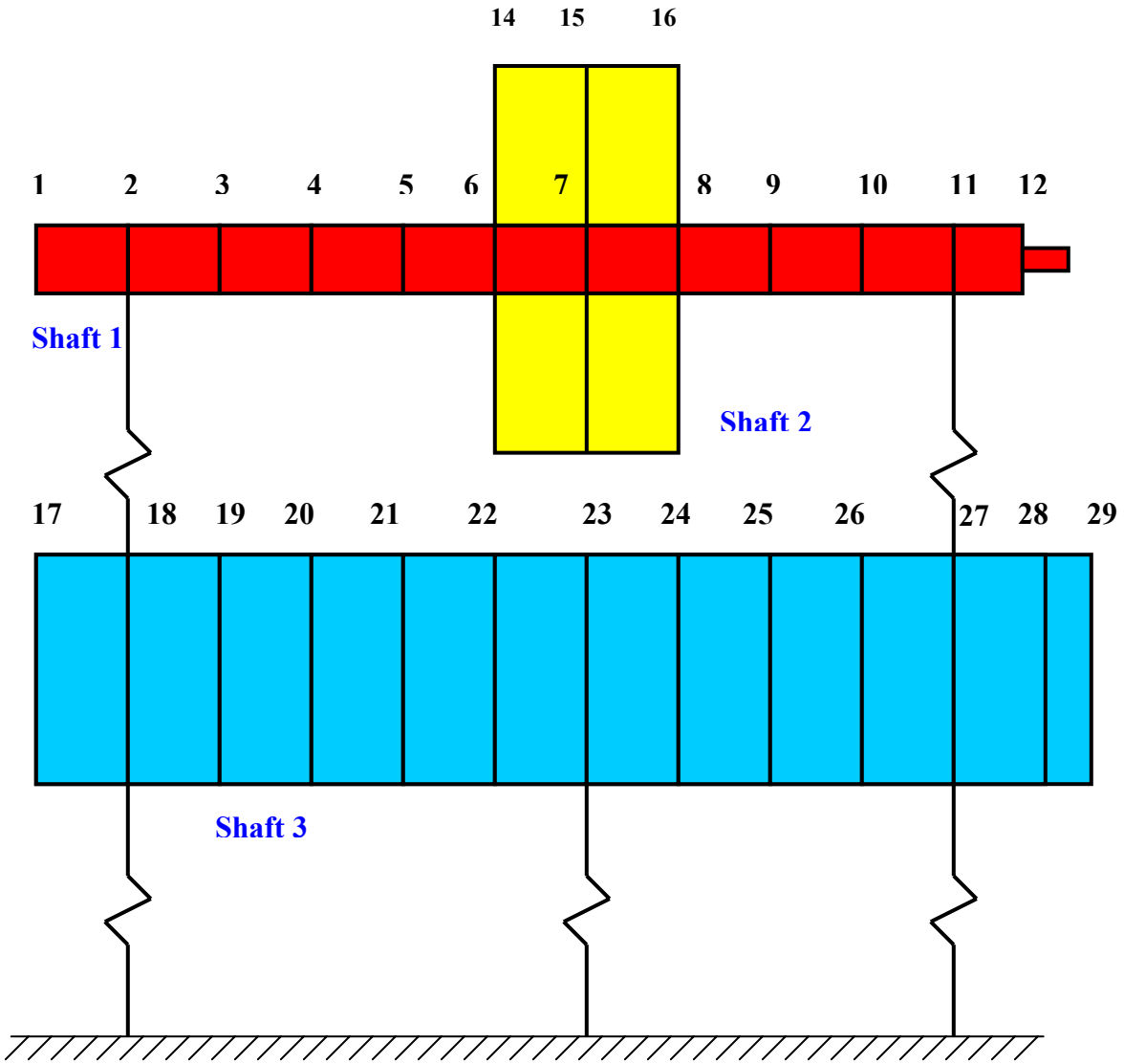

Fig. 49 Rotor model with bearings and foundation included

Fig. 49 shows the foundation included with the rotor model. The foundation is modeled as Shaft 3, which is non-rotating. It is seen from Fig.49 that the foundation is connected to the bearings at the station numbers 18 and 27. Thus the rotor is connected to the bearings through stations 2 and 11 and the bearings are connected to the

foundation through 2 to 18 and 11 to 27. Then the foundation modal parameters are connected to the ground through 18, 23 and 27. Thus, in XLTRC^{TM}, the connections will be as: stations 2 to 18, ball bearing connection; stations 11 to 27, ball bearing connection; stations 18 to 0, user-defined (and experimentally obtained) foundation modal parameters and similarly, for stations 23 to 0 and 27 to 0, foundation modal parameters will be the connecting file.

(d) Modeling of internal friction

In order to model the internal friction that acts at the interface of Shafts 1 and 2 (the main rotor shaft and the disk, respectively), use is made of a user-defined moment coefficients file, which is called as XLUseMoM in XLTRC^{TM}. In this file, the internal friction forces and moments (in the plane of the disk) can be modeled by inputting various stiffness and damping coefficients. For forces, there are direct and cross-coupled stiffness coefficients as well as the damping coefficients. For moments, there are similarly direct and cross-coupled moment coefficients. Once the inputs are established, then the title of the file is copied and pasted to the "Brg" worksheets, under the column, "Connection". In establishing the internal friction moments, it should be noted from Fig. 3 that the connection will occur between stations 6 to 14 and 8 to 16. That is, the three points at the interface of Shaft 1 and Shaft 2. This is illustrated in Fig.50 below:

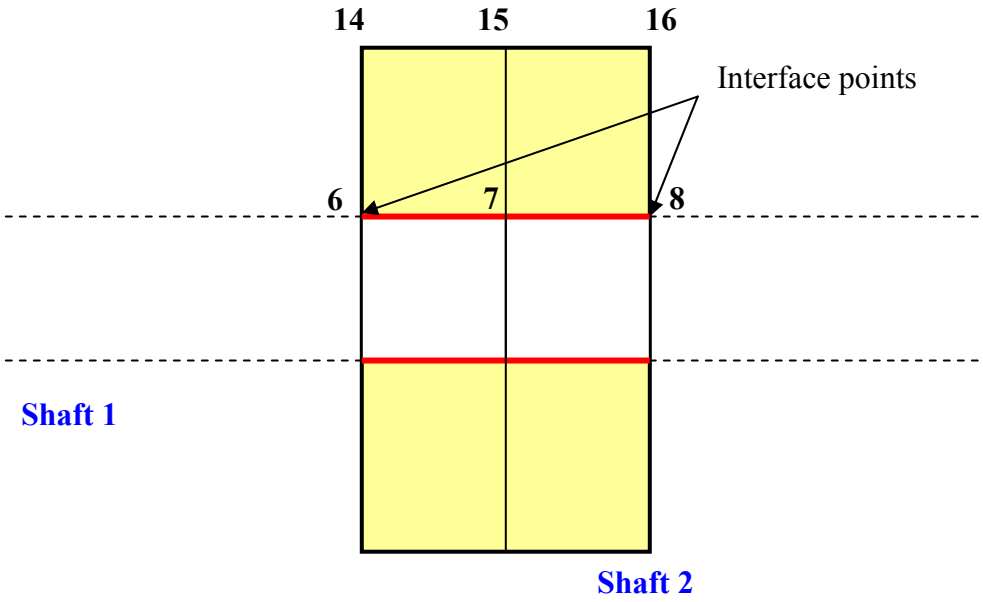

Fig. 50 Interface points of Shafts 1 and 2, where internal friction parameters are specified. The points are connected through a user-defined moment coefficients file.

After completing the steps to model the rotor, the model can be analyzed using various options to simulate rotordynamics of the rotor. To analyze the stability, the 'EIG' worksheet is run to evaluate the damped eigenvalues of the rotor-bearing system. A negative damped eigenvalue (damping ratio) indicates an unstable mode. The eigenvalues are generated in XLTRC^{TM} as pair. The real part of an eigenvalue is the damping ratio, whereas imaginary part is the damped natural frequency. Therefore, both the stability and frequency of mode are calculated using the "EIG" tool in XLTRC^{TM}.

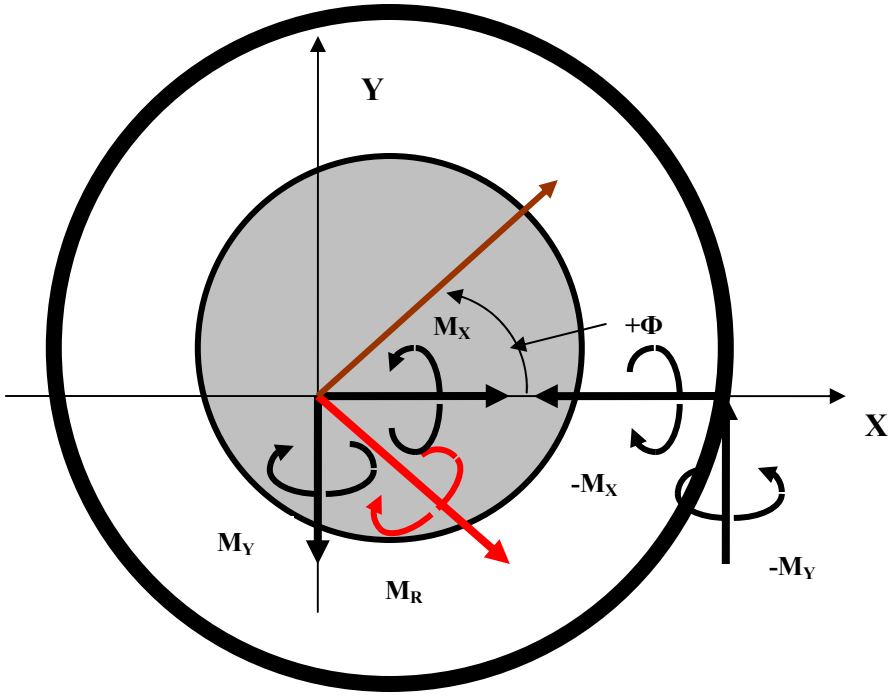

Fig. 51 Internal moments acting on the rotor disks (in its plane of deflection) in X and Y directions and their resultant moment vector, $\mathbf{M_R}$. The resultant moment tends to bend the shaft in the direction of forward whirl.

The shrink fit between the shaft and the disk is modeled in XLTRC^{TM} using *XLUseMoM* file. Physically, the shrink fit is modeled as if there are linear translational and torsional springs and dampers between the sleeve and the disk interface.

In XLTRC^{TM}, there is no force that can be specified internal or external to the model in axial (Z) direction. Physically, the internal friction moment acts so as to develop a forward whirl of the rotor (Fig.51). With the help of *XLUseMoM* file, the internal friction moments are modeled as internal moments to the system i.e., no reaction acting on the ground (which is an incorrect approach).

XLTRC^{TM} models the internal forces and moments based on the following equation:

$$\begin{bmatrix} F_X \\ F_Y \\ M_X \\ M_Y \end{bmatrix} = -\begin{bmatrix} K_{xx} & K_{xy} & K_{xax} & K_{xay} \\ K_{yy} & K_{yx} & K_{yax} & K_{yay} \\ K_{xax} & K_{xay} & K_{axax} & K_{axay} \\ K_{yax} & K_{yay} & K_{ayax} & K_{ayay} \end{bmatrix} \begin{bmatrix} X \\ Y \\ \alpha \\ \beta \end{bmatrix} - \begin{bmatrix} C_{xx} & C_{xy} & C_{xax} & C_{xay} \\ C_{yx} & C_{yy} & C_{yax} & C_{yay} \\ C_{xax} & C_{xay} & C_{axax} & C_{axay} \\ C_{yax} & C_{yay} & C_{ayax} & C_{ayay} \end{bmatrix} \begin{bmatrix} \dot{X} \\ \dot{Y} \\ \dot{\alpha} \\ \dot{\beta} \end{bmatrix}$$

(60)

From equation (60) above, it can be seen that the forces and the moments acting as internal loadings in the system can be modeled with the specified stiffness and damping coefficients. In particular, the moments M_X and M_Y can be modeled. As shown in Fig.51 and Fig.52, the coefficients can be so selected such that these moments act to bend the shaft in the direction of forward whirl.

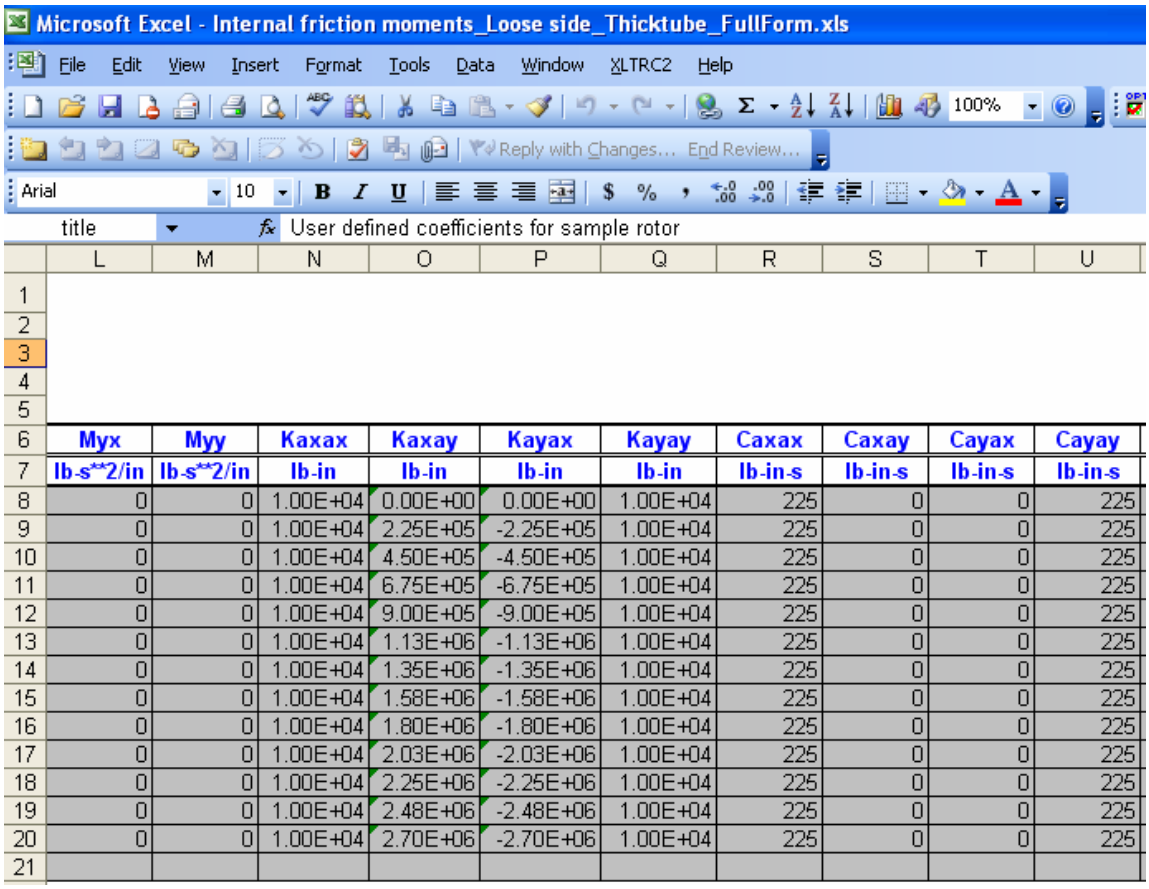

	L	M	N	O	P	Q	R	S	T	U
1										
2										
3										
4										
5										
6	Myx	Myy	Kaxax	Kaxay	Kayax	Kayay	Caxax	Caxay	Cayax	Cayay
7	lb-s**2/in	lb-s**2/in	lb-in	lb-in	lb-in	lb-in	lb-in-s	lb-in-s	lb-in-s	lb-in-s
8	0	0	1.00E+04	0.00E+00	0.00E+00	1.00E+04	225	0	0	225
9	0	0	1.00E+04	2.25E+05	-2.25E+05	1.00E+04	225	0	0	225
10	0	0	1.00E+04	4.50E+05	-4.50E+05	1.00E+04	225	0	0	225
11	0	0	1.00E+04	6.75E+05	-6.75E+05	1.00E+04	225	0	0	225
12	0	0	1.00E+04	9.00E+05	-9.00E+05	1.00E+04	225	0	0	225
13	0	0	1.00E+04	1.13E+06	-1.13E+06	1.00E+04	225	0	0	225
14	0	0	1.00E+04	1.35E+06	-1.35E+06	1.00E+04	225	0	0	225
15	0	0	1.00E+04	1.58E+06	-1.58E+06	1.00E+04	225	0	0	225
16	0	0	1.00E+04	1.80E+06	-1.80E+06	1.00E+04	225	0	0	225
17	0	0	1.00E+04	2.03E+06	-2.03E+06	1.00E+04	225	0	0	225
18	0	0	1.00E+04	2.25E+06	-2.25E+06	1.00E+04	225	0	0	225
19	0	0	1.00E+04	2.48E+06	-2.48E+06	1.00E+04	225	0	0	225
20	0	0	1.00E+04	2.70E+06	-2.70E+06	1.00E+04	225	0	0	225
21										

Fig. 52 *XLUseMoM* Worksheet for entering of internal friction parameters

CHAPTER VII

ROTORDYNAMIC SIMULATIONS OF EXPERIMENTS USING THE INTERNAL MOMENTS MODEL

As discussed in Chapter IV, the cross-coupled moment expressions for various interface friction models contain de-stabilizing terms. The effect of these cross-coupled terms is to add energy to the rotor-bearing system above the first critical speed and to dissipate energy from the system below the first critical speed. As described in Chapter III, the internal moment model is the physically correct model for interface friction in shrink fit joints. This chapter details the application of the internal moment model using XLTRC^{TM} rotordynamics software to the rotordynamics and stability study of the experimental rotor-bearing systems with shrink fit and interference fit interfaces, as described in Chapter II. The results of the simulations show that the internal moment model can be used to predict the stability of the experimental setups without having the need to use physically incorrect follower force model. The simulation results from this chapter are the first step towards the application of a physically correct model of the shrink fit interface friction. The simulation results from this chapter also provide a motivation for an advanced research on the determination of the unknown interface friction parameters such as direct moment stiffness and damping coefficients that can be used to determine the threshold speeds of instability of a rotor-bearing system with shrink fit interfaces, rather than using the physically incorrect follower force model (Gunter's model) to determine the stability of a rotor-bearing system.

The simulations of various experimental rotor setups with shrink fit interfaces are described in the following pages.

SINGLE-DISK ROTOR SIMULATIONS

The single-disk rotor has an interference fit interface through a tapered sleeve between the disk and the shaft, as described in Chapter II. In modeling the single-disk rotor using XLTRC^{TM}, the internal moments are specified as the moment coefficients between the disk and the shaft, thereby modeling the interface friction. The interface is shown in Fig.53:

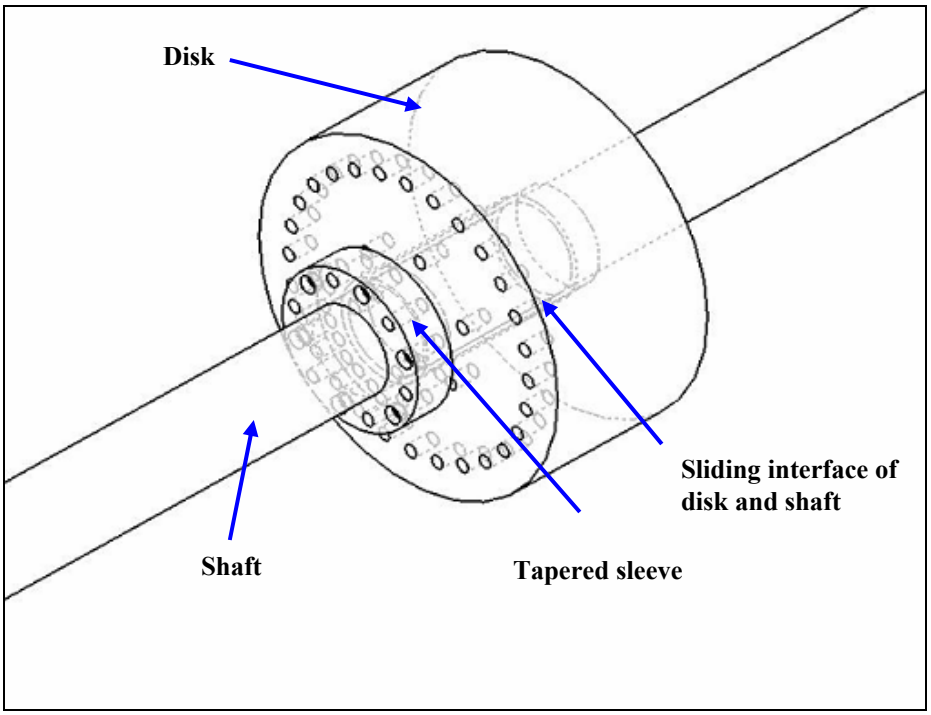

Fig. 53 Close-up view of the single-disk rotor showing the shaft and disk interface through tapered sleeve.

The single-disk rotor model with the foundation is shown in Fig.54:

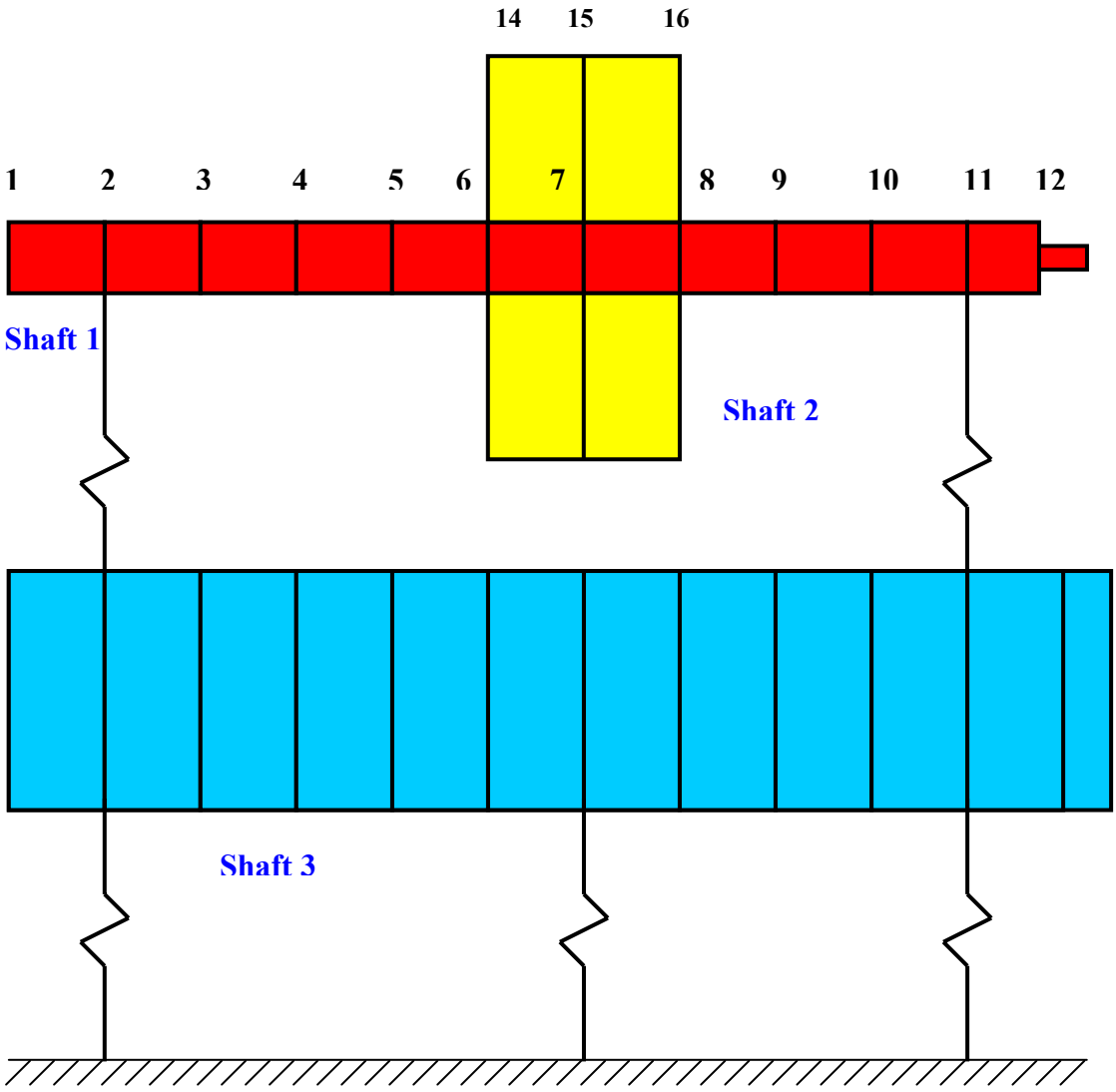

Fig. 54 Single-disk rotor simulation using XLTRC™

Fig.54 shows the model of the single-disk rotor which is analyzed using XLTRC™ software. In modeling the single-disk rotor-bearing system, the system is modeled as three shafts. 'Shaft 1' is the steel shaft with a uniform diameter of 2.5 inches, and 52.50 inches long. 'Shaft 2' is the steel disk with an outside diameter of 10 inches,

and an axial length of 5 inches, mounted at the mid-span of ‘Shaft 1’, which is the steel shaft. ‘Shaft 3’ is the foundation, which does not participate in rotation and whirling, but vibrates in horizontal and vertical directions due to its stiffness and inertia properties.

To simulate the interface friction between the disk (Shaft 2) and the shaft (Shaft 1), the internal moment bearing file is used to make a connection between the two shafts. In the experimental setup for the single-disk rotor as described in Chapter II, the tapered sleeve that creates the interference fit between the uniform shaft and the disk acts such that the relative sliding between the shaft and the disk during whirling motion of the rotor takes place at the end which is inside the disk. The other end of the tapered sleeve which is used to fasten the sleeve to the disk through the push bolts is less likely to slide relative to the shaft due to higher interface pressures at that location.

With this reasoning, the internal moment bearing connection is applied between the points 6 and 14, whereas points 7-15 and 8-16 are constrained through kinematical constraint of executing the same translational and rotational motion. In other words, the sliding is specified at the interface 6-14, but no sliding is specified between other points on the interface.

The foundation which is modeled as ‘Shaft 3’ is connected to the rotor through ball bearing files and to the ground through user-defined stiffness and damping coefficients. The user-defined stiffness and damping coefficients are estimated using modal tests on the foundation in the horizontal and vertical directions.

1. Loose fit simulation

In simulating the rotordynamic instability of the single-disk rotor with looser fit due to which the rotor-bearing system became unstable at 5800 rpm, the interface coefficients were determined by trial and error until the simulation results matched with the experimental results. In the experiments, the single-disk rotor became unstable at a threshold speed of 5800 rpm, with the unstable sub-synchronous vibrations occurring at the first eigenvalue of the rotor-bearing system, which is around 3000 cpm.

Table 1. Coefficients of the internal moment applied at the interface of the shaft and the disk for loose fit.

Speed	K_{XX}	K_{YY}	C_{XX}	C_{YY}	K_{aXaX}	K_{aXaY}	K_{aYaX}	K_{aYaY}	C_{aXaX}	C_{aYaY}
RPM	**Lb/in**	**Lb/in**	**Lb-s/in**	**Lb-s/in**	**Lb-in**	**Lb-in**	**Lb-in**	**Lb-in**	**Lb-in-s**	**Lb-in-s**
0	8.5e+8	8.5e+8	1000	1000	1e+4	0	0	1e+4	6923.2	6923.2
1000	8.5e+8	8.5e+8	1000	1000	1e+4	7.25e+5	-7.25e+5	1e+4	6923.2	6923.2
2000	8.5e+8	8.5e+8	1000	1000	1e+4	1.45e+6	-1.45e+6	1e+4	6923.2	6923.2
3000	8.5e+8	8.5e+8	1000	1000	1e+4	2.18e+6	-2.18e+6	1e+4	6923.2	6923.2
4000	8.5e+8	8.5e+8	1000	1000	1e+4	2.90e+6	-2.90e+6	1e+4	6923.2	6923.2
5000	8.5e+8	8.5e+8	1000	1000	1e+4	3.63e+6	-3.63e+6	1e+4	6923.2	6923.2
6000	8.5e+8	8.5e+8	1000	1000	1e+4	4.35e+6	-4.35e+6	1e+4	6923.2	6923.2
7000	8.5e+8	8.5e+8	1000	1000	1e+4	5.08e+6	-5.08e+6	1e+4	6923.2	6923.2
8000	8.5e+8	8.5e+8	1000	1000	1e+4	5.80e+6	-5.80e+6	1e+4	6923.2	6923.2
9000	8.5e+8	8.5e+8	1000	1000	1e+4	6.53e+6	-6.53e+6	1e+4	6923.2	6923.2
10000	8.5e+8	8.5e+8	1000	1000	1e+4	7.25e+6	-7.25e+6	1e+4	6923.2	6923.2
11000	8.5e+8	8.5e+8	1000	1000	1e+4	7.98e+6	-7.98e+6	1e+4	6923.2	6923.2
12000	8.5e+8	8.5e+8	1000	1000	1e+4	8.70e+6	-8.70e+6	1e+4	6923.2	6923.2

Table 1 shows the user-defined interface friction parameters that are applied between points 6 and 14 in the single-disk rotor to model to simulate the rotordynamic instability due to slip at the shaft-disk interface. The cross-coupled stiffness coefficients (K_{aXaY}, K_{aYaX}) are functions of the rotational speed, as discussed in Chapter IV. As shown in Chapter IV, the cross-coupled moment coefficients are related to the direct moment damping coefficients (C_{aXaX}, C_{aYaY}) with the following equations:

$$K_{aXaY} = C_{aXaY}\omega \tag{61}$$

$$K_{aYaX} = -C_{aYaX}\omega \tag{62}$$

In equations (61) and (62), the rotational speed is expressed in the units of radians per second (rad/s) rather than rotations per minute (rpm).

The remaining stiffness and damping coefficients which are not shown in Table 1 are assumed to be zero. From Table 1, the value of the interface moment damping value is 4060 lb-in-s/rad, and the direct moment stiffness coefficient is 1e+04 lb-in/rad. The high values of the direct translational stiffness and damping coefficients (K_{XX}, K_{YY}, C_{XX}, C_{YY}) are indicative of relatively tight connection between the points 6 and 14, thereby indicating that the relative translational motion in X and Y directions is negligible at the interface. However, the values of the direct moment stiffness and damping coefficients (K_{aXaX}, K_{aYaY}, C_{aXaX}, C_{aYaY}) are indicative of how easily the shaft can slide independent of the disk. The simulated eigenvalues using the coefficients indicated in Table 1 show that the threshold speed of instability of the rotor-bearing system is 5800 rpm, with the unstable mode frequency as the first eigenvalue of the rotor-bearing system, which is 3100 cpm.

An output from XLTRC^{TM} in Fig. 52 shows the unstable mode shape of the rotor-bearing system above the threshold speed of instability:

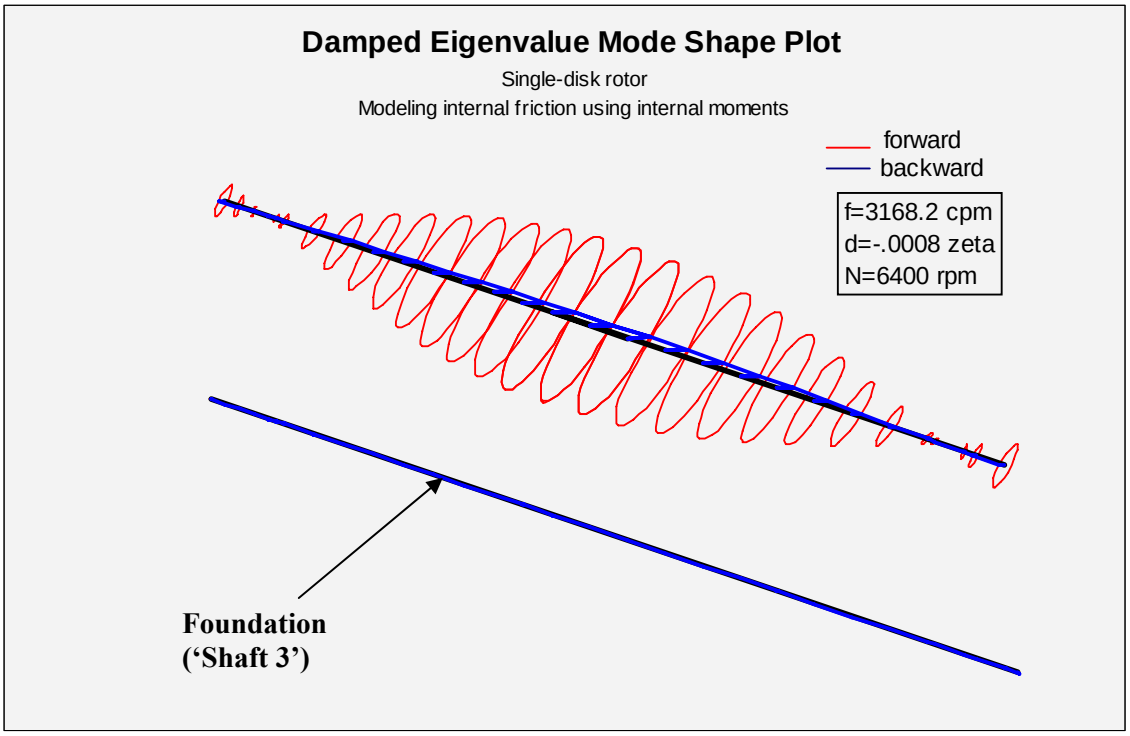

Fig. 55 Unstable mode shape of the single-disk rotor above the threshold speed

Fig.55 shows the unstable mode shape of the single-disk rotor evaluated using XLTRC^{TM}. The speed of rotation is 6400 rpm which is above the threshold speed of instability (5800 rpm). The frequency of the unstable mode is 3168 cpm, which is equal to the first eigenvalue of the rotor-bearing system. The value of the damping ratio is -0.0008 which shows that the mode is unstable. Fig.55 shows that the unstable mode shape involves bending of the shaft and no motion from the foundation. This is the most favorable condition for instability due to shrink fit to occur. In this mode of shaft bending only, the relative sliding between the disk and the shaft will create friction forces (and the equivalent friction moments) at the interface and initiate instability. In addition, the mode shape shows that although the shaft whirls with elliptical orbits, the orbits are not totally planar, and therefore energy can be added to the orbits to initiate instability. The mode shape is a function of several factors, such as foundation stiffness

asymmetry, amount of internal friction (as specified in Table 1) and rotor-bearing physical parameters.

2. Tight fit simulation

As shown in Chapter II, when the interference fit between the disk and the shaft is increased (radially around 2.2 mils), the threshold speed of instability of the single-disk rotor is increased to around 11000 rpm, as compared to 5800 rpm when the fit is loose (1.16 mils radially). This section discusses the simulation of the single-disk rotor with the tight fit. The simulations show that the cross-coupled moment stiffness coefficients required to predict the threshold speed of instability of about 11000 rpm are smaller in magnitude as compared to the coefficients required to predict the threshold speed of instability of 5800 rpm. The simulations also show that the values of the direct moment stiffness coefficients are larger as compared to the case of loose fit. The direct moment stiffness coefficients indicate how easily the shaft can slide relative to the sleeve and disk. Larger value of the direct stiffness coefficients will mean that the shaft will not slide relative to the sleeve with the same ease in case of tight fit (due to high interface pressures) as it slid relative to the sleeve when the interference fit was relatively small (resulting in lower interface pressures). This physically means that increasing the tightness of the fit corresponds to lesser slip between the sleeve and the shaft (due to high interface pressures) and therefore decreased amount of internal moments at the interface. As shown in Chapter IV, the magnitude of friction moments for viscous friction model is proportional to the amplitude of micro-slip at the interface. The amplitude of micro-slip decreases with the increase of interference fit, which corresponds with the higher values of direct moment stiffness coefficients and lower values of the micro-slip amplitudes. The internal moment coefficients required to simulate the experimental setup of the single-disk rotor with the tight fit is shown in Table 2 on the next page:

Table 2. Coefficients of the internal moment applied at the interface of the shaft and the disk for tight fit.

Speed	K_{XX}	K_{YY}	C_{XX}	C_{YY}	K_{aXaX}	K_{aXaY}	K_{aYaX}	K_{aYaY}	C_{aXaX}	C_{aYaY}
RPM	**Lb/in**	**Lb/in**	**Lb-s/in**	**Lb-s/in**	**Lb-in**	**Lb-in**	**Lb-in**	**Lb-in**	**Lb-in-s**	**Lb-in-s**
0	8.5e+8	8.5e+8	1000	1000	1e+5	0	0	1e+5	2148.6	2148.6
1000	8.5e+8	8.5e+8	1000	1000	1e+5	2.25e+5	-2.25e+5	1e+5	2148.6	2148.6
2000	8.5e+8	8.5e+8	1000	1000	1e+5	4.50e+5	-4.50e+5	1e+5	2148.6	2148.6
3000	8.5e+8	8.5e+8	1000	1000	1e+5	6.75e+5	-6.75e+5	1e+5	2148.6	2148.6
4000	8.5e+8	8.5e+8	1000	1000	1e+5	9.0e+5	-9.0e+5	1e+5	2148.6	2148.6
5000	8.5e+8	8.5e+8	1000	1000	1e+5	1.125e+6	-1.125e+6	1e+5	2148.6	2148.6
6000	8.5e+8	8.5e+8	1000	1000	1e+5	1.35e+6	-1.35e+6	1e+5	2148.6	2148.6
7000	8.5e+8	8.5e+8	1000	1000	1e+5	1.575e+6	-1.575e+6	1e+5	2148.6	2148.6
8000	8.5e+8	8.5e+8	1000	1000	1e+5	1.80e+6	-1.80e+6	1e+5	2148.6	2148.6
9000	8.5e+8	8.5e+8	1000	1000	1e+5	2.025e+6	-2.025e+6	1e+5	2148.6	2148.6
10000	8.5e+8	8.5e+8	1000	1000	1e+5	2.25e+6	-2.25e+6	1e+5	2148.6	2148.6
11000	8.5e+8	8.5e+8	1000	1000	1e+5	2.475e+6	-2.475e+6	1e+5	2148.6	2148.6
12000	8.5e+8	8.5e+8	1000	1000	1e+5	2.70e+6	-2.70e+6	1e+5	2148.6	2148.6

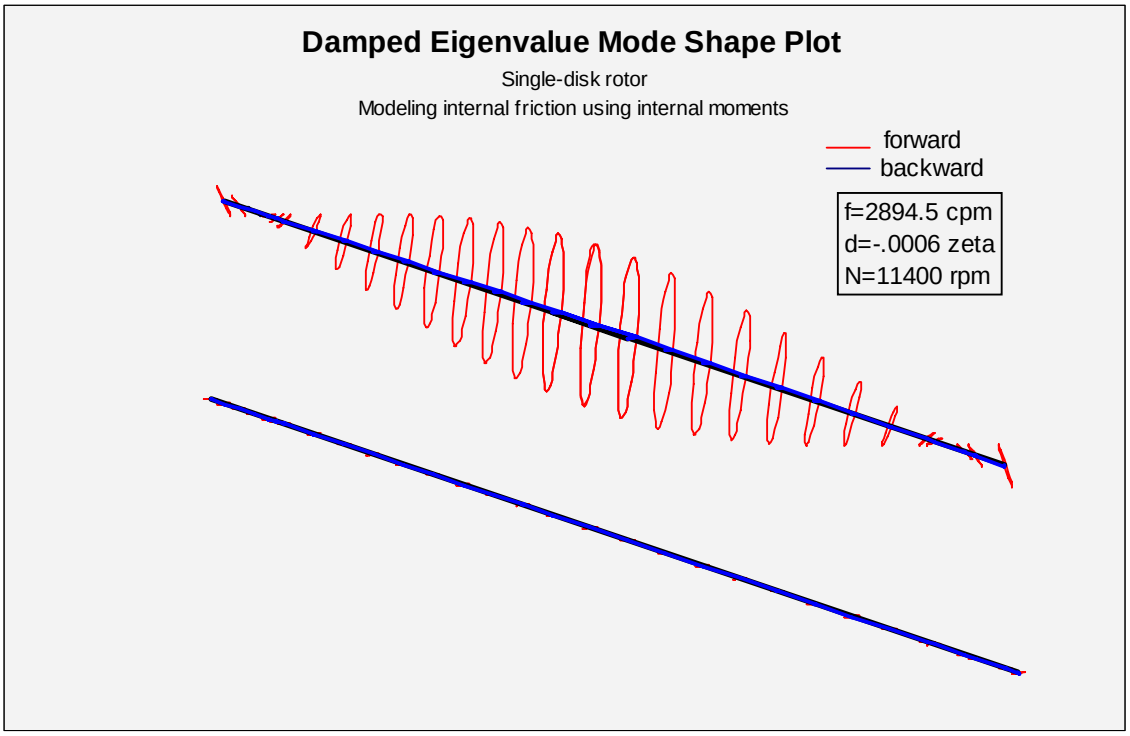

Fig. 56 Unstable mode shape of the single-disk rotor above the threshold speed (for the case of tight fit)

Fig.56 shows the unstable mode plot using XLTRC^{TM} for the single-disk rotor model with the tight fit case. The threshold speed of instability for the tight fit is 11000 rpm and the mode shape in Fig.56 is plotted at the speed of 11400 rpm. As in the case of loose fit (Fig.55), the mode shape shows that the rotor shaft bends but the foundation does not vibrate in this mode. The mode shapes are not totally planar, which shows that the energy can be added to the system through rotor motion and the system has a tendency to grow in unstable motion. The unstable mode frequency is 2900 cpm, which is the same as the experimentally determined frequency of the unstable sub-synchronous whirl motion. The damping ratio is -0.0006, which shows that the mode is unstable.

TWO-DISK ROTOR SIMULATIONS

The internal friction moments model is applied to the rotordynamic simulations of the two-disk rotor setup as discussed in Chapter II. As noted in Chapter II, several configurations of the two-disk rotor with different sleeve geometries and shrink fits were experimentally tested, of which only one configuration is unstable. This section will demonstrate the application of the internal moments model to predict the rotordynamic stability of experimentally tested two-disk rotor configurations. An isometric view of the two-disk rotor with various internal features visible is shown in Fig.57:

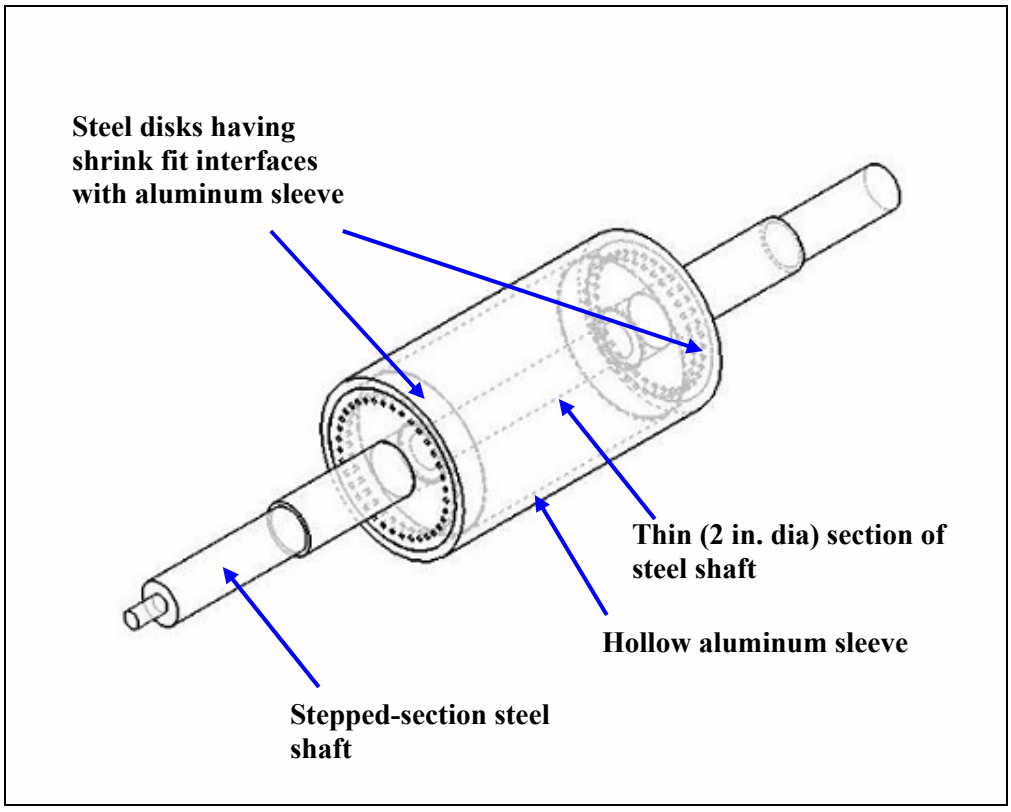

Fig. 57 Isometric view of the two-disk rotor showing internal features

1. Tight fit at one end, loose fit at the other end

In this configuration, the aluminum sleeve has an outside diameter of 10 inches. The sleeve has an undercut at one of the ends (see Chapter II, put picture in Chapter II of undercut sleeve). The undercut end has 5 mils diametral shrink fit with the steel disk, whereas the other interface of the sleeve and disk have 12 mils diametral shrink fit. As shown in the experimental results in Chapter II, this rotor configuration became unstable at a threshold speed of instability of 9600 rpm, and eventually wrecked during the coast-down. The internal moments model is applied to the two-disk rotor model to demonstrate the instability of this rotor configuration. In modeling the shrink fits at the two ends, the tight fit end is made to have high values of direct moment stiffness coefficients with zero cross-coupling stiffness coefficients to simulate the condition of very tight fit (with zero slip and friction). The other end with the undercut is connected to the steel disks in the rotor model through internal moment coefficients that have relatively lower values of direct stiffness coefficients and high values of cross-coupled moment stiffness coefficients as compared to the tight fit end to simulate the relative slip between the disk and the sleeve at that end. In addition, the modal parameters of the foundation connecting to the ground (stiffness and damping) for the two-disk rotor setup are input in XLTRC^{TM}. The stiffness and damping coefficients of the foundation for the two-disk rotor setup are different from the ones for the single-disk rotor setup, because an additional stiffener was installed on the foundation in an attempt to reduce stiffness asymmetry for the experiments involving the two-disk rotor. These coefficients are described in Appendix C. The coefficients of the internal moment bearing file for each of the two ends are shown on next pages in Tables 3 and 4:

Table 3. Coefficients of internal moment applied at the undercut end for two-disk rotor simulation.

Speed	K_{XX}	K_{YY}	C_{XX}	C_{YY}	K_{aXaX}	K_{aXaY}	K_{aYaX}	K_{aYaY}	C_{aXaX}	C_{aYaY}
RPM	**Lb/in**	**Lb/in**	**Lb-s/in**	**Lb-s/in**	**Lb-in**	**Lb-in**	**Lb-in**	**Lb-in**	**Lb-in-s**	**Lb-in-s**
0	8.5e+8	8.5e+8	1000	1000	1e+4	0	0	1e+4	2150	2150
1000	8.5e+8	8.5e+8	1000	1000	1e+4	2.25e+5	-2.25e+5	1e+4	2150	2150
2000	8.5e+8	8.5e+8	1000	1000	1e+4	4.50e+5	-4.50e+5	1e+4	2150	2150
3000	8.5e+8	8.5e+8	1000	1000	1e+4	6.75e+5	-6.75e+5	1e+4	2150	2150
4000	8.5e+8	8.5e+8	1000	1000	1e+4	9.00e+5	-9.00e+5	1e+4	2150	2150
5000	8.5e+8	8.5e+8	1000	1000	1e+4	1.13e+6	-1.13e+6	1e+4	2150	2150
6000	8.5e+8	8.5e+8	1000	1000	1e+4	1.35e+6	-1.35e+6	1e+4	2150	2150
7000	8.5e+8	8.5e+8	1000	1000	1e+4	1.58e+6	-1.58e+6	1e+4	2150	2150
8000	8.5e+8	8.5e+8	1000	1000	1e+4	1.80e+6	-1.80e+6	1e+4	2150	2150
9000	8.5e+8	8.5e+8	1000	1000	1e+4	2.03e+6	-2.03e+6	1e+4	2150	2150
10000	8.5e+8	8.5e+8	1000	1000	1e+4	2.25e+6	-2.25e+6	1e+4	2150	2150
11000	8.5e+8	8.5e+8	1000	1000	1e+4	2.48e+6	-2.48e+6	1e+4	2150	2150
12000	8.5e+8	8.5e+8	1000	1000	1e+4	2.70e+6	-2.70e+6	1e+4	2150	2150

Table 4. Coefficients of internal moment applied at the tight fit end for two-disk rotor simulation.

Speed	K_{XX}	K_{YY}	C_{XX}	C_{YY}	K_{aXaX}	K_{aXaY}	K_{aYaX}	K_{aYaY}	C_{aXaX}	C_{aYaY}
RPM	**Lb/in**	**Lb/in**	**Lb-s/in**	**Lb-s/in**	**Lb-in**	**Lb-in**	**Lb-in**	**Lb-in**	**Lb-in-s**	**Lb-in-s**
0	8.5e+8	8.5e+8	1000	1000	5e+8	0	0	5e+8	0	0
1000	8.5e+8	8.5e+8	1000	1000	5e+8	0	0	5e+8	0	0
2000	8.5e+8	8.5e+8	1000	1000	5e+8	0	0	5e+8	0	0
3000	8.5e+8	8.5e+8	1000	1000	5e+8	0	0	5e+8	0	0
4000	8.5e+8	8.5e+8	1000	1000	5e+8	0	0	5e+8	0	0
5000	8.5e+8	8.5e+8	1000	1000	5e+8	0	0	5e+8	0	0
6000	8.5e+8	8.5e+8	1000	1000	5e+8	0	0	5e+8	0	0
7000	8.5e+8	8.5e+8	1000	1000	5e+8	0	0	5e+8	0	0
8000	8.5e+8	8.5e+8	1000	1000	5e+8	0	0	5e+8	0	0
9000	8.5e+8	8.5e+8	1000	1000	5e+8	0	0	5e+8	0	0
10000	8.5e+8	8.5e+8	1000	1000	5e+8	0	0	5e+8	0	0
11000	8.5e+8	8.5e+8	1000	1000	5e+8	0	0	5e+8	0	0
12000	8.5e+8	8.5e+8	1000	1000	5e+8	0	0	5e+8	0	0

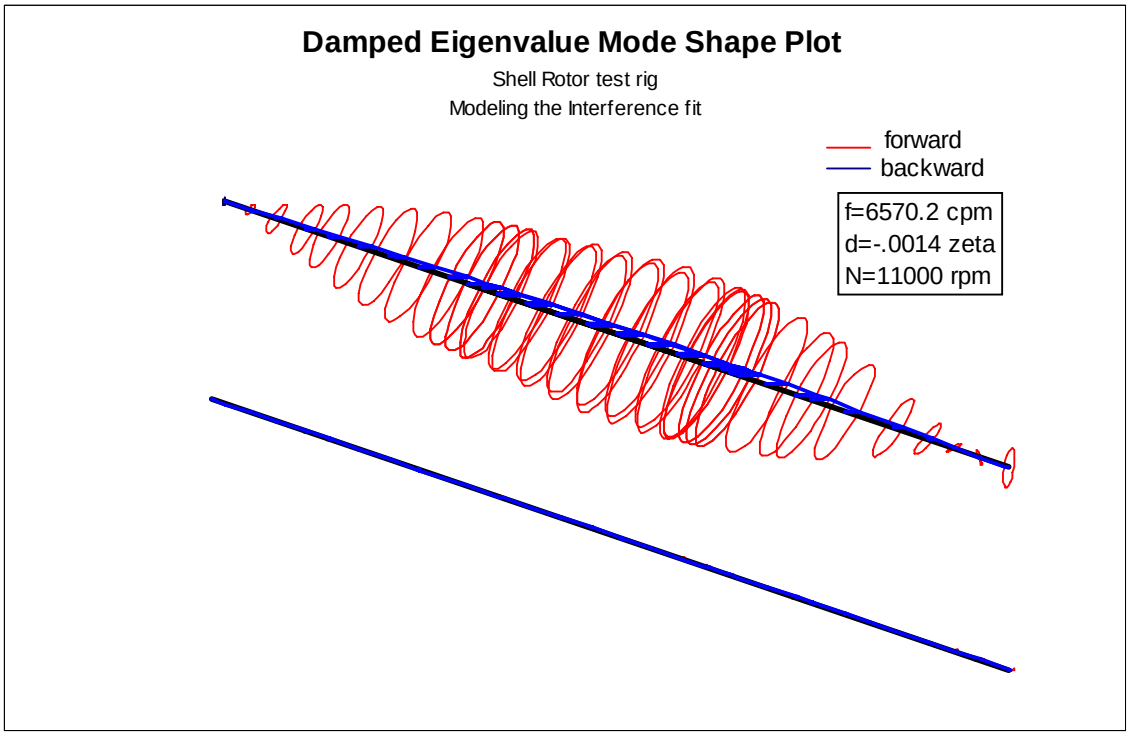

Fig. 58 Unstable mode shape of two-disk rotor model with different fits at two interfaces

Table 3 shows the internal moment coefficients at the loose fit end, whereas Table 4 shows the internal moment coefficients at the tight fit with no cross-coupling.

Fig.58 shows the mode shape plot for the two-disk rotor model at a speed of 11000 rpm. The plot is generated using the XLTRC^{TM} software. The mode shape shows that the unstable whirling frequency is 6570 cpm (109.5 Hz) which was one of the unstable modes excited and measured in the experimental results for the two-disk rotor with different fits at two interfaces. The damping ratio is -0.0014, which shows that the mode is unstable.

2. Same fit at both ends

To simulate same tightness of fit at both ends, the internal moment coefficients at both ends are provided with the same direct moment stiffness and damping coefficients. The experimental setup with the same tightness of fits is discussed in Chapter II. In this experimental setup for the two-disk rotor, the outside diameter of the aluminum sleeve was 9.5 inches in one setup, and 9.25 inches in another setup. In both cases, the shrink fit was the same at both the disks (10 mils diametrally). The experimental results showed that the rotor-bearing system did not become unstable in either of those configurations, when the shrink fit was the same at both the ends. Even though in one of the configurations, the sleeve was heated at around 11000 rpm until the shrink fit contact was lost, still no instability was observed in the rotor-bearing system. The possible reason that the rotor-bearing system did not become unstable in the symmetric fit configurations may be because of sleeve's bending together with the steel shaft (due to smaller outside diameters, that is, 9.5 inches or 9.25 inches as compared to 10 inches outside diameter for unstable configurations), due to which no appreciable relative sliding took place and no friction is generated. The other reason may be an inherently small amount of direct damping in the joint for these particular configurations, which maybe a function of sleeve's geometry and shrink fit values.

The application of internal moments model to the case of same fit at both the disks shows that for some choice of direct moment stiffness and damping coefficients, the two-disk rotor bearing system does not show instability. This indicates that the internal moment coefficients are functions of sleeve geometry and shrink fit values. A high value of the shrink fit corresponds to corresponding high values of the direct moment stiffness coefficients (K_{aXaX}, K_{aYaY}). In addition to this, the direct moment damping coefficients (C_{aXaX}, C_{aYaY}) are also possibly the functions of sleeve geometry are the shrink fit values.

The coefficients of the internal moment are presented in Table 5 on the next page:

Table 5. Coefficients of the internal moment applied at the two interfaces for the same fit case of the two-disk model.

Speed	K_{XX}	K_{YY}	C_{XX}	C_{YY}	K_{aXaX}	K_{aXaY}	K_{aYaX}	K_{aYaY}	C_{aXaX}	C_{aYaY}
RPM	**Lb/in**	**Lb/in**	**Lb-s/in**	**Lb-s/in**	**Lb-in**	**Lb-in**	**Lb-in**	**Lb-in**	**Lb-in-s**	**Lb-in-s**
0	8.5e+8	8.5e+8	1000	1000	1e+4	0	0	1e+4	95.49	95.49
1000	8.5e+8	8.5e+8	1000	1000	1e+4	1e+4	-1e+4	1e+4	95.49	95.49
2000	8.5e+8	8.5e+8	1000	1000	1e+4	2e+4	-2e+4	1e+4	95.49	95.49
3000	8.5e+8	8.5e+8	1000	1000	1e+4	3e+4	-3e+4	1e+4	95.49	95.49
4000	8.5e+8	8.5e+8	1000	1000	1e+4	4e+4	-4e+4	1e+4	95.49	95.49
5000	8.5e+8	8.5e+8	1000	1000	1e+4	5e+4	-5e+4	1e+4	95.49	95.49
6000	8.5e+8	8.5e+8	1000	1000	1e+4	6e+4	-6e+4	1e+4	95.49	95.49
7000	8.5e+8	8.5e+8	1000	1000	1e+4	7e+4	-7e+4	1e+4	95.49	95.49
8000	8.5e+8	8.5e+8	1000	1000	1e+4	8e+4	-8e+4	1e+4	95.49	95.49
9000	8.5e+8	8.5e+8	1000	1000	1e+4	9e+4	-9e+4	1e+4	95.49	95.49
10000	8.5e+8	8.5e+8	1000	1000	1e+4	1e+5	-1e+5	1e+4	95.49	95.49
11000	8.5e+8	8.5e+8	1000	1000	1e+4	1.1e+5	-1.1e+5	1e+4	95.49	95.49
12000	8.5e+8	8.5e+8	1000	1000	1e+4	1.2e+5	-1.2e+5	1e+4	95.49	95.49

The simulations of the experimental results on configurations of the single-disk and the two-disk rotors provide some values of the internal moment coefficients for different configurations. The simulations show that the internal moment coefficients vary from configuration to configuration, and therefore it is challenging to use the internal moments model to analyze the internal friction and stability of a rotor-bearing system. In Appendix C, an attempt has been made to analyze the stability of various imagined rotor configurations (both single-disk and the two-disk) that are different from the experimental rotor configurations. The imagined rotor models are developed and analyzed using XLTRC^{TM} software. The internal moments model is used in each of the imagined configurations to model shrink fit or interference fit interface internal friction. Although the simulation results are not supported by experimental data, the simulations nevertheless provide a first step towards modeling, designing and analyzing the imagined rotor configurations with shrink fit and interference fit interfaces. Another objective of including the imagined configurations is to assess some stability trend that can be achieved by varying several rotor elastic, material and geometric properties. See Appendix C for imagined rotor configurations stability simulations and their discussion.

CHAPTER VIII

CONCLUSIONS

The research presented in this dissertation provides an experimental and theoretical study of the effect of slippage at shrink fit and interference fit interfaces on the rotordynamic stability of rotor-bearing systems. The experimental study confirms that the instability caused by the slippage in shrink fit and interference fit joints in a rotor is potentially catastrophic for rotor-bearing systems. The experimental study also confirms that the instability caused by internal friction in shrink fit and interference fit joints is sub-synchronous and usually occurs at the first eigenvalue of the rotor-bearing system at an operating speed above the first critical speed of the rotor-bearing system. From the experimental study of the single-disk rotor for steel-steel interface on this particular rotor setup, it was found that there is a critical value of the interference fit (1 mils radial at speed) that causes the rotor to become unstable above the first critical speed. It is therefore necessary to have an analysis available that predicts the interference as a function of speed.

For the two-disk rotor, there is only one configuration out of several tested that became unstable. In the configuration that became unstable, the shrink fit was very tight at one end and fairly loose at the other end. Therefore, it seems likely that the loose and tight distribution of shrink fits along the two-disk rotor interfaces is a significant factor affecting the stability of the rotor-bearing system.

The theoretical study shows that the internal friction can be modeled more realistically using the internal friction moments model. However, there are several variables and unknowns in the internal moments model, such as the direct moment damping in the joint and the direct moment stiffness coefficients, which make the use of this model dependent on measurements, such as the experimental value of the threshold speed of rotordynamic instability. Using the experimental results, the direct moment damping and stiffness coefficients can be found using XLTRC^{TM} simulations by trial and error until the simulated results match the experimental values of the first critical

speed, the frequency of the unstable mode and the threshold speed of rotordynamic instability of a rotor-bearing system. This is the procedure that was adopted to compute the internal friction moment coefficients of the experimental rotors which showed instability. The same procedure was also used to compute the values of the internal moment coefficients for the two-disk rotor configurations that did not become unstable. The experimental results show that the internal moment coefficients vary with different configurations of the rotor-bearing systems. In the configurations for the two-disk rotor that did not become unstable during the operating speed range of 0-12000 rpm, the sleeve outside diameter were 9.5 inches and 9.25 inches, with the same tightness of fits (about 10 mils diametral on both interfaces, with complete 2 inches axial contact) at the two interfaces. The simulations of these configurations using the XLTRC^{TM} software show that the rotor will be stable if the values of the direct moment damping coefficients are smaller in magnitude as compared to the unstable rotor configuration (for which the sleeve outside diameter is 10 inches, with a 2 inches axial contact, 12 mils radial fit at one end and an under-cut 1 inch axial contact, 2.5 mils radial loose fit at the other interface).

The simulations of the imagined single-disk and two-disk rotor configurations with shrink fit or interference fit interfaces, though not supported by experimental data, provide the first step towards assessing stability trends caused by a rotor's elastic and geometric properties. The simulations also extend the application of the internal friction moments model from the experimental rotors to the imagined rotor configurations.

RECOMMENDATIONS FOR FUTURE RESEARCH

For further research on the subject of internal friction caused by slippage in shrink fit and interference fit joints and their effects on rotordynamic stability, the parameters involved in the internal moments model such as the direct moment stiffness and damping coefficients for the viscous friction model, need to be studied in more detail for predictions of threshold speeds of rotordynamic instability in a rotor-bearing system. As concluded from the experimental and theoretical study presented in this

dissertation, the internal moment coefficients vary from one rotor configuration to another rotor configuration. In addition, the internal moment coefficients can be functions of several other system parameters such as rotor mode shape on the bearings, slope of the mode shape, tightness of fits and geometry of the interface, to name but a few. An advanced study must look into this problem and derive analytical and computational methods to determine the internal moment coefficients for viscous damping model as a function of the rotor parameters as mentioned. In addition, adding more body of experimental data on rotor configurations with shrink fit and interference fit joints can give more insight into the proposed analytical work.

In addition, the computational software such as XLTRC^{TM} should be modified to include the Coulomb friction model to analyze the stability of the rotor-bearing systems with shrink fit and interference fit interfaces.

REFERENCES

1. Walton, J., Artilles, A., Lund, J., Dill, J., Zorzi, E., 1990, "Internal Rotor Friction Instability", Mechanical Technology Incorporated Report, 88TR39
2. Newkirk, B.L., 1924, "Shaft Whipping", General Electric Review, **27**(3), pp. 169-178
3. Jeffcott, H.H., 1919, "The Lateral Vibration of Loaded Shafts in the Neighbourhood of a Whirling Speed: The Effect of Want of Balance," Philosophical Magazine, Ser.6, **37**, pp.304
4. Kimball, A.L. Jr., 1924, "Internal Friction Theory of Shaft Whirling", General Electric Review, **27**(4), pp.244-251
5. Gunter, E.J., 1966, "Dynamic Stability of Rotor-Bearing Systems", NASA Technical Report, SP-113
6. Walton, J.F.Jr.,Martin, M.R., 1993, "Internal Rotor Friction Induced Instability in High-speed Rotating Machinery", Vibration of Rotating Systems, DE-Vol.**60**, pp. 297-305
7. Kimball, A.L. Jr., 1925, "Measurement of Internal Friction in a Revolving Deflected Shaft,", General Electric Review, **28**, pp.554-558
8. Kimball, A.L. Jr., Lovell, D.E., 1926, " Internal Friction in Solids," Transactions of ASME, **48**, pp.479-500
9. Lund, J.W., 1986, "Destabilization of Rotors from Friction in Internal Joints with Micro-slip," International Conference in Rotordynamics, JSME, pp. 487-491
10. Artilles, Antonio F., 1991, " The Effects of Friction in Axial Splines on Rotor System Stability," IGTA Congress and Exposition, pp. 1-7
11. Black, H.F., 1976, "The Stabilizing Capacity of Bearings for Flexible Rotors with Hysteresis", Transactions of the ASME, pp.87-91
12. Ehrich, F.F., 1964, "Shaft Whirl Induced by Rotor Internal Damping", Journal of Applied Mechanics, **31**, pp. 279-282

13. Yamamoto,T., Ishida, Y., *Linear and Nonlinear Rotordynamics*, 2001, John Wiley Publications, NY
14. Vance, J.M., Ying, D., "Effects of Interference Fits on Threshold Speeds of Rotordynamic Instability", Paper No. 2007, Proceedings of the International Symposium on Stability Control of Rotating Machinery, August 20-24, 2001, South Lake, Tahoe, California
15. Mir, Mohammad M., "Effects of Shrink Fits on Threshold Speeds of Rotordynamic Instability", MS thesis, 2001, Texas A&M University, College Station
16. Srinivasan, A., "Effects of Shrink fits on Threshold Speeds of Rotordynamic Instability", MS thesis, 2003, Texas A&M University, College Station
17. Murphy, B.T., "Eigenvalues of Rotating Machinery", PhD dissertation, 1984, Texas A&M University, College Station
18. Robertson, D., 1935, "Hysteretic Influences on the Whirling of Rotors", Proceedings of the Institute of Mechanical Engineers, London, **131**, pp. 513-537
19. Smalley, A.J., Pantermuehl, P.J., Hollingsworth, J.R., Camatti, M., 2002, " How Interference Fits Stiffen the Flexible Rotors of Centrifugal Compressors," IFToMM Sixth International Conference on Rotordynamics
20. Nelson, H.D., McVaugh, J.M., 1976, "The Dynamics of Rotor-Bearing Systems Using Finite Elements," Transactions of ASME, Journal of Engineering for Industry, **98**(2), pp. 593-600
21. Zorzi, E.S., Nelson, H.D., 1977 "Finite Element Simulation of Rotor-Bearing Systems With Internal Damping", Journal of Engineering for Power, **99**, pp. 71-76
22. Hashish, E., Sankar, T.S., 1984, "Finite Element and Modal Analyses of Rotor-Bearing Systems Under Stochastic Loading Conditions", Transactions of the ASME, Journal of Vibrations, Acoustics, Stress, and Reliability in Design, **106**, pp. 80-89

23. Ginsberg, Jerry H., 2001, *Mechanical and Structural Vibrations*, John Wiley Publications, NY

24. Meriam, L.G., Kraige, J.C., 1995, *Statics*, John Wiley Publications, NY

APPENDIX A

ANALYSIS OF SHRINK FIT INTERFACE STRESSES FOR ROTATING CIRCULAR DISKS

Determination of machine stresses at shrink fit interfaces due to shrink fits constitutes an important study from two points of views: machine design and rotordynamic instability. From machine design point of view of machines with shrink fits, it is often required that the components in contact retain their elastic behavior and are not stressed beyond their plastic limit. Moreover, when such machines execute rotational motion, it is desired that shrink fits be tight enough, so that the components do not loose contact with each other due to centripetal effects and resulting looseness of the contact. From rotordynamic instability point of view, the determination of machine stresses is important because it enables an engineer to estimate magnitude of the frictional moments that are generated as micro-slip takes place between shrink fitted components. It has been experimentally verified **[4, 5]** that this micro-slip results in potentially dangerous forward whirl instability of the shrink fitted rotors when they are operated above their first critical speeds. Therefore, any rotordynamic predictions for assessing stability of the rotors, especially in regards to predicting threshold speeds of instability, which require estimate of these contact stresses to formulate frictional stresses and equivalent frictional moments, are extremely important to ensure safe and stable operation of machines with shrink fit interfaces. This study is directed at deriving analytical formulae for an example three-disk model with shrink fits at the two interfaces. The stresses are assumed to be functions of radial dimension of the materials involved only (one-dimensional). The equations thus derived show how interface stresses and shrink fits are functions of component material properties, interface size, initial shrink fit values and rotational speed.

DESCRIPTION OF THE MODEL

The model, shown in Fig.A1, is comprised of a hollow elastic disk (labeled '1'), mounted over another hollow elastic disk (labeled '2'), which in turn is mounted over a solid elastic disk (labeled '3'). The thickness of the disks is assumed to be small compared to their diameters and therefore stresses are assumed to be independent of axial and circumferential coordinates. An analysis using axisymmetric deformation of the disks by utilizing basic equations of elasticity has been carried out for this system of three synchronously spinning bodies, shrink fitted together, each one of which is elastic and thus experiences radial and tangential deformations due to centripetal forces and shrink fits. The radii indicated for the three disks in Fig.1 are the pre-assembly radii and therefore, the shrink fits at the interfaces (at assembly) are given by differences in radii for the mating disks. In this analysis, these initial shrink fits will be treated as given (known) parameters along with other material and geometric parameters of the system, such as Young's elastic modulii, Poisson's ratio, and initial radii (a, b and c) of all the disks. The model can be extended to cover multiple shrink fitted disks.

The importance of this model is in its direct application to the case of the two-disk rotor used in the experimental research of shrink fits as described in the main body of dissertation.

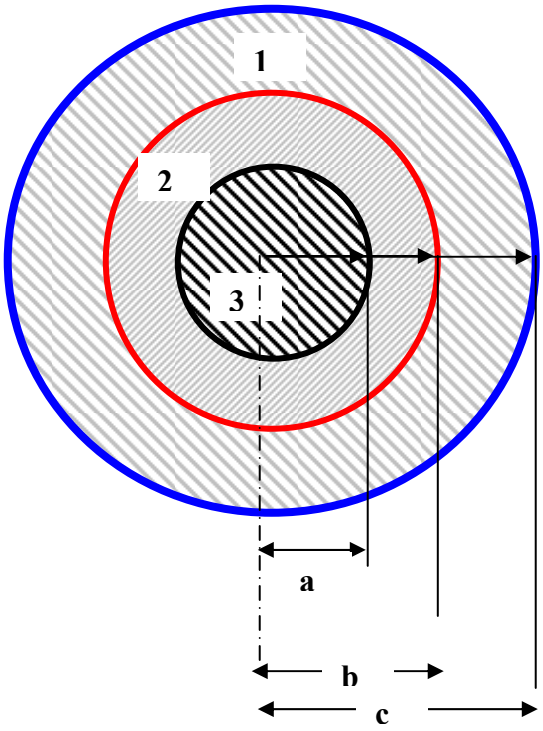

Fig.A1 Three cylindrical shafts shrink fitted together. Top two are hollow, while the smallest one is solid

DERIVATION OF EQUATIONS FOR STRESSES

An analysis based on equations of elasticity for axisymmetric deformations can be developed by considering the three shaft model as shown in Fig.1. The analysis utilizes the principle of superposition, since the assumptions about material and its deformation are strictly of linearity. For this purpose, consider cylinders '1' and '2' as shown in Fig.A1, separately, as shown in Fig.A2 below:

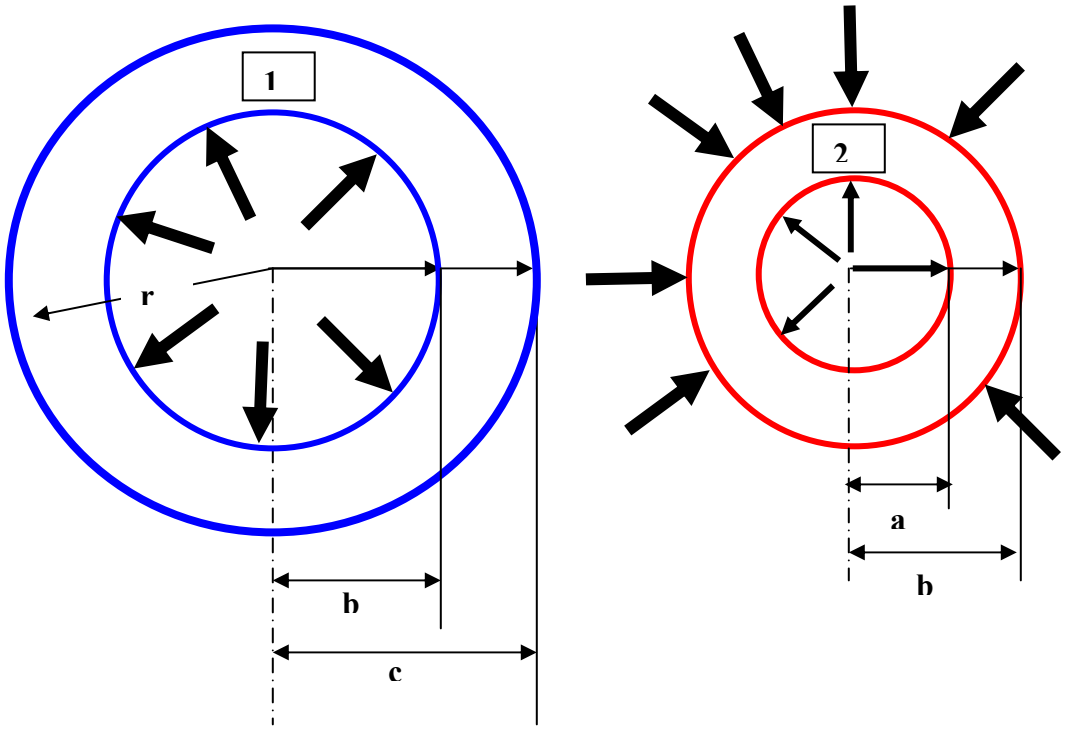

Fig.A2 Cylinders '1' and '2' shown separated (free-body diagrams) subjected to internal shrink fit stresses

STATIC INTERFACE STRESSES

When the three-disk assembly is not rotating and is in static equilibrium, the interface stresses can be formulated by considering the deformations at the interfaces as well as magnitudes of the shrink fits and relating them to the radial interface stresses.

From Fig.A1, disk 1 is subjected to the inner stress only (at the interface with disk 2), whereas disk 2 is subjected to both the inner and the outer stresses. These stresses are unknowns and need to be determined from system's given parameters.

The radial displacements in the disks can be related to the initial shrink fit values through the following equations:

$$u_1(r=b)-u_2(r=b)=\delta_0 \tag{A1}$$

$$u_2(r=a)-u_3(r=a)=\delta_1 \tag{A2}$$

In terms of the as yet unknown radial stresses at the interfaces, namely 'P_{12}' and 'P_{23}', the equations for radial displacements can be written as:

$$u_1(r=b)=\frac{bP_{12}}{E_1}\left(\frac{b^2+c^2}{c^2-b^2}+\nu_1\right) \tag{A3}$$

$$u_2(r=b)=\frac{1-\nu_2}{E_2}b\frac{a^2P_{23}-b^2P_{12}}{b^2-a^2}+\frac{1+\nu_2}{E_2}\frac{a^2b^2(P_{23}-P_{12})}{b(b^2-a^2)} \tag{A4}$$

$$u_2(r=a)=\frac{1-\nu_2}{E_2}a\frac{a^2P_{23}-b^2P_{12}}{b^2-a^2}+\frac{1+\nu_2}{E_2}\frac{a^2b^2(P_{23}-P_{12})}{a(b^2-a^2)} \tag{A5}$$

$$u_3(r=a)=\frac{-aP_{23}}{E_3}(1-\nu_3) \tag{A6}$$

Substituting equations (A2) through (A6) into equations (A1) and (A2), a system of two linear equations in the interface stresses 'P_{12}' and 'P_{23}' is obtained, which can be expressed as follows:

$$C_1P_{12}+C_2P_{23}=\delta_0 \tag{A7}$$

$$C_3P_{12}+C_4P_{23}=\delta_1 \tag{A8}$$

The coefficients C_1, C_2, C_3, and C_4 in equations (A7) and (A8) are defined as follows:

$$C_1 = \frac{b}{E_1}\left(\frac{b^2 + c^2}{c^2 - b^2} + \nu_1\right) + \frac{1-\nu_2}{E_2}\frac{b^3}{b^2 - a^2} + \frac{1+\nu_2}{E_2}\frac{a^2 b}{b^2 - a^2} \qquad \text{(A9)}$$

$$C_2 = \frac{-a^2 b}{b^2 - a^2}\frac{1-\nu_2}{E_2} - \frac{a^2 b}{b^2 - a^2}\frac{1+\nu_2}{E_2} \qquad \text{(A10)}$$

$$C_3 = \frac{-b^2 a}{b^2 - a^2}\frac{1-\nu_2}{E_2} - \frac{1+\nu_2}{E_2}\frac{a^2 b^2}{a(b^2 - a^2)} \qquad \text{(A11)}$$

$$C_4 = \frac{a^3}{b^2 - a^2}\frac{1-\nu_2}{E_2} + \frac{ab^2}{b^2 - a^2}\frac{1+\nu_2}{E_2} + \frac{a(1-\nu_3)}{E_3} \qquad \text{(A12)}$$

The solution of equations (A7) and (A8) can therefore be expressed as follows:

$$P_{12} = \frac{\delta_0 C_4 - \delta_1 C_2}{C_1 C_4 - C_3 C_2} \qquad \text{(A13)}$$

$$P_{23} = \frac{\delta_0 C_3 - \delta_1 C_1}{C_2 C_3 - C_4 C_1} \qquad \text{(A14)}$$

Equations (A13) and (A14) express the values of the static radial interface stresses as functions of such system variables as magnitude of the initial shrink fits at the interfaces, and geometric and elastic properties of the disks.

(b) Interface radius

The interface radius for the static assembly can be determined by using equations (A3) and (A5) or equations (A4) and (A6). The interface radii for the disks '1' and '2' after the assembly are:

$$R_{m12} = u_1(r = b) + b \tag{A15}$$

$$R_{m23} = u_3(r = a) + a \tag{A16}$$

In equations (A15) and (A16), the radial displacements u_1 and u_3 can be calculated using equations (A3), (A6), (A13), and (A14). Therefore, the interface radius can be computed as a function of the initial shrink fit and the other system parameters.

DYNAMIC STRESSES AND SHRINK FIT

Cylinder 1

Let the elastic modulus and Poisson's ratio of cylinders '1' and '2' be E_1, ν_1 and E_2, ν_2, respectively. From theory of elasticity, the stress distribution equations for cylinder '1' which is subjected to centripetal stresses as well are given by:

$$\sigma_{r1}(r) = A_1 - \frac{B_1}{r^2} - \frac{3+\nu_1}{8}\rho_1\omega^2 r^2 \tag{A17}$$

$$\sigma_{t1}(r) = A_1 + \frac{B_1}{r^2} - \frac{1+3\nu_1}{8}\rho_1\omega^2 r^2 \tag{A18}$$

In equations (A1) and (A2), 'r' is the radial coordinate to locate any point between and including inside and outside radii of the cylinder '1' and 'ρ_1' is the mass density of material which comprises cylinder '1'. Subscripts 'r' and't' denote radial and tangential stresses, respectively. Also, let 'a', 'b' and 'c' be the radii of the cylinders in

their undeformed positions (i.e., before they are shrink fitted together). 'A_1' and 'B_1' are constants to be evaluated from boundary conditions of the problem. The boundary conditions are as follows:

(1) At r = b, $\sigma_{r1} = -p_{12}$ (interface stress due to shrink fit)
(2) At r = c, $\sigma_{r1} = 0$ (no external load)

Using these boundary conditions in equation (A1), following equations result:

$$-p_{12} = A_1 - \frac{B_1}{b^2} - \frac{3+\nu_1}{8}\rho_1\omega^2 b^2 \tag{A19}$$

$$0 = A_1 - \frac{B_1}{c^2} - \frac{3+\nu_1}{8}\rho_1\omega^2 c^2 \tag{A20}$$

From equations (A3) and (A4):

$$-p_{12} = \frac{-B_1}{b^2} + \frac{B_1}{c^2} - \frac{3+\nu_1}{8}\rho_1\omega^2(b^2 - c^2) \tag{A21}$$

Solving equation (A5) for constant 'B_1':

$$B_1 = \frac{-b^2c^2}{b^2 - c^2}p_{12} + \frac{3+\nu_1}{8}\rho_1\omega^2 b^2 c^2 \tag{A22}$$

From equation (A4), 'A_1' can be expressed in terms of 'B_1'as follows:

$$A_1 = \frac{B_1}{c^2} + \frac{3+\nu_1}{8}\rho_1\omega^2 c^2 \tag{A23}$$

From equations (A2) and (A7):

$$\sigma_{t1}(r)=\frac{B_1}{c^2}+\frac{3+\nu_1}{8}\rho_1\omega^2c^2+\frac{B_1}{r^2}-\frac{1+3\nu_1}{8}\rho_1\omega^2r^2 \tag{A24}$$

By utilizing boundary conditions of the problem and equations (A8) and (A6), the following values for radial and tangential stresses are obtained at the interface radius 'b':

$$\sigma_{t1}(r=b)=\frac{b^2+c^2}{c^2-b^2}p_{12}+2(\frac{3+\nu_1}{8})\rho_1\omega^2c^2+2(\frac{1+\nu_1}{8})\rho_1\omega^2b^2 \tag{A25}$$

$$\sigma_{r1}(r=b)=-p_{12} \tag{A26}$$

Therefore, the radial deformation of the cylinder '1' at interface radius 'b' can be calculated using the modified Hooke's Law as expressed in polar coordinates as follows:

$$u_1(r=b)=b\varepsilon_{t1}(r=b) \tag{A27}$$

The tangential strain 'ε_{t1}' can be expressed as follows:

$$\varepsilon_{t1}(r=b)=\frac{1}{E_1}(\sigma_{t1}(r=b)-\nu_1\sigma_{r1}(r=b)) \tag{A28}$$

Using equations (A9) and (A10) and substituting them in equation (A12) and (A11), the following expression for the radial deformation at the interface radius is obtained:

$$u_1(r=b)=\frac{bp_{12}}{E_1}[\nu_1+\frac{b^2+c^2}{c^2-b^2}]+2(\frac{3+\nu_1}{8E_1})\rho_1\omega^2bc^2+2(\frac{1+\nu_1}{8E_1})\rho_1\omega^2b^3 \tag{A29}$$

Cylinder 2

In a similar manner to cylinder '1', equations of stress distribution for inside cylinder '2' can be written as follows:

$$\sigma_{r2}(r) = A_2 - \frac{B_2}{r^2} - \frac{3+\nu_2}{8}\rho_2\omega^2 r^2 \tag{A30}$$

$$\sigma_{t2}(r) = A_2 + \frac{B_2}{r^2} - \frac{1+3\nu_2}{8}\rho_2\omega^2 r^2 \tag{A31}$$

However, the boundary conditions are different in this case because the inner cylinder is subjected to both internal and external stresses due to shrink fits at both locations. These can be expressed as follows:

(3) At r = a, $\sigma_{r2} = -p_{23}$
(4) At r = b, $\sigma_{r2} = -p_{12}$

Using boundary conditions (3) and (4) above, equation (14) yields the following two equations:

$$-p_{23} = A_2 - \frac{B_2}{a^2} - \frac{3+\nu_2}{8}\rho_2\omega^2 a^2 \tag{A32}$$

$$-p_{12} = A_2 - \frac{B_2}{b^2} - \frac{3+\nu_2}{8}\rho_2\omega^2 b^2 \tag{A33}$$

Using equation (A16) to express 'A_2' in terms of 'B_2' and substituting the result in equation (A15) and finally calculating the tangential stress at interface radius r = b, yields the following result:

$$\sigma_{t2}(r=b) = -p_{23} + \frac{a^2+b^2}{a^2-b^2}(p_{12}-p_{23}) + 2\left(\frac{3+\nu_2}{8}\right)\rho_2\omega^2 a^2 + 2\left(\frac{1+\nu_2}{8}\right)\rho_2\omega^2 b^2 \tag{A34}$$

$$\sigma_{r2}(r=b) = -p_{12} \tag{A35}$$

Using equations (A18) and (A19), the tangential strain in cylinder '2' at interface radius 'b' is expressed as follows:

$$\varepsilon_{t2}(r=b)=\frac{1}{E_2}(\sigma_{t2}(r=b)-\nu_2\sigma_{r2}(r=b)) \tag{A36}$$

Therefore, the final result for radial deformation in cylinder '2' (using equations (A18), (A19) and (A20)) is as follows:

$$u_2(r=b)=\frac{bp_{12}}{E_2}[\nu_2+\frac{a^2+b^2}{a^2-b^2}]-\frac{bp_{23}}{E_2}[1+\frac{a^2+b^2}{a^2-b^2}]+2(\frac{3+\nu_2}{8E_2})\rho_2\omega^2ba^2+2(\frac{1+\nu_2}{8E_2})\rho_2\omega^2b^3$$

(A37)

Subtracting equation (A21) from equation (A13) yields the equation for variable shrink fit as a function of rotational speed 'ω' as follows:

$$\delta(\omega)=u_1(r=b)-u_2(r=b)=\delta_0+2(\frac{3+\nu_2}{8E_2})\rho_2\omega^2a^2b-2(\frac{3+\nu_1}{8E_1})\rho_1\omega^2bc^2+2(\frac{1+\nu_2}{8E_2})\rho_2\omega^2b^3$$
$$-2(\frac{1+\nu_1}{8E_1})\rho_1\omega^2b^3$$

(A38)

In equation (A22), 'δ_0' is the shrink fit at zero speed (initial shrink fit) and it appears due to the interface stress terms that are originally present in equations (A13) and (A21). Therefore, equation (A22) provides the variation of shrink fit between outermost cylinders as a function of rotational speed, given some initial shrink fit at interface at zero speed.

The dynamic stresses at the interface between disks 1 and 2 can be approximated by using equations (A13) and (A25) as follows:

$$\sigma_r(\omega) = \frac{\delta_0(\omega)C_4 - \delta_1 C_2}{C_1 C_4 - C_3 C_2} \tag{A39}$$

$$\sigma_{t1}(\omega) = \frac{b^2 + c^2}{c^2 - b^2}\sigma_r(\omega) \tag{A40}$$

NORMALIZATION OF INTERFACE STRESSES

The static radial and tangential stresses acting on the disk 1 at the interface between disks 1 and 2 as shown in equations (A13) and (A25) (by setting ω=0) can be normalized with respect to the yield stress of the material which comprises disk 1. The reason for normalizing the stresses is to find out what value of the interface shrink fit δ_0 causes the initiation of failure of the material comprising disk 1. This is in accordance with the maximum shear stress theory as a failure criterion of engineering materials. The maximum shearing stress criterion states that for ductile materials such as various grades of steel and aluminum, the failure initiates when the stress acting on the body is equal to or greater than the yield strength of the material, provided the stresses are of the same numerical sign, as in the case of outer disk in the model considered. As long as the stresses are less than the yield stress, the material's failure will not initiate due to static loading.

Dividing equations (A13) and (A25) by the yield stress of the material, the following equations for the normalized stresses are obtained:

$$\Sigma_r = \frac{\sigma_r}{\sigma_Y} = \frac{1}{\sigma_Y}\left(\frac{\delta_0 C_4 - \delta_1 C_2}{C_1 C_4 - C_3 C_2}\right) \tag{A41}$$

$$\Sigma_t = \frac{\sigma_t}{\sigma_Y} = \frac{1}{\sigma_Y}\left(\frac{\delta_0 C_4 - \delta_1 C_2}{C_1 C_4 - C_3 C_2}\right)\frac{b^2 + c^2}{c^2 - b^2} \tag{A42}$$

The graphs of equations (A41) and (A42) are shown on the following pages. On vertical axis are the normalized stresses, whereas on horizontal axis are the values of the initial shrink fit δ_0. The graphs are plotted for the following set of data:

- c = 5 in. b= 4.37 in. a = 1.5 in.
- $E_1 = 10 \times 10^6$ psi $E_2 = E_3 = 30 \times 10^6$ psi
- $\nu_1 = 0.28$ $\nu_2 = \nu_3 = 0.30$
- $\gamma_1 = 0.1$ lb/in^3 $\gamma_2 = \gamma_3 = 0.28$ lb/in^3
- $\delta_1 = 2$ mils $\sigma_Y = 35$ ksi
- $\rho = \gamma / g$

The data values shown above are from the experimental rotor (the two disk rotor).

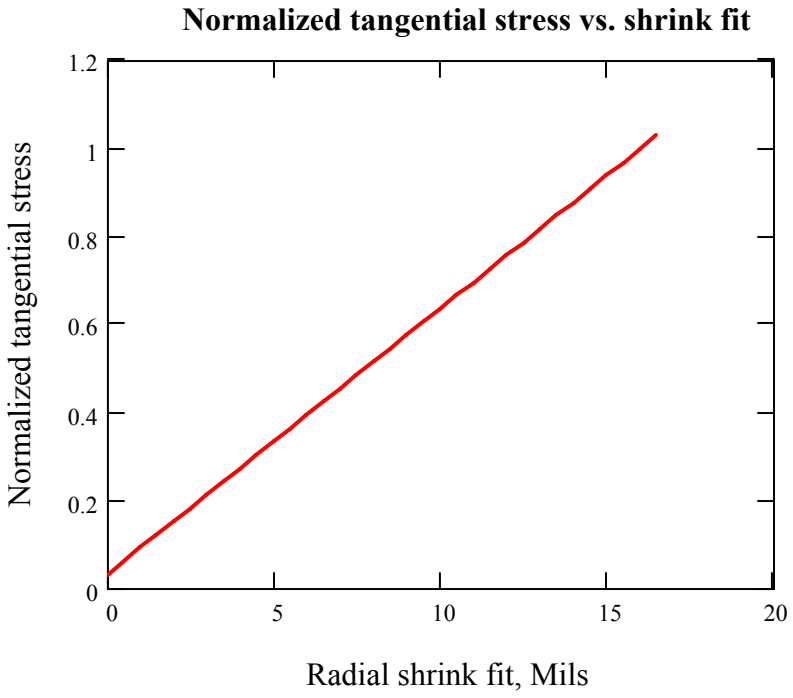

Fig. A3 Normalized tangential stress as a function of radial shrink fit at outer interface

Fig.A3 shows the normalized tangential stresses acting on disk 1 as a function of radial shrink fit at the outer interface (δ_0). From Fig.A3, the material of outer disk (in this case, aluminum) will yield (when the value on vertical axis reads 1.0) when the radial shrink fit is about 16 Mils. This corresponds to a diametral shrink fit of 32 Mils. In any of the experiments involving the two disk rotor, the initial radial shrink fit value did not exceed 7 Mils. Therefore, the aluminum sleeve did not undergo plastic deformation at assembly.

The radial stresses are much smaller in magnitude. The normalized radial stress as a function of radial shrink fit (δ_0) is shown below:

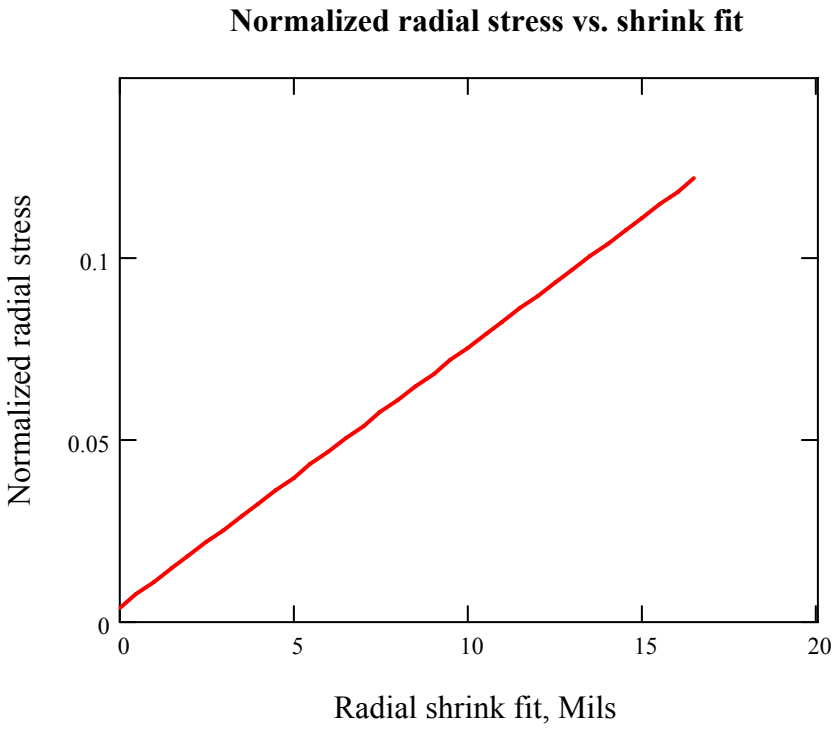

Fig. A4 Normalized radial stress as a function of radial shrink fit at outer interface

Fig.A4 shows that the radial stresses acting on the disk 1 (aluminum sleeve) are well within safe limits for radial shrink fits limits.

Fig.A5 shows the graphs of equation (A38) with two different initial shrink fit values as parameter. Fig.A5 shows that the radial shrink fit at the interface is a decreasing function of rotational speed. For an initial shrink fit of 3.5 Mils as shown by the solid line in Fig.A5, the value of the radial shrink fit at a speed of 12000 rpm decreases to less than 1 Mil. For an initial radial shrink fit of 2.5 Mils, the value drops down to 0 Mils at 12000 rpm. A value of zero radial fit indicates that the outer disk looses contact with the inner disk. The analysis developed for the rotating disks is also important from point of view of predicting before finalizing a design whether the design is safe in so far as contact of the disks during operating speed range is concerned.

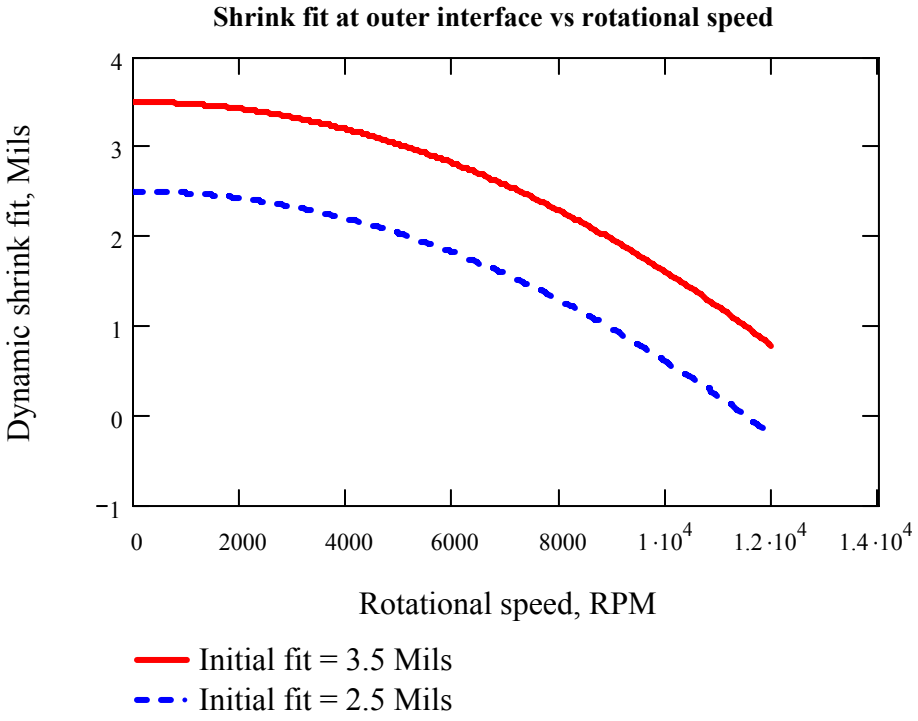

Fig. A5 Radial shrink fit variation with rotational speed.

SINGLE SHRINK FIT INTERFACE MODEL

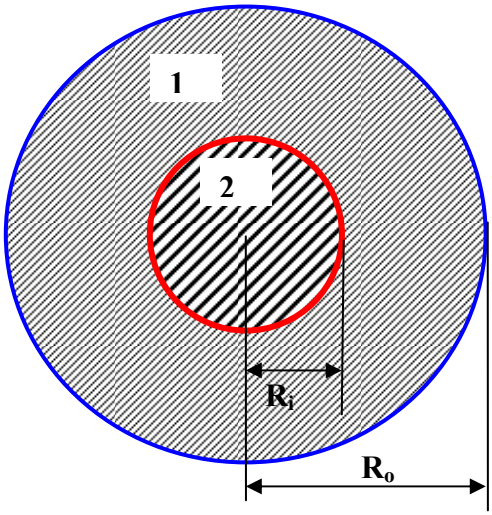

Fig.A6 Two cylindrical shafts shrink fitted together.

The procedure to analyze the interface stresses and shrink fits for a model comprised of two circular elastic disks is the same as for the three-disk model considered earlier. The analysis is considerably simplified due to the presence of only one interface as compared to two interfaces considered in the previous model. The importance of this model is in its direct application to the case of the single-disk uniform shaft rotor used in the experimental research of interference fits as described in the main body of dissertation. The model shown in Fig.6 consists of two circular elastic disks shrink fitted with a known amount of radial interference fit. The material properties for the disks are known. The outer disk (labeled disk '1') is a hollow disk, with an outside diameter R_o, whereas the inside disk is a solid disk (labeled disk '2') with an initial outside diameter R_i. The dimensions shown in Fig.A6 are pre-assembly dimensions, that is, when the disks are not connected through shrink fit. When they are assembled or connected through shrink fit, the dimensions will change due to elasticity of the materials of disks.

STATIC INTERFACE STRESS

For the two disks shown, equations for radial displacements at the interface can be written. The equations are written based on the assumption that the outer disk (disk 1) is subjected to only inner interface stress (no outer or external stress) whereas the inner disk (disk 2) is subjected to external stress (which is the interface stress) at its outer surface.

The radial displacement of the outer disk at the interface is given by:

$$u_1 = \frac{R_i p_{12}}{E_1}\left(\frac{R_i^2 + R_o^2}{R_o^2 - R_i^2} + \nu_1\right) \tag{A43}$$

$$u_2 = \frac{-R_i p_{12}}{E_2}(1 - \nu_2) \tag{A44}$$

In equations (A43) and (A44), p_{12} is the radial interface pressure. If the disks 1 and 2 are made of same material, the analysis can be simplified. The difference of the radial displacements is equal to the initial value of the radial shrink fit, that is:

$$u_1 - u_2 = \delta_o = \frac{2R_i R_o^2 p_{12}}{E(R_o^2 - R_i^2)} \tag{A45}$$

Using equation (A45), the static radial interface pressure can be calculated as:

$$p_{12} = \frac{E\delta_o(R_o^2 - R_i^2)}{2R_i R_o^2} \tag{A46}$$

The static tangential stress at the interface can be calculated using the radial stress. From the theory of thick disks, the static radial and tangential stress distributions as a function of radial coordinate are given as:

$$\sigma_r(r) = A_1 - \frac{B_1}{r^2} \tag{A47}$$

$$\sigma_t(r) = A_1 + \frac{B_1}{r^2} \tag{A48}$$

Using equation (A47), the following boundary conditions can be applied:

(a) At r = R_o, σ_r (R_o) = 0

(b) At r = R_i, σ_r (R_m) = -p_{12}

In the boundary condition above, R_m is the interface radius and its value can be computed from the following equation:

$$R_m = R_i + u_2 \tag{A49}$$

The following two equations result from the application of boundary conditions on equation (A47):

$$0 = A_1 - \frac{B_1}{R_o^2} \tag{A50}$$

$$-p12 = A_1 - \frac{B_1}{R_i^2} \tag{A51}$$

Solving equations (A50) and (A51) simultaneously for the constants A_1 and B_1:

$$B_1 = p_{12}\left(\frac{R_o^2 R_m^2}{R_o^2 - R_m^2}\right) \tag{A52}$$

$$A_1 = p_{12}\left(\frac{R_m^{\,2}}{R_o^{\,2} - R_m^{\,2}}\right) \tag{A53}$$

Using equations (A48), (A52) and (A53), the tangential stress distribution at the interface can be calculated as follows:

$$\sigma_t(r = R_m) = p_{12}\left(\frac{R_o^{\,2} + R_m^{\,2}}{R_o^{\,2} - R_m^{\,2}}\right) \tag{A54}$$

NORMALIZING THE INTERFACE STRESSES

The radial and tangential stresses given by equations (A46) and (A54) can be normalized by the yield stress of the material forming disks 1 and 2 to provide knowledge of what radial shrink fit value causes yield of the material at the interface. Dividing equations (46) and (54) by the yield stress, the normalized form of the equations is obtained as follows:

$$\Sigma_r = \frac{p_{12}}{\sigma_Y} = \frac{E\delta_o(R_o^{\,2} - R_i^{\,2})}{2\sigma_Y R_i R_o^{\,2}} \tag{A55}$$

$$\Sigma_t = \frac{\sigma_t}{\sigma_Y} = \frac{E\delta_o(R_o^{\,2} + R_i^{\,2})}{2\sigma_Y R_i R_o^{\,2}} \frac{(R_o^{\,2} - R_i^{\,2})}{(R_o^{\,2} - R_m^{\,2})} \tag{A56}$$

The graphs of equations (A55) and (A56) are plotted on the next pages. For AISI 4340 steel, the yield strength is about 50 ksi. The outside diameter of the disk is taken as 10 in. (R_o= 5 in.) and the inside diameter is taken as 2.5 in. (R_i = 1.25 in.).

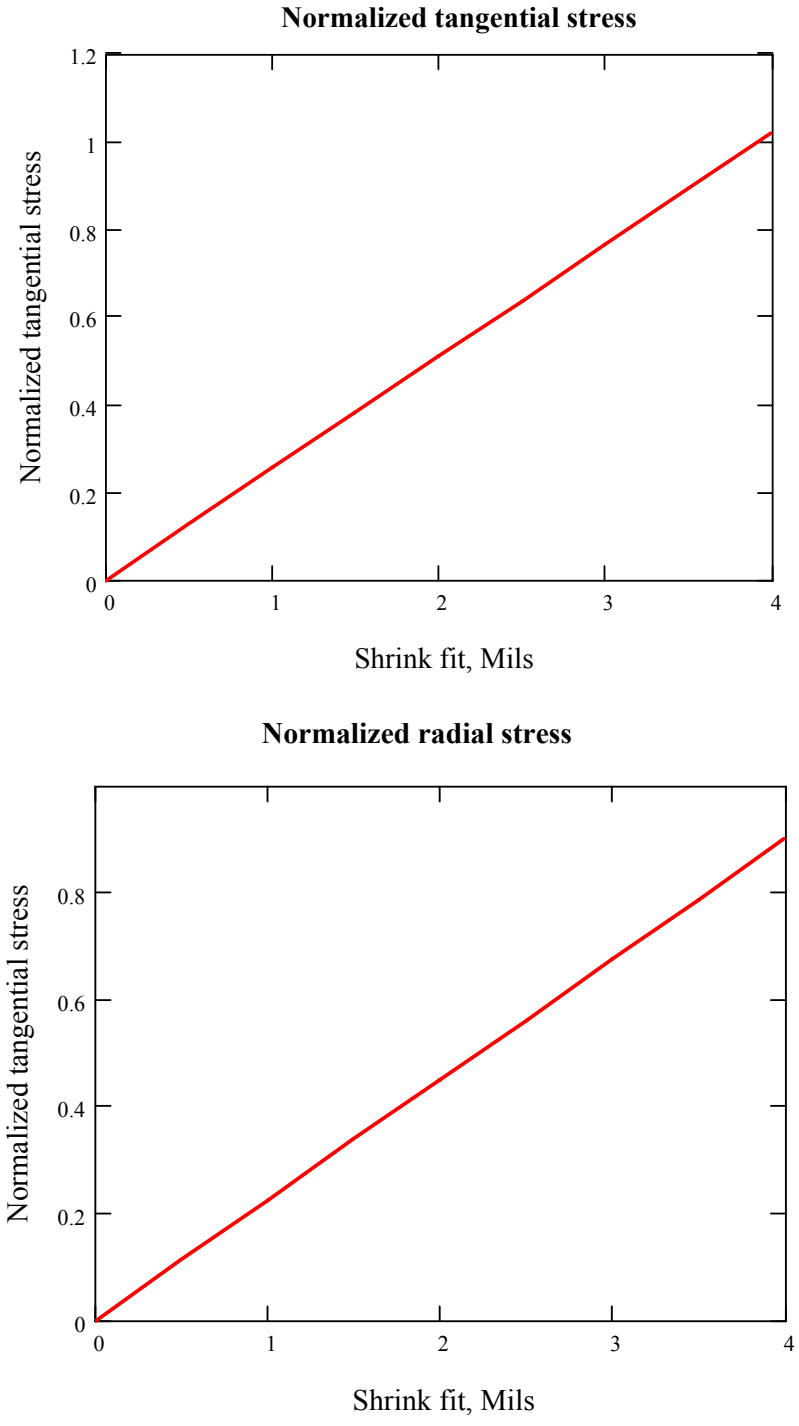

Fig. A7 Normalized tangential and radial interface stresses for disk 1

Fig.A7 shows the normalized tangential and radial stresses as functions of radial shrink fit δ_o. From Fig.A7, the material yield stress is approached at a radial shrink fit value of 4 Mils. In the experiments conducted on the single-disk rotor, the maximum interference fit that was maintained between the shaft and the disk through the tapered sleeve was 2.2 Mils radial. Therefore, the outer disk did not undergo any plastic deformations during the experiments.

DYNAMIC SHRINK FIT

The procedure to formulate the shrink fit as a function of rotational speed is the same as that used in the three-disk model. The formulation begins with equations (A17) and (A18). Appropriate boundary conditions are applied using equation (A17) and a set of linear equations is obtained in the constants A_1 and B_1. Then the displacements are formulated in terms of those constants. The difference in the displacements at a speed give an expression for the variation of shrink fit with the rotational speed. For the model of two elastic disks, the expression for dynamic shrink is obtained using this procedure as follows:

$$\delta(\omega) = \delta_o - 2(\frac{3+\nu_1}{8E})\rho\omega^2 R_i R_o{}^2 \qquad \text{(A57)}$$

The graph of equation (A57) is plotted on the next page for three different values of the initial radial shrink fit. The material is steel. The inside radius is 1.25 in. The outside radius is 5 in.

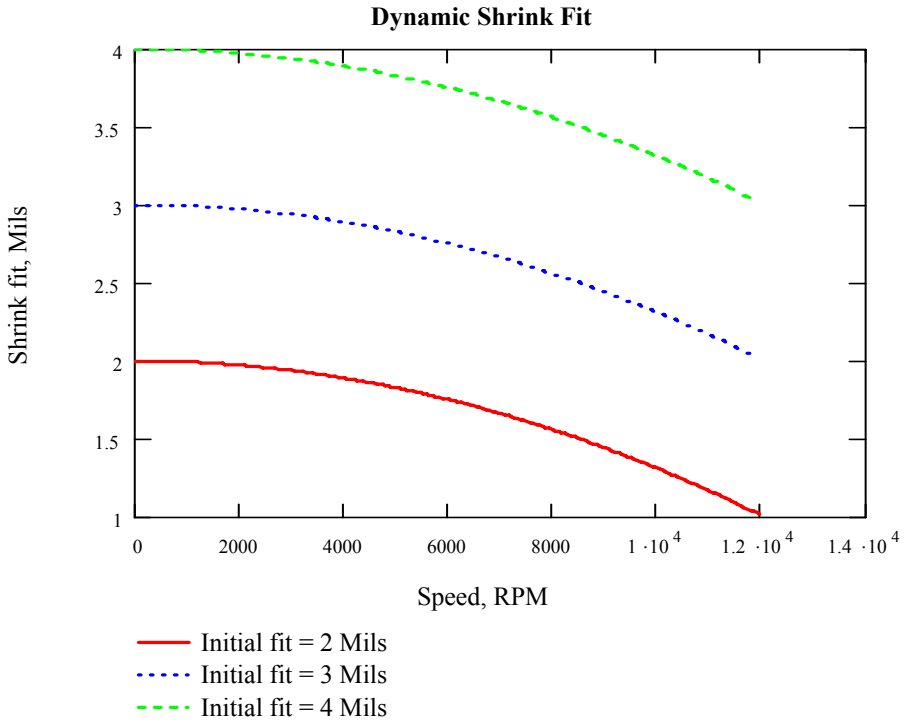

Fig. A8 Variation of radial shrink fit as a function of rotational speed for the case of two-disk model

Fig.A8 shows the shrink fit at the interface between disks 1 and 2 as a function of rotational speed for three different values of the initial shrink fit values. Fig.A8 shows that the radial shrink fit is a decreasing function of rotational speed. The higher the initial value of the shrink fit, the higher its value will be at different rotational speeds as compared to the one with the lower initial values.

APPENDIX B

FREE-FREE TESTS ON SINGLE-DISK ROTOR WITH THE DISK AT VARIOUS AXIAL LOCATIONS ALONG THE SHAFT

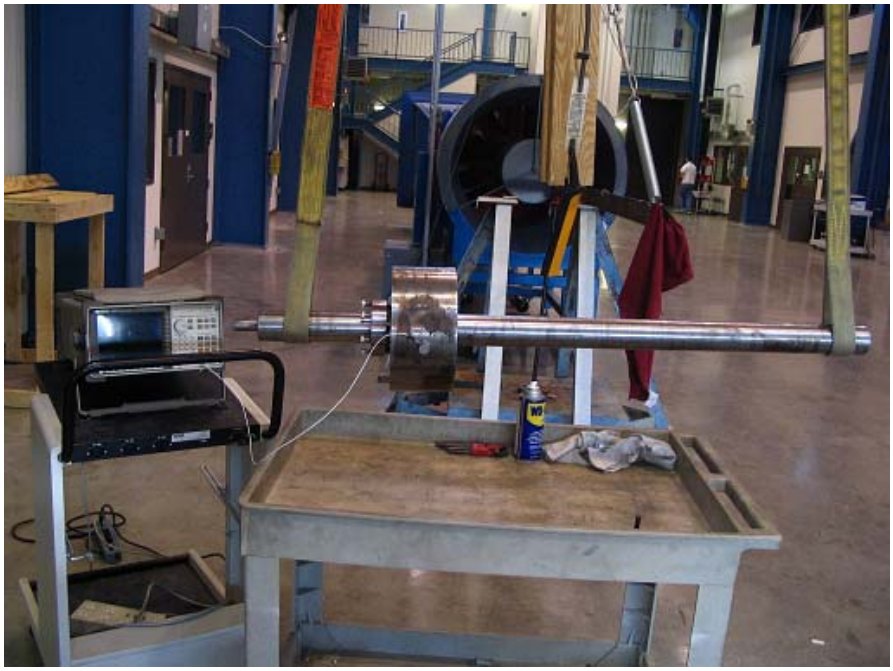

Fig.B1 Free-free testing of the single-disk rotor.

Free-free tests of the single-disk rotor were performed to estimate the amount of internal friction in the rotor. In each of the experiments, the axial location of the disk was varied along the span of the shaft, whereas the interference fit was maintained the same at each axial location. The objective of these experiments is to ascertain whether the internal damping coefficient varies with the axial location of the disk on the shaft, when the interference fit is maintained the same. For each of the axial locations of the disk on the shaft, the free-free time data of the rotor vibration was obtained.

The free-free vibration data of the single-disk rotor when the disk is at the centre and when it is near the end of the shaft is shown in Fig.B2 as follows:

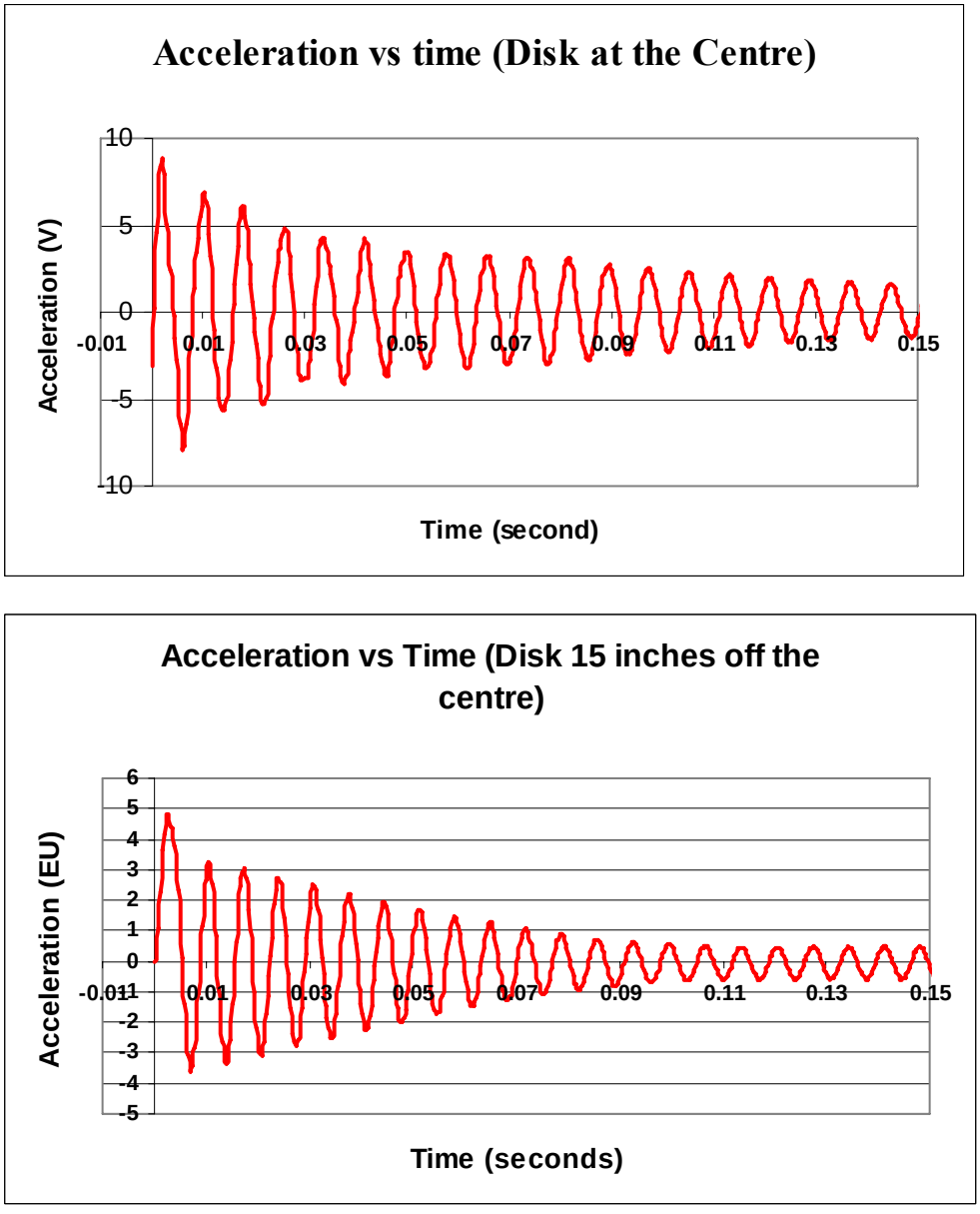

Fig.B2 Free vibration data for the single-disk rotor with different positions of the disk

Fig.B2 shows that changing the axial position of the disk considerably affects the amount of friction which is developed in the rotor due to slippage in the interference fit interface. There is considerably more amount of friction which is developed for the disk offset from the centre than in the case when the disk is at the centre, while maintaining the same interference fit in each of the case.

Through the experimental free-free vibration data, the logarithmic decrement can be calculated which in turn yields the value of the internal damping coefficient corresponding to each of the axial locations of the disk on the shaft. The value of the interference fit that was maintained constant through the experiments was 1.16 mils, radial. This value of the interference fit corresponds with the initial value of the fit that caused the rotor-bearing system to become unstable at 5800 rpm, when the rotor was mounted on ball bearings.

The data for the free-free experiments was collected using a dynamic signal analyzer and an accelerometer. The accelerometer was attached at the centre of the disk in the horizontal direction and the rotor was tapped through a soft hammer. In each of the experiments, the time traces of acceleration as measured from the accelerometer were obtained for the first mode of free vibration of the rotor. To ensure that only the data for the first mode is obtained, the signal analyzer was also setup to display the frequency spectrum on linear scale. In a frequency spectrum, the amplitude corresponding to each frequency is displayed. From the frequency spectrum, it was made sure that a high vibration amplitude of only the first mode of free-free vibration of the rotor was obtained (by trial and error, through tapping the rotor at different locations until only the first mode was visible on the spectrum plot) and that the other modes were either not excited, or else the vibration amplitudes corresponding to the higher modes were negligible as compared to the first mode. In this way, the logarithmic decrements and the damping associated with only the first modes for each of the experiments was obtained.

The experimental results from the single-disk rotor are summarized in Table 1 on the next page:

Table B1.Experimental results from free-free tests of the single-disk rotor.

Disk Location	First mode frequency (Hz)	Logarithmic Decrement	Damping Ratio
Centre	128	0.1004	0.016
4 in. left	136	0.087	0.0138
8 in. left	148	0.054	0.0086
12 in. left	152	0.0866	0.014
5 in. right	132	0.068	0.0109
11 in. right	148	0.259	0.041
15 in. right	152	0.129	0.0205

Table 1 shows that the first mode frequency of the single-disk rotor increases as the disk is made progressively offset from the centre of the shaft. As the disk is moved towards the coupling end side, the average logarithmic decrement and the corresponding damping ratios decrease. On the other hand, if the disk is moved towards the coupling end of the shaft away from the centre, the logarithmic decrement and the corresponding damping ratio increases. This opposing trend can be explained by the interface geometry of the tapered sleeve and the shaft. The tapered sleeve is more likely to slip on the shaft at one end as compared to the other end because it is fastened to the wheel through the draw bolts. As the end of the sleeve which is opposite to the fastening end moves away from the centre, it experiences more micro-slip at the interface due to the mode shape of the rotor. At the ends of the rotor farther away from the mid-point of the shaft, the rotor has higher amplitudes in its first mode, as it has high amplitude at the mid-point. In between the mid-point and the farther ends of the shaft, there is a node located. When the sliding end of the tapered sleeve is at the farther ends of the shaft, higher micro-slip takes place and as a result, the damping is higher. On the other end, when the non-fastening end of the tapered sleeve (inside the wheel) is at a node location in the first

mode, the micro-slip is negligible and therefore, the damping is small as compared to when the disk is either at the centre or at the extreme ends of the shaft.

The average moment damping coefficients are calculated from the average damping ratios as presented in Table 1 using the following equation:

$$2\zeta_1\omega_1 = [\Phi_1]^T C_{Rot} [\Phi_1] \quad (1)$$

In equation (1), the matrices on the right hand side are the normal mode matrices of the rotor in its first mode of free-vibration. The variables ζ_1 and ω_1 are the damping ratios and the first mode natural frequency respectively which are listed in Table 1. The frequency given in Table 1 is in Hz, whereas the frequency used in equation (1) is in rad/s. The frequency ω_1 can be obtained from the measured frequency by multiplying it with the factor 2π. The computation of the normal mode matrices is performed using the XLTRC^{TM} software. The models of each of the different single-disk rotor configurations are simulated as free-free rotors and their mode shapes are computed using the "Shapes" feature in the XLTRC^{TM} software. The result of using equation (1) to compute the moment damping coefficients for various configurations is summarized in Table B2:

Table B2. Calculated values of the moment damping coefficient at various disk locations

Disk Location	First Mode (Hz)	Moment damping(lb-in-s)
Centre	128	124.22
4 in. left	136	359.34
8 in. left	148	613.51
12 in. left	152	54.42
5 in. right	132	68.83
11 in. right	148	1678.45
15 in. right	152	841.58

APPENDIX C

XLTRC™ ROTORDYNAMIC SIMULATIONS OF IMAGINED ROTOR CONFIGURATIONS

This Appendix describes the rotordynamic simulations of several imagined rotor configurations (both single-disk and two-disk rotors) with shrink fit joints. The objective of presenting these simulations is an attempt to understand the effect of various system parameters such as geometry and material properties on the stability of the system. As shown in Appendix B, the location of disk at various axial locations of the shaft results in different modal damping. The simulations of various imagined configurations of single-disk and two-disk rotor with varying geometries and material properties using the internal moment model to simulate shrink fit joint internal friction are presented and discussed. None of these simulations (except one two-disk rotor model), however, is supported by any experimental data. The values of the internal moment coefficients, such as the direct moment stiffness and direct moment damping coefficients, used to simulate internal friction in each of the cases, are based on engineering judgment and should not be considered as "final" values to simulate the imagined rotor configurations. Indeed, the word "imagined" is supposed to imply the fact that there is no experimental data on rotordynamic stability to support these simulations which are presented and discussed in this Appendix. The simulations in this Appendix merely serve as a guideline for designing a single-disk and a two-disk rotor with shrink fit interfaces and to assess the rotordynamic stability trend in similar configurations of rotating machines.

SINGLE-DISK IMAGINED ROTOR CONFIGURATIONS AND SIMULATIONS

1. Disk located 1/3rd the length of shaft from the coupling end

This is the first of imagined rotor configuration simulations presented. In this configuration, all the dimensions and elastic properties of the experimental setup are retained except for the axial position of the disk on the shaft. As shown in Appendix B, the axial location of the disk on shaft results in different damping ratios and consequently, different modal damping. The 'Geo Plot' of the rotor model from XLTRC™ is shown in Fig. C1:

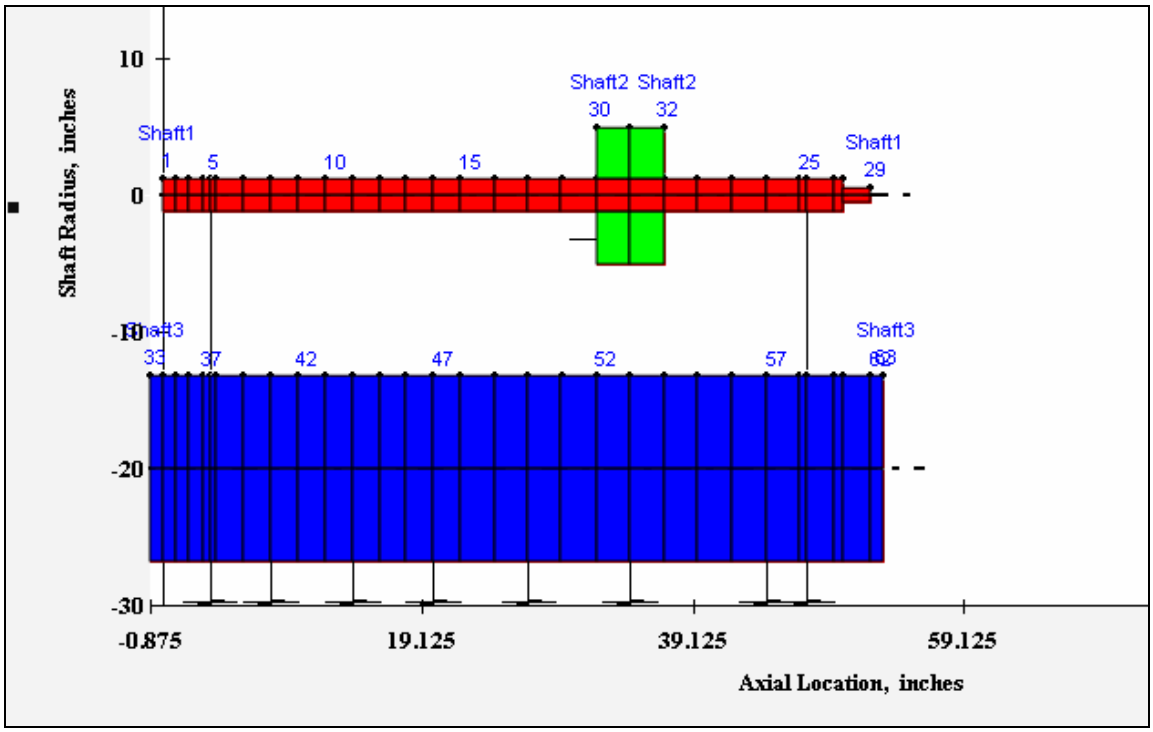

Fig.C1 Single-disk rotor model for disk offset from the centre of the shaft

The simulation of the rotor model shown in Fig.C1 shows that the model is more unstable as compared to the baseline model as shown in Chapter VI. The first critical speed of the rotor is 3590 rpm. The first critical speed of the baseline case as measured experimentally and predicted theoretically (Chapter II and VI) is around 3000 rpm. The increase in the first critical speed of the imagined rotor model is due to stiffening as introduced by shifting the disk to a location different from the centre of the shaft. However, the model is more unstable as a smaller amount of direct moment damping is required to predict a threshold speed of instability as low as 3800 rpm, which is just above the predicted critical speed. The value of the direct moment damping coefficient which predicts this threshold speed of instability is 6207 lb-in-s. A comparison with the direct damping value for this rotor model and the one from Table 1 shows that the smaller direct damping value in the disk-offset rotor model still results in a substantially more unstable rotor as compared to the one at the disk centre.

The higher unstable behavior of the disk-offset from centre model can be explained by considering the first mode shape of the rotor on the bearings. At the centre, the slope of the mode shape is zero whereas at a position offset from the centre, the slope of the mode shape is non-zero. When the friction interface is closer to the centre, the difference in the rotational deflection of the disk and the shaft will be smaller as compared to when the disk is offset. This is because when the rotor bends in the first mode shape, the disk tends to maintain its perpendicularity with respect to deflected centerline of the shaft. At a location near the centre, the slip will be very small due to disk maintaining its perpendicularity. As a result, the magnitude of the resulting internal moments will be smaller as compared to when the disk is offset from the centre, due to greater amount of relative slip between the disk and the shaft. Since internal moment will be larger in the second case, it will make this system more unstable as compared to the baseline case.

2. Disk very close to bearing

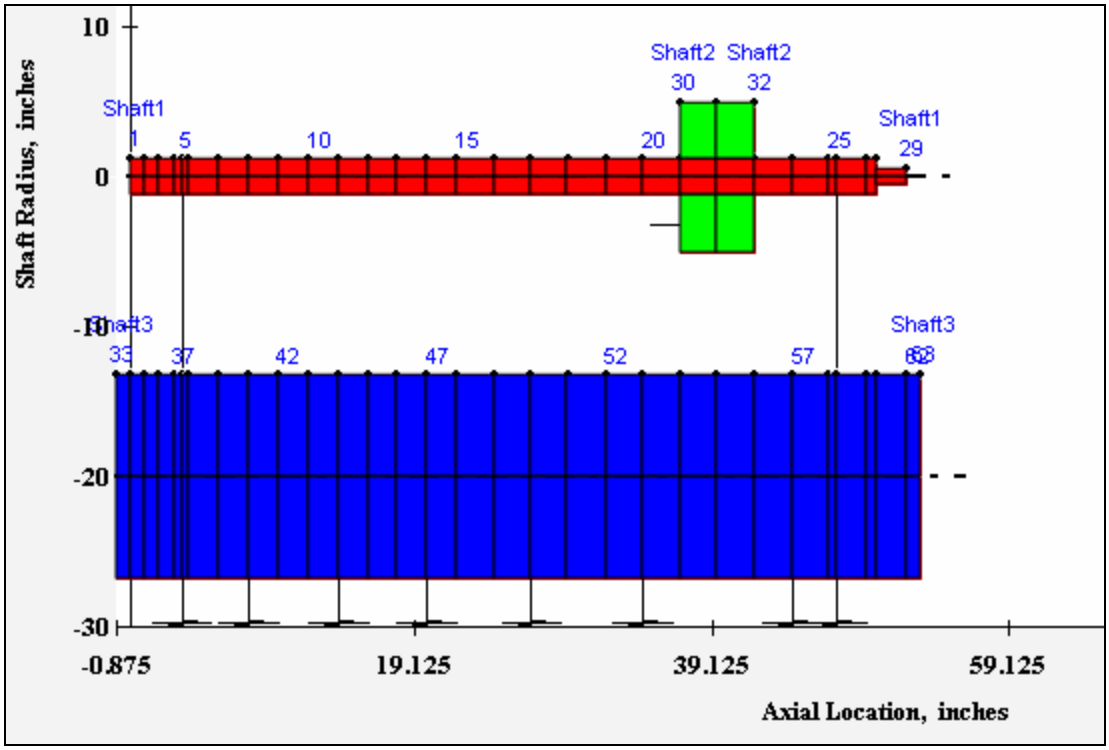

Fig.C2 Single-disk rotor model for disk very close to a bearing location

The rotor model with the disk offset from the centre of the shaft and located very close to a ball bearing location is shown schematically in Fig.C2. The remaining shaft and disk properties are the same as for the baseline case of the single-disk rotor model as discussed in Chapter VI. The XLTRC^{TM} simulations of the rotor model shown in Fig.C2 show that this model is more unstable as compared to the baseline model (with disk at the centre). That is, using a smaller direct moment damping coefficient (around 6500 lb-in-s) yields the threshold speed of instability which is slightly smaller than the threshold speed of the baseline model (5800 rpm). The simulated first critical speed of the model in Fig.C2 is about 4200 rpm. The increase in the first critical speed is an indication of

stiffening of the rotor-bearing system in Fig.C2 as compared to the baseline case (for which the first critical speed is 3000 rpm). The increase in the first critical speed can be explained by the effect of moving the disk away from the centre. When the disk is not at the centre, the modal mass involved in the first mode of vibration is decreased and therefore the first critical speed is increased. The higher instability can be explained by the free-free experimental testing of the single-disk rotor as presented in Appendix B. The farther is the friction producing interface from the centre, the more slipping will occur at the sleeve-shaft interface, resulting in large internal moments and accordingly higher instability.

3. Disk at mid-span, axial thickness of disk = 2.5 inches

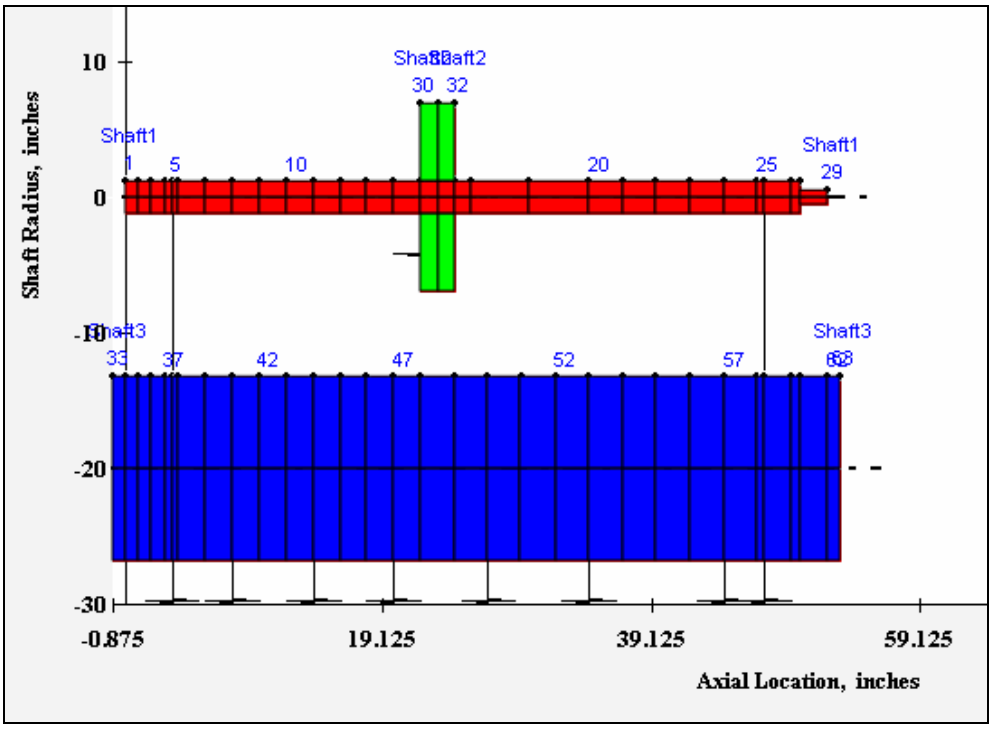

Fig.C3 Single-disk rotor model with axial width of disk = 2.5 inches

The single-disk rotor model with reduced axial width of the disk (2.5 inches, as compared to 5 inches for the baseline case) and higher outside diameter to keep the weight of the disk the same as the baseline case. The XLTRC^{TM} simulations of the rotor model show the first critical speed to be 3000 rpm, which is the same as for the baseline case. This is to be expected, because the weight of the disk as well its axial location relative to the shaft is unchanged. However, the rotor model is more stable as compared to the baseline case. The model requires a higher direct moment damping coefficient to predict the same threshold speed of instability as compared to the baseline case. This can be explained in view of experiments conducted on the single-disk rotor as described in Appendix B. The closer the friction interface is to the shaft centre, the lesser is the amount of modal damping. Therefore, the rotor will be more stable in this configuration, with a smaller direct moment damping coefficient as compared to the baseline case.

4. Disk at mid-span, axial thickness of disk = 1 inch

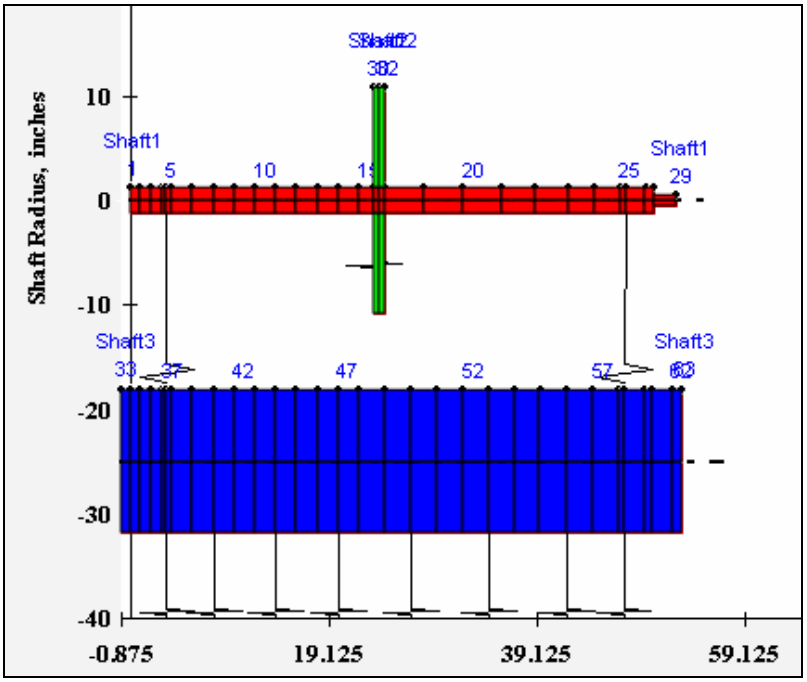

Fig.C4 Single-disk rotor model with axial width of disk = 1 inch

The single-disk rotor model with the disk axial width reduced to 1 inch (as compared to the baseline case of 5 inches) with the same weight of the disk as the baseline case is shown in Fig.C4. The simulations of the rotor model using the XLTRC^{TM} software show that the first critical speed of the rotor is around 2700 rpm, which is close to the first critical speed of the baseline case. The slight difference in the first critical speed of the baseline model and the model in Fig.C4 arises due to some stiffening effect of the baseline model due to its larger axial width (5 inches).Due to its larger axial span, the disk in the baseline model increase the effective shaft stiffness. The model in Fig.C4 can be called as an extended Jeffcott rotor model. The XLTRC^{TM} simulations show that this rotor model is more stable as compared to the baseline single-

disk model, with a higher amount of direct moment damping coefficient required to predict the same threshold speed of instability as the baseline case.

5. Disk at mid-span, axial width of disk = 10 inches

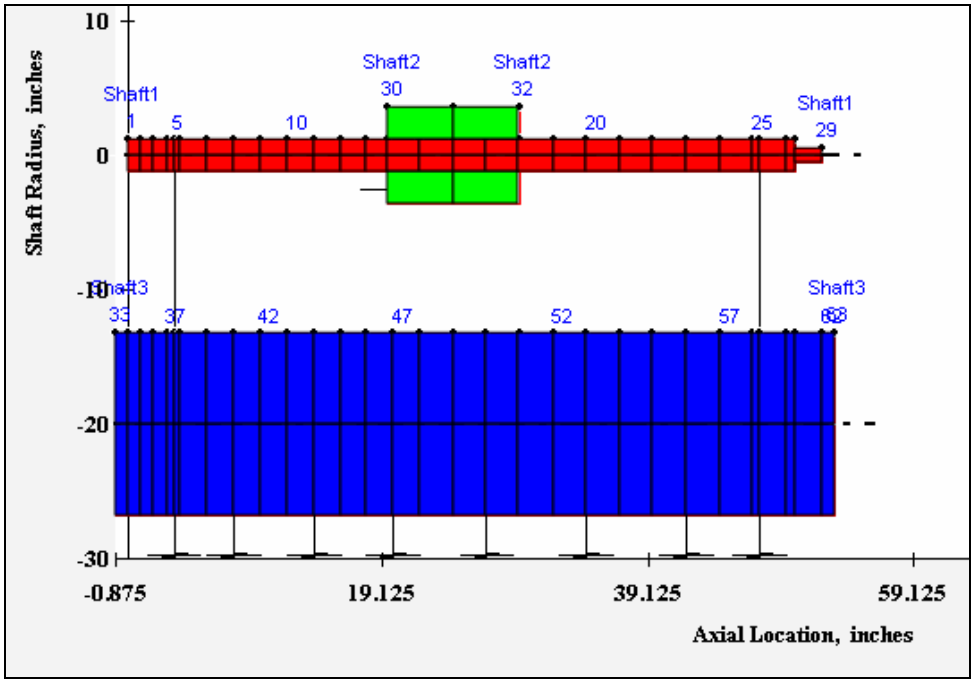

Fig.C5 Single-disk rotor model with disk axial width = 10 inches

The single-disk rotor model with the disk at mid-span of the shaft and axial width increased to 10 inches (instead of the baseline case of 5 inches) with the same weight as the baseline model disk is shown in Fig.C5. The XLTRC^{TM} simulations of the rotor model show that the first critical speed is 3600 rpm, as compared to the baseline case of

3000 rpm. The increase in the first critical speed can be attributed to the increase in stiffness of the rotor due to axial width of the disk. The disk's bending stiffness contributes to the overall increase of stiffness of the rotor. Therefore, even though the weight of the disk and the shaft are the same as the baseline case, the bending stiffness of the disk contributes to the overall stiffening of the rotor. The XLTRC^{TM} simulations show that the model shown in Fig.C5 is more unstable as compared to the baseline model. This can again be explained in view of the free-free experiments on the single-disk rotor as explained in Appendix B. Due to larger axial span of the disk, the friction interface is farther away from the centre of the shaft, resulting in larger slip and larger friction moments. Even though increasing the axial width of the disk stiffens the rotor, it also results in larger friction in the system, resulting in a more unstable system.

6. Disk at mid-span, axial width of disk = 15 inches

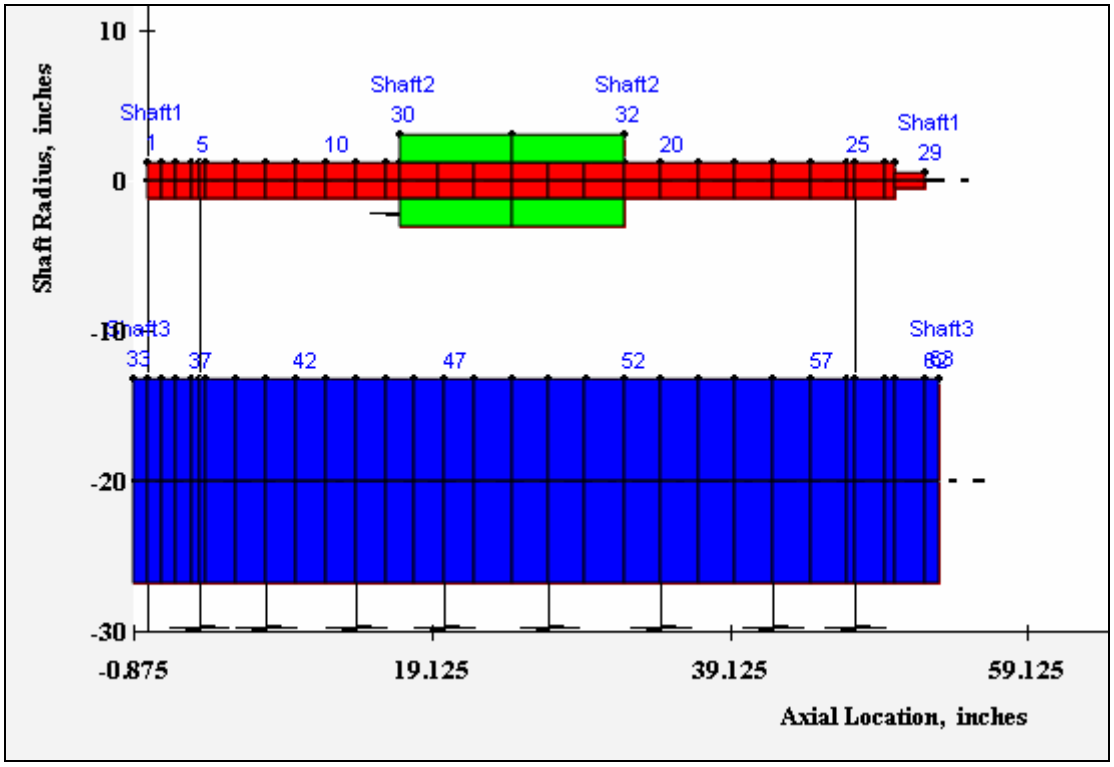

Fig.C6 Single-disk rotor model with disk axial width = 15 inches

The single-disk rotor model with axial width of the disk increased to 15 inches, while having the same weight as the baseline rotor model, is shown in Fig.C6. The disk is in this model is more of a sleeve than a disk due to its larger axial span. It can be expected that the increased axial width will increase the stiffness of the system, resulting in larger first critical speed. This conclusion is verified by simulations using XLTRC^{TM}. The simulations show that the first critical speed of the rotor is 4200 rpm, as compared to 3000 rpm for the baseline case. The increase in the stiffness of the rotor is due to the contribution of bending stiffness of the disk, which behaves more like a sleeve in this

model. In the baseline rotor case, since the axial span of the disk is smaller (5 inches as compared to 15 inches for this rotor model), it affects the mode shape of the rotor by forcing it to remain more flat for the portion of the shaft inside the disk, thereby stiffening the rotor and consequently, increasing the first critical speed.

Although the stiffness of the rotor system is increased, the system is more unstable as compared to the baseline case. This can again be explained in light of the experiments presented in Appendix B. Since the friction interface is further away from the centre of the shaft, more slipping will take place as compared to when it is near the centre of the shaft. As a result, the rotor will be more unstable for larger axial width of the disk.

7. Disk at mid-span; disk made of aluminum

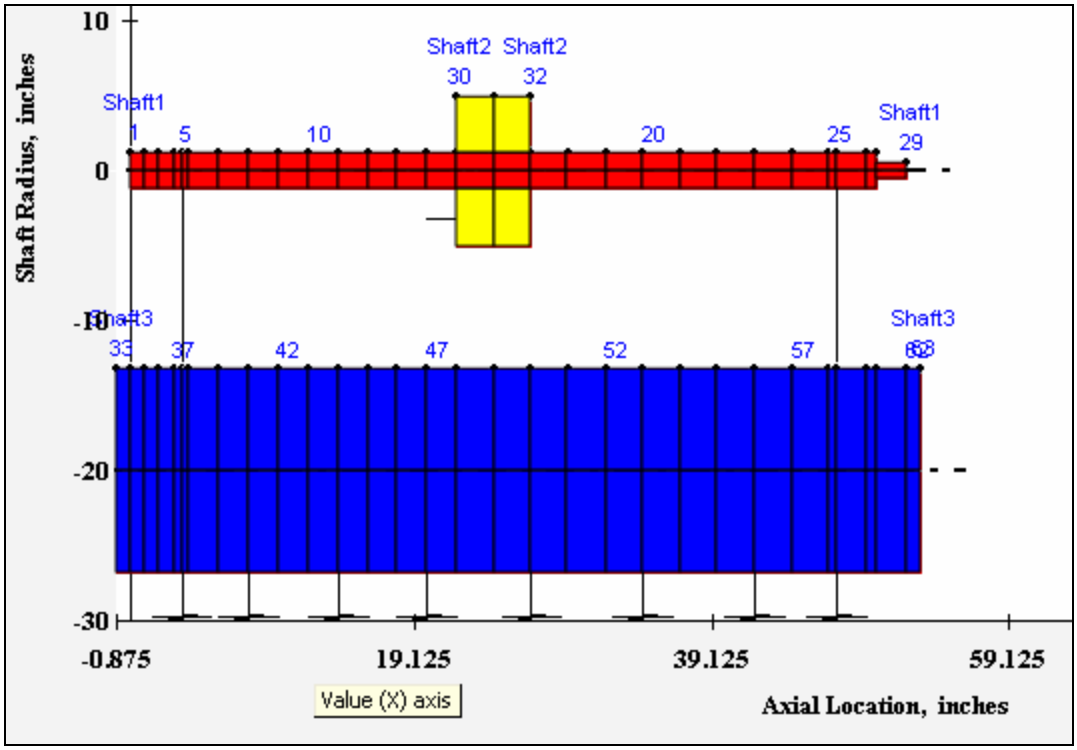

Fig.C7 Single-disk rotor model with disk at mid-span and aluminum as disk material

The single-disk rotor model with the disk at mid-span of the shaft is shown in Fig.C7. This rotor is the same as the baseline model except that the material of the disk is aluminum instead of steel. It can be expected that the rotor-bearing system will have a higher natural frequency and a higher first critical speed as compared to the baseline case due to decreased modal mass of the system, which mainly comes from the disk in the baseline case. The modal mass is reduced in the model shown in Fig.C7 because the disk is made of aluminum which has a weight density almost 33% of the weight density of steel. The simulations using XLTRC^{TM} software verify this conclusion. The predicted

first critical speed of the rotor model is around 4200 rpm as compared to 3000 rpm for the baseline case. The simulations show further that the system is marginally more stable as compared to the baseline case. A higher amount of direct moment damping coefficient as compared to the baseline case is required to predict the threshold speed of instability around 5800 rpm, which is the threshold speed of instability for the baseline case. The increased stability can be explained by considering the increase in the first critical speed of the rotor model. Even though the first critical speed is increased due to reduced modal mass of the rotor, the bending stiffness of the rotor is not increased as compared to the baseline model. Furthermore, the friction interface is still close to the centre of the shaft as in the baseline case. These factors combine to make the rotor model in Fig.C7 more stable as compared to the baseline case.

8. Disk at mid-span; disk and shaft made of aluminum

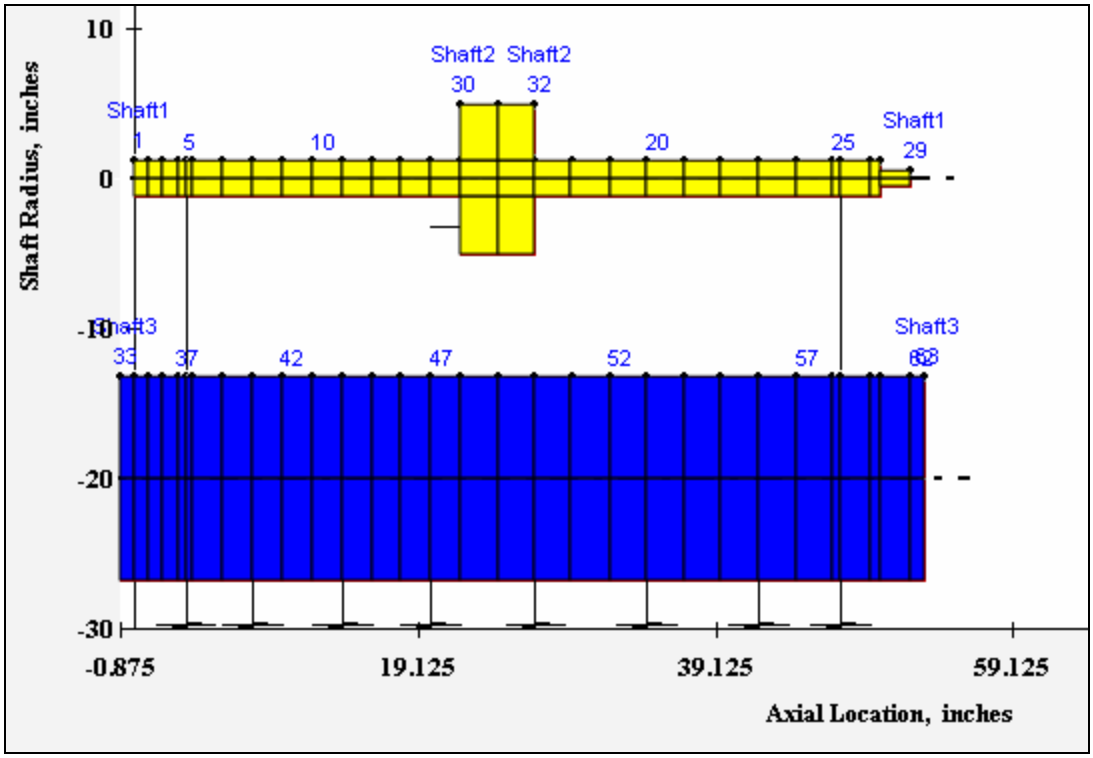

Fig.C8 Single-disk rotor with disk at the mid-span; disk and shaft made of aluminum

The single-disk rotor model with disk and rotor shaft both made of aluminum is shown in Fig.C8. The other geometric and foundation properties are the same as in the baseline case. The XLTRC^{TM} simulations of the rotor model shown in Fig.C8 show that the first critical speed of the rotor is 3000 rpm. The rotor model is more unstable as compared to the baseline case as well as the case 7 discussed. This can be explained through the material elastic properties. Since the material of the shaft and the disk is made of aluminum, the modulus of elasticity of the rotor is about 33% of the modulus of elasticity of steel. Even though the modal mass of the rotor is decreased due to reduced

weight of the shaft and the disk, the stiffness of the system is also decreased because aluminum is nearly 3 times more flexible as compared to steel. As a result, the effects of decrease in stiffness and the decrease in mass cancel each other out, and the resulting first critical speed of the rotor is the same as for the baseline case, which is 3000 rpm. The higher instability of the rotor model can be explained by considering the shaft material. The aluminum shaft in model of Fig.C8 will bend more easily under the influence of internal friction moments as compared to the steel shaft for the baseline case. This is due to lower elastic modulus of the aluminum material. Therefore, the system will be more unstable as compared to the baseline case.

9. Disk at mid-span; shaft made of aluminum

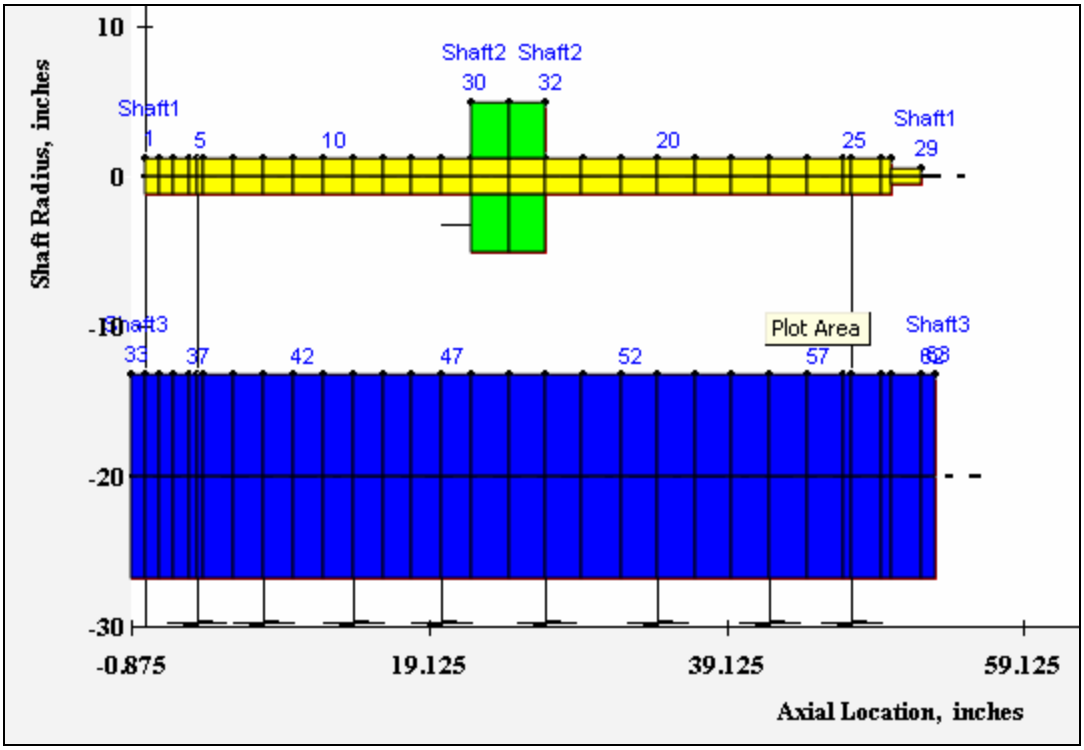

Fig.C9 Single-disk rotor model with steel disk at mid-span and shaft made of aluminum

The single-disk rotor model with the disk at the mid-span of the shaft is shown in Fig.C9. In this rotor model, the material of the disk is steel, whereas the material of the shaft is aluminum. The XLTRC^{TM} simulations of the rotor model shown in Fig.C9 show that the first critical speed of the rotor is 2000 rpm, as compared to 3000 rpm for the baseline case. The simulations also show that the rotor is more unstable as compared to the baseline case. The simulation results can be explained by considering the material elastic properties for the shaft and weight of the disk. In the model shown in Fig.C9, even though the weight of the disk remains the same as for the baseline case, the stiffness of the rotor is about 33% of the baseline case due to aluminum material for the shaft. Thus the stiffness is reduced whereas the modal mass remains almost the same. This explains the decrease in the first critical speed of the rotor. The higher instability of the rotor model can be explained by considering the flexibility of the shaft. The aluminum shaft for the rotor model in Fig.C9 will bend more easily under the action of internal friction moments, causing the system to be more unstable.

10. Disk axial width= 15 inches; disk at mid-span, shaft diameter at centre = 1.5 inches

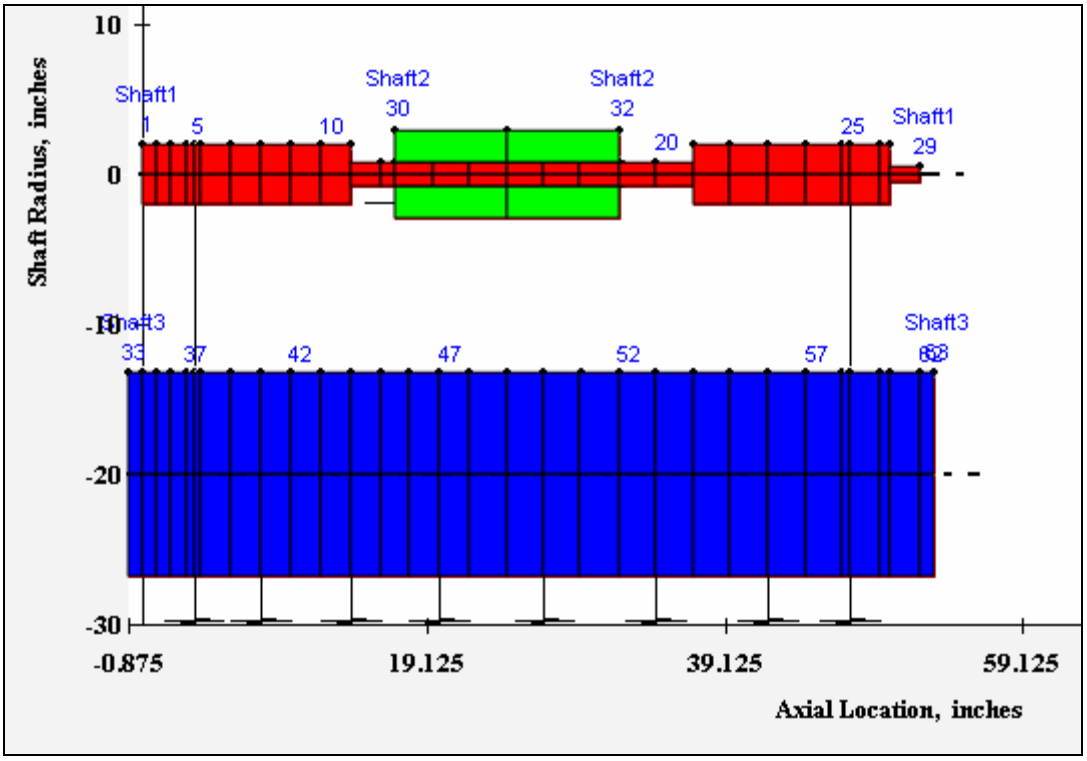

Fig.C10 Single-disk rotor with stepped shaft and disk axial width = 15 inches

The single-disk rotor model with the disk axial width of 15 inches and a stepped steel shaft is shown in Fig.C10. The diameter of the shaft at the central portion is 1.5 inches, whereas the diameter at the end portions is 4 inches. This geometry of the shaft is widely different from the geometry of the baseline case. The outside diameter of the disk is such that the weight of the disk in rotor model shown in Fig.C10 is equal to the baseline case. The material of the disk and shaft is steel. The XLTRC^{TM} simulations show that the first critical speed of the rotor is 2000 rpm. The simulations also show that

the rotor is more unstable as compared to the baseline case. This is due to a thinner shaft section in the central portion of the shaft. Since the internal friction moment is applied at the interface between the disk and the central section of the shaft (between points 13 and 30), the steel shaft bends relatively more under the action of internal moments as compared to the shaft with a diameter of 2.5 inches. The bending stiffness is proportional to the fourth power of diameter; reducing the diameter of the central section from 2.5 inches to 1.5 inches increases the flexibility of the shaft and therefore the rotor model is more unstable as compared to the baseline case.

11. Disk axial width= 15 inches; disk at mid-span, shaft diameter at centre = 2.5 inches

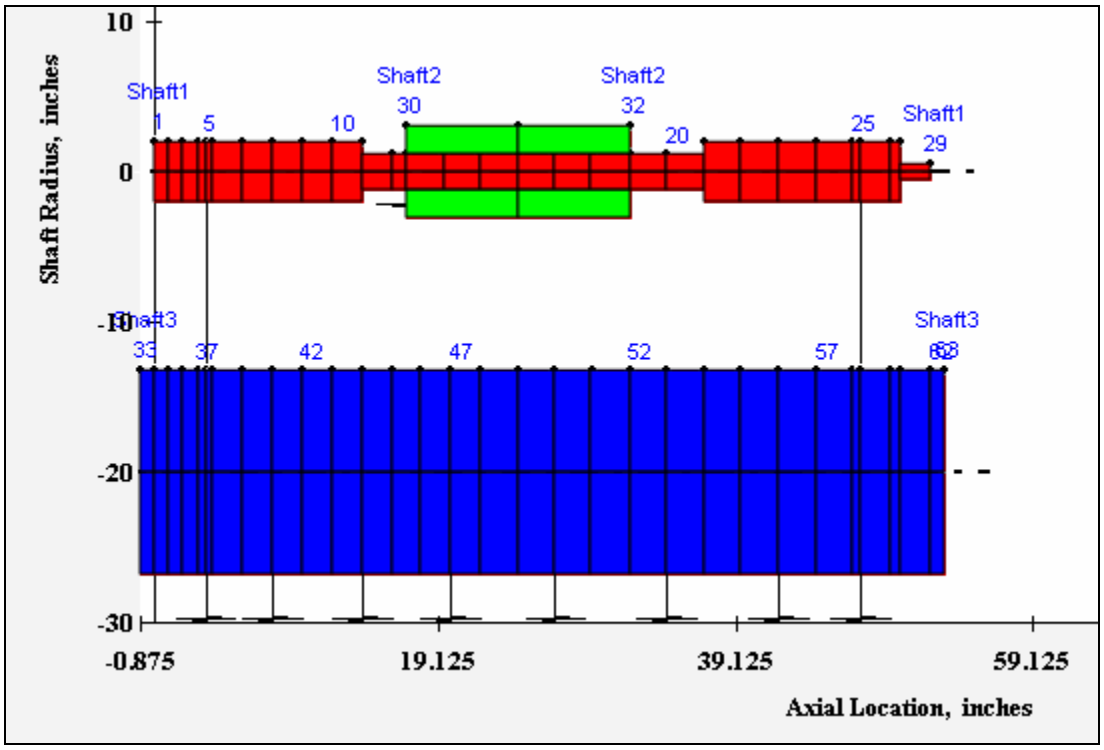

Fig.C11 Single-disk rotor with stepped shaft and shaft diameter = 2.5 inches at centre

The single-disk rotor model shown in Fig.C11 has stepped steel shaft with 4 inches and 2.5 inches diameter. The disk is 15 inches long, with the weight of the disk the same as in the baseline case. The model in Fig.C11 is similar to the model in Fig.C10, except that the central shaft diameter is 2.5 inches. The XLTRC^{TM} simulations show that the first critical speed of the rotor is 4500 rpm. The increase in the first critical speed is due to stiffening effects of the disk and the 4 inch diameter sections of the steel shaft. The simulations further show that the rotor is more unstable as compared to the baseline case. This is due to the larger axial width of the disk, resulting in larger slip at the friction interface. In addition, between the 4 inch diameter shaft section and the 2.5 inch diameter section there is more difference in slope of the mode shape of the rotor in its first mode. The two factors combine to produce more slip at the friction interface, resulting in larger magnitude of the internal moments and correspondingly larger instability of the rotor.

12. Disk axial width= 15 inches; disk at mid-span, shaft diameter = 4 inches

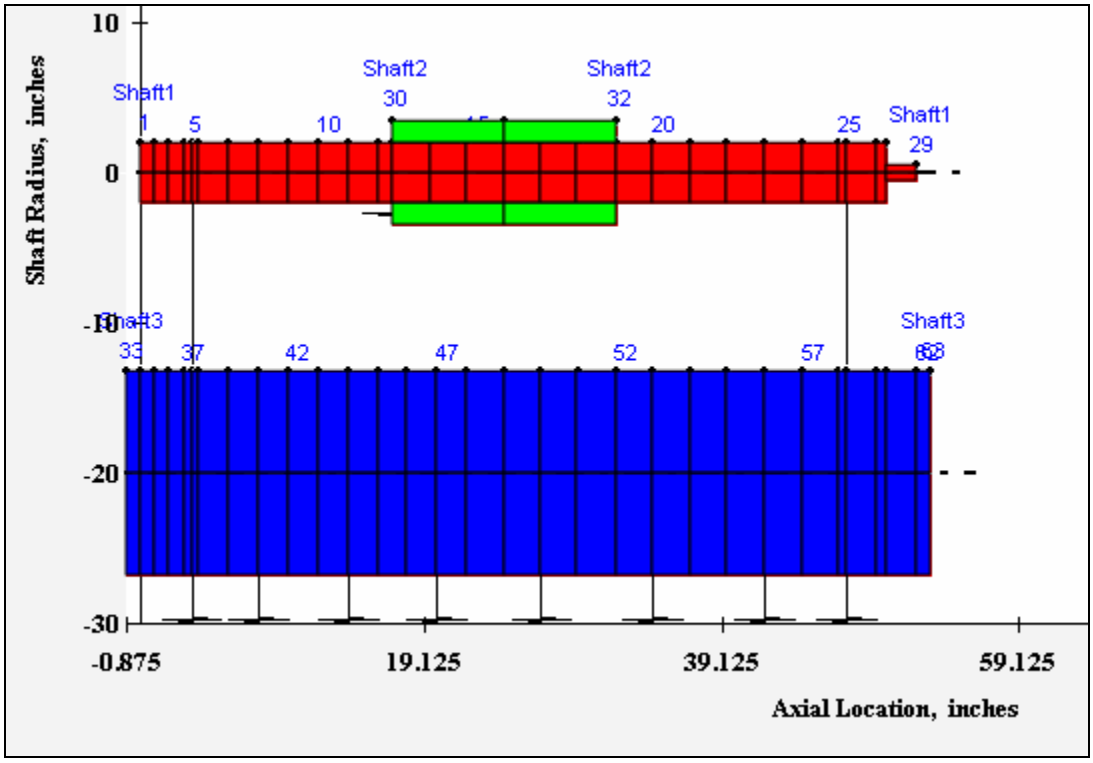

Fig.C12 Single-disk rotor with shaft diameter = 4 inches

The single-disk rotor shown in Fig.C12 has the disk at the mid-span of the shaft. The weight of the disk is the same as in the baseline model; however, the diameter of the rotor shaft is increased to 4 inches. The simulations using XLTRC^{TM} show that the rotor is stable in the speed range of 0-12000 rpm. The simulated first critical speed of the rotor is 6600 rpm in the vertical direction (Y direction) and 5100 rpm in the horizontal direction (X direction). The simulation shows that the rotor-bearing system will gain stability against the destabilizing effects of internal friction due to shrink fits if the

diameter of the shaft is increased. This can be explained by considering the action of internal friction moments on the bending of the shaft. As the shaft diameter is increased, the shaft bending stiffness is increased and therefore it requires a larger magnitude of internal friction moments to bend the shaft. If the internal moments are not large enough in magnitude, the shaft will not bend in the direction of forward whirl above the first critical speed under the action of internal friction moments, resulting in stability of the rotor-bearing system.

TWO-DISK ROTOR SIMULATIONS

Before describing the imagined two-disk rotor configurations, an experimental configuration from reference **[13]** is described and its rotordynamic simulation using the XLTRC^{TM} software is discussed.

1. Vance-Ying rotor

This rotor was constructed by some modifications made to a Bently rotor kit **[13]**. The test rotor consisted of an aluminum sleeve, which was 7.5 inches long with 2.988 inches inside diameter, and 1/8 in. thick. Two identical disks of 2.975 inches outside diameter and ¾ in. thick were mounted on a thin steel shaft 3/8 in. in diameter. The shaft was simply supported in two ball bearings (FAFNIR, model S3K).The distance between two ball bearings supports was 16 inches. A set of orthogonal proximity probes (X and Y) was mounted close to the left disk to measure the rotor vibration. A feedback controlled motor was used to run the rotor to speeds above 10,000 rpm.

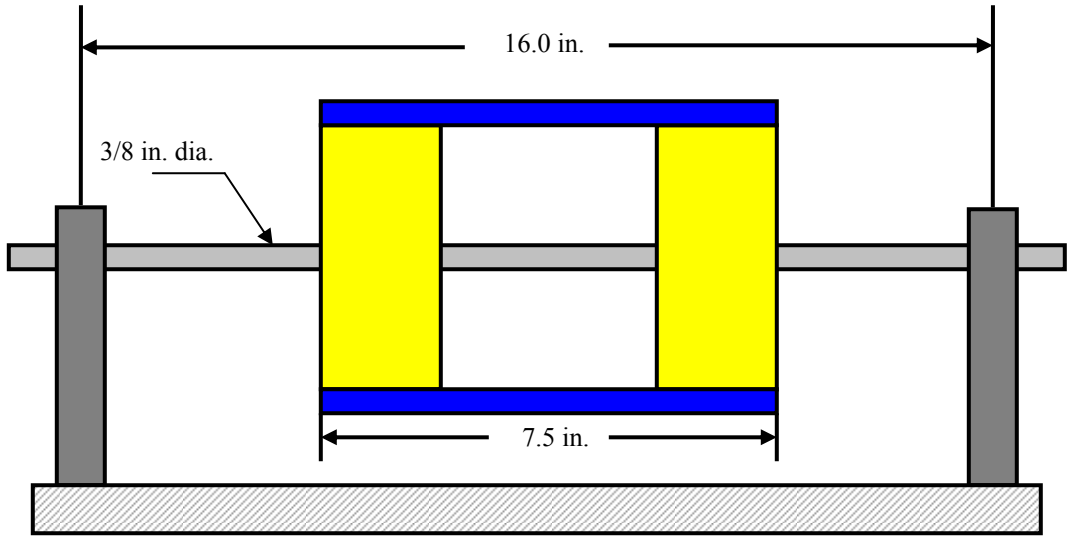

Fig. C13 Sketch of Vance-Ying rotor with sleeve and shaft dimensions indicated

In this rotor, the weight of the individual parts, based on approximate calculation from the values of dimensions of the parts, can be presented as follows:

(a) Disks: 2.90 lb for both disks
(b) Shaft: 0.50 lb
(c) Sleeve weight: 0.91 lb

As reported in **[13]**, the rotor's natural frequency (on bearings) was measured before and after the aluminum sleeve was mounted on the wheels. It was found out that the rotor's natural frequency in the X direction did not change much (45 Hz without sleeve as compared to 46.3 Hz with sleeve), but the natural frequency in the Y direction was increased by 5.6 Hz when the sleeve was put on (45 Hz without sleeve as compared to 50.6 Hz with sleeve). This indicates that the stiffness of the sleeve has a stronger effect on the natural frequency than the mass of the sleeve. This can be further explained by observing the mass of each component of the rotor. Since the sleeve mass is 0.91 lb, whereas the disks contribute 2.90 lb to the total rotor mass, therefore the disks masses are the main factor for determining the natural frequency. On the other hand, the sleeve has some thickness, which adds to the bending stiffness of the rotor. However, at the same time, this bending stiffness will be offset, to some extent, by almost 1 lb weight contribution (0.91 lb weight of the sleeve). If the shaft were heavier and made of larger diameter, than the increase in natural frequency would be higher with addition of the sleeve, due to increased bending stiffness of the sleeve, but not much substantial contribution from the weight of the sleeve. The model of Vance-Ying rotor analyzed using the XLTRC^{TM} software is shown in Fig.C14:

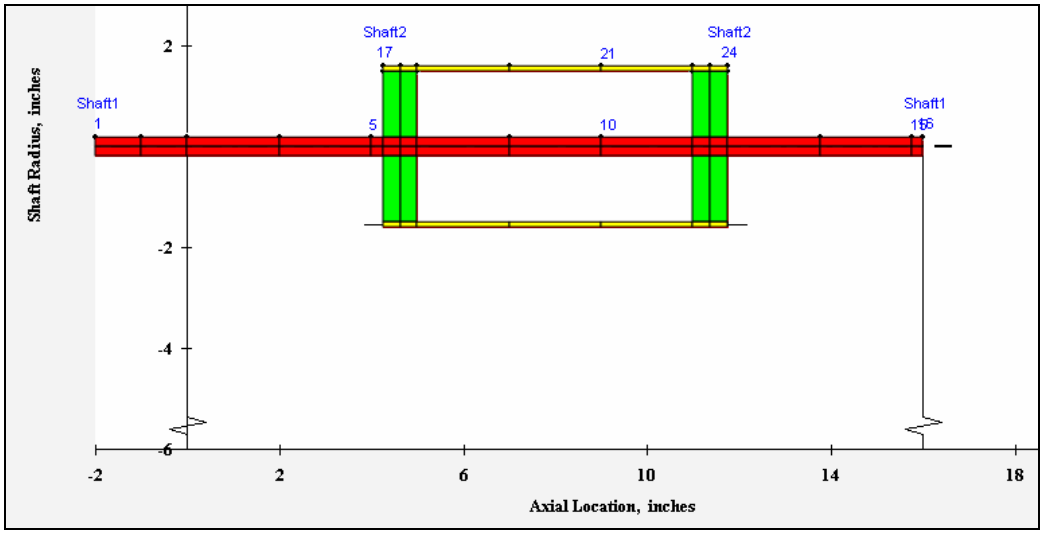

Fig.C14 XLTRC^{TM} model of Vance-Ying rotor

Simulation of the rotor shows that with symmetric fits (same internal moments at both interfaces), the rotor is unstable with substantially lower magnitudes of cross-coupled internal moments as compared to the case of experimental two-disk or single-disk rotor. This is most likely due to thin flexible rotor shaft. The more flexible the shaft is, the more likely it is to bend under the action of smaller internal friction moments developed at the interfaces. With selected internal moment parameters, the predicted first critical speed is 3000 rpm and the onset speed of instability is also 3000 rpm, with instability frequency around 2700 cpm and increasing to 2900 cpm at higher speeds.

2. Sleeve outside diameter = 10 inches; central shaft diameter = 3 inches

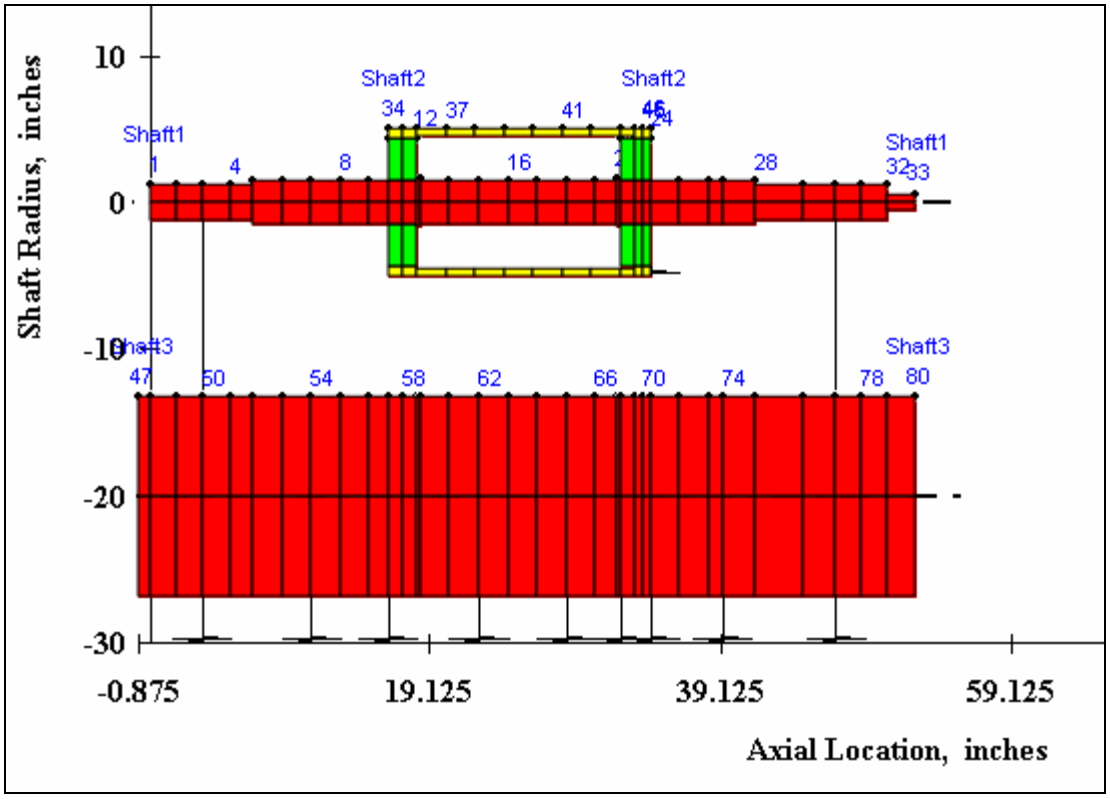

Fig.C15 Two-disk rotor model with diameter of central portion of shaft = 3 inches

The two-disk rotor model shown in Fig.C15 has the diameter of the central portion of the shaft as 3 inches, as compared to the experimental case, in which the diameter of the central portion of the shaft (inside the aluminum sleeve) is 2 inches. The rotor is modeled as having a tight interference fit at one interface (points 10-34,12-36) with no cross-coupled moments and an under-cut loose fit with cross-coupled moments at the other interface (points 22-44, 24-46), just as in the baseline model for the experimental configuration. The rotordynamic simulations using the XLTRC^{TM} software

show that the rotor is stable in the speed range of 0-12000 rpm. The stability is a result of increase in the shaft diameter of the shaft, that makes the bending stiffness of the rotor to increase and therefore the internal friction moments are not large enough to bend the shaft and induce instability in the rotor-bearing system.

3. Sleeve outside diameter = 10 inches; central shaft diameter = 4 inches

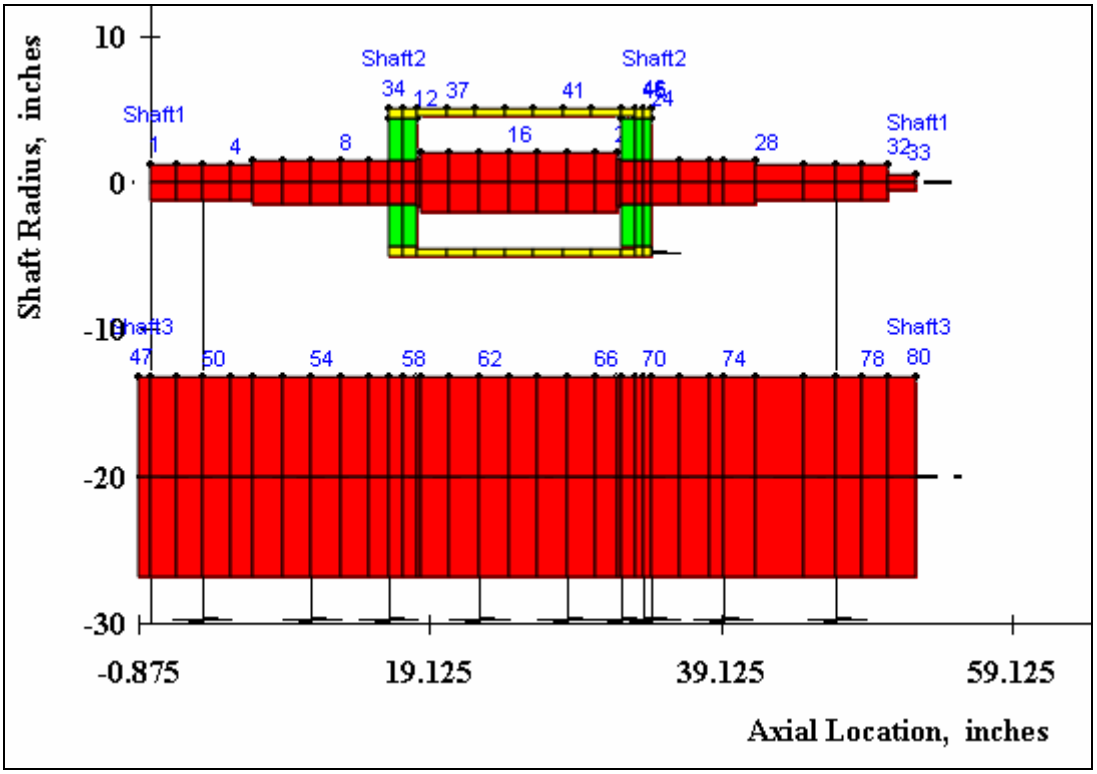

Fig.C16 Two-disk rotor model with diameter of central portion of shaft = 4 inches

The model shown in Fig.C16 is similar to that in Fig.C15, except that the shaft diameter has been further increased to 4 inches in the central portion. The simulations

using the XLTRC^{TM} software show that the rotor is completely stable in the speed range of 0-12000 rpm. This shows that increasing the shaft diameter is one of the most effective ways to increase dynamic stability of the rotor-bearing systems against the effects of internal friction.

4. Shaft length = 60 inches; sleeve length same

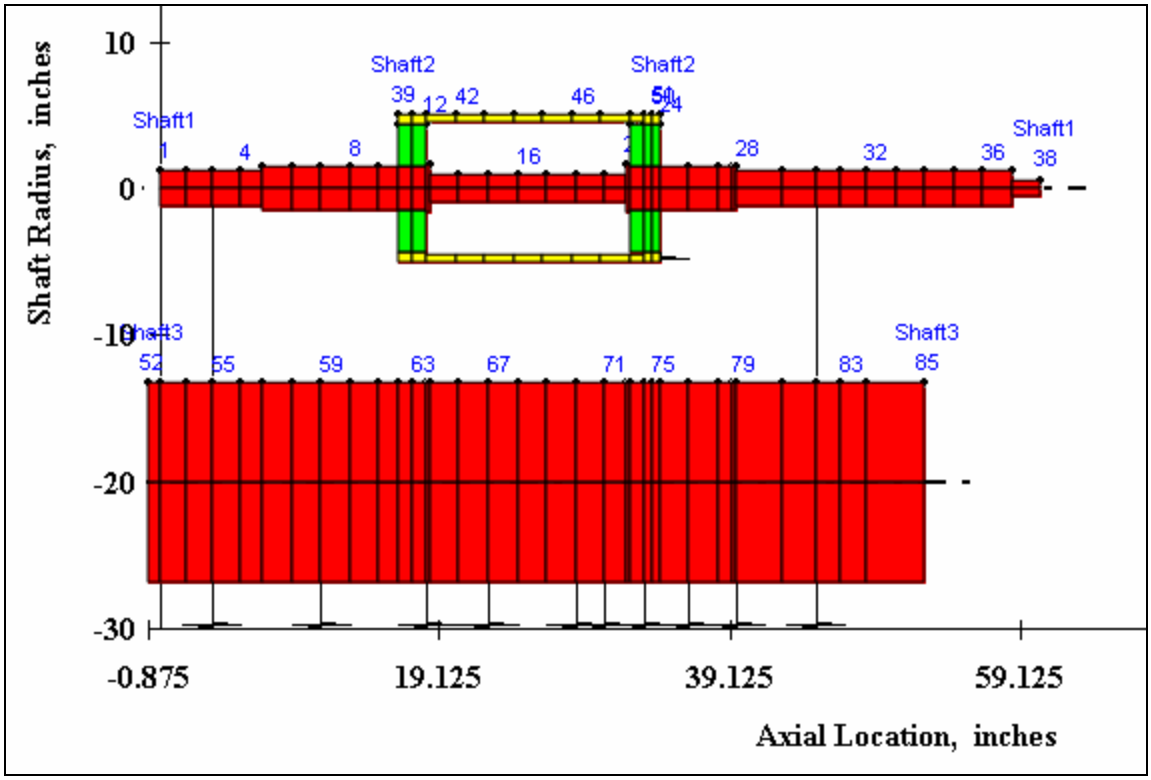

Fig.C17 Two-disk rotor model with increased shaft length (increased by 8 inches)

The model shown in Fig.C17 has an increased shaft length as compared to the baseline model. The length of the shaft is 60 inches whereas in the baseline model, the

shaft length is 52.5 inches. The distance between the bearings (42 inches) is the same in the model shown in Fig.C17 as compared to the baseline case. The simulations using the XLTRC^{TM} software show that the rotor is more unstable as compared to the baseline case. This can be explained due to increase in the deflection of the shaft caused by the increase in its length. Under the action of internal friction moments, the bending of the shaft will increase more, giving rise to larger slip at the friction interface that will result in instability of the rotor.

5. Sleeve made of steel

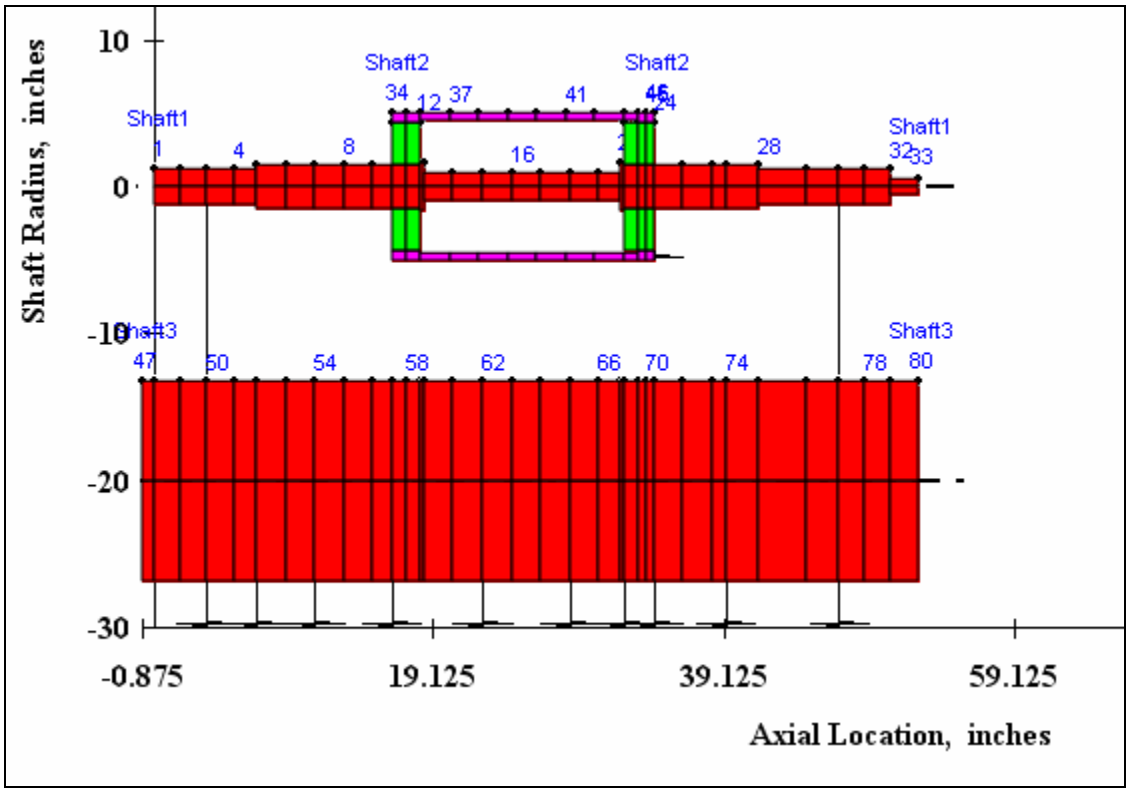

Fig.C18 Two-disk rotor model with sleeve made of steel

In the two-disk rotor model shown in Fig.C18, the rotor geometry and internal friction moments distribution is the same as in the baseline model, only the sleeve material is changed from aluminum to steel. The rotordynamic simulations using the XLTRC^{TM} software show that the rotor is more stable as compared to the baseline model, with the threshold speed of instability occurring at 11500 rpm, with the unstable mode frequency at 6034 cpm. The simulated first critical speed of the rotor is 6160 rpm. The increased stability of the rotor can be explained in terms of the stiffening effect caused by steel sleeve as compared to the aluminum sleeve in the baseline model. Steel is almost three times stiff as compared to aluminum; when the internal friction moments are applied to the rotor model, the moments required to bend the rotor in the direction of forward whirl will be higher as compared to the baseline model. This explains the increased stability of the rotor-bearing system shown in Fig.C18.

6. Sleeve length = 22 inches

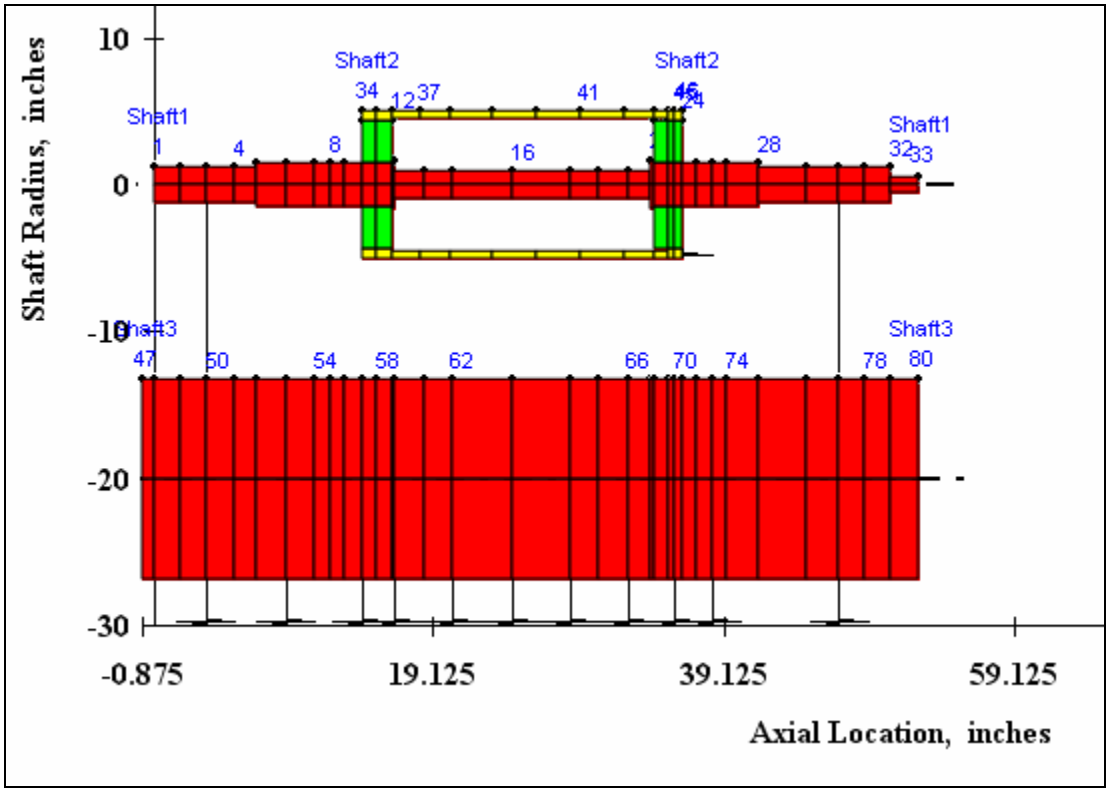

Fig.C19 Two-disk rotor with sleeve length = 22 inches

Fig.C19 shows a two-disk rotor model with the shaft length the same as in the baseline model (52.5 inches), but the sleeve length increased to 22 inches as compared to 18 inches in the baseline model. The lengths of other portions of the shaft are accordingly adjusted to make the total length equal to 52.5 inches. The distribution of the internal friction moments are the same as in the baseline model. The rotordynamic simulations using the XLTRC^{TM} software show that the rotor is slightly more unstable as compared to the baseline case. The increased instability can be explained by the effect of

flexibility caused by the central portion of the shaft which is inside the sleeve. The central portion of the shaft which has a diameter of 2 inches can bend slightly more under the action of internal friction moments as compared to the baseline model. The simulated first critical speed of the rotor is 7100 rpm, and the predicted threshold speed of instability is 8500 rpm with the frequency of unstable mode as 7062 cpm.

7. Sleeve length = 10 inches

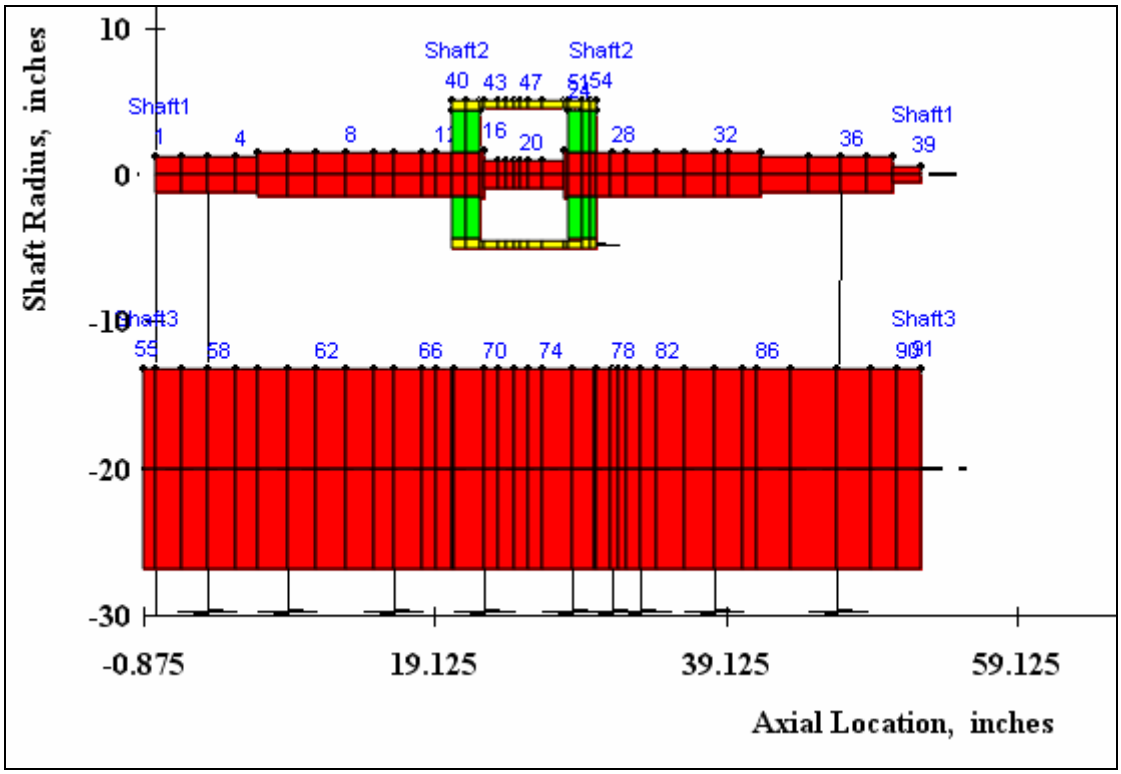

Fig.C20 Two-disk rotor with sleeve length = 10 inches

Fig.C20 shows a two-disk rotor model with the sleeve length reduced to 10 inches as compared to 18 inches in the baseline model. The total shaft length is the same as the baseline case (52.5 inches) and the distribution of internal friction moments is also the same as in the baseline model (tight fit at one interface with no cross-coupling; loose fit with substantial magnitude of cross-coupling at the other end). The rotordynamic simulations using the XLTRC^{TM} software show that the threshold speed of instability is 10500 rpm. The first critical speed of the rotor model is 5500 rpm. The stability of the rotor model in Fig.C20 as compared to the instability of the baseline model can be explained by considering the stiffening of the rotor due to decrease in length of the sleeve and central portion of the shaft. Decreasing the length of the central portion of the shaft (which has a diameter of 2 inches) results in decrease in bending deflection of the rotor under the action of internal friction moments at the interface. The rotor model is therefore more stable since the shaft will not bend in the direction of forward whirl under the action of internal moments. This rotor model shows that the effect of decreasing the central portion of the shaft is just opposite for the previous rotor model case (case 7, in which the sleeve length is increased from 18 inches to 22 inches).

8. Outside diameter of disks = 12 inches

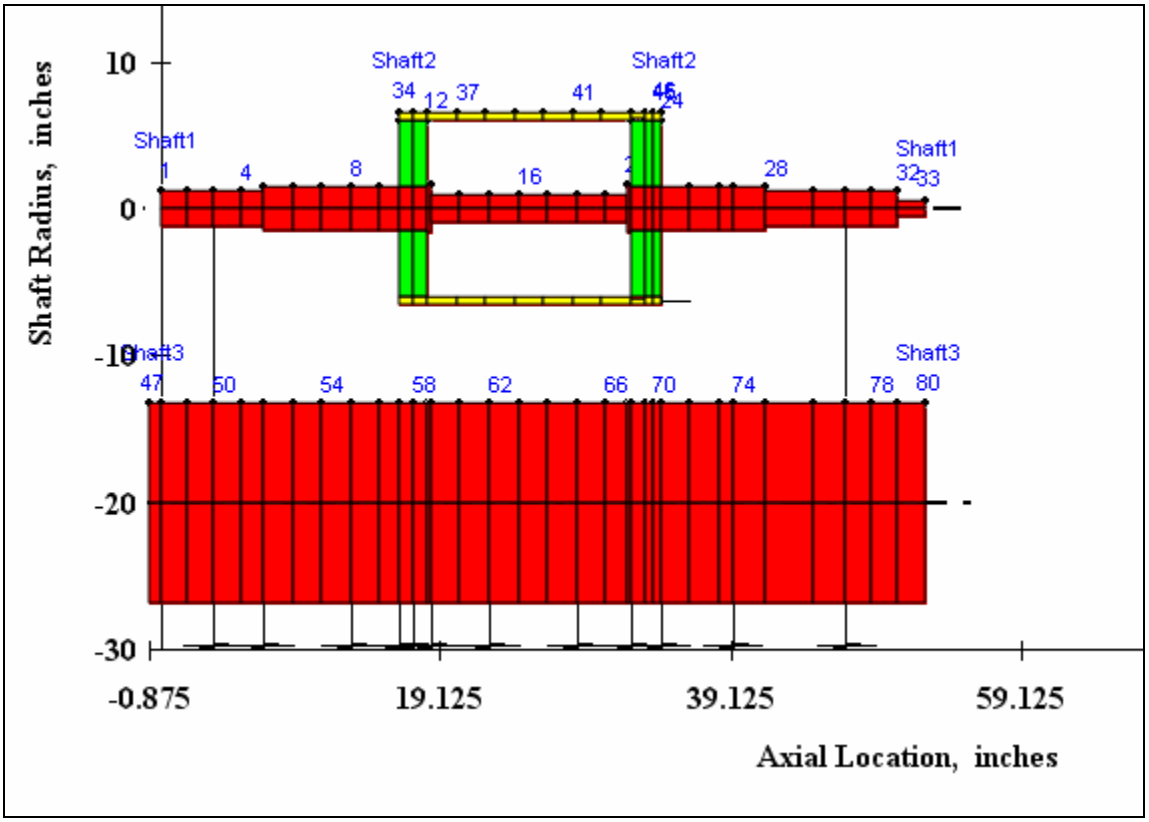

Fig.C21 Two-disk rotor model with increased outside diameter of disks

Fig.C21 shows a two-disk rotor model with the diameters of the disks increased from 9 inches to 12 inches. The thickness of the aluminum sleeve is 0.5 inches, the same as in the baseline model. The remaining geometry and material properties are the same as the baseline model. The internal friction moments are applied at one sleeve-disk interface with cross-coupling, whereas the other interface has internal moment coefficients with no cross-coupling. The simulations using the XLTRC^{TM} show that the

rotor is more unstable as compared to the baseline rotor model. The first critical speed of the rotor is 5700 rpm. The threshold speed of instability of the rotor is 7000 rpm at 5650 cpm. The increased instability of the rotor model as compared to the baseline model can be explained by increase in the diameter of the disks. As the disk diameter is increased, the bending stiffness of the aluminum sleeve increases. Due to increase in bending stiffness, larger slip is developed at the sleeve-disk interface because the sleeve is much more stiff as compared to the steel shaft, that now carries a larger weight of the disks(due to increase in disk diameters). The larger slip gives rise to the larger internal friction moments, resulting in higher instability.

9. Outside diameter of disks = 20 inches

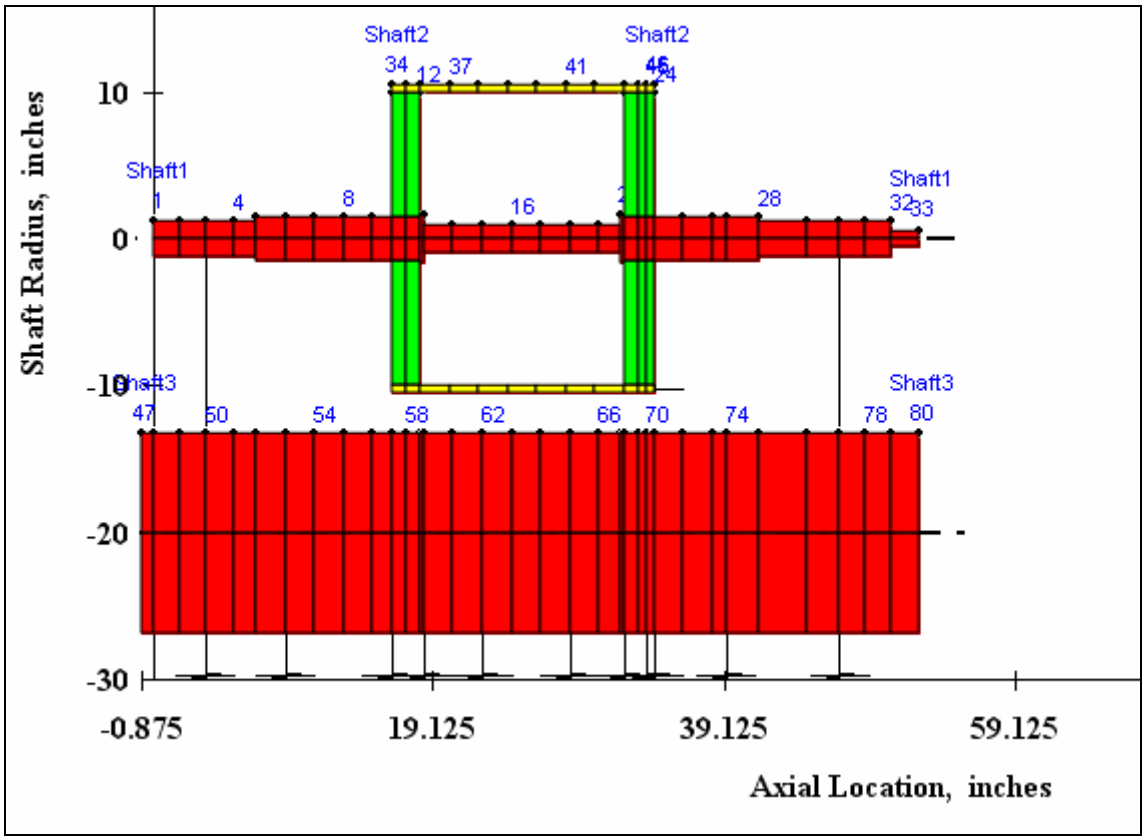

Fig.C22 Two-disk rotor model with increased outside diameter of disks

Fig.C22 shows a two-disk rotor model with outside diameter of the disks as 20 inches, whereas the thickness of the sleeve is 0.5 inches as in the baseline model. The simulations using the XLTRC^{TM} software show that the first critical speed of the rotor is 4000 rpm and the threshold speed of instability of the rotor is 6000 rpm. The increase of instability is explained by the larger bending stiffness of the sleeve and a larger slip developed at the shrink fit interface of the disk and the sleeve.

10. Disk axial width = 3 inches

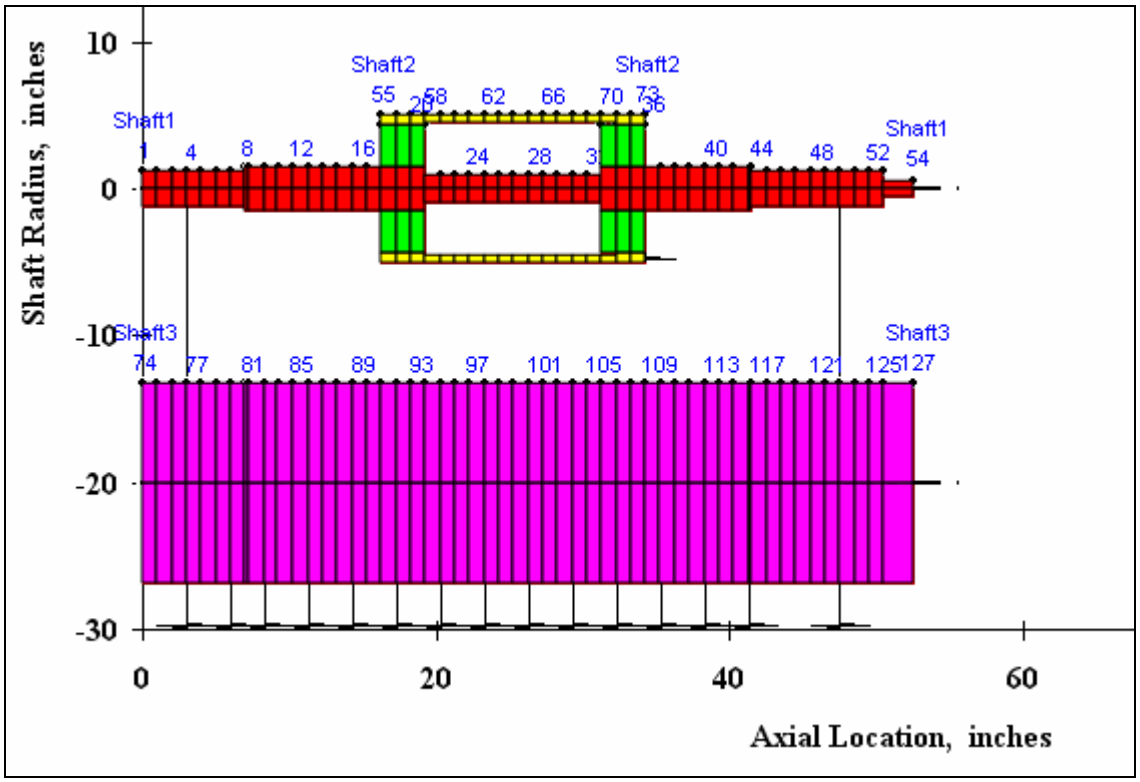

Fig.C23 Two-disk rotor model with disk axial width = 3 inches

Fig.C23 shows a two-disk rotor model with the axial width of the disks increased to 3 inches as compared to the baseline rotor model in which the axial width is 2 inches. The internal moments distribution is the same as in the baseline model. In the rotor model shown in Fig.C23, the axial contact between the sleeve and the disk at the interface where cross-coupled moment coefficients are applied is 2 inches. In the baseline rotor model, the axial contact length between the sleeve and the disk at the friction interface is 2 inches. The rotordynamic simulations using the XLTRC^{TM} software show that the the first critical speed of the rotor is 6040 rpm and the threshold speed of instability is 11500 rpm at a frequency 5927 cpm (unstable mode frequency). The increased stability of the rotor can be explained due to larger axial contact length at the friction interface. The larger the contact length is, the lesser is the amount of relative slip at the interface. A lesser amount of slip at the interface will result in smaller magnitude of the internal moments and consequently higher stability of the rotor.

APPENDIX D

FOUNDATION MODAL PARAMETERS AND BALL BEARING PARAMETERS

As described earlier, modal parameters of the foundation are estimated using impact and shaker tests on the foundation, with the rotor removed from the bearings while the measurements are conducted. In this way, only the foundation parameters are determined, which can then be inputted to a separate file linked to XLTRC^{TM} for performing the simulations of the rotor-bearing system using XLTRC^{TM}.

Both impact tests and shaker tests were performed in the horizontal direction, to check the results of those measurements against each other. In the vertical direction, only impact hammer tests were performed, since a shaker can not be used in this direction.

The impact hammer tests were conducted in the horizontal direction. It is usually the simplest method of modal testing requiring only an impact hammer and an accelerometer, along with a dynamic signal analyzer. The results are shown on the next page:

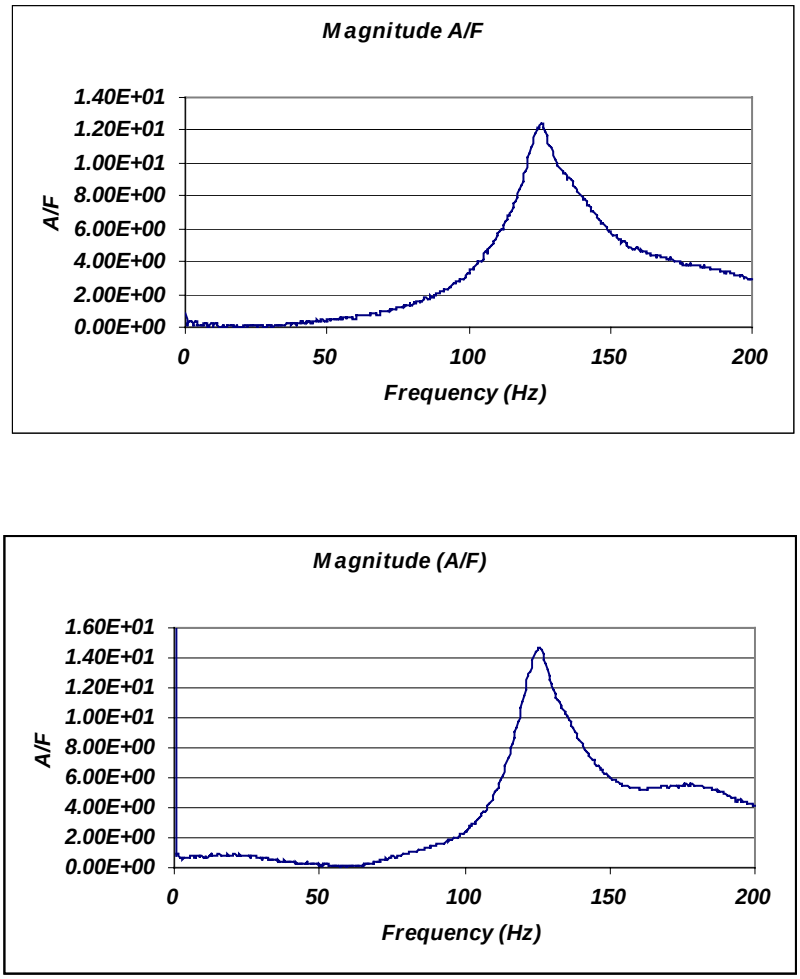

Fig. D1 Impact tests in horizontal direction

The shaker tests were also conducted in the horizontal direction to provide a check for the measurements using impact tests. A shaker was connected to the bearing housing using a small plate. On the opposite side of the bearing housing was placed a high sensitivity accelerometer. The data was collected on a dynamic signal analyzer and the results of acceleration to force ratio using several tests in horizontal direction in frequency domain are shown on the next page:

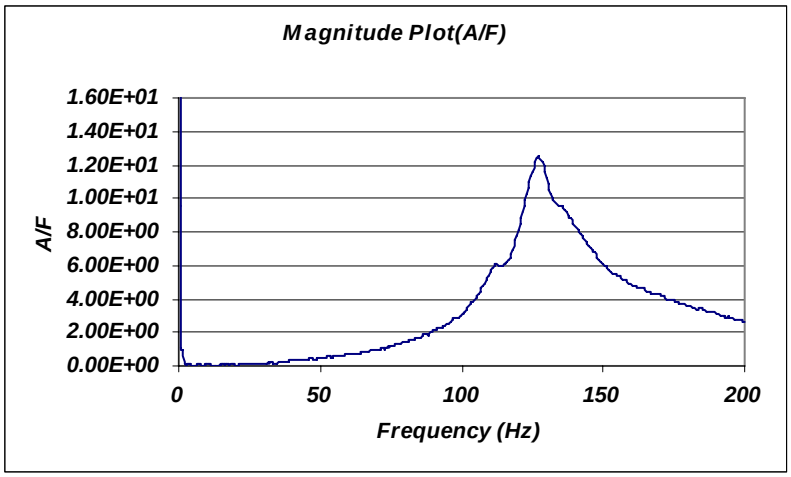

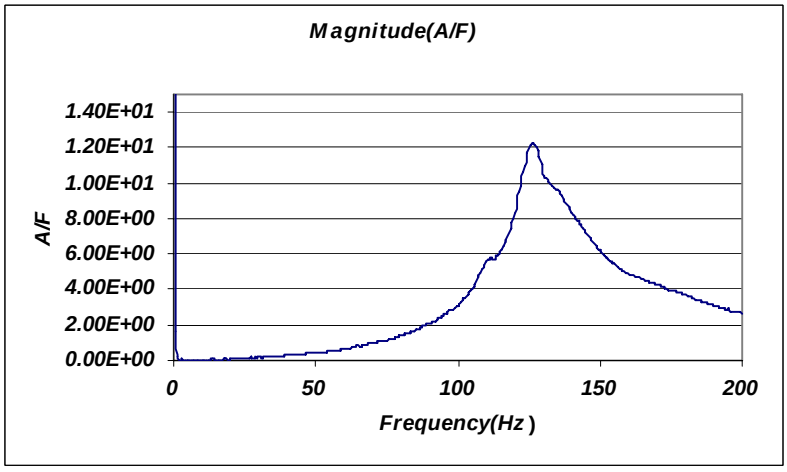

Fig. D2 Shaker test results for foundation in horizontal direction

As can be seen from the experimental data presented in Fig.D2 for two separate tests performed using the shaker, the horizontal natural frequency is around 125 Hz.

In a similar way, the impact hammer tests were conducted in the vertical direction and the following results for the ratio of acceleration to force are shown:

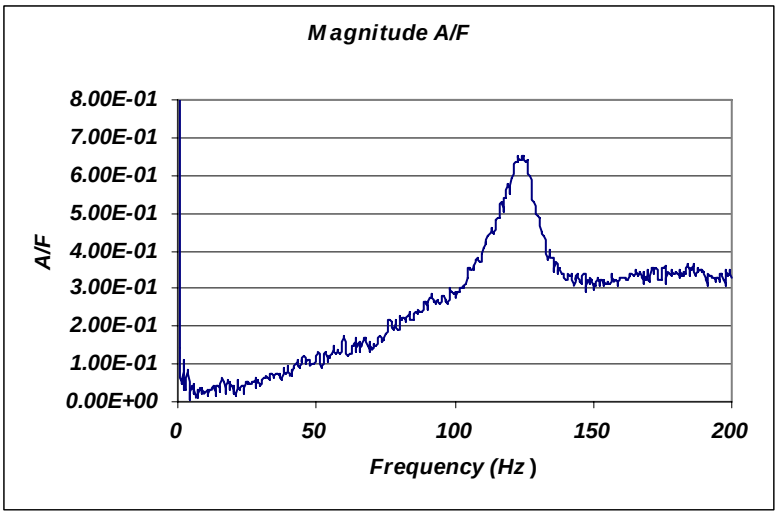

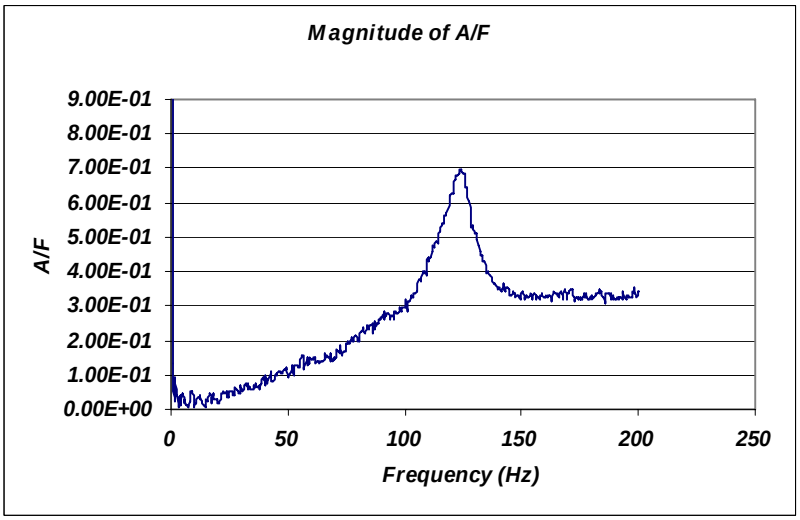

Fig. D3 Impact tests in vertical direction

From Fig.D3, it can be seen that for vertical direction also, the first natural frequency is around 125 Hz. That the two natural frequencies in the horizontal and the vertical direction are almost identical is a coincidence (not a planned result).

In order to get an estimate of the numerical values of the modal parameters in both the horizontal and the vertical direction, it is instructive first to consider the following single degree of freedom system subjected to harmonic excitation, as shown in Fig.D4 below:

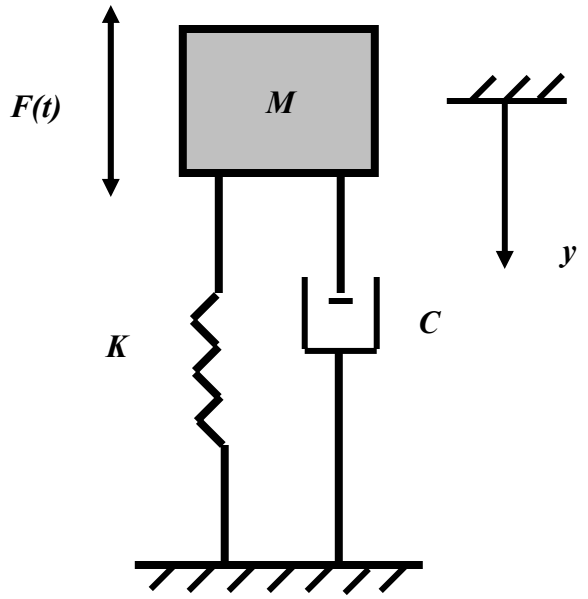

Fig. D4 Single degree of freedom system subjected to harmonic excitation

The differential equation of motion for the above simple system can be written as follows:

$$M\ddot{y}(t) + C\dot{y}(t) + Ky(t) = F(t) = F_0 \sin(\omega t) \qquad \text{(D1)}$$

In equation (1), the coefficients on left hand side for acceleration, velocity and displacement are mass, damping and stiffness, respectively. On the right hand side, there is a time dependent force, with 'ω' as the frequency of excitation.

Using the methods of complex variables that are employed to solve differential equations as (1), the following ratio for the acceleration amplitude of the mass to the amplitude of excitation force can be established:

$$\left|\frac{\ddot{Y}}{F}\right| = \frac{\omega^2}{\sqrt{(K - M\omega^2)^2 + (C\omega)^2}} \qquad \text{(D2)}$$

Based on equation (2), it can be seen that if a system is simplified as a single degree of freedom system and considering linear viscous damping, then acceleration to force ratio is dependent on the system modal parameters K, C, and M.

Equation (D2) is utilized to obtain the modal parameter values of the foundation in horizontal and the vertical directions by curve fitting equation (D2) to the shaker test data. This curve fitting is performed in Microsoft Excel and the modal parameters for the two directions are described in Table D1:

Table D1. Modal parameters of foundation in two directions

Modal Parameters	***Horizontal Direction***	***Vertical Direction***
Stiffness (lb/in)	295000	3700000
Mass (lb-s^2/in)	0.48	6.4
Damping (lb-s/in)	65.5	1350

The foundation's first natural frequency in the horizontal direction as can be seen from the measurement results is around 125 Hz. Before the stiffeners were installed, the natural frequency in the horizontal direction was 70 Hz **[18].** Thus, installation of the structures substantially enhanced the stiffness of the foundation in horizontal direction. This can be seen in the following table:

Table D2. Comparison of modal parameters in two directions

Modal Parameters	***Horizontal direction***		***Vertical direction***	
	Previous	***Current***	***Previous***	***Current***
Stiffness (lb/in)	90590	295000	NA	3700000
Mass(lb-s^2/in)	0.5	0.48	NA	6.4
Damping (lb-s/in)	45.5	65.5	NA	1350

ADDITION OF THIRD STIFFENER STRUCTURE

A third stiffener structure was added to the foundation for the experimental testing of the two-disk rotor configurations. The third structure was added to stiffen up the foundation further in the horizontal direction and to reduce the stiffness asymmetry further, because this is one of the important factors that causes rotordynamic instability due to slippage in shrink fit and interference fit joints.

The same procedure as outlined in the previous pages is applied to determine experimentally the modal parameters of the foundation. The experimental results and the values of the foundation modal parameters in the horizontal direction are described below:

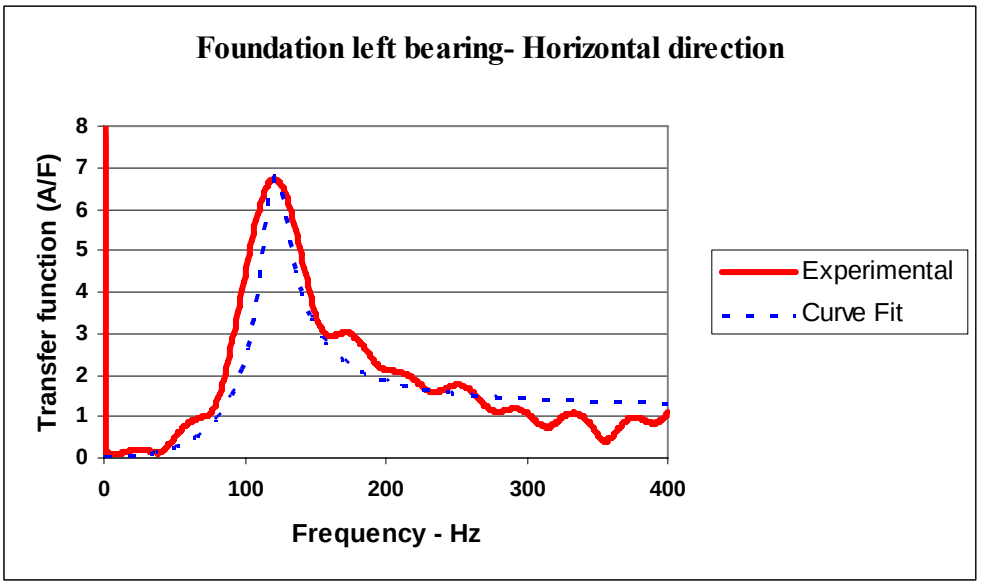

Fig.D5 Acceleration-Force transfer function graph of the foundation in horizontal direction

From the curve fitting of the acceleration /force data in the frequency domain, the following foundation modal parameters are found to best fit the experimental data:

Table D3. Foundation modal parameters after the addition of stiffener structure

Modal Parameters	***Horizontal Direction***	***Vertical Direction***
Stiffness (lb/in)	48000	3700000
Mass (lb-s^2/in)	0.835	6.4
Damping (lb-s/in)	112	1350

Table D3 shows that the addition of the third stiffener structure results in an increase of foundation's horizontal stiffness, mass and damping.

BALL BEARING PARAMETERS

The stiffness and damping parameters of the ball bearings are presented below. These parameters are calculated by specifying the bearing parameters such as the number of balls, bearing inside and outside diameters and the axial width of the bearing. The built-in code in XLTRC^{TM} calculates the corresponding bearing stiffness and damping coefficients, which can be used to perform rotordynamic simulations by connecting the ball bearing coefficients file to the ground or foundation, which is the procedure adopted in the rotordynamic simulations in this Dissertation.

The ball bearing coefficients are presented in Table D4:

Table D4. Ball bearing coefficients

Speed	Kxx	Kxy	Kyx	Kyy	Cxx	Cxy	Cyx	Cyy
RPM	Lb/in	Lb/in	Lb/in	Lb/in	Lb-s/in	Lb-s/in	Lb-s/in	Lb-s/in
0	5.6e+5	0	0	5.6e+5	0	0	0	0
2000	5.7e+5	0	0	5.7e+5	0	0	0	0
4000	5.3e+5	0	0	5.3e+5	0	0	0	0
6000	4.8e+5	0	0	4.8e+5	0	0	0	0
8000	4.5e+5	0	0	4.5e+5	0	0	0	0
10000	4.3e+5	0	0	4.3e+5	0	0	0	0

Table D4 shows that the ball bearing direct stiffness coefficients vary slightly with the rotational speed and they are of the order of magnitude of 1e+5 lb/in. There is no cross-coupling and no direct damping offered through the ball bearings.

APPENDIX E

SUMMARY OF DISSERTATION

On the recommendation of the Committee members, the final examination presentation slides given by the student in the defense of his doctorate dissertation are presented in its entire details in this Appendix. The purpose of presenting these slides is to provide the readers a quick, graphical summary of the student's doctoral research.

Shrink Fit Effects on Rotordynamic Stability: Experimental and Theoretical Study

Final Examination
for Doctor of Philosophy Degree
in Mechanical Engineering

Turbomachinery Laboratory
Texas A&M University, College Station, TX

February 28, 2007

Doctoral Candidate
SYED MUHAMMAD MOHSIN JAFRI
(MECHANICAL ENGINEERING DEPARTMENT)

Committee Members

- DR. JOHN M. VANCE (Mechanical Engineering Department)
- DR. ALAN B. PALAZZOLO (Mechanical Engineering Department)
- DR. LUCIANA R. BARROSO (Civil Engineering Department)
- DR. DAEJONG KIM (Mechanical Engineering Department) (Substituting for Dr. Barroso)
- DR. GUY BATTLE (Department of Mathematics)

TEXAS A&M UNIVERSITY, COLLEGE STATION, TX

3/68

Student's Academic and Professional Background

- B.E. in Mechanical Engineering from NED University of Engineering and Technology, Karachi, Pakistan (Jan 1995-May 1999)
- M.S. in Mechanical Engineering from Texas A&M University, College Station, TX (August 2000-May 2004)
- First author of an ASME DETC Conference Paper, published in September 2005 at Long Beach, California.
- Author of an ASME IGTI Conference Paper to be published in May 2007.
- Member of American Society of Mechanical Engineers and Pakistan Engineering Council.
- Ph.D. in Mechanical Engineering (?) from Texas A&M University, College Station, TX (June 2004-present – Expected completion : May 2007)

4/68

Presentation Overview

- Introduction and Background
- Dissertation Objectives
- Research Methodology
- Literature Review
- Conceptual Model of Internal Friction: The Internal Moments Model
- Various Internal Friction Models
- Unique Contribution of this Dissertation
- Experimental Test Facility
- Shrink Fit Analysis Code
- Summary of Experimental Results
- Rotordynamic Simulations of Experiments using XLTRC™

5/68

Presentation Overview…2

- Effect of Axial Location of Disk on Shaft for Single-Disk Rotor
- Rotordynamic Simulations of Imagined Configurations
- Conclusions
- Recommendations for Future Research
- Acknowledgements

6/68

1. Introduction and Background

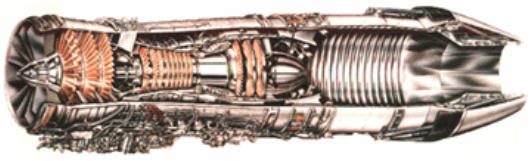

- Most industrial and commercial turbomachines such as aircraft engines (axial compressors and turbines) are constructed using shrink fits between the shaft and the impellers.

- In a centrifugal compressor construction, impellers are mounted on the compressor shaft through shrink fit.

7/68

1. Introduction and Background…2

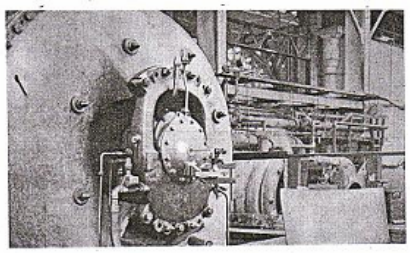

A GE blast furnace compressor (1924)

- In the early 1920's, the **General Electric Company (GE)** encountered a series of blast furnace compressor failures at speeds above the first critical speeds of the compressors.
- **Dr. Newkirk** from the GE investigated the cause of these failures, and came up with shrink fits and oil whirl as main causes of the rotor failures.

8/68

2. Dissertation Objectives

- To develop a practical capability to predict rotor threshold speeds of instability due to shrink fits using physically correct internal moments model.
- To develop a way to determine how cross-coupled moment coefficients should be used in computer codes to predict a rotor instability due to internal friction caused by shrink fits.
- To understand how shrink fits in a rotor assembly affect the dynamic stability of the rotor-bearing system.

9/68

2. Dissertation Objectives…2

Some sub-objectives are:

- Conduct rotordynamic experiments with different rotors with shrink and interference fits to establish some values of shrink fits that cause rotordynamic instability.
- To develop rotordynamic models of various rotor configurations with shrink and interference fit interfaces and understand the effect of various system parameters on stability.

10/68

3. Research Methodology

Research is divided into experimental and theoretical studies.

- For experimental study, vibration measurements results from a single-disk and a two-disk rotor with interference and shrink fit interfaces form the basis of fundamental hypothesis such as numerical values of shrink fits and their distribution on rotordynamic stability.
- For theoretical study, rotordynamic models of single-disk and two-disk rotor configurations (both experimental as well as imagined) are analyzed using the XLTRC^{TM} software.

11/68

4. Literature Review

- **Newkirk and Kimball** (1924) through experiments concluded shrink fit joints as one of the main causes of rotordynamic instability.
- Their experiments showed that the sub-synchronous unstable whirling occurs above the first critical speed of a rotor.
- The unstable whirling frequency is equal to the first natural frequency of the rotor-bearing system.
- The threshold speed of instability is unaffected by rotor balance.

12/68

4. Literature Review…2

- **Gunter** (1965) modeled the internal friction force as a cross-coupled follower force.
- By applying the model of a follower force to an extended Jeffcott rotor model, he derived stability criteria for the rotor.
- He showed through his analysis that the support stiffness asymmetry and external damping stabilize the rotor.
- External damping raises the threshold speed of instability of the rotor-bearing system.

13/68

4. Literature Review…3

- **Black** (1976) analyzed internal friction in a flexible rotor supported on damped, flexible supports.
- He modeled internal friction as a follower force.
- He analyzed three different internal friction models:
  - A. Viscous friction
  - B. Coulomb friction
  - C. Hysteretic friction

14/68

4. Literature Review…4

- Black's analysis showed that:

1. The **viscous friction** model predicts a threshold speed of instability that exceeds the rotor first critical speed.
2. The threshold speed depends upon the external and internal damping of the rotor-bearing system.
3. Once the threshold speed is reached, the subsequent higher speeds are all unstable.

15/68

4. Literature Review…5

4. The **Coulomb friction** model predicts a rotor instability as soon as the rotor first critical speed is traversed, if a certain rotor internal friction parameter (the relaxation strength) exceeds the external damping ratio.

5. The **hysteretic friction** model predicts an unstable speed range, above which the rotor will be stable.

- **Vance and Ying** (1992) validated Black's theoretical predictions of Coulomb and hysteretic models experimentally.

16/68

4. Literature Review…6

- **Walton, Martin and Lund** (1993) proposed the internal friction due to slippage in interference and shrink fit joints as a system of de-stabilizing cross-coupled internal moments.

- They experimentally showed the unstable sub-synchronous vibrations due to slippage in axial splines and shrink fit joints.

- **Lund** (1975) formulated the internal moments due to slippage in shrink fits and axial spline joints in terms of viscous friction, the Coulomb friction and the hysteretic friction models.

17/68

4. Literature Review…7

- Lund's analysis showed that the internal moments for each model are cross-coupled and contain de-stabilizing terms in their mathematical expressions.
- The viscous friction model shows linear expressions for the cross-coupled moments, whereas the Coulomb and the hysteretic friction models are mathematically non-linear.

5. Internal Friction Models….Background

18/68

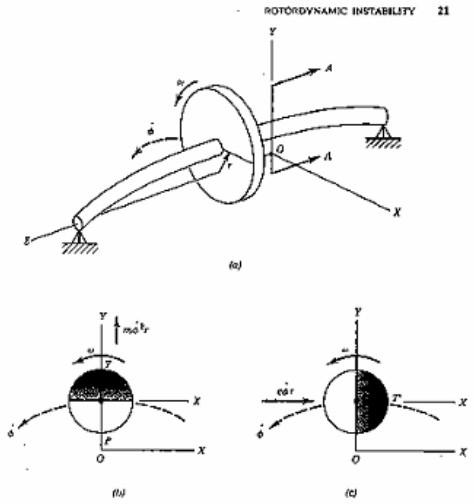

KIMBALL-1924 identified internal friction as destabilizing, with the friction modeled as material hysteresis.

5. Internal Friction Models…2

19/68

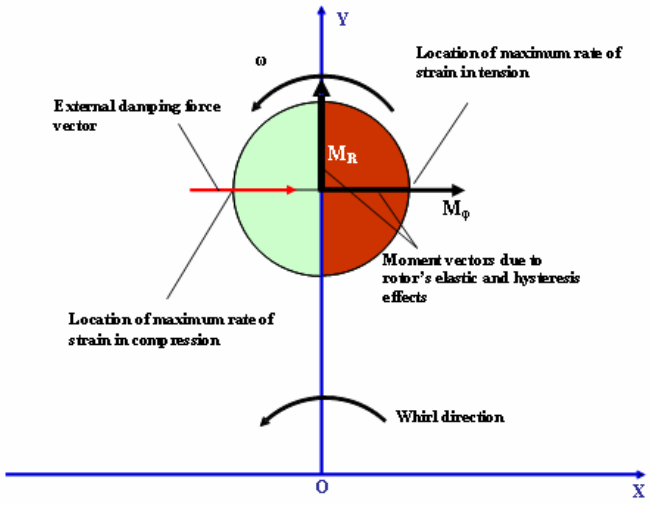

...Back...

5. Internal Friction Models…3

20/68

$$F_X = -K_{XY}Y$$
$$F_Y = -K_{YX}X$$
$$K_{XY} > 0$$
$$K_{XY} = -K_{YX}$$

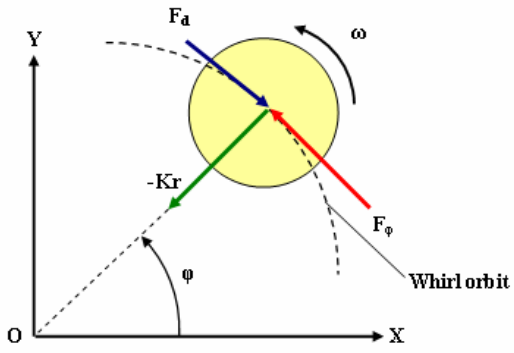

Gunter's follower force model for internal friction

5. Internal Friction Models…4

21/68

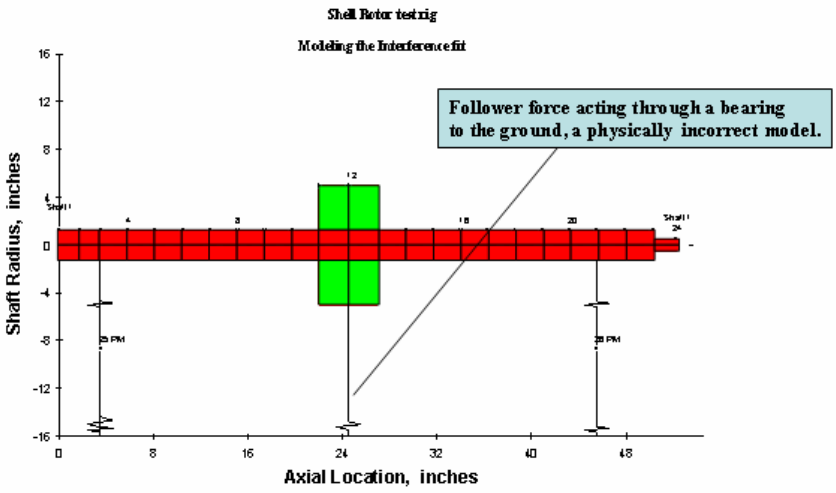

5. Internal Friction Models- The Internal Moments Model…5

22/68

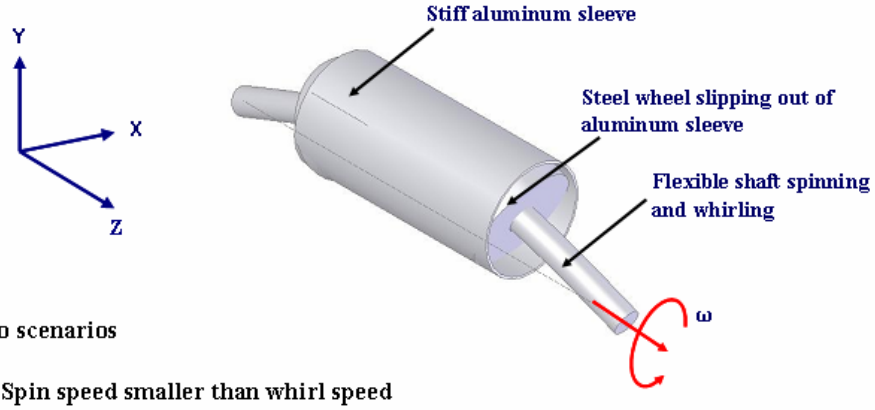

Two scenarios

A. Spin speed smaller than whirl speed

B. Spin speed larger than whirl speed

5. Internal Friction Models- The Internal Moments Model…6

23/68

Free-body diagram of the steel shaft -showing internal friction forces on the wheels

$$V_{Sliding} = R\dot{\alpha}\cos\psi - R\dot{\beta}\sin\psi = R\sqrt{\dot{\alpha}^2 + \dot{\beta}^2}\,\sin(\psi - \gamma)$$

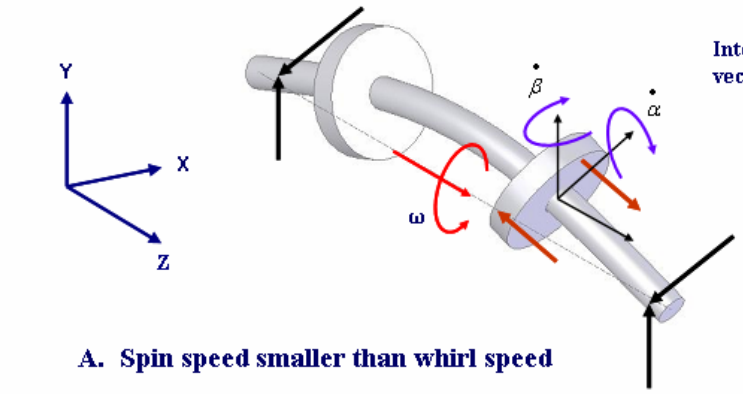

A. Spin speed smaller than whirl speed

5. Internal Friction Models - The Internal Moments Model…7

24/68

Equivalent internal friction moment vectors at the interface

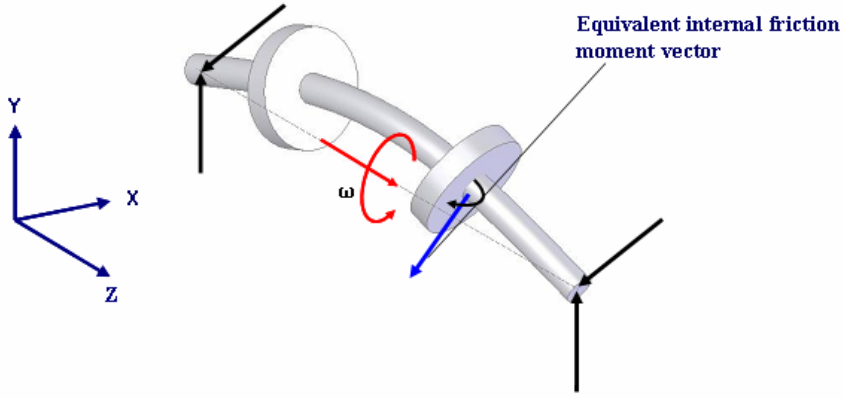

A. Spin speed smaller than whirl speed

5. Internal Friction Models - The Internal Moments Model…8

25/68

Free-body diagram of steel shaft

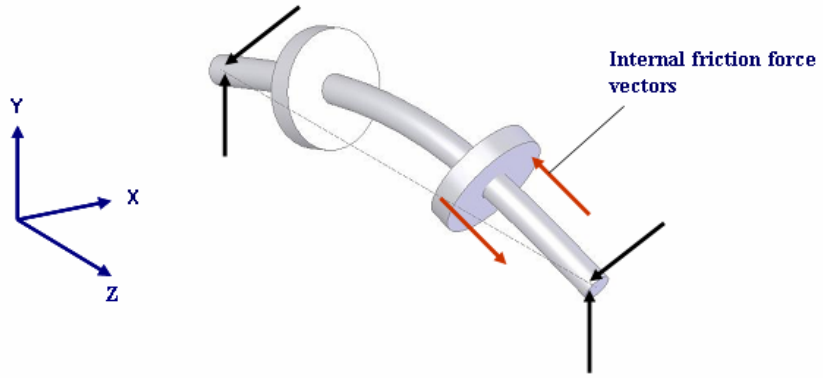

B. Spin speed larger than whirl speed

5. Internal Friction Models - The Internal Moments Model…9

26/68

Equivalent internal friction moment vectors at the interface

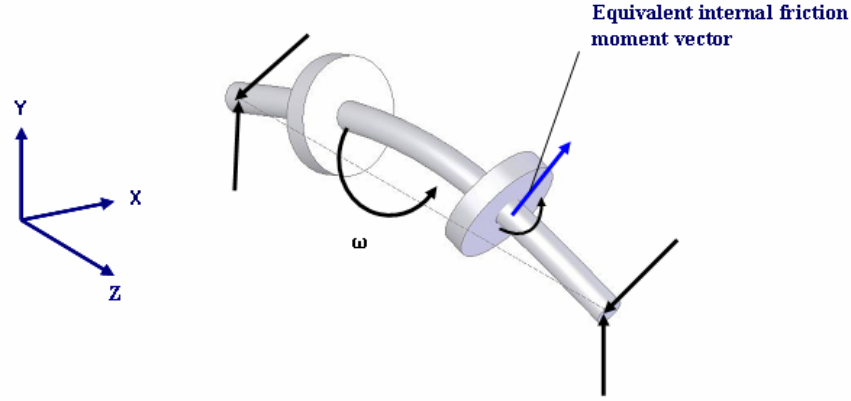

B. Spin speed larger than whirl speed

27/68

6. Unique Contribution of this Dissertation

- Experimental validation of the internal friction moment model using shrink fitted rotor assemblies (a single-disk and a two-disk rotor)
- Implementation of the internal friction moments model in XLTRC^{TM} software to predict threshold speeds of instability for a rotor-bearing system.
- Theoretical study of various system parameters on a rotor system stability.

28/68

7. Internal Moments – Various Models

The viscous friction model

$$M_X = K\alpha_X + C(\dot{\alpha}_X + \omega\alpha_Y)$$

$$M_Y = K\alpha_Y + C(\dot{\alpha}_Y - \omega\alpha_X)$$

$$K_{\alpha X\alpha Y} = C\omega$$

$$K_{\alpha Y\alpha X} = -C\omega$$

$$\boxed{K_{\alpha X\alpha Y} = -K_{\alpha Y\alpha X}}$$

Destabilizing cross-coupled terms

29/68

7. Internal Moments – Various Models…2

The Coulomb friction model

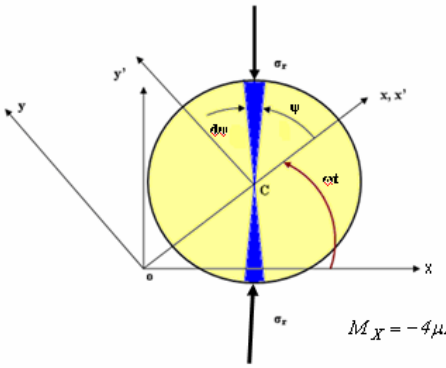

Cross-coupling terms

$$M_X = -4\mu R^2 L\sigma_r \frac{(\dot{\alpha}_X + \omega\alpha_Y)}{\sqrt{(\dot{\alpha}_X + \omega\alpha_Y)^2 + (\dot{\alpha}_Y - \omega\alpha_X)^2}}$$

$$M_Y = -4\mu R^2 L\sigma_r \frac{(\dot{\alpha}_Y - \omega\dot{\alpha}_X)}{\sqrt{(\dot{\alpha}_X + \omega\alpha_Y)^2 + (\dot{\alpha}_Y - \omega\alpha_X)^2}}$$

30/68

7. Internal Moments – Various Models…3

The hysteretic friction model

$$M_X = [K + i\frac{1}{2}C(sgn(\Omega+\omega) + sgn(\Omega-\omega))]\alpha_X + \frac{1}{2}C(sgn(\Omega+\omega) - sgn(\Omega-\omega))\alpha_Y$$

$$M_Y = [K + i\frac{1}{2}C(sgn(\Omega+\omega) + sgn(\Omega-\omega))]\alpha_Y - \frac{1}{2}C(sgn(\Omega+\omega) - sgn(\Omega-\omega))\alpha_X$$

8. Experimental Test Facility

31/68

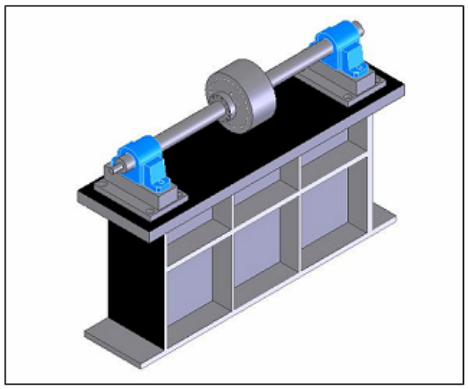

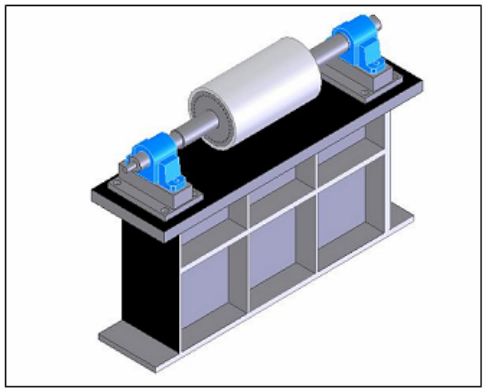

Two types of rotors tested experimentally:

1. A single-disk rotor
2. A two-disk rotor

32/68

8. Experimental Test Facility…2

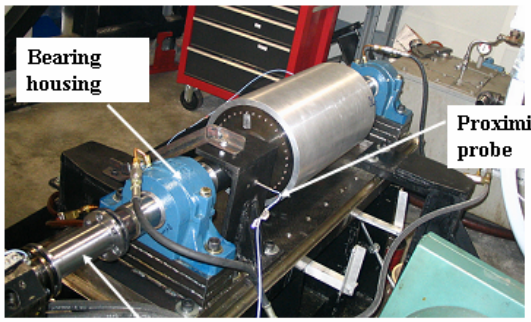

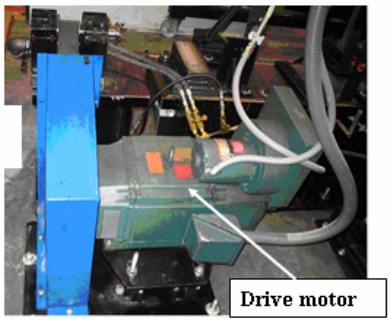

Speed limit = 12000 rpm

33/68

8. Experimental Test Facility…3

ADRE DAQ

LVTRC DAQ

SPEED CONTROLLER UNIT

34/68

8. Experimental Test Facility…4

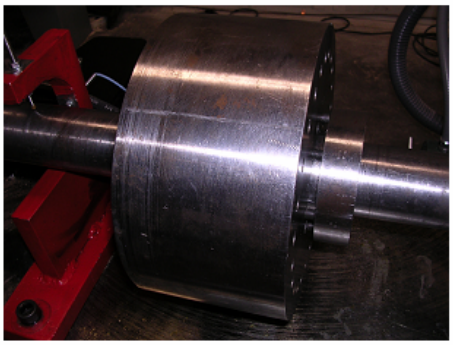

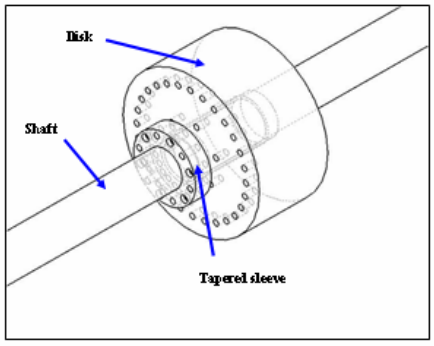

- Tapered sleeve designed and developed by Revolve Technologies, Inc.
- Tapered sleeve between the shaft and the disk creates an interference fit.

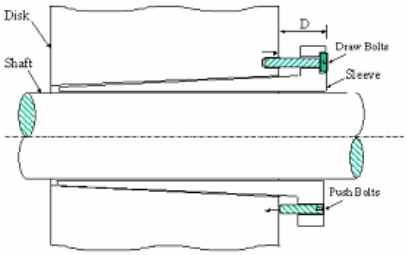

35/68

8. Experimental Test Facility…5

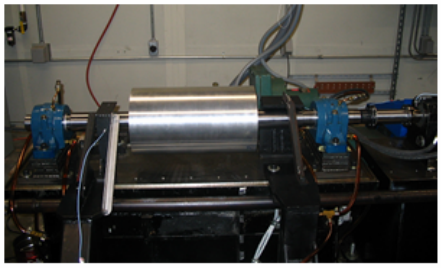

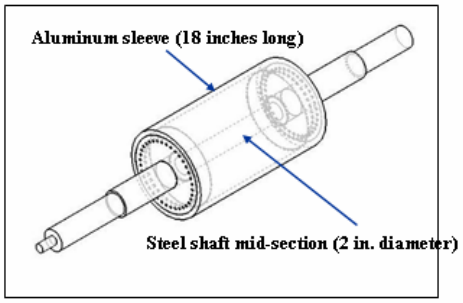

Various configurations for the two-disk rotor with different shrink fit distributions tested. Some configurations are:

1. Unsymmetric shrink fits with 10 in. OD sleeve (Unstable)
2. Symmetric fits (7 Mils Diametral)with 9.25 in OD sleeve (Stable)
3. Symmetric fits (10 Mils Diametral) with 9.5 in. OD sleeve (Stable)

36/68

8. Experimental Test Facility…6

Undercut sleeve end

Full contact sleeve end

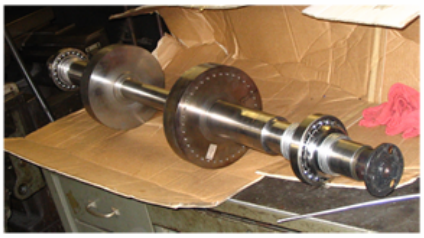

9. Shrink Fit Analysis Code

37/68

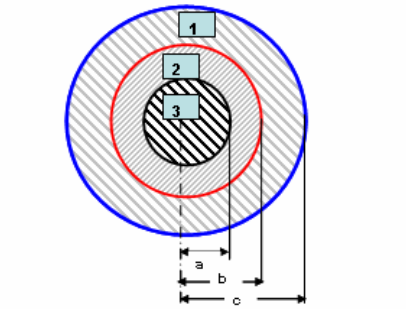

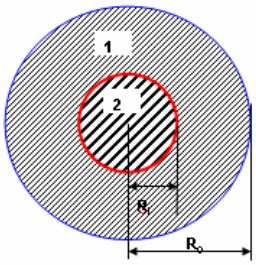

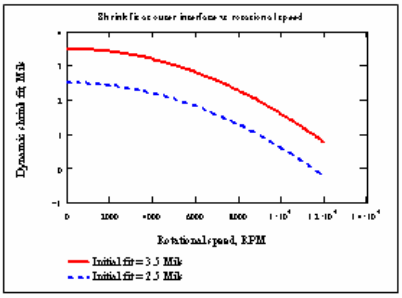

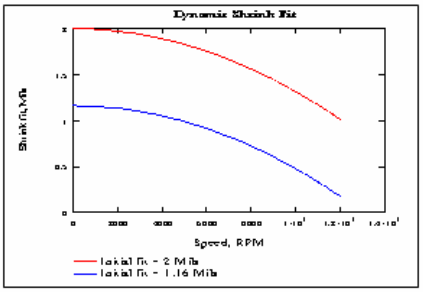

9. Shrink Fit Analysis Code…2

38/68

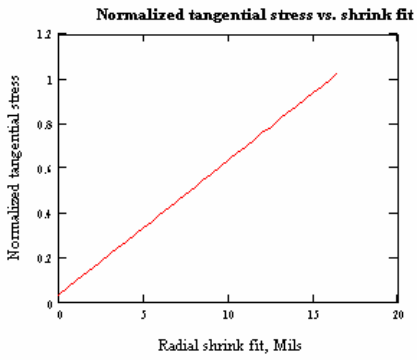

Aluminum-Steel interface
(Two-disk rotor)

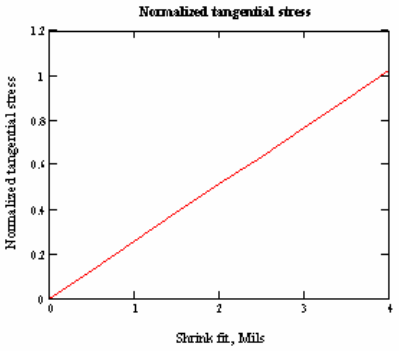

Steel-Steel interface
(Single-disk rotor)

39/68

10. Experimental Results

Single-disk rotor : Loose fit results (1 Mils radial at 6000 rpm)

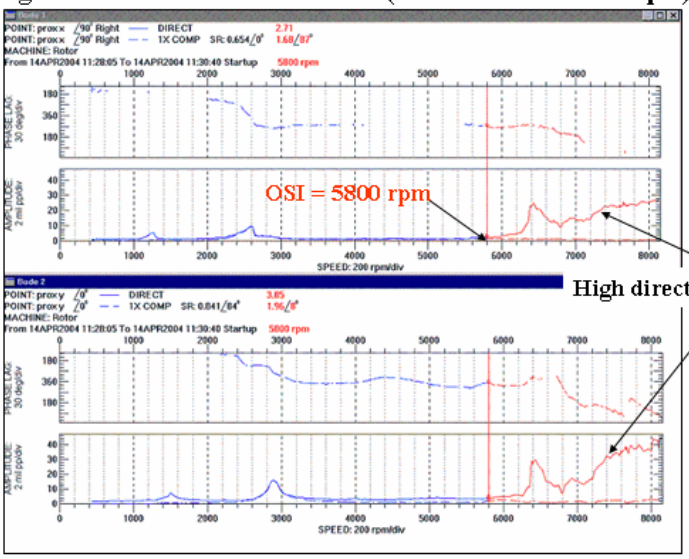

40/68

10. Experimental Results…2

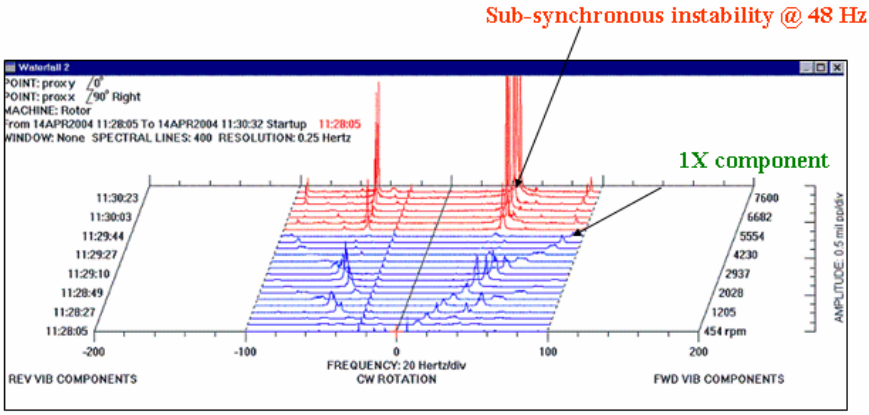

Single-disk rotor : Loose fit results (Waterfall Plot)

41/68

10. Experimental Results…3

Single-disk rotor : Tight fit results (1 Mils radial at 11000 rpm)

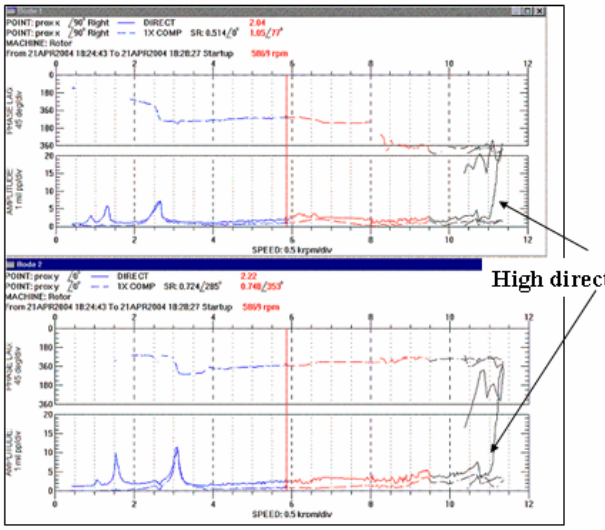

42/68

10. Experimental Results…4

Sub-synchronous instability @ 48 Hz

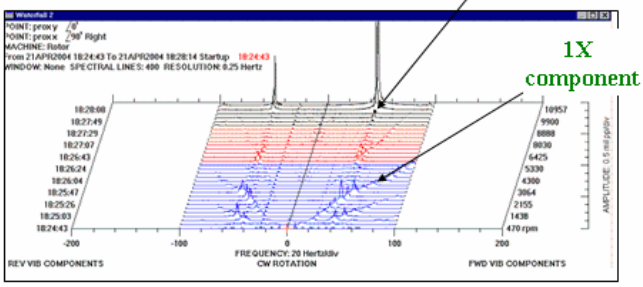

Single-disk rotor : Tight fit results (Waterfall Plot)

43/68

10. Experimental Results…5

Two-disk rotor : Unsymmetric fit results (ADRE Data)

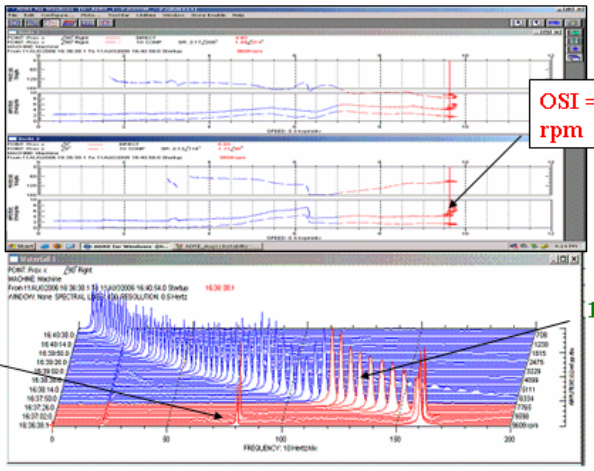

44/68

10. Experimental Results…6

Two-disk rotor : Unsymmetric fit results (LVTRC Data)

Spectrum Plot at 9720 rpm

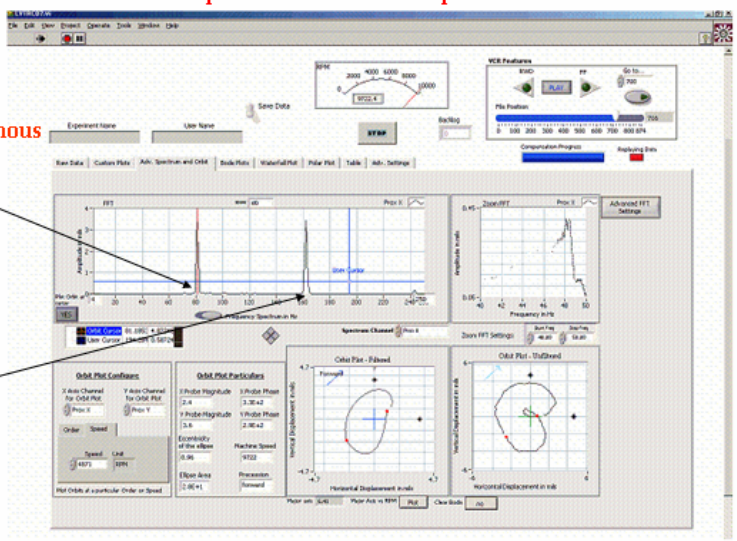

10. Experimental Results…7

45/68

Two-disk rotor : Unsymmetric fit results (LVTRC Data)

Spectrum Plot at 9330 rpm

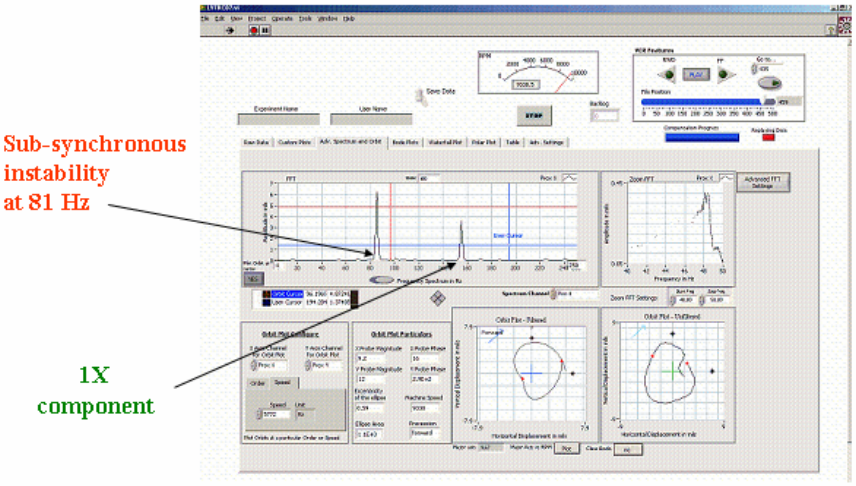

10. Experimental Results…8

46/68

Two-disk rotor : Unsymmetric fit results (LVTRC Data)

Spectrum Plot at 7350 rpm

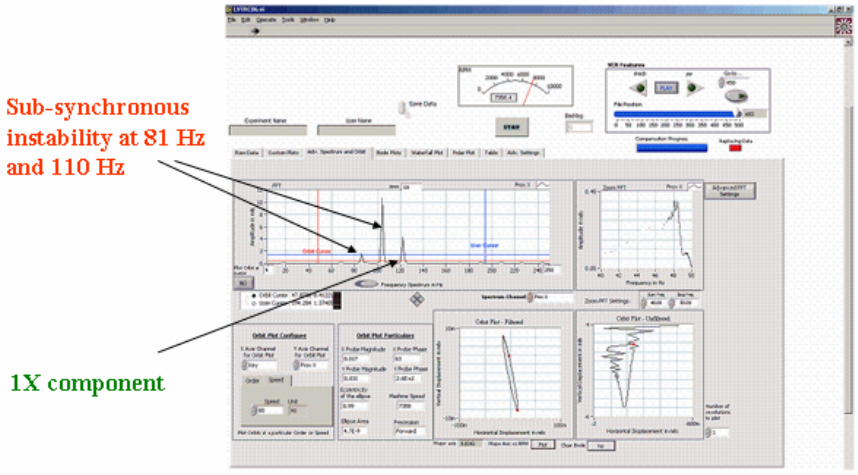

Rotor wreckage took place in this testing at 7000 rpm during coast-down.

47/68

10. Experimental Results…8

48/68

11. Rotordynamic Simulations of Experiments using XLTRC™

- XLTRC™ is a finite element method-based software for rotordynamic analysis.

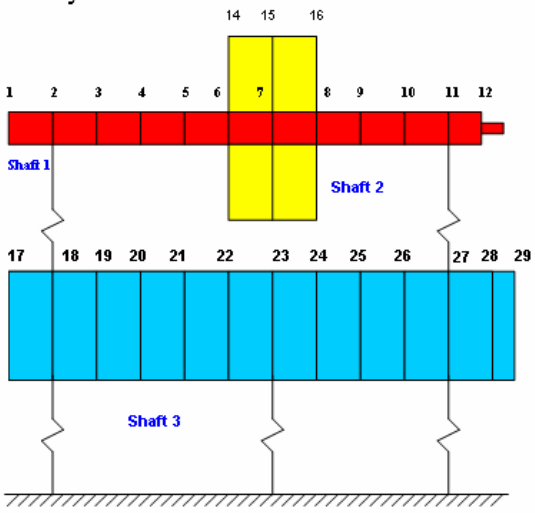

11. Rotordynamic Simulations…2

49/68

Shrink fit interface modeling

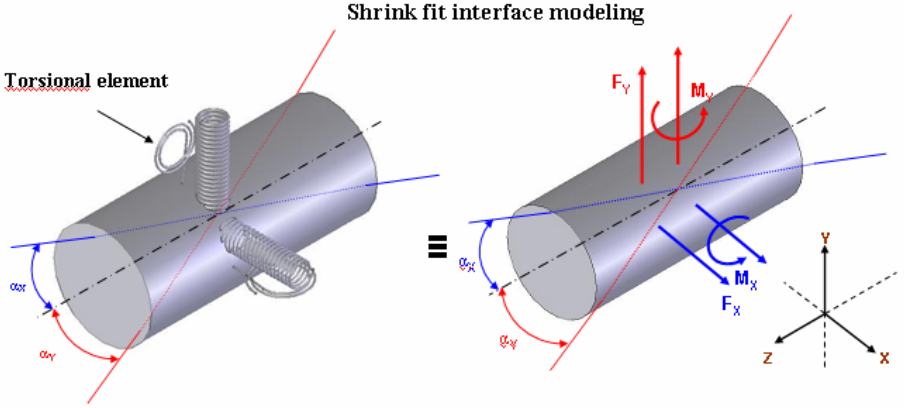

- Shrink fit is modeled as a system of cross-coupled moments.
- The interface friction is defined as a moment bearing file between the shaft and the disk.

11. Rotordynamic Simulations…3

50/68

$$M_X = K\alpha_X + C(\dot{\alpha}_X + \omega\alpha_Y)$$

$$M_Y = K\alpha_Y + C(\dot{\alpha}_Y - \omega\alpha_X)$$

Microsoft Excel - Internal friction moments_Loose side_Thicktube_FullForm.xls

User defined coefficients for sample rotor

Myx	Myy	Kaxax	Kaxay	Kayax	Kayay	Caxax	Caxay	Cayax	Cayay
lb-s**2/in	lb-s**2/in	lb-in	lb-in	lb-in	lb-in	lb-in-s	lb-in-s	lb-in-s	lb-in-s
0	0	1.00E+04	0.00E+00	0.00E+00	1.00E+04	225	0	0	225
0	0	1.00E+04	2.25E+05	-2.25E+05	1.00E+04	225	0	0	225
0	0	1.00E+04	4.50E+05	-4.50E+05	1.00E+04	225	0	0	225
0	0	1.00E+04	6.75E+05	-6.75E+05	1.00E+04	225	0	0	225
0	0	1.00E+04	9.00E+05	-9.00E+05	1.00E+04	225	0	0	225
0	0	1.00E+04	1.13E+06	-1.13E+06	1.00E+04	225	0	0	225
0	0	1.00E+04	1.35E+06	-1.35E+06	1.00E+04	225	0	0	225
0	0	1.00E+04	1.58E+06	-1.58E+06	1.00E+04	225	0	0	225
0	0	1.00E+04	1.80E+06	-1.80E+06	1.00E+04	225	0	0	225
0	0	1.00E+04	2.03E+06	-2.03E+06	1.00E+04	225	0	0	225
0	0	1.00E+04	2.25E+06	-2.25E+06	1.00E+04	225	0	0	225
0	0	1.00E+04	2.48E+06	-2.48E+06	1.00E+04	225	0	0	225
0	0	1.00E+04	2.70E+06	-2.70E+06	1.00E+04	225	0	0	225

51/68

11. Rotordynamic Simulations…4

Single-disk rotor simulation: Loose fit

$K_{aXaX} = K_{aYaY} = 1 \times 10^4 lb - in / rad$

$C = 6923.2$ lb-in-s/rad

- Predicted OSI = 5800 rpm @ 3000 cpm
- Predicted first critical speed = 3000 rpm

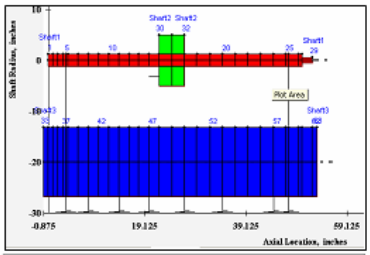

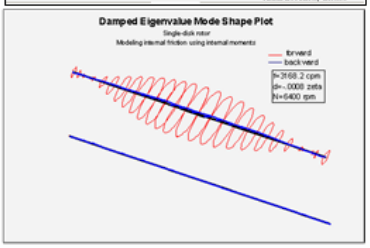

52/68

11. Rotordynamic Simulations…5

Single-disk rotor simulation: Tight fit

$K_{aXaX} = K_{aYaY} = 1 \times 10^5 lb - in / rad$

$C = 2148.6$ lb-in-s/rad

- Predicted OSI =11400 rpm @ 2900 cpm
- Predicted first critical speed = 3000 rpm

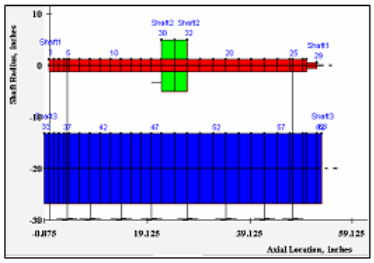

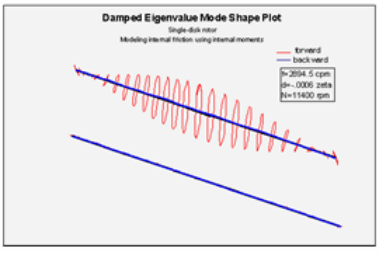

11. Rotordynamic Simulations…6

53/68

Two-disk rotor simulation: Unsymmetric fit

Tight end

$K_{aXaX} = K_{aYaY} = 5 \times 10^8 \, lb-in/rad$

$C = 0 \quad lb\text{-}in\text{-}s/rad$

- Predicted OSI =9500 rpm @ 6600 cpm
- Predicted first critical speed = 6480 rpm

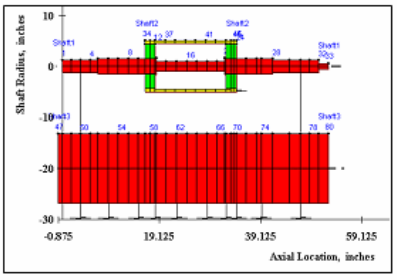

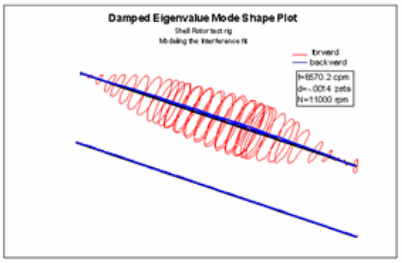

Loose end

$K_{aXaX} = K_{aYaY} = 1 \times 10^9 \, lb-in/rad$

$C = 2148.6 \, lb\text{-}in\text{-}s/rad$

12. Free-free tests on the single-disk rotor

54/68

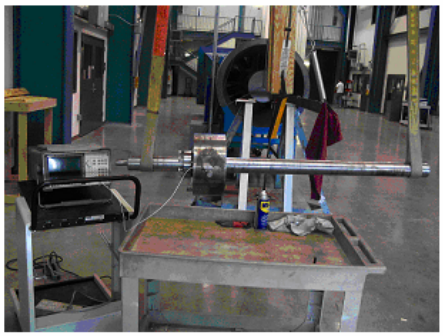

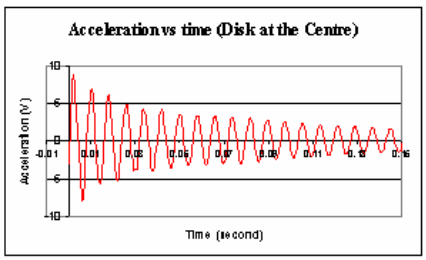

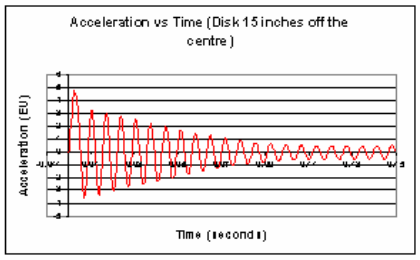

55/68

13. Simulations of imagined rotor configurations

Model 1. Disk offset from the centre

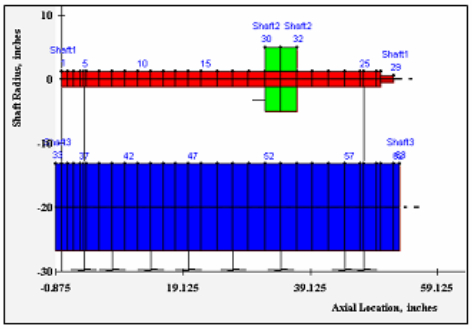

- Predicted first critical speed = 3590 rpm.
- Increase in critical speed caused by shifting of the disk, thus reducing the modal mass.
- More unstable as compared to the disk at the centre.
- C = 6207 lb-in-s/rad for OSI = 3800 rpm.

56/68

13. Simulations of imagined rotor configurations…2

Model 2. Disk axial width = 15 inches with same weight (as compared to 5 inches in baseline)

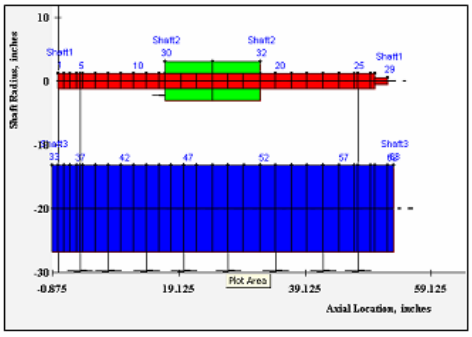

- Predicted first critical speed = 4200 rpm
- Increase in critical speed caused by stiffening effect of the disk, which acts more as a long sleeve.
- More unstable as compared to the loose fit experimental case (due to larger width of disk)
- C = 6207 lb-in-s/rad for OSI = 5800 rpm

13. Simulations of imagined rotor configurations…3

57/68

Model 3. Disk axial width = 1 inches with same weight (as compared to 5 inches in baseline)

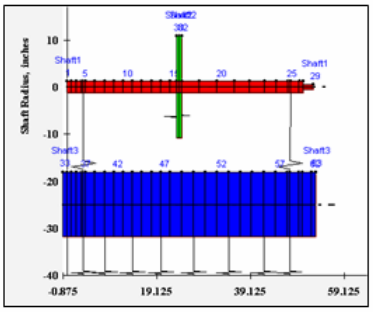

- Predicted first critical speed = 2700 rpm
- Slight decrease in critical speed caused by reduced width of the disk, resulting in less stiffening.
- Slightly more stable as compared to the loose fit experimental case (due to smaller width of disk)
- C = 7100 lb-in-s/rad for OSI = 5800 rpm

13. Simulations of imagined rotor configurations…4

58/68

Model 4. Vance-Ying Rotor (Experimental case; not imagined)

- Shaft diameter = 0.375 in.
- Bearing span = 16 in.
- Disk OD = 2.9 in.
- Sleeve length = 7.5 in.
- Sleeve thickness = 1/8 in.

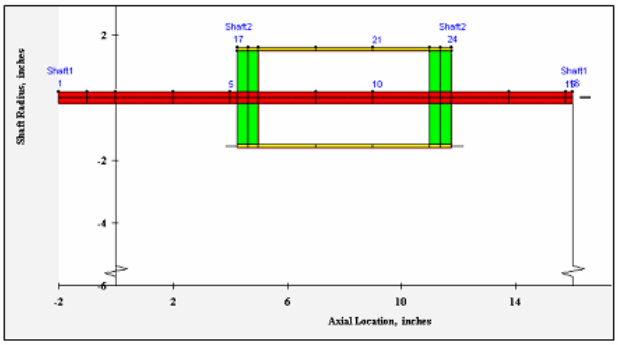

- Predicted first critical speed = 3000 rpm (same as experimental)
- OSI = 3000 rpm @ 2932 cpm
- C = 0.14 lb-in-s/rad for above OSI

13. Simulations of imagined rotor configurations…5

59/68

Model 5. Mid-shaft section diameter = 3 inches

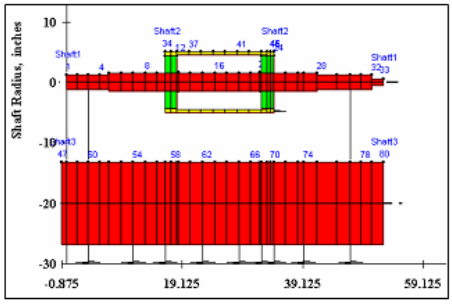

- Predicted first critical speed = 6700 rpm
- Slight increase in critical speed (as compared to experiment) caused by increased diameter of the shaft.
- More stable as compared to the experimental case (due to increased shaft bending stiffness)
- Stable for speeds up to 12000 rpm and above.

13. Simulations of imagined rotor configurations…6

60/68

Model 6. Sleeve length = 10 inches (as compared to 18 inches in the experimental case)

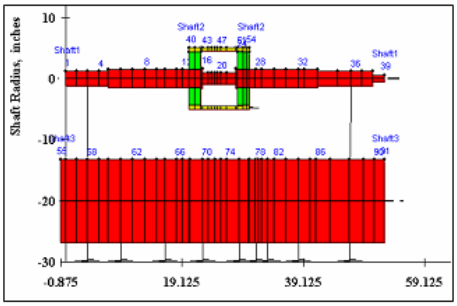

- Predicted first critical speed = 5500 rpm
- More stable as compared to the experimental case (due to lesser bending of mid-section of the shaft)
- C > 7100 lb-in-s/rad for OSI = 10500 rpm

14. Conclusions

61/68

- The internal friction moments model of Lund is shown to be physically correct model that predicts rotordynamic instability on different experimental setups.
- For the single-disk rotor, there is a repeatable value of radial interference fit (1 mils) that shows experimental evidence of sub-synchronous instability due to internal friction.
- For the two-disk rotor, the tight and loose fit distribution (with an undercut) produced catastrophic rotordynamic instability.
- The value of fit for the two-disk rotor in unstable configuration is also close to 1 mils radial interference.

14. Conclusions…2

62/68

- The internal moments model is physically correct, though possibly no more useful or easier model, than the widely followed Gunter's follower force model for modeling internal friction.
- The internal moments model requires experimental measurements such as first critical speed and threshold speed of instability to determine the internal moments parameters such as joint moment stiffness and damping coefficients to predict the rotordynamics of a rotor-bearing system.

14. Conclusions…3

- XLTRC™ simulations of the experiments show that the internal friction moment parameters, specifically the required moment damping coefficients to predict correct threshold speeds of instability, vary from configuration to configuration of the rotors.

- XLTRC™ simulations of imagined rotor configurations show that the axial width for a single-disk rotor affects the dynamic stability. An increased axial width leads to a more unstable rotor as compared to a decreased axial width.

14. Conclusions…4

- XLTRC™ simulations of imagined configurations also show that the axial location of the disk on the single-disk rotor affects the dynamic stability and amount of internal friction (verified experimentally using free-free tests). A disk off-centered from mid-span of the shaft is more unstable.

- XLTRC™ simulations for both the single-disk and the two-disk rotor show that the increase of shaft diameter where the disk is shrink fitted to the shaft is one of the most reliable ways to stabilize the rotor-bearing system against internal friction instability.

65/68

15. Recommendations for Future Research

- The internal friction moment model parameters such as the direct moment stiffness and damping coefficients need to be analyzed in more detail.
- Analytical and computational procedures for computation of moment coefficients as functions of several rotor-bearing parameters such as mode shape, slope of the mode shape, tightness of the fits and geometry of the interface should be derived and developed.
- More body of experimental data with shrink and interference fit rotors can add significantly to an understanding of the proposed analytical work.

66/68

15. Recommendations…2

- XLTRC^{TM} can be improved by adapting to accept the non-linear models such as the Coulomb friction model to predict the rotordynamics of a rotor-bearing system with internal friction due to shrink and interference fits.

67/68

16. Acknowledgements

- Turbomachinery Research Consortium (TRC) for their financial support of the Internal Friction Project, from September 2003-May 2006.
- Dr. John M. Vance for giving me an opportunity to work on the project and be able to greatly expand my experimental and theoretical knowledge.
- All the other Committee Members for agreeing to serve on the committee. Special thanks to Dr. Kim for agreeing to substitute for Dr. Barroso.
- My colleagues and co-workers at the Turbomachinery Laboratory, especially Eddie Denk, for helping me in the machine shop and hardware issues in the test cell .
- My family.

68/68

Thank You

VITA

Syed Muhammad Mohsin Jafri received his Bachelor of Engineering degree from NED University of Engineering and Technology, Karachi, Pakistan in May 1999. He enrolled in the Mechanical Engineering Department at Texas A&M University, College Station in August 2000 to pursue a Master of Science degree, and received the degree in May 2004. He continued his education to pursue a Doctor of Philosophy degree in Mechanical Engineering at Texas A&M University, College Station. His research and educational background during the graduate studies include dynamics, vibrations and rotordynamics.

Mr. Jafri can be reached at Deep Sea Engineering & Management, Inc., 10333 Richmond Avenue, Suite 250, Houston, TX 77042. His e-mail address is mjafri@neo.tamu.edu.